Planetary processes active and ancient: Hollowing on Mercury, early crust formation on Mars, and identifying habitats in Mars-analog landscapes.

A Dissertation Presented for the
Doctor of Philosophy
Degree
The University of Tennessee, Knoxville

Michael S. Phillips
August 2021

Copyright © 2021 by Michael S. Phillips.
All rights reserved.

ACKNOWLEDGEMENTS

There are countless people who have helped me achieve my Ph.D. and for whom I am immensely grateful. I would like to thank my advisor, Dr. Jeffrey Moersch, whose guidance shaped me into a better critical thinker, communicator, and scientist. Jeff has been incredibly supportive, not only by sharpening my skills as a scientist, but by facilitating connections for me in the scientific community that have led to amazing opportunities in the field and the lab. I would like to thank my committee, Drs. Christina Viviano, Hap McSween, Josh Emery, Ania Szynkiewicz, and Liem Tran for their helpful feedback throughout my six years at UTK. I would especially like to thank Christina Viviano, for taking a chance on me as her intern at the Applied Physics Laboratory, for her continued and invaluable input on my work, and for always helping me improve my figures.

I would also like to thank my mentors outside of UTK, Drs. Nathalie Cabrol, Kim Warren-Rhodes, Kevin Rhodes, Nancy Hinman, Pablo Sabron, and many others. I am grateful to Nathalie for her conversation, mentorship, and the opportunity to join the SETI-NAI team in Chile working in some of the most starkly beautiful places I've ever seen. I would like to thank Kim, Kevin, Nancy, and Pablo for being such great friends in the field, for their collaborative mindset, and for including me in their science (and also for the rum!).

I would like to recognize the funding sources that made my dissertation possible. The graduate research assistantship for Chapter Three was provided by NAI grant no. NNX15BB01A, "Changing Planetary Environments and the Fingerprints of Life", awarded to the SETI institute NAI team with PI Dr. Nathalie Cabrol. Chapter Two was funded, in part, by NASA Mars Data Analysis Program grant number NNX14AM16G awarded to Dr. Christina Viviano and by the CRISM investigation on the Mars Reconnaissance Orbiter through JPL subcontract 1277793. Chapter Two was also funded, in part, by NASA Mars Data Analysis Program grant number 80NSSC20K0938 awarded to me. Additionally, I am grateful to Dr. Dawn Taylor and her late husband Dr. Larry Taylor, for endowing the Dawn and Lawrence Taylor Doctoral Research Fellowship, of which I was a recipient in the Spring of 2020. Lastly, the first four years of my research at UTK were subsidized by the Chancellor's fellowship provided by UTK.

I cannot thank enough the EPS staff, Angie Staley, Melody Branch, Teresa Parrot, and Diane Pealor, who keep our department functioning every day.

I would not have made it through my first few years in graduate school without the support of my friends and fellow grad students Audrey Martin, Jessi Ende, and Cameron McCarty. Thank you to all my friends who helped me along the way, especially Tony Maue, Eric MacLennan, Diego Sanchez, Haley Horbaly, Hannah

McCarty, Robert Jacobsen, Hannah Jacobsen, Sam Gwizd, Cam Hughes, Johnathan Cox, Rhianna Moore, Ben Carey, and many others.

Thank you to my parents, Jack and Christina, my siblings Jay and Erin, Katie and Joe, Kenny, and Mark, and my nieces and nephews for their love, support, and interest (feigned or otherwise) in my work.

Lastly, I want to thank Hannah Rigoni, my climbing partner, best friend, co-parent to our cats, and wife-to-be, for her love, support, and beta.

ABSTRACT

This dissertation comprises a thermophysical model that shows elemental sulfur may be involved in the potentially active processes that form enigmatic features called hollows on the Mercurian surface, a suite of remote sensing techniques that unveil anorthositic rocks in ancient crust on Mars, and deep learning to discover the spatial resolutions necessary to identify astrobiology targets in images of Mars analog landscapes.

On Mercury, hollows are high-reflectance, flat-floored depressions observed nearly globally. Hollows are thought to form via sublimation, or a “sublimation-like” process, but the identity of the sublimating phase is poorly constrained. To better understand which phase might be responsible for hollow formation, I calculated sublimation rates for 57 candidate hollow-forming volatile phases at Mercury-relevant conditions. I found that elemental sulfur is the phase most likely responsible for hollow formation. Several limitations with previously published hollow-formation models lead me to suggest a novel model, inspired by terrestrial thermokarst processes, that I dub “Sublimation Cycling Around Fumarole Systems”.

Mars offers a unique opportunity to constrain models of planetary differentiation given its observable record of ancient crust and its middling size among terrestrial planets. Unlike on Earth, where plate tectonic processes have erased the earliest rocks from the geologic record, remnants of martian crust older than ~4.1 Ga (pre-Noachian) are exposed at the surface. Here I present evidence for an extensive, pre-Noachian layered igneous complex north of Hellas basin containing feldspathic rocks, which I interpret as anorthositic. These feldspathic outcrops raise the intriguing possibility that the Hellas-forming impact uplifted a sample of a deep, global, low-density component of the ancient martian crust.

With sample return as an imminent goal for the NASA Mars Exploration Program, precise targeting of rocks and outcrops with significant science value, especially those with the highest probability of containing biosignatures, is a top priority. The increased focus of scientific objectives on locating biosignature-bearing outcrops comes with a need for more precise identification of rover-explorable targets from orbit. Therefore, I established a deep-learning based method for determining the spatial resolutions necessary to identify high-priority, astrobiology targets with a specified confidence level and applied this method to the identification of habitats in images of Mars-analog landscapes. This study serves as a template for quantifying identification confidence as a function of image spatial resolution for habitats across many Mars-analog environments, which could inform the decision making-process for future targets of Mars exploration.

TABLE OF CONTENTS

INTRODUCTION 1
Enigmatic Mercury 1
Ancient Mars 2
CHAPTER I The Lifecycle of Hollows on Mercury: An Evaluation of Candidate Volatile Phases and a Novel Model of Formation. 3
Abstract 4
1. Introduction 5
1.1. Distribution of Hollows on Mercury and Their Association with Mercury's Low Reflectance Material 5
1.2. Relationship to Craters 11
1.3 The Apparent Youth of Hollows 12
1.4. Hollow Formation Models and Candidate Volatiles 13
1.5. Hypothesis 18
2. Method 19
2.1. Thermophysical Model 20
2.2 Sublimation Rate Equations and Choice of Volatile Phases 31
2.2.2 Diffusion Through a Regolith Cover 38
2.3 Metrics for Comparison: Hollow Formation Rates, Timescales, and Latitudinal Extent 41
3. Results 44
3.1 Hollow-Formation Timescales 45
3.2 Regolith Lag Deposits 46
3.3 Model-Predicted Latitudinal Ranges 53
4. Discussion 56
4.1 Elemental Sulfur 58
4.2 Fullerenes 65
4.3 Sulfides 69
4.4 A Novel Model for Hollow Formation: Sublimation Cycling Around Fumarole Systems (SCArFS) 75
4.5 Future Work 91
4.6 Possible Implications 94
5. Conclusions 95
Appendix I 98
CHAPTER II Widespread anorthositic rocks in a pre-noachian layered igneous complex on mars 110
Abstract 111
1. Introduction 112
2. Methods 115
2.1 Detection of primary minerals with VSWIR reflectance spectra 115
2.2 Thermal infrared analysis 117
2.1 Visible image analysis 118
3. Results 118

3.1. VSWIR Detections of Fe-plagioclase 118
3.2 Thermal infrared analysis 121
3.3 Morphologic characterization 122
4. Discussion 124
4.1 Possible lithology and petrogenesis 124
Appendix II 129
Item A: Detecting feldspar in the VSWIR 129
Item B: Constraints on plagioclase petrogenesis given its detectability in the VSWIR 132
Chapter III Establishing thresholds of identification for planetary features using Fully convolutional neural networks: Application to habitats in a Mars-analog landscape 141
Abstract 142
1 Introduction 143
1.1 Motivation 144
1.2 Habitability and habitats 144
1.3 Detecting and identifying 147
1.4 Identifying habitats on Mars 147
1.5 Organization 148
2 Background 148
2.1 Relevant background on convolutional neural networks 149
2.2 Geologic Background: Salar de Pajonales as an Analog to Mars 151
3 Data 154
4 Methods 157
4.1 Data preparation 158
4.2 Network design 163
4.3 Network training 170
4.4 Network evaluation 172
5 Results 178
5.1 RGB-Networks 179
5.2 DEM-Networks 187
5.3 RGB-DEM-Networks 194
6. Discussion 202
6.1 Interpretation of Confidence Scores 202
6.2 General trends in performance metrics and habitat identifiability 202
6.3 A template for building identification confidence curves 205
6.4 DEM data do not enhance semantic segmentation 206
7. Conclusions 207
Appendix III 208
Item A: Primer on Neural Networks 208
Item B: Neural Network Architecture 217
Item C: Supplementary Results 218
CONCLUSIONS 219
Mercury: one less enigma? 219

A periscope into ancient Mars 219
A basis for comparing the identifiability of habitats 220
References 221
VITA 253

LIST OF TABLES

Table 1. 1. Chemical formulas, names, molecular masses, densities, and constants A and B (used in **Eq. 9)** for candidate hollow-forming volatile phases explored in this study. 22
Table 1. 2 Range of parameter values explored and useful model outputs (dw, TI, dt) 25
Table 1. 3 "Best Fit" Parameters 27
Table 1. 4 Comparison to HH02 free parameters 32
Table 1. 5. Estimated hollow-formation rates based on the average depth of hollows within 30° latitudinal bins with two estimates for the timescale of hollow formation (300 Myr and 4 Gyr). Rates are presented in m Gyr^{-1}. 39

Table A1. 1. Phases likely delivered to or generated on Mercury. a: Botta and Bada (2002), b: Pierazzo and Chyba (1999), c: Kerber et al. (2009). 104
Table A1. 2. molecular diameter and mean free path of volatile phases explored in this study. Phases with mean free paths highlighted in red do not meet the assumptions outlined in *Section 2.2.2.* 106
Table A1. 3. Time in years for each phase to sublimate to the depth of a typical hollow at each latitude (c.f., Table 5).**Table A1. 4**. molecular diameter and mean free path of volatile phases explored in this study. Phases with mean free paths highlighted in red do not meet the assumptions outlined in *Section 2.2.2.* 106
Table A1. 5. Time in years for each phase to sublimate to the depth of a typical hollow at each latitude (c.f., Table 5). 108

Table A2. 1. CRISM targeted IDs for all previously published detections of Fe-plagioclase on Mars. See Fig. 2.1. 139
Table A2. 2. CRISM mapping data IDs from which spectra were derived for figures in this publication. 140

Table 3. 1. sUAS camera specifications 156
Table 3. 2. Ground sampling distance (GSD), and empirically-determined spatial resolution metrics for the orthophotomosaics generated in this study. 162
Table 3. 3. Description of the feature classes defined for this study. Classes that are the primary habitats at SdP are highlighted in green. 164
Table 3. 4. Size of the input images at each ground resolved distance expressed in pixels and meters 168
Table 3. 5. Mathematical and qualitative description of network performance metrics used in this study. 173
Table 3. 6. Performance metrics for RGB-Networks 183
Table 3. 7. Certainty Scores (%) for RGB-Networks 185
Table 3. 8. Performance metrics for DEM-Networks 191
Table 3. 9. Certainty Scores (%) for DEM-Networks 193

Table 3. 10. Performance metrics for RGB-DEM-Networks 198
Table 3. 11. Certainty Scores (%) for RGB-DEM-Networks 200

LIST OF FIGURES

Fig. 1. 1 A) Context of hollows in **B**) and **C**) on the south side of a crater southwest of Dali Basin. MESSENGER Narrow Angle Camera frames shown in **B**) and **C**) are outlined in white. **B**) Hollow ID# 6211 from the global database of Thomas et al., 2016, located at ~115.4°E, 43.0°N. NAC image ID: EN0251429891M. **C**) Hollow ID# 6051 from the global database of Thomas et al., 2016 located at ~116.4°E, 42.7°N. NAC image IDs: EN0251401087M, EN0251401092M. Notice the irregular shape, flat floors, and bright rims characteristic of hollows. 6

Fig. 1. 2 Maps of **a)** density of impact craters > 25 km diameter per 10^5 km. Data from Marchi et al. (2013), map reproduced from Weider et al. (2015); **b)** distribution of hollows relative to the northern smooth plains (solid black line) and high-Mg region (solid white line); **c)** distribution of hollows relative to the low-reflectance material (LRM). LRM is highlighted in lavender. It should be noted that many small patches of LRM are covered by dots indicating hollow locations. In **b)** & **c)**, the areas (km^2) of individual hollows/hollow clusters are represented by color on a natural log scale. Hollow location and area data are from Thomas et al. (2014, 2016). Base map is MESSENGER MDIS LOI mosaic (astrogeology.usgs.gov); Vertical dashed lines are the Warm Meridians and the vertical solid line is the Hot Meridian (the other Hot Meridian is at the map edges). **d)** Hollow mean depth binned by 10° latitudinal bins in the northern hemisphere. Error bars are the standard error for hollow depth in each latitudinal bin. Hollow depth data are taken from Blewett et al. (2016). 7

Fig. 1. 3. Conceptual model for hollow formation in a Surface Exposure And Lag Sequestration (SEALS) model (see text in *Section 1.4*). **A**) Three-stage hollow-formation model proposed in Blewett et al. (2013). The basic stages of this model are perhaps the most widely accepted of any hollow-formation model (see, e.g., Thomas et al., 2016). The mechanisms differ between models for how a volatile layer forms (e.g., volcanic sequestration, fractionation in volcanic flows, slag formation in impact melts and lavas, etc.), but the processes proposed by Blewett et al. (2011, 2013) are shown in part A (Stages 1 and 2) of this Figure. In Stage 3, and in all SEALS models, hollows form by loss of a volatile phase upon exposure to the surface via solar heating (or space weathering). Hollow formation ceases after a lag deposit develops and shields the volatile phase. **B**) A more detailed depiction of the process by which hollows form in a SEALS hollow formation model. The depth scale of the cartoon represents ~0.5 to 1 m of regolith. Dots represent a volatile phase and its loss rate at different temperatures: cold and stable (dark dots, left, low volatile loss rate) to hot and unstable (light dots, right, high volatile loss rate). If the loss rate for a given volatile is low at the equilibrium temperature but fast at daytime surface/near-surface temperatures (as the example volatile loss rate shown

with the vertical dashed line), then such a volatile could be responsible for hollow formation within a SEALS model framework. However, if a compound's loss rate at subsurface temperatures is fast at or below equilibrium temperatures, then such a volatile would be unstable under a lag deposit and inconsistent with a hollow formation model that includes sequestration beneath a regolith lag deposit. 14
Fig. 1. 4. Comparison between the volatility temperatures of Zhang and Paige (2009) and those calculated in this work. See text for details on differences. 34
Fig. 1. 5. Sublimation rates vs. temperature for the volatiles in this study. Volatiles are grouped into different plots by compound classes. Legends for the bottom two plots list phases from left to right. Colors correspond to Table 1. Values listed in Table 1 were used to calculate rates using **Eq. 9**..... 36
Fig. 1. 6. Hollows at the cold limit of hollow formation. North-south oriented elevation profiles showing the slopes for hollow 4008 at 71.4°N (A to A') and 4051 at 71.1°N (B to B'). Vertical black bars in the elevation profile show the locations of each hollow along the profiles. Hollow ID numbers are from the global hollow database of Thomas et al. (2016). The elevation profiles show that the slopes on which these hollows have formed are slightly north facing (~1.2° for hollow 4008 and ~0.6° for hollow 4051). Analysis was done with MDIS images <20 m/pixel and with the USGS digital topography map (665 m/pixel resolution) in JMARS. 42
Fig. 1. 7. The vertical axis shows the time in years it would take to sublimate each substance to the average hollow depth for each latitudinal range (Table 5). Colors correspond to the compound classes in Table 1. Horizontal lines are drawn at 1 yr, 1 kyr, 1 Myr, 300 Myr, 4 Gyr to facilitate interpretation. The estimated timescale for hollow formation (derived from hollows in Balanchine crater, Blewett et al., 2016) corresponds to the dashed line at 300 Myr. The circle markers represent the hollow formation timescale for each volatile phase at latitude 40°N, the upper bar is for 71°N, and the lower bar is for 0°N (see legend). If a candidate hollow-forming phase plots below the dashed line at 40°N along the warm meridian and below the solid line at 4 Gyr along the warm meridian, it is considered a viable candidate. Sulfides and graphite (C) do not meet this requirement. The mid-latitude sublimation timescale for fullerenes are the closest match to the mid-latitude timescale of 300 Myr, but fullerenes cannot form hollows quickly enough at the cold limit of 71°N. Note that graphite and sulfides more refractory than Na_2S plot off the top of the chart; values for these species are provided in Table S3 of the appendix. . 47
Fig. 1. 8. Volatile loss rates as a function of depth on Mercury at the hot limit of hollow formation. Colors correspond to the compound classes in Table 1. For simple organics (green), aromatic hydrocarbons (blue), linear amides (yellow), and carboxylic acids (magenta) only the minimum and maximum of the compound classes are plotted for simplicity. Vertical lines are the minimum effective (6.4 m Gyr^{-1}) and the characteristic rate (85.6 m Gyr^{-1}) for

hollow formation at 0°N (Table 5). A viable candidate volatile is expected to plot to the right of the rightmost vertical black line at the surface (depth approaches 0) and, at minimum, to the left of the leftmost vertical black line in the subsurface. Thus, a candidate volatile crosses both vertical black lines..... 48
Fig. 1. 9. Volatile loss rates as a function of depth on Mercury at the cold limit (71°N along the warm meridian). Colors correspond to the compound classes in Table 1. Vertical lines are the minimum effective rate (3.3 m Gyr^{-1}) and the characteristic rate (44.2 m Gyr^{-1}). In a SEALS hollow formation model, a viable candidate volatile is expected to plot to the right of the rightmost vertical black line at the surface (depth approaches 0) and to the left of the leftmost vertical black line at some point in the subsurface. Thus, a candidate volatile crosses both vertical black lines. 50
Fig. 1. 10. Lag thickness at which volatile loss rate is equal to specified threshold loss rate values (see legends for values), which correspond to the vertical lines in Figs. 8 and 9. Thicker lag deposits are necessary to suppress volatile loss rates to lower values. Percent purity of the volatile layer for a given lag thickness is plotted on the right axes. Values without lower bars indicate that a lag deposit 100 m-thick is not sufficient to suppress the loss rate to < 1 mm Gyr^{-1}. The two volatiles that are viable at both the hot and cold limits are S and $C_{18}H_{36}O_2$. Volatiles that either do not sublimate fast enough at the surface or cannot be suppressed beneath a volatile lag are not plotted. 54
Fig. 1. 11. Model predicted range of latitudes over which each volatile phase is expected to form hollows on horizontal surfaces in a SEALS model framework. The highest model-predicted latitude depends on the timescale used for hollow formation. If the estimate from Blewett et al. (2016) of 300 Myr is used, then the highest latitude predicted for hollow formation is at the top of the solid colored bars. If a conservative estimate of 4 Gyr is used, then the highest latitude predicted for hollow formation is extended as indicated by the black portion of the colored bars. The light gray region between 0°N (hot limit for hollow formation) and 71.4°N (cold limit for hollow formation) indicates the observed limits of hollow formation on a horizontal surface. See *Section 2.3* for details on the hot and cold limits of hollow formation. 55
Fig. 1. 12. Sulfide loss rates as a function of temperature between 600 K and 1500 K. Dashed lines are loss rates for sulfides buried at 1 km. At temperatures relevant to a post-impact environment, Na_2S can be thermally decomposed rapidly at the surface, and above the estimated hollow formation rate at temperatures above ~1100 K buried at 1 km. CaS buried at 1 km falls off the plot. 74
Fig. 1. 13. Sublimation Cycling Around Fumarole Systems (SCArFS) model for hollow formation. Top panel shows a complex crater in the first several thousand years after impact into sulfide-bearing LRM and gives context for Stages 1-4 of the model. *Stage 1:* Heating of LRM produces volatile phases,

for instance by thermal decomposition of sulfides. Volatile phases are driven toward the surface along fractures in a fumarole system. The processes of Stage 1 occur throughout hollow formation until hollow formation ceases in Stage 4. To show this, a small panel displaying the processes of Stage 1 is located at the bottom of the Stage 2 and 3 panels beneath a dashed line that indicates a break in space. *Stage 2:* Sulfur and other phases accumulate in the vicinity of fumarole vents on the surface and in near-surface pore spaces at night, becoming structurally integral members of the surface in a "sulfur-rich permafrost" layer. Some amount of gases, especially highly volatile species such as H_2S, would likely continue to vent at night. *Stage 3:* Phases that precipitated on the surface and within the near-surface at night sublimate during the day, widening and deepening hollows. Stages 2 and 3 would repeat on a diurnal cycle. *Stage 4:* Fresh sulfides may precipitate along hollow floors, walls, and rims developing a low porosity capping unit that impedes hollow growth. Hollow formation may also slow when the subsurface heat source cools and thermal decomposition of sulfides terminates. Retention of a S-rich reservoir is anticipated below the influence of diurnal temperature swings and above the influence of subsurface heating. 79

Fig. A1. 1. Diurnal surface temperature at 90°E 0°N. notice the anomalies on the nightside due to Mercury's unique orbital characteristics discussed in Section 1.1. 98
Fig. A1. 2. Polynomial fits to heat capacity data for lunar regolith. Our fit (red) is compared to previous fits. 99
Fig. A1. 3. Surface diurnal temperatures for models run with various parameter configurations. See Table 2 and text for details. Values are compared to Mariner 10 IRR data from Chase et al. (1976), and to model data from Hale and Hapke (2002) (HH02) and Yan et al. (2006) (Y06). 100
Fig. A1. 4. Noon and pre-dawn temperatures as a function of depth for various parameter configurations (same as those shown in Fig. 1.A3). Values are compared to model runs from Hale and Hapke (2002) (HH02) and Yan et al. (2006) (Y06). 101
Fig. A1. 5. Upper and lower limit density profiles as a function of depth used in our thermal model. 102
Fig. A1. 6. Percent error between theoretically and experimentally derived vapor pressure curves for PbS. At 340 K the two curves cross and percent error asymptotically approaches zero. 103
Fig. A1. 7. Collage of representative complex craters that host hollows. The crater name is presented in the center and north is up in all images. Red squares are locations where hollow depths were measured by Blewett et al. (2016). Larger squares represent a deeper value for hollow depth. Note that hollows occur predominantly along central peaks and peak rings and

terraced walls. Hollows generally appear to be deeper closer to the central complexes than further from them. 109

Fig. 2. 1. Map of northern Hellas feldspathic outcrops. a, Context map of Fe-plagioclase-bearing outcrops previously identified on Mars, red squares, see Appendix II Table A2.1 for details. VM = Valles Marineris, A = Argyre, H = Hellas, I = Isidis. **b,** 255 Fe-plagioclase-bearing outcrops mapped in this study in yellow (outlines exaggerated for visibility). Fe-plagioclase-bearing outcrops occur nearly exclusively in Noachian crater (Nc), Noachian hilly (Nh) and Noachian massif (Nm) geological units (Leonard and Tanaka, 2001) displayed overlaid on MOLA/HRSC blended topography. **c,** percent area of primary igneous minerals mapped in this study as a function of distance from the Hellas basin center (ΔR) at 50-km intervals and corrected for the percentage of Nc, Nh, and Nm units in each radial bin. PL = Fe-plagioclase, OL = olivine, LCP = low-Ca pyroxene, HCP = high-Ca pyroxene. Y-axis labels are the maximum radius for each bin and the 800 km bin includes all values < 800km. Note context for Figs. 2.2-2.4 and Appendix II Figs. A2.2-A2.3 (SF.2, 3). See Appendix II Fig. A2.1 for OL, LCP, and HCP mapping. 114

Fig. 2. 2. Fe-plagioclase-bearing massif and associated CRISM spectra. a, Light-toned feldspathic outcrop, outlined in white in panels **a-c,** in a Context Camera mosaic of a Hellas rim massif. **b,** THEMIS thermal inertia (tiu = thermal inertia units) showing relatively high thermal inertia values for the Fe-plagioclase-bearing outcrop. **c,** False-color composite CRISM mosaic with spectral parameters in the RGB channels indicated in the lower right. Yellow tones are consistent with Fe-plagioclase. **d,** CRISM spectra extracted from the 8 regions shown in panel **c** and compared to a laboratory spectrum of plagioclase convolved to CRISM spectral resolution. Ticks are separated by 0.1. 119

Fig. 2. 3. THEMIS analysis of CRISM-detected feldspathic outcrop. a, CTX mosaic of light-toned feldspathic outcrop in a Hellas-rim massif. **b,** THEMIS thermal inertia (tiu = thermal inertia units) of feldspathic outcrop. **c,** False color composite CRISM mosaic, yellow tones are consistent with Fe-plagioclase. **d,** Decorrelation stretch of THEMIS bands 8, 7, and 5 of THEMIS scene I17073002. In panels **a-d** areas 1-3 indicate locations of extracted CRISM and THEMIS spectra (panels **e** and **f**). **e,** THEMIS spectra compared to TES surface types 1 and 2, martian dust, and lab references[19] convolved to THEMIS band passes. **f,** Ratioed CRISM I/F spectra extracted from areas 1-3 in panels **a-d**. Ticks are separated by 0.1. **g,** cubic spline fit minima of THEMIS spectra, TES surface types, and lab references. Colors match panel **e**. PL1-3 are the SFM of the three Fe-plagioclase areas. SFM standard deviations are contained within the size of the markers. 120

Fig. 2. 4. HiRISE images of CRISM-detected feldspathic outcrops. a, HiRISE image ESP_011683_1540 showing massive texture and light-toned nature

of Fe-plagioclase-bearing outcrop on a northern Hellas massif. Location indicated in Fig. 1. **b,** Fe-plagioclase-bearing massif with jointing at ~90° angles (HiRISE scene ESP_037502_1540, location indicated in Appendix II Fig. A2.1). **c,** HiRISE image ESP_011683_1540 showing dark- and light-toned layers in a feldspathic outcrop on a Noachian massif. Location indicated in Fig 2.1..... 123

Fig. A2. 1. CRISM-identified outcrops of primary igneous minerals. PL = Fe-plagioclase, OL = olivine, LCP = low-Ca pyroxene, HCP = high-Ca pyroxene; Nc = Noachian crater, Nh = Noachian hilly, and Nm = Noachian massif units (see Leonard and Tanaka (2001) of the main text). 134

Fig. A2. 2. THEMIS analysis of CRISM-detected feldspathic outcrop and associated low-Ca pyroxene. **a,** CTX mosaic overlaid by THEMIS thermal inertia of feldspathic outcrops (Pl1-3) on a northern Hellas massif and associated with ejecta from an nearby impact, as well as a low-Ca pyroxene (LCP) outcrop and an area containing alteration minerals (Altn). **b,** Decorrelation stretch of THEMIS bands 8, 7, and 5 of THEMIS scene I08749001. **c,** CRISM browse product mapping tile, yellow tones consistent with Fe-plagioclase, blue tones consistent with low-Ca pyroxene. Note the white areas of interest that indicate locations from which CRISM and THEMIS spectra were extracted for panels **d** and **e**. **d,** CRISM spectra over the areas shown in in panels **a-d**. Note the subtle 1.9-μm band present in Pl3 and to a lesser degree in Pl2. Ticks are separated by 0.1. **e,** THEMIS spectra extracted from regions shown in panels **a-d** and compared to TES surface types 1 and 2 and lab references from Rogers and Nekvasil (2015). Note how the character of spectra Pl1-3 change with increasing alteration. **f,** cubic spline fit minima of THEMIS spectra, TES surface types, and lab references. Marker colors correspond to panel **e**. SFM standard deviations are contained within the size of the markers. 135

Fig. A2. 3. THEMIS analysis of CRISM-detected feldspathic outcrop and associated olivine. **a,** CTX mosaic overlaid by THEMIS thermal inertia of feldspathic (Pl1-2), olivine-bearing (Ol1-4), and alteration mineral-bearing (Altn) outcrops on a northern Hellas massif. The white areas of interest in panels a-d indicate areas from which CRISM and THEMIS spectra were extracted for panels **e-f**. **b,** Decorrelation stretch of THEMIS bands 8, 7, and 5 of THEMIS scene I08749001.**c,** CRISM browse product mapping tile, yellow tones consistent with Fe-plagioclase, red tones consistent with olivine. **d,** CRISM browse product mapping tile, cyan tones consistent with alteration minerals Fe/Mg smectite. **e,** CRISM spectra over the areas shown in in panels **a-d**. Note the subtle 1.9-μm band present in Pl1. Ticks are separated by 0.1. **f,** THEMIS spectra extracted from regions shown in panels **a-d** and compared to TES surface types 1 and 2 and lab references from Roger and Nekvasil (2015). **g,** cubic spline fit minima of THEMIS spectra,

TES surface types, and lab references. Marker colors correspond to panel **e**. SFM standard deviations are contained within the size of the markers..... 137

Fig. 3. 1. (**a**) Context map showing location of Salar de Pajonales within Chile. Dashed lines indicate boundaries of the Atacama Desert (horizontal bars) and the Altiplano (solid gray). Solid lines denote country borders. (**b**) Salar de Pajonales basin outlined in black with the locations of the orthophotomosaics (**c**) and DEMs (**d**) processed for this study..... 153
Fig. 3. 2. Ground-based and aerial views of the three microbial habitats at Salar de Pajonales: (**a**) polygon ridge; (**b**) dome; (**c**) patterned ground. For scale, the white quadrat in **a**-**c** is 1 m by 1 m. (**d**) Green and pink pigments associated with the microbial organisms found in these habitats, and (**e**) an aerial view with arrows indicating the habitats. 155
Fig. 3. 3. Flow chart delineating the methodology for this study from collection of images in the field to final assessment of neural network results. OPM = orthophotomosaic. *Ecological survey is described in detail in Warren-Rhodes et al. (in review). 159
Fig. 3. 4. Example edge response functions derived from orthophotomosaics by measuring a response profile across a sharp edge. 161
Fig. 3. 5. Feature classes defined for the Salar de Pajonales basin in this study. See Table 3 for class descriptions. 166
Fig. 3. 6. Probability distributions functions (PDFs) of SoftMax input values of each class for a single pixel. For high certainty pixels (**a**), the expected value of the PDF with the highest mean SoftMax input activation value (PDF_{max}) is much larger than the expected value of any other PDF. For a low certainty pixel (**b**), the expected value of PDF_{max} is not significantly larger than the expected value of other PDFs. 177
Fig. 3. 7 Examples of RGB-Network predictions (center column) with associated Certainty Scores (right column, black = 0%, white = 100%) and compared to ground truth labels (left column). Pink = PolygonRide, Blue = AeolianCover, Purple = MottledGround, Red = Dome.**Fig. 3. 7 continued**..... 180
Fig. 3. 8. Performance metrics for RGB-Networks as a function of GRD. (**a**) Confidence Score, (**b**) BF-Score, (**c**) Recall, (**d**) Precision. Range of HiRISE GRDs (75 to 99 cm) is taken as three times typical HiRISE GSDs of 25 to 33 cm. 182
Fig. 3. 9. Certainty Scores for RGB-Network. Note the general decrease in Certainty Score values with increasing GRD. 184
Fig. 3. 10. Examples of DEM-Network predictions (center column) with associated Certainty Scores (right column, black = 0%, white = 100%) and compared to ground truth labels (left column). 188
Fig. 3. 11. Performance metrics for DEM-Networks as a function of GRD. (**a**) Confidence Score, (**b**) BF-Score, (**c**) Recall, (**d**) Precision. Range of HiRISE GRDs (75 to 99 cm) is taken as three times typical HiRISE GSDs of 25 to 33 cm. 190

Fig. 3. 12. Certainty Score for DEM-Networks as a function of GRD. 192
Fig. 3. 13. Examples of DEM-Network predictions (center column) with associated Certainty Scores (right column, black = 0%, white = 100%) and compared to ground truth labels (left column).**Figure 3. 13 continued** 195
Fig. 3. 14. Performance metrics for RGB-DEM-Networks as a function of GRD. (**a**) Confidence Score, (**b**) BF-Score, (**c**) Recall, (**d**) Precision. Range of HiRISE GRDs (75 to 99 cm) is taken as three times typical HiRISE GSDs of 25 to 33 cm. 197
Fig. 3. 15. Certainty Score for RGB-DEM-Networks as a function of GRD. 199
Fig. 3. 16. Comparison of performance metrics for RGB-, DEM-, and RGB-DEM-Networks as a function of GRD. (**a**) Confidence Score, (**b**) BF-Score, (**c**) Recall, (**d**) Precision. Range of HiRISE GRDs (75 to 99 cm) is taken as three times typical HiRISE GSDs of 25 to 33 cm. 203

Fig. A3. 1 Multilayer perceptron network with 2 hidden layers. Colored circles represent neurons and black lines represent connections between neurons. 209
Fig. A3. 2 Network design for RGB- and DEM-Networks used in this study. RGB-DEM-Networks consist of two networks assembled in parallel using the late fusion technique. 217
Fig. A3. 3 RGB-Network Confidence Scores as a function of GRD for 9 classes of natural features in this study (excluding Road, BorderPixel, and Object classes because they are not natural features). Note the general trend for all classes is a relatively linear decrease in confidence with increasing GRD. This behavior is distinct from the BF-Score, Recall, and Precision observed for the habitat classes and described in the main text. A plausible cause for the difference in behavior is that as network accuracy decreases, its uncertainty increases. The networks perform better on classes that cover large swaths of terrain, such as the SaltPan, AeolianCover, MottledGround, and MudCrack classes than they do on classes comprised of individual features. 218

LIST OF ATTACHMENTS

Attachment A2. 1. Location and CRISM mapping strip ID for all Fe-plagioclase spectra used in this study, attached as a .csv file..... **Error! Bookmark not defined.**

Attachment A3. 1: Two files containing details on the orthophotomosaic and DEM processing for sUAS Flights 1 and 2 of this study are attached as .pdfs. ..... **Error! Bookmark not defined.**

INTRODUCTION

Here, I explore processes, active and ancient, on the inner solar system rocky bodies Mercury, Mars, and – as an analog to Mars – Earth. In these investigations thermal and geochemical modelling, reflectance and emission spectroscopy, and deep-learning based image analysis were employed. Chapter-I focuses on the materials and mechanisms involved in the formation of enigmatic pits on Mercury called hollows. Chapter-II describes newly discovered feldspathic rocks in an ancient layered igneous complex on Mars. Lastly, in Chapter-III, a deep-learning based method to quantify feature identification confidence as a function of image spatial resolution is proposed. I apply this method to the identification of habitats in aerial images of Mars-analog landscapes on Earth.

Enigmatic Mercury

The innermost planet, Mercury, is an endmember in more ways than one. Mercury is the smallest planet, smaller even than the Galilean moon Ganymede and the saturnian satellite Titan. Despite its size, Mercury is the densest planet (if the effects of gravitational compression are ignored) with a core that makes up ~85% of its radius, the largest fraction of any solar system body. Throughout its orbit, Mercury's distance from the Sun ranges from 0.31 to 0.46 AU, giving it the highest eccentricity of any planet. Its eccentricity conspires with a 3:2 spin-orbit resonance and a near-zero obliquity, the lowest obliquity of any planet, to produce a distinctive thermal signature on the surface. The proximity of Mercury to the Sun along with its orbital parameters make for an extreme surface temperature environment. It is within this context that features known as hollows, unique in the solar system, occur.

Hollows form by sublimation, which is a phase transition from solid to gas, of some yet unknown substance over a relatively unconstrained timeframe. Sublimation is a common process across the solar system, but the sublimating substances are planetary ices (e.g., water, nitrogen, carbon dioxide, etc.). In the

case of hollows on Mercury, the sublimating substance is unlikely to be a planetary ice, but some more refractory (i.e., “rocky”) material owing to the extremely hot temperatures (up to ~700 K) on the mercurian surface.

In Chapter-I, I address the problem of hollow formation on Mercury by using thermal and geochemical modeling to estimate the sublimation rates of 57 candidate hollow-forming volatiles from various depths across the surface of Mercury.

Ancient Mars

The martian pre-Noachian through Noachian (~4.5 – 3.8 Ga) timeframe is key for understanding many aspects of not only the geological and climatological evolution of Mars, but of terrestrial planets in our solar system and beyond. Mars records its most ancient geologic past pristinely compared to Earth where the oldest rocks have been recycled through plate tectonic processes. Indeed, other than the Moon, the martian pre-Noachian crust is the most ancient and accessible crust for which detailed observations are available. In addition to its observable rock record, Mars is a middling-sized terrestrial body making it a crucial data point for understanding how rocky planets differentiate and generate their primary crusts. Before Mars lost its atmosphere and magnetic field, it was likely quite similar to the Earth in terms of its potential to host life. Understanding any co-evolution between life and its environment on Mars would be critical for understanding how life may have emerged and evolved in its nascent stages on Earth. Thus, studying the pre-Noachian of Mars holds the key to understanding the differentiation and primary crust formation of rocky worlds, as well as the solar system’s most ancient habitable environments.

In Chapters-II and III, I address both aspects of ancient Mars that have broad implications for the field of planetary science: the composition of its most ancient crust and the likelihood of identifying habitats in orbital images of the red planet by way of analog environments on Earth.

CHAPTER I
THE LIFECYCLE OF HOLLOWS ON MERCURY: AN EVALUATION OF CANDIDATE VOLATILE PHASES AND A NOVEL MODEL OF FORMATION.

A version of this chapter was originally published by Michael S. Phillips, Jeffrey E. Moersch, Christina E. Viviano, and Joshua P. Emery:

Phillips, M.S., et al., "The lifecycle of hollows on Mercury: An evaluation of candidate volatile phases and a novel model of formation." *Icarus* 359: 114306. (2021).

The chapter has been updated from its originally published version as per committee member suggestions to include a section on oxidation pathways for sulfur in hermeothermal systems.

Abstract

On Mercury, high-reflectance, flat-floored depressions called hollows are observed nearly globally within low-reflectance material (LRM), one of Mercury's major color units. Hollows are thought to be young, or even currently active, features that form via sublimation, or a "sublimation-like" process. The apparent abundance of sulfides within LRM combined with spectral detections of sulfides associated with hollows suggest that sulfides may be the phase responsible for hollow formation. Despite the association of sulfides with hollows, it is still not clear whether sulfides are the hollow-forming phase. To better understand which phase(s) might be responsible for hollow formation, we calculated sublimation rates for 57 candidate hollow-forming volatile phases from the surface of Mercury and as a function of depth beneath regolith lag deposits of various thicknesses. We found that stearic acid ($C_{18}H_{36}O_2$), fullerenes (C_{60}, C_{70}), and elemental sulfur (S) have the appropriate thermophysical properties to explain hollow formation. Stearic acid and fullerenes are implausible hollow-forming phases because they are unlikely to have been delivered to or generated on Mercury in high enough volume to account for hollows. We suggest that S is most likely the phase responsible for hollow formation based on the abundance of sulfur on Mercury (primarily in the form of sulfides, Sprague et al., 1995; Weider et al., 2012) and the thermophysical properties of S. We discuss the possibility that S is the phase responsible for hollow formation within the hollow-formation model framework proposed by Blewett et al. (2013). However, several potential limitations with that model lead us to suggest an alternative hollow-formation model: a subsurface

heat source (most often impact-induced) generates thermal systems that drive sulfur-rich fumaroles in which S and other phases accumulate on and within the surface at night and sublimate during the day to create hollows. We call this hollow-formation model “Sublimation Cycling Around Fumarole Systems” (SCArFS). We suggest that thermal decomposition of sulfides within LRM is a main contributor to S and S-bearing gases within the proposed fumarole systems and that (re-)precipitation of sulfides may occur at the surface along hollow floors and rims.

1. Introduction

Mercury hosts features unique in the solar system that were first observed in Mariner 10 images and described as bright crater floor deposits (BCFDs, Dzurisin, 1977). Images from instruments onboard the MErcury Surface, Space ENvironment, GEochemistry, and Ranging (MESSENGER, Solomon et al., 2007) spacecraft have revealed that many BCFDs host sub-kilometer-scale, flat-floored, rimless depressions with a typical depth of around 20-50 m (Fig. 1.1) and lateral extents that range from meters to kilometers (Blewett et al., 2011; Blewett et al., 2013; Thomas et al., 2014). These features have become known as hollows to distinguish them from structures such as pyroclastic vents and pits (Head et al., 2009; Kerber et al., 2011; Goudge et al., 2014).

1.1. Distribution of Hollows on Mercury and Their Association with Mercury’s Low Reflectance Material

Hollows are nearly global in extent, though some spatial variability has been noted (Fig. 1.2). Thomas et al. (2014) showed that hollows are more abundant and cover more area at equatorial latitudes and on slopes with equator-facing aspects than at higher latitudes and on slopes that face away from the equator. This result agreed with Blewett et al. (2011, 2013), who first noted some examples of hollows at mid- to high-latitudes on equator- facing

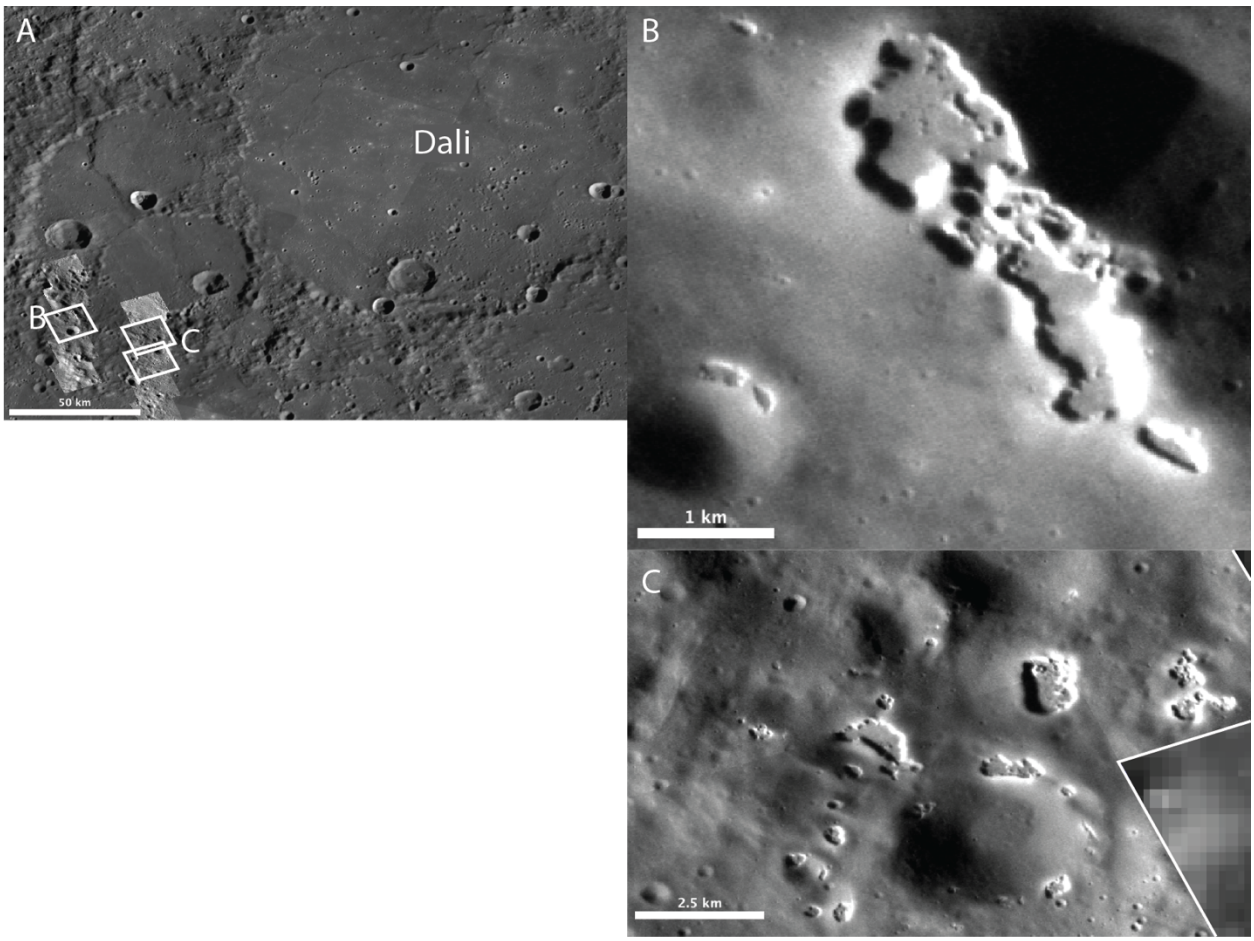

Fig. 1. 1 A) Context of hollows in **B**) and **C**) on the south side of a crater southwest of Dali Basin. MESSENGER Narrow Angle Camera frames shown in **B**) and **C**) are outlined in white. **B**) Hollow ID# 6211 from the global database of Thomas et al., 2016, located at ~115.4°E, 43.0°N. NAC image ID: EN0251429891M. **C**) Hollow ID# 6051 from the global database of Thomas et al., 2016 located at ~116.4°E, 42.7°N. NAC image IDs: EN0251401087M, EN0251401092M. Notice the irregular shape, flat floors, and bright rims characteristic of hollows.

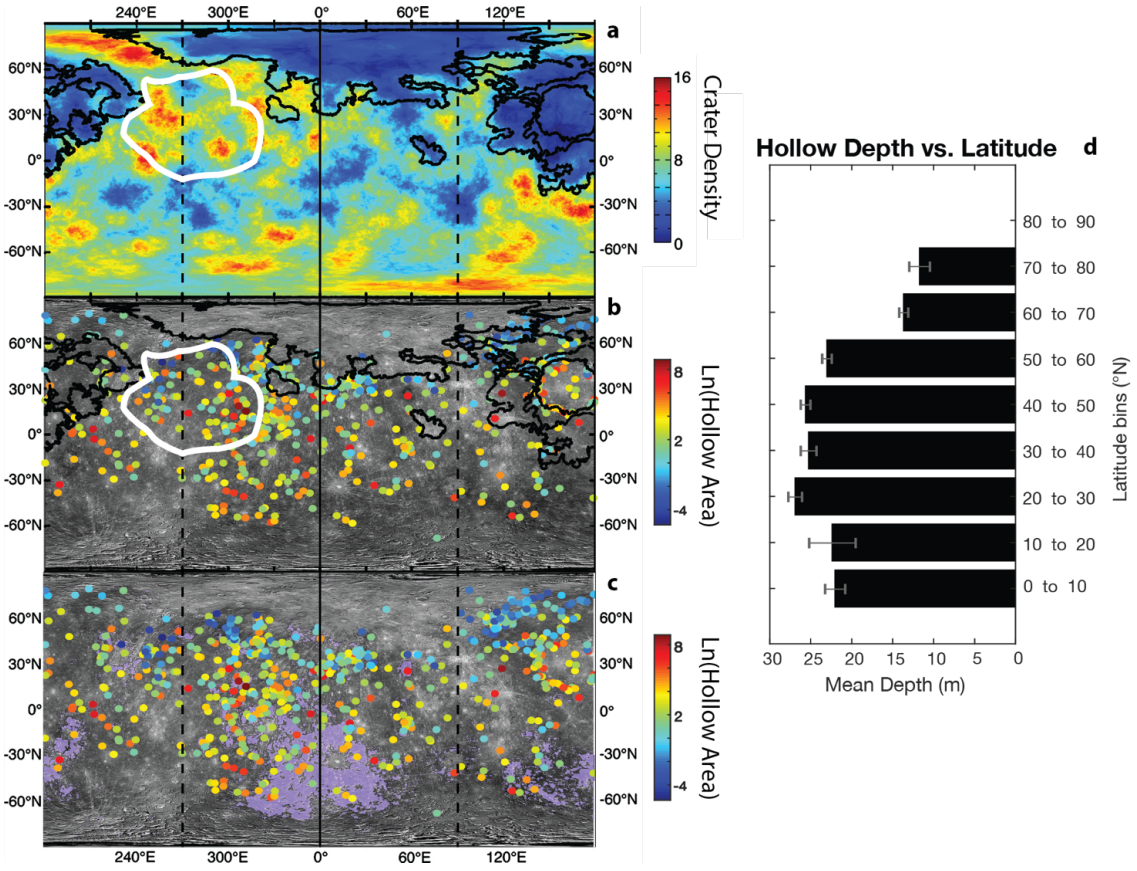

Fig. 1. 2 Maps of **a)** density of impact craters > 25 km diameter per 10^5 km. Data from Marchi et al. (2013), map reproduced from Weider et al. (2015); **b)** distribution of hollows relative to the northern smooth plains (solid black line) and high-Mg region (solid white line); **c)** distribution of hollows relative to the low-reflectance material (LRM). LRM is highlighted in lavender. It should be noted that many small patches of LRM are covered by dots indicating hollow locations. In **b)** & **c)**, the areas (km^2) of individual hollows/hollow clusters are represented by color on a natural log scale. Hollow location and area data are from Thomas et al. (2014, 2016). Base map is MESSENGER MDIS LOI mosaic (astrogeology.usgs.gov); Vertical dashed lines are the Warm Meridians and the vertical solid line is the Hot Meridian (the other Hot Meridian is at the map edges). **d)** Hollow mean depth binned by 10° latitudinal bins in the northern hemisphere. Error bars are the standard error for hollow depth in each latitudinal bin. Hollow depth data are taken from Blewett et al. (2016).

slopes. Blewett et al. (2016) measured the depth of hollows using shadow length measurements on 565 high-resolution images (< 20 m/pixel) of Mercury's northern hemisphere and found that hollows have a mean depth of 24 m, a minimum depth of 1.6 m and a maximum of 110.5 m. These depth measurements indicate a lower average depth than those from Thomas et al. (2014), but the uncertainty is smaller because the image resolution was much higher (< 20 m/pixel versus < 180 m/pixel). We used the data collected by Blewett et al. (2016) to show that hollow depth decreases as latitude increases (Fig. 1.2d). The apparent preference of hollows to cover more area at equatorial latitudes and to preferentially form on slopes with equator-facing aspects at mid- to high-latitudes has led previous workers to suggest that solar heating drives a sublimation process responsible for hollow formation (Blewett et al., 2011; Blewett et al., 2013; Thomas et al., 2014). The trend of decreasing hollow depth with increasing latitude further supports this suggestion (Fig. 1.2d).

Mercury's surface has an extreme thermal environment due to the planet's high orbital eccentricity (0.206) and proximity to the Sun (0.308-0.467 AU). Mercury is also in a 3:2 spin-orbit resonance, which means it has 3 sidereal days (and 1 synodic day) every 2 hermean[1] years (Colombo, 1965; Pettengill and Dyce, 1965). The combined effect of the 3:2 resonance and high eccentricity is that (i) two meridians (0°E and 180°E) experience solar noon at alternate perihelia and receive maximum solar insolation ("hot meridians" maximum temperatures ~700 K), whereas (ii) two meridians (90°E and 270°E) experience solar noon at alternate aphelia and receive minimum solar insolation ("warm meridians" maximum temperatures ~590 K). Because Mercury also has an obliquity near zero, the intersections of the hot meridians with the equator are known as Mercury's "hot poles" and the intersections of the warm meridians with

[1] Hermean is an adjectival form for Mercury synonymous with mercurian. Hermes is the Greek messenger god and the apparent inspiration for the god Mercury in Roman mythology.

the equator are Mercury's "warm poles" (e.g., Soter and Ulrichs, 1967). An additional oddity resulting from Mercury's orbit is that for a portion of its orbit surrounding perihelion the orbital angular velocity exceeds the rotational angular velocity. Thus, for an observer on Mercury, the apparent motion of the sun across the sky is retrograde. This effectively lengthens noon-time heating for the hot poles because the sun passes through its apex three times and causes a double sunset/sunrise at the warm poles that imparts a signature on the diurnal temperature curve (Fig. 1.A1 of the appendix). Mercury has most likely been in its present-day 3:2 spin-orbit resonance since near the end of the Late Heavy Bombardment ~3.8 Ga (Knibbe and van Westrenen, 2017). Prior to capture into its present-day resonance, Mercury may have been in either a 1:1 or 2:1 spin-orbit resonance (Correia and Laskar, 2009; Correia and Laskar, 2010; Wieczorek et al., 2012; Knibbe and van Westrenen, 2017). Because hollows are generally considered the youngest features on Mercury (and potentially currently active), the ancestral resonance is not likely to have affected hollow formation, but it may have implications for the sequestration of a hypothesized hollow-sourcing volatile layer between ~4.6 Ga and ~3.8 Ga (Wieczorek et al., 2012; Knibbe and van Westrenen, 2017), as will be discussed in more detail in *Section 4.1.1*.

Despite Mercury's longitudinal asymmetry in insolation and the apparent dependence of hollow formation on thermal environment, there does not appear to be a clear correlation between Mercury's hot meridians and hollow occurrence. Thomas et al. (2014) report a lower areal extent of hollows near the cold poles between 30°S and 30°N and an uptick in areal extent of hollows near the 0°E hot pole in this same latitudinal band, indicating that solar insolation may impart some control on hollow formation. This has led previous authors to suggest that equatorial temperatures on Mercury are sufficient to create hollows at all longitudes (Thomas et al., 2014). The higher concentration of hollows around Mercury's 180°E hot meridian at latitudes above 50°N than at other longitudes can be explained by the distribution of the northern smooth plains in this region,

which are anticorrelated with hollow distribution (Fig. 1.2a,b) as suggested by (Blewett et al., 2013).

Hollows are not clearly correlated with Mercury's hot poles, but they are also not uniformly distributed across all longitudes. An anomalously high concentration of hollows between longitudes 300°E and 320°E (Blewett et al., 2013; Thomas et al., 2014), could be considered to extend between ~280°E and 340°E (Fig. 1.2b,c; Blewett et al., 2013). Possible causes for this nonuniform longitudinal distribution of hollows are formation-age differences and lateral differences in surface material composition. If there are processes erasing hollows, such as impact gardening and space weathering, then areas with realtively numerous hollows may host relatively younger hollows; however, a preliminary investigation of hollow reflectance across Mercury as a proxy for surface exposure age showed no geographic trend in reflectance, potentially indicating that hollows do not differ in age across Mercury (Phillips et al., 2016). The distribution of hollows may also depend on Mercury's low-reflectance material (LRM), which is one of Mercury's major color units (Robinson et al., 2008; Denevi et al., 2009) and assumed by association to be the source of hollow-forming volatiles (Blewett et al., 2013; Thomas et al., 2014). There is a high concentration of LRM between ~280°E and 360°E in the northern hemisphere (Fig. 1.2c). The coexistence of hollows and the LRM in this region may indicate that surface composition controls the longitudinal distribution of hollows (Blewett et al., 2013).

The hollow-forming volatile is suggested to be sourced from the LRM because hollows almost exclusively form in this unit (96%, Thomas et al., 2014; Thomas et al., 2016). The distributions of hollows and the LRM are shown in Figure 1.2c. Murchie et al. (2015) explored several hypotheses for the nature and origin of the LRM and concluded that it is a stratigraphically deep component of Mercury's crust (estimated to be ~30 km below the surface, Denevi et al., 2009; Rivera-Valentin and Barr, 2014; Ernst et al., 2015). The LRM is exhumed and emplaced on the surface via impact cratering (Klima et al., 2018). The darkening

agent within LRM is likely endogenic to Mercury and may be some form of carbon (Riner et al., 2009; Nittler et al., 2011; Xiao et al., 2013; Murchie et al., 2015; Peplowski et al., 2015; Trang et al., 2017). The hypothesis that carbon is the darkening agent is consistent with elevated carbon content in LRM and the idea that Mercury had an early carbon-bearing crust (Peplowski et al., 2016), such as a primary graphite flotation crust (Vander Kaaden and McCubbin, 2015). Spectral modeling of MESSENGER Visible and Infrared Spectrograph (VIRS) data by Trang et al. (2017) supports the idea that carbon is a plausible darkening agent for the LRM.

Additionally, Weider et al. (2015) identified a region with MESSENGER's X-Ray Spectrometer in the northern hemisphere between ~230°E and 320°E that is anomalously high in Mg called the high magnesium region (HMR; Fig. 1.2a & b). The HMR was proposed by Weider et al. (2015) to be either an ancient impact basin or related to large degrees of partial melting in the mantle. The HMR is also high in Ca and S, and as such is thought to be rich in (Ca, Mg) sulfides (e.g., Zolotov et al., 2013). Magma ocean models by Boukaré et al. (2019) suggest that Mercury's magma ocean may have hosted sulfide layers that, depending on the magma ocean composition, could have floated to form a sulfide crust or risen through the crust as sulfide-rich plumes. The sulfur-rich terrains on Mercury are also correlated with the LRM (Nittler et al., 2011), and have caused some to suggest that sulfides may be a darkening agent within the LRM (Nittler et al., 2011; Weider et al., 2012; Blewett et al., 2013; Helbert et al., 2013).

1.2. Relationship to Craters

Approximately 97% of hollows (by surface area) are within impact craters or impact crater-related material such as rims and ejecta (Thomas et al., 2014). Though the close association of hollows with craters implies a genetic link between the two (Blewett et al., 2011, 2013), the precise role that craters play in hollow formation is unclear. Impacts may simply be the mechanism by which

hollow-forming material is exhumed (Blewett et al., 2011), or the heat and/or melt generated by impacts may play an active role in hollow formation (Vaughan et al., 2012; Blewett et al., 2016).

The distribution of hollows within craters differs between simple and complex craters. In simple craters, hollows are almost exclusively found on or proximal to the rims (Thomas et al., 2014). However, in complex craters hollows are predominantly observed on terraced walls and central complexes, such as central peaks and peak rings (Thomas et al., 2014). There are also instances of hollows extensively covering the floors of some complex craters, such as Tyagaraja and Sander craters (Blewett et al., 2011). Depth measurements made by Blewett et al. (2016) show that hollows near/on the central complexes of these craters tend to be deeper than the hollows along the floors (Blewett et al. 2016, supplementary materials). Our preliminary visual inspection in JMARS of the depth measurements made by Blewett et al. (2016) within complex craters suggests it may be true more generally that within complex craters deeper hollows are found nearer the central complexes. However, more work is necessary to support this suggestion.

1.3 The Apparent Youth of Hollows

Several lines of evidence point to the apparent youth of hollows: cross-cutting relationships with rayed craters, “crisp” morphology and delicate structures, and lack of superposed craters (Blewett et al., 2011; Blewett et al., 2013; Blewett et al., 2018). Perhaps the most direct line of evidence in support of a young age for some hollows is that at least 6 rayed craters with ages estimated at ≤ ~270 Ma (Xiao et al., 2012) are host to hollows. Because hollows occur within the craters, hollows must be younger than the craters. Hollows also show little evidence of modification by impacts or topographic muting through space weathering, although some examples of morphologically muted and dark (i.e., “old”) hollows exist (Blewett et al., 2018). There is only one published example of a small (~30 m diameter) crater within a hollow (Wang et al., 2020b). Additionally,

the bright floors and halos of hollows would presumably not survive long periods of exposure to the hermean space weathering environment, which includes solar wind and micrometeoroids (Domingue et al., 2014), further indicating a young age for at least the bright surfaces of hollows, if not the hollows themselves. However, as noted by Blewett et al. (2018), there is likely an observational bias toward imaging bright (i.e., “young”) hollows. This is because hollows are generally small features and the brightness of ostensibly young hollows is what drew MESSENGER team members to target these features (Blewett et al., 2018).

1.4. Hollow Formation Models and Candidate Volatiles

Several models have been proposed to explain hollow formation. Blewett et al. (2011) first posited a sublimation origin for hollows, noting their resemblance to martian “swiss cheese” terrain formed by sublimation of polar carbon dioxide ice (Malin et al., 2001). Blewett et al. (2013), further developed this idea into a three-stage model for hollow formation (Fig. 1.3a): 1) hollow-forming volatiles are deposited on the cold, night-side of Mercury from volcanic eruptions and/or magmatic outgassing events; 2) hollow-forming volatiles are rapidly buried and sequestered by lava flows and pyroclastic deposits; and 3) hollow-forming materials are exhumed by impact craters and emplaced on the surface where they are unstable and sublimate to form hollows. Thomas et al. (2014) suggested that endogenic processes, such as heating by magma in the subsurface, may drive volatiles to the surface, but ultimately concluded that the most probable mechanism for the delivery of volatiles to the surface is by exhumation from an impact. In general, the model of Blewett et al. (2013) proposes that hollows initially grow downward and laterally, but downward progression halts once a sufficient lag is built-up or when the volatile layer is exhausted. Lateral growth progresses through the extent of the volatile-bearing unit because the steep sides of hollows do not allow for a lag to build in the lateral direction. Blewett et al. (2016) suggest that because hollows have a

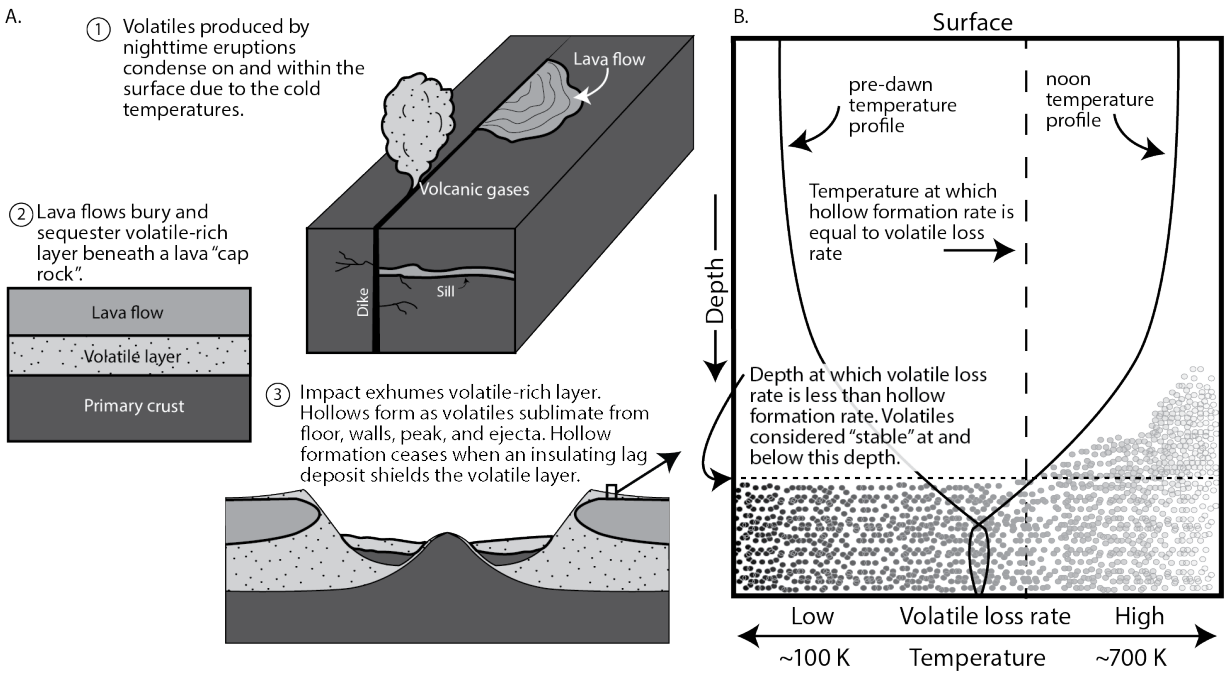

Fig. 1. 3. Conceptual model for hollow formation in a Surface Exposure And Lag Sequestration (SEALS) model (see text in *Section 1.4*). **A**) Three-stage hollow-formation model proposed in Blewett et al. (2013). The basic stages of this model are perhaps the most widely accepted of any hollow-formation model (see, e.g., Thomas et al., 2016). The mechanisms differ between models for how a volatile layer forms (e.g., volcanic sequestration, fractionation in volcanic flows, slag formation in impact melts and lavas, etc.), but the processes proposed by Blewett et al. (2011, 2013) are shown in part A (Stages 1 and 2) of this Figure. In Stage 3, and in all SEALS models, hollows form by loss of a volatile phase upon exposure to the surface via solar heating (or space weathering). Hollow formation ceases after a lag deposit develops and shields the volatile phase. **B**) A more detailed depiction of the process by which hollows form in a SEALS hollow formation model. The depth scale of the cartoon represents ~0.5 to 1 m of regolith. Dots represent a volatile phase and its loss rate at different temperatures: cold and stable (dark dots, left, low volatile loss rate) to hot and unstable (light dots, right, high volatile loss rate). If the loss rate for a given volatile is low at the equilibrium temperature but fast at daytime surface/near-surface temperatures (as the example volatile loss rate shown with the vertical dashed line), then such a volatile could be responsible for hollow formation within a SEALS model framework. However, if a compound's loss rate at subsurface temperatures is fast at or below equilibrium temperatures, then such a volatile would be unstable under a lag deposit and inconsistent with a hollow formation model that includes sequestration beneath a regolith lag deposit.

relatively constant depth that is shallow compared to the thickness of the LRM, the downward growth of hollows is limited by the build-up of a lag deposit rather than limited by the thickness of the volatile-bearing unit. Additionally, Thomas et al. (2014) noted that some hollows are hosted in small craters and on thrust faults nested within larger impact craters that have hollows. From this observation, the authors suggest that some hollow-forming volatile material remains in the subsurface after hollow formation, within the original larger crater, has ceased, further indicating that a lag deposit suppresses hollow formation. If a lag deposit halts downward growth, then the thickness of the lag deposit would be a function of the temperature-dependent sublimation rate of the hollow-forming volatile, the physical characteristics of the lag deposit (e.g., porosity and tortuosity), and the thermal insulating properties of the lag deposit.

Blewett et al. (2013) further proposed that sulfur-bearing volatiles (H_2S, SO_2), or sulfides (that decompose to produce elemental sulfur) are likely candidate hollow-forming materials because of the volatility of sulfur-bearing phases on Mercury and the high abundance of sulfur within the LRM (Nittler et al., 2011; Weider et al., 2011). The suggestion that sulfides play a role in hollow formation has also been made by several other workers (Vaughan et al., 2012; Helbert et al., 2013; Xiao et al., 2013; Thomas et al., 2014; Thomas et al., 2016; Vilas et al., 2016; Lucchetti et al., 2018; Pajola et al., 2021). Thomas et al. (2016) investigated the spectral reflectance characteristics of hollows, their bright halos, and the surrounding LRM and concluded that formation of hollows leaves behind a lag that is darker and bluer-sloped (i.e., relatively high reflectance values at shorter, bluer, wavelengths than at longer, redder, wavelengths in the UV/VIS) compared to the volatile material that is lost, which is brighter and redder-sloped than the parent material (i.e., LRM). The authors suggest that (Ca, Mg) sulfides are plausible candidate hollow-forming materials and that graphite may be the darkening agent of the LRM based on the relative spectral characteristics. A direct comparison of hollow spectra to sulfide spectra was made by Vilas et al. (2016). The authors showed that MESSENGER Mercury Dual Imaging System

(MDIS) Wide-Angle Camera (WAC) (Hawkins et al., 2007) 8-band spectra of hollows from Dominici and Hopper craters are similar to spectra of MgS and, to a lesser extent, CaS samples measured in the lab. However, Lucchetti et al. (2018) suggest that sulfides alone do not explain the spectra of hollows and that pyroxenes could contribute to the spectra.

Blewett et al. (2016) offered another mechanism for hollow formation in which carbon-rich LRM starting materials are lost through ion sputtering or converted to methane (or other carbon-bearing volatile species) through ion bombardment. From this model, we infer that the subsequent vaporization of carbon or the carbon-bearing volatiles would create hollows. If ion bombardment is responsible for the conversion of carbon to a volatile gas, such as methane, or if ion sputtering causes direct loss of carbon, then hollows should occur anywhere there is carbon-bearing material on the surface and perhaps not nearly exclusively within craters. Additionally, the processes of ion sputtering and ion-bombardment act on the uppermost layer of the surface, so unless the carbon-bearing material is pure, one might expect this process to self-limit after a very thin lag develops. Impact gardening may allow for the processes to continue as fresh material is brought to the surface, but the rate of turnover due to impact gardening is slow relative to plausible hollow growth rates (e.g., lateral growth rate of at least 1 cm per 10 kyr was inferred by Blewett et al., 2016). Killen et al. (2007) estimate that 1 cm of regolith will turn over every 150 kyr with 50% probability, although new preliminary models for impact gardening rates on Mercury indicate that the rate might be much slower (e.g., Costello et al., 2019). Blewett et al. (2016) estimate the rate of lateral hollow growth at Balanchine crater to be at least 1 cm per 10 kyr. Because downward growth of hollows is inferred to happen first, and more quickly (Blewett et al., 2018), this lateral growth rate can be considered conservative. Therefore, it seems unlikely that impact gardening can replenish volatiles to the surface quickly enough to account for the rate of hollow formation, perhaps casting doubt on whether surficial space weathering processes can account for hollow formation. However, Blewett et al.

(2016) also propose that carbon-rich starting material heated and mixed with solar-wind-saturated material, for example by impact melting, could also produce methane and other carbon-bearing volatile species. In this scenario, crater-related heating is necessary for hollow formation because it generates new volatile phases that were not already present on the surface or in the subsurface. These volatile phases would ostensibly be lost as they are created within or adjacent to impact melt at the surface and hollows would subsequently form through collapse of the void space. It is not clear how the latitudinal dependence on hollow depth and areal extent is explained in this model.

Vaughan et al., (2012) proposed a model in which hollows form via differentiation of impact melt. In this model, hollow-forming materials, sulfides or chlorides as suggested by the authors, rise to the top of impact melt where they form a “slag” layer susceptible to photodissociation and subsequent vaporization in a “sublimation-like” process. This model has some limitations. Photodissociation of sulfides is a surficial process, so a relatively pure and thick (≥ depth of the hollow) sulfide slag is necessary. Otherwise, hollow growth would be limited by development of a thin lag (such as in the case of ion bombardment and ion sputtering as described above). Additionally, hollows forming on steep slopes, on Caloris knobs (Wright et al., 2020), and proximal to the northern smooth plains unit (Denevi et al., 2013a; Thomas et al., 2014) are not easily explained by differentiated impact melt.

Helbert et al. (2013) provided a slightly different model from that of Vaughan et al. (2012), in which sulfides form as a slag product in Mg, Ca, and S-rich lavas instead of impact melts. Helbert et al. (2013) proposed thermal decomposition as the mechanism to dissociate sulfides rather than photodissociation from surficial space-weathering processes. The mechanism of thermal decomposition may play an important role in hollow formation if sulfides are the volatile substance that drives hollowing. This model, however, does not explain the 97% association of hollows with craters or the 96% association with

the LRM (Thomas et al., 2014), because hollows would be expected to form in any sufficiently sulfide-rich lava.

The processes by which volatiles are delivered to or generated at the surface vary across hollow formation models, but most models in the literature have two aspects in common: 1) a volatile phase sublimates, or is otherwise decomposed via space weathering processes, when exposed at the surface, and 2) an insulating lag deposit is the mechanism by which downward hollow growth is halted. In this work, we will call models that have these characteristics Surface Exposure And Lag Sequestration (SEALS) models. The most complete version of a SEALS hollow-formation model is the three-stage model proposed in Blewett et al. (2013), and there appears to be a consensus in the literature that the basic framework of this model best explains hollow formation (see, e.g., Thomas et al., 2016).

The viability of all three stages of the Blewett et al. (2013) model (concentration and deposition of a volatile phase into a volatile layer, sequestration of that layer, and exhumation and sublimation of that layer to form hollows, see Fig. 1.3) depend on the composition of the hollow-forming phase. Although sulfides are the phase most commonly proposed as the hollow-forming volatile phase (Vaughan et al., 2012; Helbert et al., 2013; Xiao et al., 2013; Thomas et al., 2014; Thomas et al., 2016; Vilas et al., 2016), there has been no detailed exploration of how sulfides are expected to behave at hermean surface and subsurface temperatures. Additionally, no exhaustive exploration of the thermophysical properties of other possible hollow-forming volatile phases has been done. Identifying the likely phase responsible for hollow formation will allow for a more informed evaluation of the plausibility of the three-stage model of Blewett et al. (2013) and of SEALS models for hollow formation more generally.

1.5. Hypothesis

Our null hypothesis is that no volatile phase exists that is unstable at hermean surface/near-surface temperatures but is stable under a lag deposit.

The alternative hypothesis is that one or more such volatile phases exist that are unstable at hermean surface/near-surface temperatures and stable under a lag deposit. We would reject our null hypothesis in favor of the alternative if a volatile phase can be found with the appropriate characteristics. For any volatile phases that show the appropriate thermophysical characteristics for hollow formation, we will then address their geological plausibility on Mercury. To address our null hypothesis, we solve the 1D time-dependent heat equation to calculate hermean diurnal temperature profiles across Mercury and then use these temperatures to calculate the loss rate of candidate volatiles at different depths using standard temperature-dependent sublimation and diffusion rate equations. In this way, we will narrow down the field of possible volatile phases involved in hollow formation, which will allow for a more informed evaluation of Stages 1 and 2 of the hollow-formation model of Blewett et al. (2013) and of the viability of SEALS models for hollow formation more generally. We describe the thermophysical model and discuss our choice of volatile phases and the calculation of volatile loss rates in *Section 2*. We report our results and discuss the implications in *Sections 3* and *4*, respectively. Additionally, we propose an alternative to a SEALS hollow-formation model in *Section 4.4*.

2. Method

For a host of possible hollow-forming phases, we will calculate volatile loss rates, hollow-formation timescales, and an expected latitudinal range of hollow formation and compare these to hollow-formation rates, timescales, and the latitudinal range that have been derived from observations of hollows on Mercury. We consider 57 volatile phases that can be generally categorized as inorganics, simple organics, aromatic hydrocarbons, linear amides, carboxylic acids, carbon (i.e., fullerenes and graphite), and sulfides (Table 1.1). We compiled this list based on volatile phases commonly found on solid solar system bodies (e.g., comets, asteroids) and in hermean volcanic eruptions (see Table S1 for information on volatile sources). It should be noted that while these phases

are *possible* not all are geologically *plausible* candidate hollow-forming phases. We consider this wide range of phases to explore the thermophysical parameter space and so as not to discount phases *a priori* that may lead to interesting considerations for hollow formation and hermean geology more generally.

2.1. Thermophysical Model

2.1.1. Heat Diffusion Equation

There have been several thermophysical models for Mercury formulated in past studies (e.g., Ulrichs and Campbell, 1969; Morrison, 1970; Chase et al., 1976; Mitchell and de Pater, 1994; Salvail and Fanale, 1994; Emery et al., 1998; Vasavada et al., 1999; Hale and Hapke, 2002; Yan et al., 2006; Paige et al., 2013; Bandfield et al., 2019).

Similar to past models, we consider heat conduction along the vertical dimension, and use the 1D time-dependent heat equation (Fourier, 1822):

Eq. 1

$$\rho c_p \frac{\partial T}{\partial t} = \frac{\partial}{\partial \mathrm{z}} k \frac{\partial T}{\partial z}$$

Where ρ is density, c_p is the specific heat capacity, and k is the effective thermal conductivity. We allow ρ to vary with depth (z), c_p to vary with temperature (T), and k to vary with z and T. For ρ, we use Carrier et al.'s (1991) empirically derived formula for lunar cores (**Eq. 2**) because these data serve as the best available analog to a hermean regolith density profile due to likely similarities (at least in gross properties) between the physical properties of hermean and lunar regolith (e.g., Chase et al., 1976; Hale and Hapke, 2002):

Eq. 2

$$\rho(z) = \rho_b \left(\frac{z + 0.122}{z + 0.18} \right)$$

Where $\rho(z)$ is density (kg m^{-3}) as a function of depth (z, in meters) and the subscript b indicates evaluation at the bottom boundary. We adopt a larger value for ρ_b than is used by Carrier et al. (1991) to account for Mercury's higher surface

gravity (Tables 2 and 3, see Carrier et al., 1991 for details). c_p is calculated using a fourth degree polynomial (**Eq. 3**) fit to data from Hemingway et al. (1973), Hemingway et al. (1981), Ledlow et al. (1992), and Wakabayashi and Matsumoto (2006).

Eq. 3

$$c_p = c_0 + c_1 T + c_2 T^2 + c_3 T^3 + c_4 T^4$$

This polynomial fit is valid for regolith and a range of temperatures between ~30 < T < ~1000 K (Fig. 1.A2) and is thus appropriate for our model. Polynomial coefficients are presented in Tables 1.2 and 1.3. We allow k to vary with temperature using an expression for effective thermal conductivity used in previous modeling that incorporates an empirical term for radiative heat transfer (e.g., Whipple, 1950; Watson, 1964; Cuzzi, 1974; Mitchell and de Pater, 1994):

Eq. 4

$$k = k_c + \beta T^3$$

Where k_c is the contact conductivity and β, defined as $4\sigma\epsilon l$, is a factor that incorporates the effects of inter-grain radiative transfer (Whipple, 1950). The values σ, ϵ, and l are the Stefan-Boltzmann constant, thermal emissivity, and the inter-grain length scale respectively. Empirical calculations by Fountain and West (1970) show that contact conductivity varies linearly with regolith density according to:

Eq. 5

$$k_c = k_b - (k_b - k_s)\frac{\rho_b - \rho(z)}{\rho_b - \rho_s}$$

where the subscript s indicates evaluation at the surface boundary. Because of the dependence of k and c_p on temperature, the thermal inertia ($TI = \sqrt{k\rho c_p}$) varies with time and depth. These dependencies will be important when comparing our model results to others where TI is an input parameter to the model (*Section 2.1.3*).

Table 1. 1. Chemical formulas, names, molecular masses, densities, and constants A and B (used in **Eq. 9)** for candidate hollow-forming volatile phases explored in this study.

Class	Molecular form	Name	Mass (amu)	Density (g/cc)	A	B	Ref
Inorganics	NH_3	Ammonia	17.031	0.82	19.6831	-3548.4791	[1]
	H_2O	Water	18.02	1.00	20.1454	-5709.7220	[1]
	CO	Carbon monoxide	28.01	0.99	15.8039	-901.2444	[1]
	N_2	Nitrogen	28.02	0.95	15.5330	-829.0949	[1]
	S^*	Sulfur	32.07	2.07	17.5020	-9028.6679	[1]
	H_2S	Hydrogen sulfide	34.09	1.20	17.7081	-2751.9756	[1]
	Ar	Argon	39.948	1.62	15.2978	-930.0365	[1]
	CO_2	Carbon Dioxide	44.01	1.51	20.9568	-3176.1315	[1]
	SO_2	Sulfur Dioxide	64.07	1.90	18.4501	-3600.7217	[1]
	Kr	Krypton	83.798	2.72	15.8999	-1342.6834	[1]
	Xe	Xenon	131.129	3.54	16.4629	-1939.6153	[1]
Simple Organics	CH_4	Methane	16.04	0.49	15.3208	-1174.8802	[1]
	HCN	Hydrogen Cyanide	27.026	1.03	18.0122	-3973.2133	[1]
	COS	Carbonyl Sulfide	60.08	1.56	15.7027	-2461.6665	[1]
	C_5H_{12}	Pentane	72.151	0.91	16.9266	-3632.1135	[1]
	CS_2	Carbon disulfide	76.15	1.55	16.2058	-3662.1778	[1]
	$C_5H_{10}O$	Pentanal	86.134	1.06	16.1700	-4166.2888	[1]
	C_7H_8	Toluene	92.141	1.03	15.8398	-4082.7779	[1]
	$C_5H_{10}O_2$	Ethyl Propanoate	102.133	1.15	17.2577	-4562.1276	[1]
Aromatic Hydrocarbons	C_6H_7N	Aniline	93.129	1.22	16.4401	-4961.9649	[1]
	C_6H_6O	Phenol	94.119	1.13	20.7498	-7182.3973	[1]
	C_7H_6O	Benzaldehyde	106.13	1.04	17.7545	-5870.3926	[1]
	C_7H_8O	Benzyl alcohol	108.146	1.10	18.0859	-5675.4731	[1]
	$C_7H_6O_2$	Salicylaldehyde	122.129	1.37	17.3999	-5965.0204	[1]
	$C_6H_5NO_2$	Nitrobenzene	123.111	1.34	17.7701	-6297.2056	[1]
	$C_{10}H_8$	Naphthalene	128.174	1.16	19.9823	-7289.6827	[1]
	$C_{10}H_8O$	1-Naphthol	144.173	1.10	17.6694	-7301.9245	[1]

Table1.1 continued

Class	Molecular form	Name	Mass (amu)	Density (g/cc)	A	B	Ref
Aromatic Hydrocarbons	$C_{10}H_8O$	2-Naphthol	144.173	1.28	17.6694	-7301.9245	[1]
	$C_{12}H_{10}$	Biphenyl	154.212	1.18	16.9013	-6739.6483	[1]
	$C_{12}H_{18}$	Hexamethylbenzene	162.276	0.98	17.4820	-6439.3143	[1]
	$C_{14}H_{10}$	Anthracene	178.22	1.25	22.4380	-10494.5425	[1]
	$C_{14}H_{10}$	Phenanthrene	178.234	1.15	22.4380	-10494.5425	[1]
	CH_3NO	Formamide	45.041	1.26	18.5481	-6812.7311	[1]
Linear Amides	C_2H_5NO	N-Methylformamide	59.068	1.20	18.8778	-6676.9254	[1]
	C_2H_5NO	Acetamide	59.068	1.16	18.8778	-6676.9254	[1]
	C_3H_7NO	Dimethylformamide	70.1	0.95	18.9430	-5974.6286	[1]
	C_3H_7NO	N-Methylacetamide	70.1	1.00	18.9430	-5974.6286	[1]
	C_4H_9NO	Dimethylacetamide	87.12	1.14	17.2279	-5058.8581	[1]
	C_4H_9NO	Methylpropanamide	87.12	1.01	17.2279	-5058.8581	[1]
	$C_5H_{10}O_2$	Valeric Acid	102.13	1.11	17.2577	-4562.1276	[1]
Carboxylic Acids	$C_6H_{12}O_2$	Caproic Acid	116.172	1.07	20.1922	-5939.0959	[1]
	$C_7H_{14}O_2$	Enanthic Acid	130.187	1.02	16.8860	-5040.5091	[1]
	$C_8H_{16}O_2$	Octanoic Acid	144.214	1.03	16.7891	-5271.9032	[1]
	$C_9H_{18}O_2$	Nonanoic Acid	158.241	1.05	16.8661	-5528.8777	[1]
	$C_{10}H_{20}O_2$	Capric Acid	172.268	0.87	19.6859	-6746.3687	[1]
	$C_{12}H_{24}O_2$	Lauric Acid	200.346	1.01	18.6443	-7174.2935	[1]
	$C_{16}H_{32}O_2$	Palmitic Acid	256.43	0.98	22.4353	-10900.4317	[1]
	$C_{18}H_{36}O_2$	Stearic Acid	256.43	0.88	22.6120	-11419.0224	[1]
	C_{60}	Buckminster Fullerene	720.6	1.57	26.6685	-22512.3745	[2,3]
Carbon	C_{70}	Fullerene C70	840.7	1.57	26.7008	-23530.1171	[2,3]
	C	Graphite	12.011	2.27	29.0706	-95618.4913	[1]

Class	Molecular form	Name	Mass (amu)	Density (g/cc)	A	B	Ref
Sulfides	K_2S	Potassium Sulfide	110.262	1.80	27.6517	-29972.0000	[1]
	Na_2S	Sodium Sulfide	78.0452	1.86	28.0546	-30987.0000	[1]
	MgS	Magnesium Sulfide	56.38	2.68	28.7618	-44693.0000	[1]
	MnS	Manganese Sulfide	87.003	4.00	28.5099	-44838.0000	[1]
	FeS	Iron Sulfide	87.92	4.84	31.2236	-46553.0000	[1]
	CaS	Calcium Sulfide	72.143	2.59	28.7698	-58092.0000	[1]
	CaS	Calcium Sulfide	72.143	2.59	28.7698	-58092.0000	[1]
	CaS	Calcium Sulfide	72.143	2.59	28.7698	-58092.0000	[1]

* In this study we use the S_8 allotrope of solid sulfur form the CRC handbook (ref. 1).

Table 1. 2 Range of parameter values explored and useful model outputs (dw, TI, dt)

				dw (m)	TI (time-averaged)	dt (s)
median values				0.1247	70.1	410.6
Albedo, A		Lower A	0.06	0.1247	70.7	410.6
		Upper A	0.14	0.1247	69.6	410.6
Emissivity, ϵ		Lower ϵ	0.9	0.1226	70.2	455.3
		Upper ϵ	1	0.1268	70.1	401.0
inter-grain length, l (μm) $\beta = 4\sigma\epsilon l$		Lower l	20	0.0903	58.7	675.5
		Upper l	130	0.1485	79.9	807.5
Density (kg m^{-3}) $\rho(z) = \rho_b\left(\frac{z+0.122}{z+0.18}\right)$	Lower ρ	ρ_b	1920	0.1454	59.9	807.5
	Upper ρ	ρ_b	3300	0.1109	79.2	746.2

Table 1.2 continued.

				dw (m)	TI (time-averaged)	dt (s)
Contact conductivity $(W\ m^{-1}\ K^{-1})$ $K_c = K_b - (K_b - K_s)\frac{\rho_b - \rho(z)}{\rho_b - \rho_s}$	Lower K_c	K_s	0.00005	0.1014	40.6	37.4 (min)
		K_b	0.00009			
	Upper K_c	K_s	0.09	0.4171	317.9	202.0
		K_b	0.1			
Heat Capacity $(J\ kg^{-1}\ K^{-1})$ $c_p = c0 + c1T + c2T^2 + c3T^3 + c4T^4$	Lower c_p confidence interval	$c0$	-1.47E+02	0.1371	59.4	807.4
		$c1$	4.12E+00			
		$c2$	-5.29E-03			
		$c3$	2.43E-06			
		$c4$	-4.75E-10			
	Upper c_p confidence interval	$c0$	-8.05E+01	0.1117	76.2	807.2
		$c1$	5.14E+00			
		$c2$	-8.73E-03			
		$c3$	7.64E-06			
		$c4$	-2.38E-09			

Table 1. 3 "Best Fit" Parameters

Parameter		Value
A		0.06
ϵ		0.95
l (μm)		75
ρ_b $(kg\ m^{-3})$		3100
K_c $(W\ m^{-1}\ K^{-1})$	K_s	0.004
	K_b	0.007
C_p $(J\ kg^{-1}\ K^{-1})$	$c0$	-8.05E+01
	$c1$	5.14E+00
	$c2$	-8.73E-03
	$c3$	7.64E-06
	$c4$	-2.38E-09
d_w (m)		0.1066
dt (s)		807.1
Time-averaged TI		92.7
kE_t		53.3

2.1.2 Boundary Conditions

2.1.2.1 Surface Boundary Condition

The temperature at the surface is controlled by a balance between incident solar flux, thermal conduction of endogenic heat, and radiative energy loss, such that the surface boundary condition can be written as:

Eq. 6

$$\rho c_p \frac{\partial T_s}{\partial t} = \frac{(1-A) * F_\odot}{R^2} \cos(\Theta_z) - k \frac{\partial^2 T}{\partial z^2}\bigg|_s - \sigma \epsilon (T_s^4)$$

The subscript s, again, denotes evaluation at the surface. A is the bolometric albedo and ϵ is the infrared emissivity of the surface[74,75]. R is the orbital radius of Mercury in AU, which varies from 0.308 to 0.467 AU. The solar constant, $F_\odot$, is 1367 W m^{-2} and is multiplied by the cosine of the solar incidence angle (Θ_z). Θ_z depends on the latitude and longitude of a horizontal surface facet and the subsolar latitude and longitude. We set $\cos(\Theta_z)$ to zero on the night side of the planet.

2.1.2.2 Bottom Boundary Condition

A profile of 10 m depth measured from the surface was chosen to ensure our model encompassed the depth at which the equilibrium temperature is achieved (~1 m in our model). The boundary condition at depth can be written:

Eq. 7

$$\rho c_p \frac{\partial T_b}{\partial z} = \frac{\partial}{\partial z}\left(k_b \frac{\partial T}{\partial z}\right)\bigg|_b + \frac{Q}{z} dz_b$$

The subscript b denotes evaluation at the bottom boundary, dz_b is the depth step at the bottom boundary, and Q is the internal thermal heat flux. Q has been calculated at 20 mW m^{-2} by Schubert et al. (1988) and Hauck et al. (2004), and contributes relatively little to the subsurface temperature at the depths explored by our model.

With the described boundary conditions, the implicit method of Crank and Nicolson (1947) is used to solve **Eq. 1**. We split our model into three grid layers to sample more finely near the surface and more coarsely with depth. The thickness of the first grid layer is calculated as 10% of the diurnal thermal skin depth (d_w, typically ~11 cm in our model, Table 2). The first layer samples the first ~cm of the surface at ~100 μm, approximately the scale of a regolith grain (c.f., Hale and Hapke, 2002). The second grid layer extends from 1 cm to 1 m depth and is sampled at twice the depth interval as used in the first layer. The third grid layer extends from 1 to 10 m in depth and samples at a depth interval that is 10 times larger than that used for the first layer. We used the maximum time step for explicit stability, typically ~5 to 7 minutes in our model (see, e.g., Hayne et al., 2017). Solutions were said to reach equilibrium when the change in integrated surface temperature between consecutive model days became < 0.005 K.

2.1.3 Model Sensitivity, Comparison to Mariner 10 IRR Data and to Other Thermal Models

We explored a range of physically plausible values for $A, \epsilon, l, \rho_b, k_s, k_b,$ and c_p to test the sensitivity of our model to variations in these parameters (c.f., BeipColombo-STR, 2000; Clark, 2015). Table 2 shows upper and lower parameter values and some model outputs ($d_w, TI,$ and dt) that are useful for evaluating the behavior of the model. When exploring the extremes of an individual parameter, all other values were set to median values to isolate the effect of the parameter of interest on the model. The diurnal surface temperatures and noon and pre-dawn temperature profiles for these model runs are presented in Figures 1.A3 and 1.A4. We compare our model results to the model results produced by Yan et al. (2006) (hereafter referred to as Y06) and Hale and Hapke (2002) (hereafter referred to as HH02). The model produced by Y06 is a relatively recent effort with a similar approach to that presented here, and the model by HH02 is more detailed and formally considers the effects of

radiative heat transfer. We also compare our surface temperatures to Mariner 10 Infrared Radiometer (IRR) nighttime surface temperatures (Chase et al., 1976). The parameter values ultimately used to calculate temperature profiles used for sublimation and diffusion rate calculations are presented in Table 3.

Albedo, A, controls how much insolation is absorbed by the surface. We considered a range from 0.06 to 0.14, which encompasses values commonly considered for Mercury (e.g., Clark, 2015; Rothery, 2015). Infrared emissivity, ϵ, modulates the amount of energy emitted by the surface according to the Stefan-Boltzmann law. We considered a range for ϵ from 0.9 to 1, values typical for silicate-dominated planetary surface materials. While variations in A and ϵ values can produce large effects on surface temperatures, the ranges of values plausible for Mercury are relatively small and as such these parameters do not greatly affect temperatures in our model (Figs. 1.A3 and 1.A4).

The inter-grain length scale, l, is used to calculate β in **Eq. 4**. l is typically on the order of a grain size, so we used values ranging from 20 to 130 μm (e.g., Carrier, 1973).

The value for density at depth, ρ_b, controls the density profile as described by **Eq. 2**. Values for ρ_b ranged from 1920 kg m^{-3} to 3300 kg m^{-3}, which correspond to surface densities of 1301 kg m^{-3} and 2236 kg m^{-3}, respectively (see Fig. 1.A5, c.f., Clark, 2015). The lower value was chosen because it is typical for lunar density profiles (Carrier et al., 1991) and the upper value was chosen to encompass an upper end density of gabbro (a reasonable upper limit estimate for hermean density at depth).

Thermal conductivity values can range over orders of magnitude; consequently, thermal conductivity has the largest effect on both surface and subsurface temperatures and, therefore, on uncertainty within our model (Figs. 1.A3 and 1.A4). We used a range that encompasses more than the variability in thermal conductivity found in lunar regolith (e.g., Heiken et al., 1991; Schreiner et al., 2016) to account for possible differences between the properties of hermean regolith and lunar regolith. Values for k_s range from 5 x 10^{-5} to 9 x 10^{-2} W m^{-1} K^{-1}

and values for k_b range from 9 x 10^{-5} to 1 x 10^{-1} W m^{-1} K^{-1}. Y06 calculated a value for k_c by fitting their model to a model run from HH02 and determined 5 x 10^{-5} W m^{-1} K^{-1} as the best-fit value. Our model results for the lower values of $k_{s,b}$ match well with the results of Y06 (diamond symbols in Fig. 1.A4). The HH02 temperature-depth profile we use for comparison (squares, Fig. 1.A4) is that which the authors suggested best represented the hermean regolith. Note that increasing values of $k_{s,b}$ has the expected effect of decreasing the equilibrium temperature and increasing the penetration depth of the thermal wave.

For T-dependent c_p, a fourth-degree polynomial (**Eq. 3**) was fit to lunar regolith data (see Fig. 1.A2 for data and citations). To incorporate possible differences in c_p between hermean and lunar regolith, we added an uncertainty of ±75 J kg^{-1} K^1 to the data and calculated ±85% confidence intervals ("upper" and "lower" c_p, Table 2). Our fits are compared to those of Hemingway et al. (1973); Ledlow et al. (1992); Hayne et al. (2017) in Figure 1.A2.

As a check for the reasonableness of the range of parameter space explored, we compared our range to the range investigated by HH02. The free parameters in HH02's model were TI and the "conductivity ratio" ($kE_t \equiv k_c/L_{Ex}$, where L_{Ex} is the thermal extinction length). We calculated a value for the conductivity ratio in our model using l, the inter-grain length, as an estimate of L_{Ex}, which was suggested to be comparable for hermean regolith by HH02. Our lower limit of kE_t is 0.7 and our upper limit is 1200, compared to 1 and 1000 by HH02. Our min, max, and median time-averaged TI values were 40.6, 317.9, and 70.1 J m^{-2} K^{-1} $s^{-1/2}$ compared to 43, 67, and 65 J m^{-2} K^{-1} $s^{-1/2}$ by HH02 (Table 4).

2.2 Sublimation Rate Equations and Choice of Volatile Phases

2.2.1 Sublimation at the Surface

We considered volatiles that are likely to exist on Mercury from impact delivery (Pierazzo and Chyba, 1999; Botta and Bada, 2002), emplacement from volcanic processes (Kerber et al., 2009), or from space weathering

Table 1. 4 Comparison to HH02 free parameters

Parameter	This Work	HH02
Lower kE_t	0.7	1
Upper kE_t	1200.0	1000
Median kE_t	40.0	50
Lower TI	40.6	43
Upper TI	317.9	67
Median TI	70.1	65

(Domingue et al., 2014). Table S1 lists common volatiles and their concentrations found in meteorites (Botta and Bada, 2002), comets (Ferris et al., 2007), and hermean magmas (Kerber et al., 2009, 2011). For the behavior of volatiles at the surface, we are interested in the rate at which these volatiles will sublimate as a function of temperature in vacuum. To calculate the sublimation rate, we us the Hertz-Knudsen equation (e.g., Watson et al., 1961):

Eq. 8

$$E_i = P_v \left(\frac{\mu_i}{2\pi \mathrm{R} T}\right)^{\frac{1}{2}}$$

Where E_i is the mass sublimation rate of volatile i (kg m^{-2} s^{-1}); μ_i is the molar mass of volatile i (kg mol^{-1}); R is the gas constant (m^2 kg s^{-2} K^{-1} mol^{-1}); T is the temperature (K); and P_v is the temperature-dependent solid-vapor equilibrium pressure (Pa). P_v is calculated using the standard vapor pressure equation (e.g., Lodders and Fegley, 1998):

Eq. 9

$$\ln\big(P_v(T)\big) = A_i + \frac{B_i}{T}$$

Where A_i and B_i are constants for volatile phase i derived by fitting **Eq. 9** to laboratory-derived pressure and temperature data from Rumble (2018) and Rankin (2009). The coefficients derived from our fitting are presented in Table 1.

We convert E_i into a sublimation rate in m Gyr^{-1} by dividing by the density of each volatile phase (from Yaws, 2014) and converting seconds to Gyr. For each volatile, one can calculate a "volatility temperature" defined as the temperature at which E_i equals some desired rate. Zhang and Paige (2009) calculated a "volatility temperature", T_{vz}, using E_i = 1 mm Gyr^{-1}. We calculated values for T_{vz} and compared to those of Zhang and Paige (2009) (Fig. 1.4). Differences between our calculated temperatures and those of Zhang and Paige (2009) arise from differences in the P-T data used to derive constants A_i and B_i (**Eq. 9**) and in our choices for volatile densities. Our calculation uses the density of each volatile phase (ρ_i) whereas Zhang and Paige (2009) used 1000 kg m^{-3} in

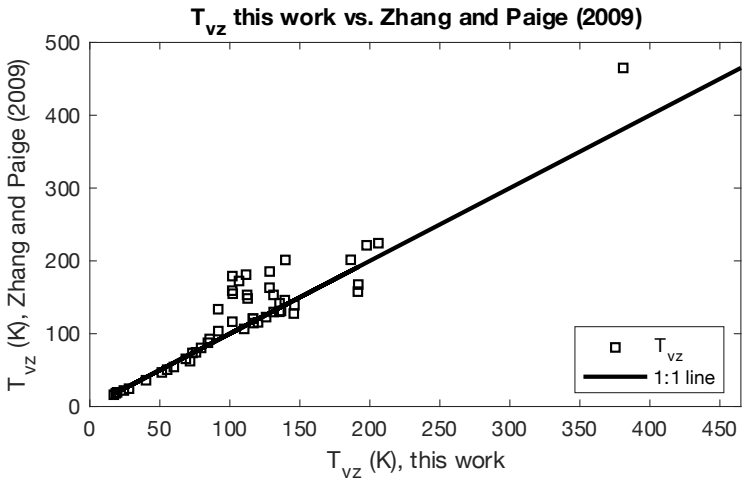

Fig. 1. 4. Comparison between the volatility temperatures of Zhang and Paige (2009) and those calculated in this work. See text for details on differences.

all calculations. The results of our sublimation rate calculations are reported in Figure 1.5. These sublimation rates are for pure volatile phases and do not incorporate possible chemical and physical interactions with other constituents of the regolith and should be thought of as ideal upper limits (i.e., phases may be stable on the surface for longer than modelled here).

Sulfides must be treated differently because they do not simply sublimate as do the other volatile phases considered here. Sulfides will decompose into their elemental constituents at temperatures below their melting point through a process called reactive sublimation or thermal decomposition. We use reactive sublimation to refer to surface reactions because it encapsulates both the decomposition of the metal-sulfide bond and the subsequent sublimation to vacuum of the gas phase products, and we use thermal decomposition to refer more generally to the decomposition reaction. Where this work refers to the "sublimation" of sulfides, reactive sublimation is implied. The thermal decomposition of Na_2S, MnS, MgS, and/or CaS is a proposed mechanism for hollow formation (Vaughan et al., 2012; Helbert et al., 2013; Thomas et al., 2016). Therefore, we consider these sulfides along with other sulfides that plausibly exist on or within Mercury as potential hollow-forming materials (Table 1). A general equation for the decomposition reaction of a sulfide can be written as:

Eq. 10

$$\mathrm{M_xS_{y(s)}} \rightarrow \mathrm{xM_{(g)}} + \frac{y}{2} S_{2(g)}$$

Vapor pressure data are not available for the decomposition reactions we consider. However, an ideal maximum rate as a function of temperature can be calculated from analysis of the Gibb's free energy of the reactions (assuming the change in heat capacity between the products and reactants is independent of temperature) according to:

Eq. 11

$$\Delta \mathrm{G} = \Delta \mathrm{G}^{\circ} + \mathrm{R}T\ln\left(\mathrm{K_{eq}}\right)$$

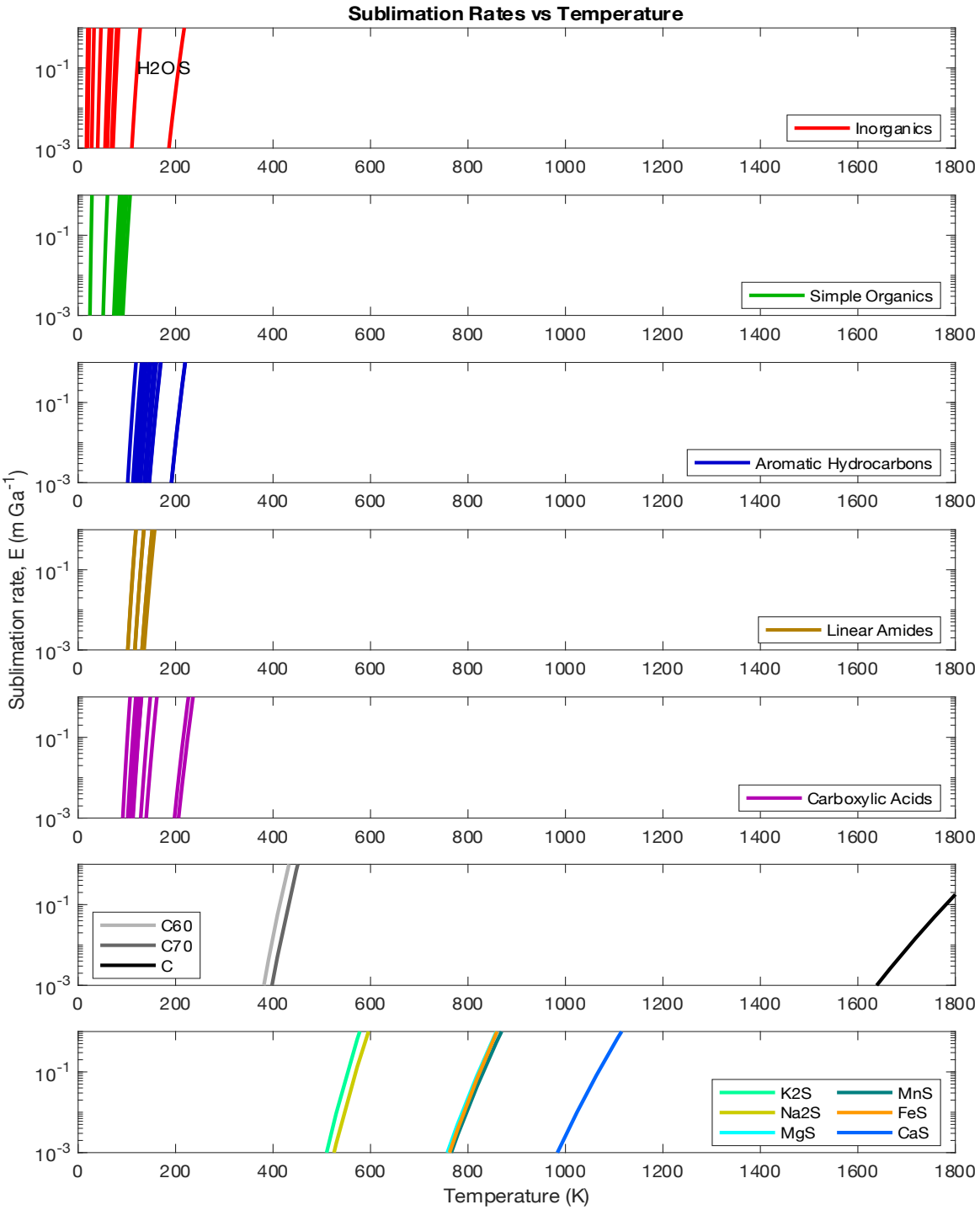

Fig. 1. 5. Sublimation rates vs. temperature for the volatiles in this study. Volatiles are grouped into different plots by compound classes. Legends for the bottom two plots list phases from left to right. Colors correspond to Table 1. Values listed in Table 1 were used to calculate rates using **Eq. 9**.

Where ΔG is the Gibbs free energy of the reaction and ΔG° is the standard state Gibb's free energy of the reaction given by:

Eq. 12

$$\Delta G^{\circ} = \Delta H^{\circ} - T\Delta S^{\circ}$$

$\Delta H^{\circ}$and ΔS° are the change in enthalpy and entropy, respectively, between products and reactants at standard state. The equilibrium constant, K_{eq}, is given by the expression:

Eq. 13

$$K_{eq} = P_M^x P_{S_2}^{\frac{y}{2}}$$

Where, P_M^x and $P_{S_2}^{\frac{y}{2}}$ are the partial pressures of the gas-phase products of the reaction, that is, the sulfide metal cation and disulfur, exponentiated by their molar concentrations, x and $\frac{y}{2}$. Substituting **Eq. 13** and **Eq. 12** into **Eq. 11** and noting that $P_{S_2} = \frac{y}{2x} P_M$, we solved for the vapor pressure (in atmospheres) of the reaction in terms of the vapor pressure of the metal, M (e.g., Leckey and Nulf, 1994):

Eq. 14

$$\ln\left(P_M(T)\right) = \frac{y}{2x + y} \ln\left(\frac{2x}{y}\right) + \frac{\Delta S^{\circ}}{\left(x + \frac{y}{2}\right) R} - \frac{\Delta H^{\circ}}{\left(x + \frac{y}{2}\right) RT}$$

In this form, we can see that the constants A_i and B_i from **Eq. 9** are equal to:

$$A_i = \frac{y}{2x + y} \ln\left(\frac{2x}{y}\right) + \frac{\Delta S^{\circ}}{\left(x + \frac{y}{2}\right) R}$$

$$B_i = -\frac{\Delta H^{\circ}}{\left(x + \frac{y}{2}\right) R}$$

With an equation for vapor pressure, the sublimation rate is calculated as before with **Eq. 8**. Note that converting the vapor pressure from atmospheres to pascals requires an addition of $\ln(101{,}325)$ to the constant A_i. Using the method

delineated above, we calculated constants A_{PbS} and B_{PbS} for the thermal decomposition of PbS, for which vapor pressure data do exist in the CRC handbook (and references therein), to compare to the constants derived by fitting **Eq. 9** to experimental data. Table 1 shows the coefficients derived from both methods ($A_{PbS,theory} = 27.6, B_{PbS,theory} = -28{,}801;\ A_{PbS,experiment} = 21.9, B_{PbS,experiment} = -26{,}851.9$).

For comparison on the effect each coefficient has on the vapor pressure, we calculated the percent error between the theoretically and experimentally derived vapor pressure curves (Fig. 1.A6). The percent error is a function of temperature and is highest at low temperatures because the vapor pressure values are very low. The error between the curves is zero at 340 K and is ~94% at 710 K. The vapor pressure calculated from theory is higher (at temperatures > 340 K) than those calculated from experimental data, as expected, which results in calculated sublimation rates that are faster than those determined experimentally. We emphasize that our thermal decomposition rate calculations for sulfides are theoretical upper limits.

Lastly, we derived a surface sublimation rate for each volatile phase over one hermean day (i.e., two hermean years) by integrating **Eq. 8** over a diurnal surface temperature profile produced by our thermal model. The model-derived rates are compared to rates estimated for hollow formation based on observations of hollows on Mercury in *Section 3*.

2.2.2 Diffusion Through a Regolith Cover

To assess the rate of volatile loss through a regolith cover we use Fick's law:

Eq. 15

$$F_i = D_k(T)\frac{\phi}{\tau}\frac{\delta N_i(T)}{\delta z}$$

Where, F_i is the loss flux (kg m^{-2} s^{-1}) of volatile i, ϕ is porosity, τ is tortuosity, and $\frac{\delta N_i(T)}{\delta z}$ is the gradient in vapor density (mol m^{-3}) from the volatile

Table 1. 5. Estimated hollow-formation rates based on the average depth of hollows within 30° latitudinal bins with two estimates for the timescale of hollow formation (300 Myr and 4 Gyr). Rates are presented in m Gyr^{-1}.

Latitude	Average Depth (m)	Characteristic vertical growth rate depth/0.3 Gyr	Minimum effective vertical growth rates depth/4 Gyr
0°N to 30°N	25.7	85.6	6.4
30°N to 60°N	24.5	81.8	6.1
60°N to 90°N	13.3	44.2	3.3

layer to the surface, assuming the surface is at vacuum. We calculate vapor density from vapor pressure (**Eq. 9**) using the ideal gas law. The diffusion coefficient, $D_k(T)$, is equal to $\frac{4}{3} r \left(\frac{2RT}{\mu_i \pi}\right)^{\frac{1}{2}}$, and is calculated from Knudsen diffusion theory considering the mean molecular speed within a cylindrical pore of radius r (e.g., Pollard and Present, 1948; Moore et al., 1996). Knudsen diffusion is valid when r is comparable to or smaller than the mean free molecular path of the volatile phase, that is, when molecular collisions with the pore wall dominate over molecule-molecule collisions. This condition is true for the volatile phases and conditions explored here with the exception of simple organic molecules and the most-volatile inorganics (Table S2). Molecules for which this condition is not true have regolith diffusion rates that are likely over estimated.

We define a column integrated porosity after Carrier et al. (1991) as $\phi = 1 - \frac{\bar{\rho}(z)}{G_h \rho_w}$, where z is the thickness of the regolith cover, $\bar{\rho}(z)$ is the mean column density calculated from **Eq. 2**, G_h is the specific gravity of hermean regolith and ρ_w is the density of water. Values for ϕ range from 52.1% to 29.7% for 1 mm and 100 m regolith covers respectively. Tortuosity, τ, captures the degree to which the diffusive path deviates from a straight line. Typical values of τ for various regolith and regolith-simulant materials range from ~1.5 to 7, but values can be as low as 1 to as high as 12.5 (Reiss, 2019 and references therein). In the absence of experimental data describing τ for hermean regolith, we use the Bruggeman model describing tortuosity as a function of porosity for cylinders in which $\tau = \phi^{-1}$ (Bruggeman, 1935; Tjaden et al., 2016). As with our values for the surface sublimation rate, E_i, we convert F_i into a sublimation rate in m Gyr^{-1} by dividing by the density of each sulfide phase (from Yaws, 2014) and converting seconds to Gyr.

F_i was calculated for each volatile phase using time-varying temperature versus depth profiles of volatile-free regolith derived from our thermal model as inputs into **Eq. 15**. Rates were integrated over a hermean day (two hermean

years) to derive loss rates as a function of depth along the hot and warm meridians. If the effects of volatile species in the pore space of regolith were included in our temperature profile calculations, it would enhance heat transfer (by enhancing contact conductivity), increase the temperature in volatile-bearing zones, and therefore increase sublimation rates. We comment on the implications of neglecting the effects of pore-filling volatiles on the thermal profile in our results (*Section 3*).

2.3 Metrics for Comparison: Hollow Formation Rates, Timescales, and Latitudinal Extent

In *Section 3*, we compare our model-derived hollow-formation rates and timescales for each volatile phase to rates and timescales derived from observations of hollows on the surface made in Blewett et al. (2016) because that study offers an analysis of over 500 images of hollows at pixel scales of < 20 m, which is ~10 times higher resolution than other large-scale studies of hollows. To calculate hollow formation rates, we require hollow depths and an estimate for the timescale over which hollows formed. As shown in Figure 1.2d, the average depth of hollows is latitude-dependent, so we chose to calculate latitude-dependent rates by averaging the depth of hollows between 0°N and 30°N, 30°N and 60°N, and 60°N and 90°N (Table 5). The tightest observationally derived constraint for the timescale over which hollows form is 300 Myr, and comes from hollows in the rayed crater Balanchine at 38.6°N, 175.3°E (Blewett et al., 2016). Blewett et al. floor of Balanchine by taking the lateral extent of the hollows (300 m) and dividing that by the estimated age of the crater (300 Ma). Because we are interested in the rate of downward growth, we instead estimate a vertical-growth rate by using the depth of hollows rather than their lateral extent. The 300 Myr timescale for hollow formation in Balanchine crater is an upper limit for how long the hollows in Balanchine may have taken to form. The hollows in Balanchine are the only

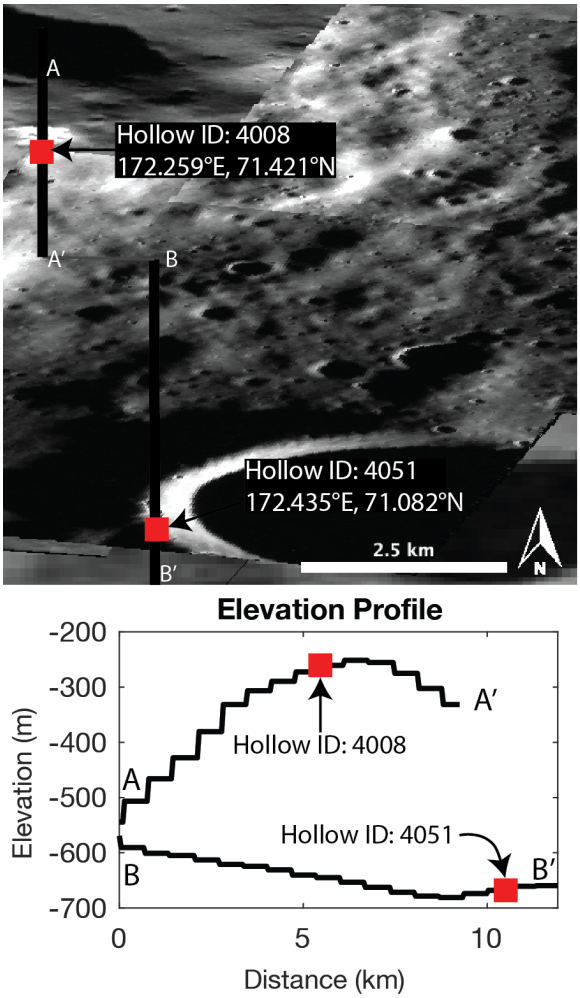

Fig. 1. 6. Hollows at the cold limit of hollow formation. North-south oriented elevation profiles showing the slopes for hollow 4008 at 71.4°N (A to A') and 4051 at 71.1°N (B to B'). Vertical black bars in the elevation profile show the locations of each hollow along the profiles. Hollow ID numbers are from the global hollow database of Thomas et al. (2016). The elevation profiles show that the slopes on which these hollows have formed are slightly north facing (~1.2° for hollow 4008 and ~0.6° for hollow 4051). Analysis was done with MDIS images <20 m/pixel and with the USGS digital topography map (665 m/pixel resolution) in JMARS.

hollows for which a published timescale estimate exists, so we used this timescale along with the average hollow depths over each latitudinal range to calculate “characteristic” vertical-growth rates of hollows (characteristic vertical-growth rate, Table 1.5). The possibility that hollows in Balanchine formed over a faster timescale cannot be precluded, and therefore our characteristic rates are lower limit estimates of actual hollow formation rates.

In addition to the characteristic rates of hollow formation, it is also necessary to estimate a rate below which hollow growth can be considered effectively inactive. We call these rates the “minimum effective” vertical-growth rates (Table 1.5). These rates were calculated for each latitudinal range based on an estimate for the absolute maximum timescale over which hollows could form coupled with average hollow depth values over each latitudinal range. For the upper limit timescale estimate, we used 4 Gyr based on an age estimate for heavily cratered terrain (the oldest terrain where hollows are commonly found) from Marchi et al. (2013)

Another metric for comparison between our model-derived results and observations of hollows is the range of latitudes over which hollows are observed on Mercury. Hollows are found at the hot poles. Therefore, a candidate hollow-forming volatile must be able to be sequestered beneath a regolith lag deposit of reasonable thickness (i.e., < 100 m). That is, the loss rate of a candidate hollow-forming phase must be suppressed to a slow enough rate when buried beneath a regolith lag deposit at the hot pole such that hollow formation can be considered effectively inactive. We call this constraint the “hot limit” of hollow formation. The hot limit can be considered a soft constraint because in addition to being limited by a lag deposit, hollow growth could be limited by exhaustion of the volatile phase. However, volatile exhaustion is considered a less favorable mechanism for hollow growth cessation than lag development because the thickness of the volatile-sourcing LRM is several km-thick, whereas hollows are only 10s to ~100 m-deep (Blewett et al., 2016). The second constraint is imposed by the location of the northernmost observed hollows and is twofold: 1) whether a phase can

sublimate quickly enough at that latitude to account for hollow formation; and 2) whether a phase is refractory enough that it is not expected to form hollows at that latitude. We call this constraint the “cold limit” of hollow formation, which we discuss in more detail below.

The solar insolation received by a surface facet depends on its location on Mercury, its albedo, its orientation, and whether the facet suffers from target adjacency effects (i.e., if adjacent topography fills any portion of its “sky”, contributing radiation to, and thereby warming, the target). Our model takes into account the location and physical properties of a surface facet, but we assume a horizontal surface freely radiating to space, which means our calculations do not include the effects that surface facet orientation or that target adjacency might have on the local thermal environment of a hollow. Therefore, we set the cold limit of hollow formation for our model using the latitude of the northernmost hollows that form on a horizontal surface and have no obvious local topography that might produce target adjacency effects. We found that this occurred at ~71°N with hollows 4008 and 4051 of the Thomas et al. (2016) database. All 20 hollows north of 4008 and 4051 occur along the south-facing walls of their host craters (Fig. 1.6). Hollow 4008 is on a regional north-dipping slope (~1.2° as measured using a global MESSENGER-derived 665 m/pixel elevation raster from Denevi et al., 2018), and hollow 4051 occurs on the crest of the western rim of an approximately 5 km-diameter crater, which gently dips northward at ~0.6° (Fig. 1.6). Both hollows are near the apexes of their local topography, satisfying the target adjacency condition, and are on near-horizontal surfaces (slopes < ~1.2°) that do not dip toward the equator. From these two hollows, we will set the cold limit of hollow formation at 71°N.

3. Results

We have calculated hollow-formation rates along the hot and warm meridians at 1° latitudinal increments at the surface and as a function of depth for 57 different candidate hollow-forming volatile phases (listed in Table 1). Our

mass-loss rate calculations are upper limits for pure volatiles that are assumed to be heated to the ambient temperatures of surrounding hermean regolith at the surface and in the subsurface (see *Section*s *2.2.1* and *2.2.2* for details). The assumption of "pure volatiles" means that we ignore possible chemical and physical interactions between volatiles and regolith grains that could inhibit sublimation, such as local increases in vapor pressure or adsorption of volatiles onto regolith grains; however, for volatiles covered by regolith, we explicitly model volatile diffusion through a porous regolith cover (*Section 2.2.2*). For the input temperature profiles that we use, our results should be interpreted as ideal upper limit sublimation rates. We also assume that hollow depth is equal to the amount of volatile substance lost, i.e., the volatile mass-loss rate equals the hollow formation rate. For each volatile phase, we used our model-derived hollow-formation rates to 1) estimate hollow-formation timescales at various latitudes assuming typical hollow depths at those latitudes (see Table 5); 2) estimate the thickness of a regolith lag deposit necessary to suppress hollow formation rates to inactive levels at the hot and cold limits of hollow formation; 3) predict a range of latitudes over which hollows would be observed on Mercury. We compare these model results to observations of hollows on the surface (see *Section 2.3* for an explanation of comparison metrics).

3.1 Hollow-Formation Timescales

Figure 1.7 shows the model-derived hollow-formation timescales at mid-latitude and at the hot and cold limits of hollow formation for each of the 57 phases in our study. Along the hot meridian (Fig. 1.7 top panel), most substances would form hollows in less than a year even at the cold limit of 71°N. Sulfur would form hollows in ~0.1 and 10 yrs at the hot and cold limits, respectively. Fullerenes would form hollows in ~1 kyr and 100 Myr at the hot and cold limits, respectively. The only substances that do not sublimate quickly enough to explain hollow formation at the cold limit are sulfides. However, the mid-latitude rate for K_2S is the closest match to the characteristic timescale estimate for hollow formation of

300 Myr (Table 5), which was derived from a hollow at mid-latitude (~39°N, Blewett et al., 2016).

Along the warm meridian, most substances would form hollows in less than 100 yrs even at 71°N (Fig. 1.7 bottom panel). Elemental sulfur would form hollows in ~10 and 100 yrs at the hot and cold limits, respectively. The mid-latitude sublimation timescale for fullerenes is the closest match to the fast timescale estimate of 300 Myr, but fullerenes cannot form hollows in less than 4 Gyr at 71°N. Sulfides cannot form hollows in less than 4 Gyr even at 0°N along the warm meridian. There are no volatile phases with mid-latitude rates that closely match the characteristic timescale of 300 Myr and yet can also form hollows faster than the minimum necessary timescale of 4 Gyr at the cold limit of 71°N. Therefore, hollows most likely form over a timescale shorter than 300 Myr, consistent with recent results from Wang et al. (2020b).

3.2 Regolith Lag Deposits

Loss rates as a function of depth (see *Section 2.2.2* for details on calculation methods) were used to calculate the thicknesses of regolith lag deposits necessary to suppress volatile loss to less than relevant threshold values at the hot and cold limits of hollow formation (Figs. 1.8, 1.9, and 1.10). We estimate a range of lag deposit thicknesses for each volatile phase by calculating lag thicknesses at the hot (thickest lag) and cold (thinnest lag) limits of hollow formation. The threshold rate values we use are the minimum effective rate values listed in Table 1.5 (see *Section 2.3* for how these rates were calculated) because hollow formation that proceeds slower than these rates is considered effectively inactive. Regolith lag deposit thicknesses were calculated as the point in the subsurface where the mass-loss rate is equal to the minimum effective hollow-formation rate value (Table 1.5). In Figures 1.8 and 1.9, this is the depth at which the left vertical black line intersects the mass-loss rate curves. For some volatile phases, the mass-loss rate is never suppressed to below the minimum

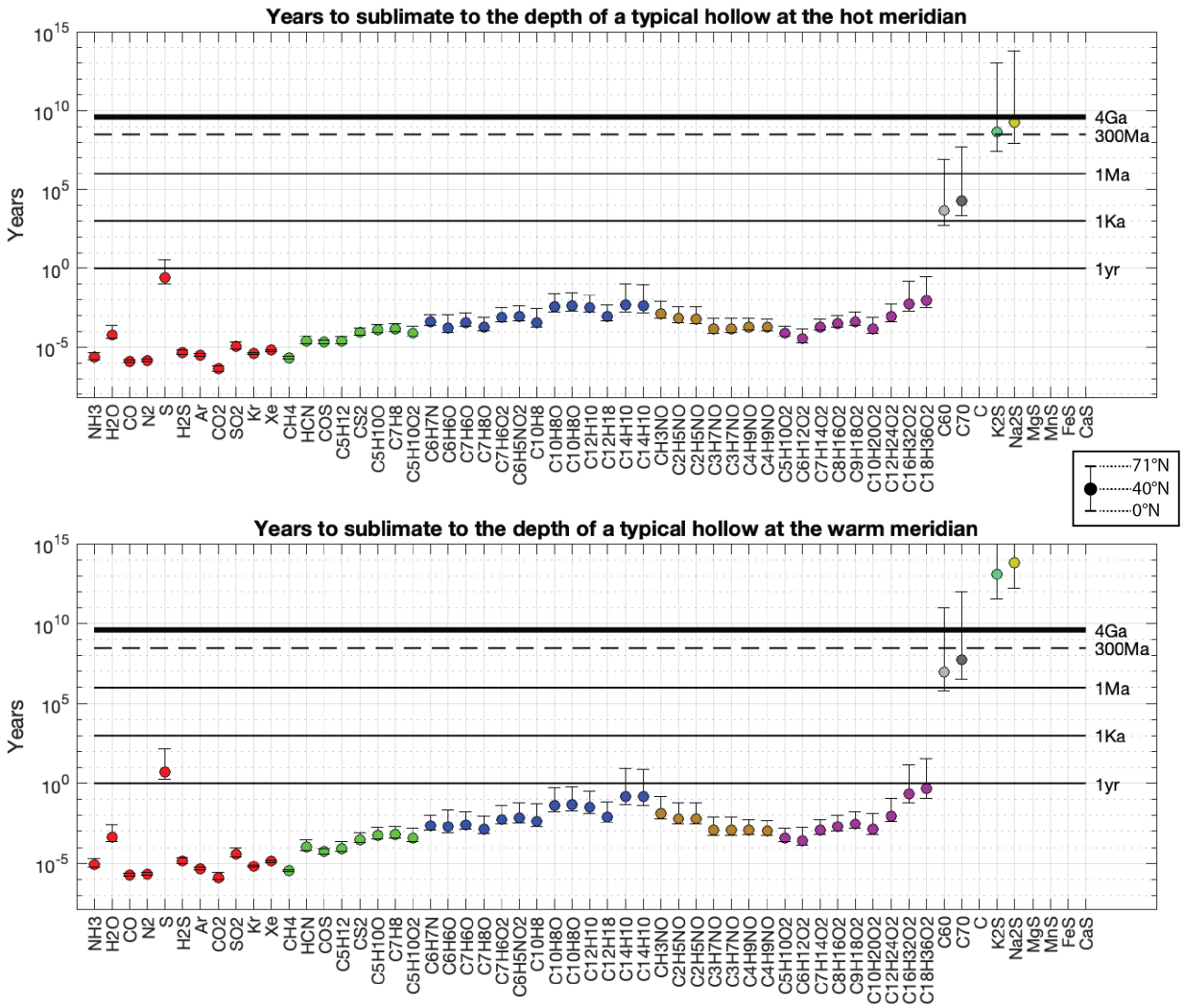

Fig. 1. 7. The vertical axis shows the time in years it would take to sublimate each substance to the average hollow depth for each latitudinal range (Table 5). Colors correspond to the compound classes in Table 1. Horizontal lines are drawn at 1 yr, 1 kyr, 1 Myr, 300 Myr, 4 Gyr to facilitate interpretation. The estimated timescale for hollow formation (derived from hollows in Balanchine crater, Blewett et al., 2016) corresponds to the dashed line at 300 Myr. The circle markers represent the hollow formation timescale for each volatile phase at latitude 40°N, the upper bar is for 71°N, and the lower bar is for 0°N (see legend). If a candidate hollow-forming phase plots below the dashed line at 40°N along the warm meridian and below the solid line at 4 Gyr along the warm meridian, it is considered a viable candidate. Sulfides and graphite (C) do not meet this requirement. The mid-latitude sublimation timescale for fullerenes are the closest match to the mid-latitude timescale of 300 Myr, but fullerenes cannot form hollows quickly enough at the cold limit of 71°N. Note that graphite and sulfides more refractory than Na_2S plot off the top of the chart; values for these species are provided in Table S3 of the appendix.

Fig. 1. 8. Volatile loss rates as a function of depth on Mercury at the hot limit of hollow formation. Colors correspond to the compound classes in Table 1. For simple organics (green), aromatic hydrocarbons (blue), linear amides (yellow), and carboxylic acids (magenta) only the minimum and maximum of the compound classes are plotted for simplicity. Vertical lines are the minimum effective (6.4 m Gyr^{-1}) and the characteristic rate (85.6 m Gyr^{-1}) for hollow formation at 0°N (Table 5). A viable candidate volatile is expected to plot to the right of the rightmost vertical black line at the surface (depth approaches 0) and, at minimum, to the left of the leftmost vertical black line in the subsurface. Thus, a candidate volatile crosses both vertical black lines.

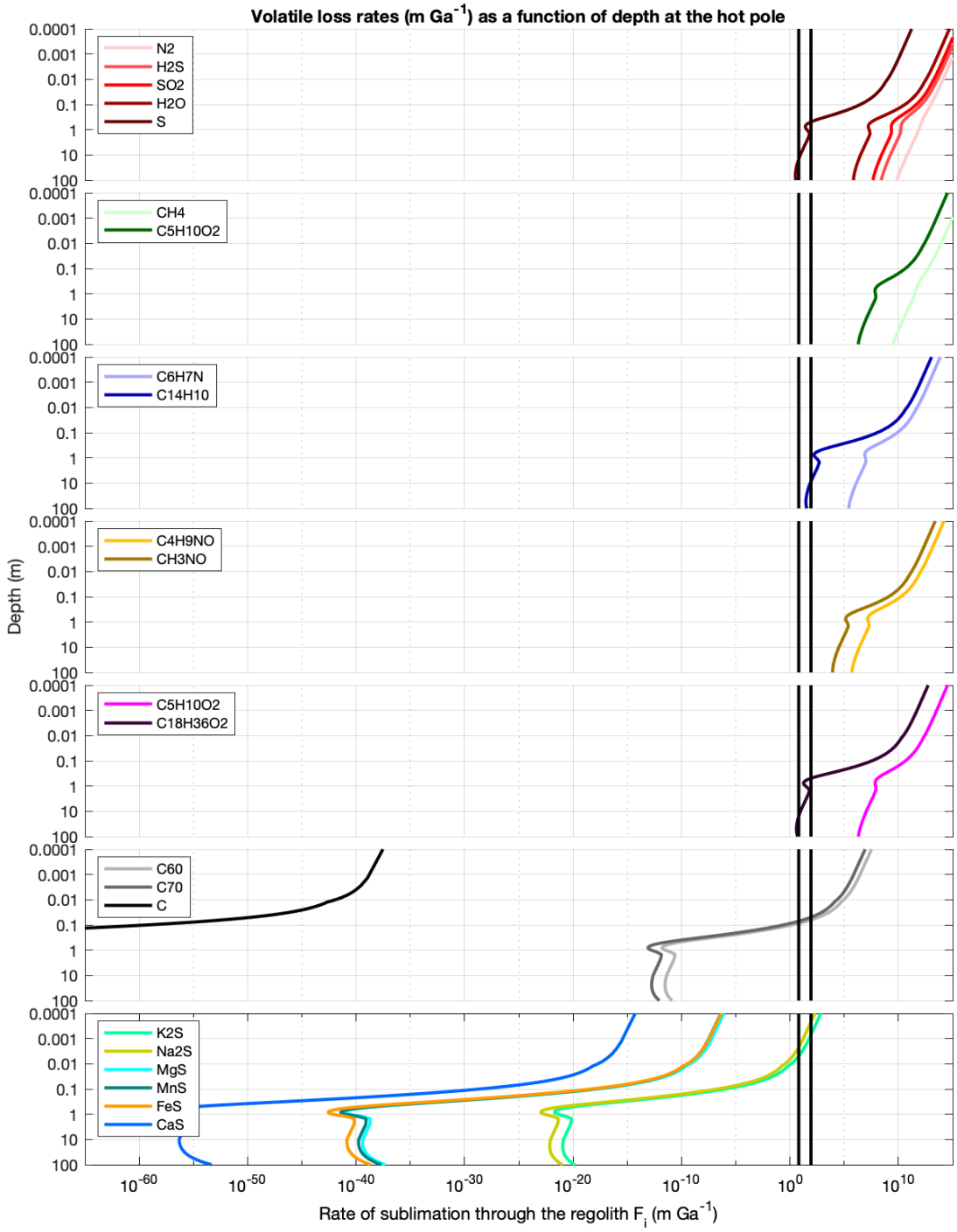
Volatile loss rates (m Ga^{-1}) as a function of depth at the hot pole
Depth (m)
0.0001
0.001
0.01
0.1
1
10
100
N2
H2S
SO2
H2O
S
CH4
C5H10O2
C6H7N
C14H10
C4H9NO
CH3NO
C5H10O2
C18H36O2
C60
C70
C
K2S
Na2S
MgS
MnS
FeS
CaS
10^{-60}
10^{-50}
10^{-40}
10^{-30}
10^{-20}
10^{-10}
10^{0}
10^{10}
Rate of sublimation through the regolith F_i (m Ga^{-1})

Fig. 1. 9. Volatile loss rates as a function of depth on Mercury at the cold limit (71°N along the warm meridian). Colors correspond to the compound classes in Table 1. Vertical lines are the minimum effective rate (3.3 m Gyr^{-1}) and the characteristic rate (44.2 m Gyr^{-1}). In a SEALS hollow formation model, a viable candidate volatile is expected to plot to the right of the rightmost vertical black line at the surface (depth approaches 0) and to the left of the leftmost vertical black line at some point in the subsurface. Thus, a candidate volatile crosses both vertical black lines.

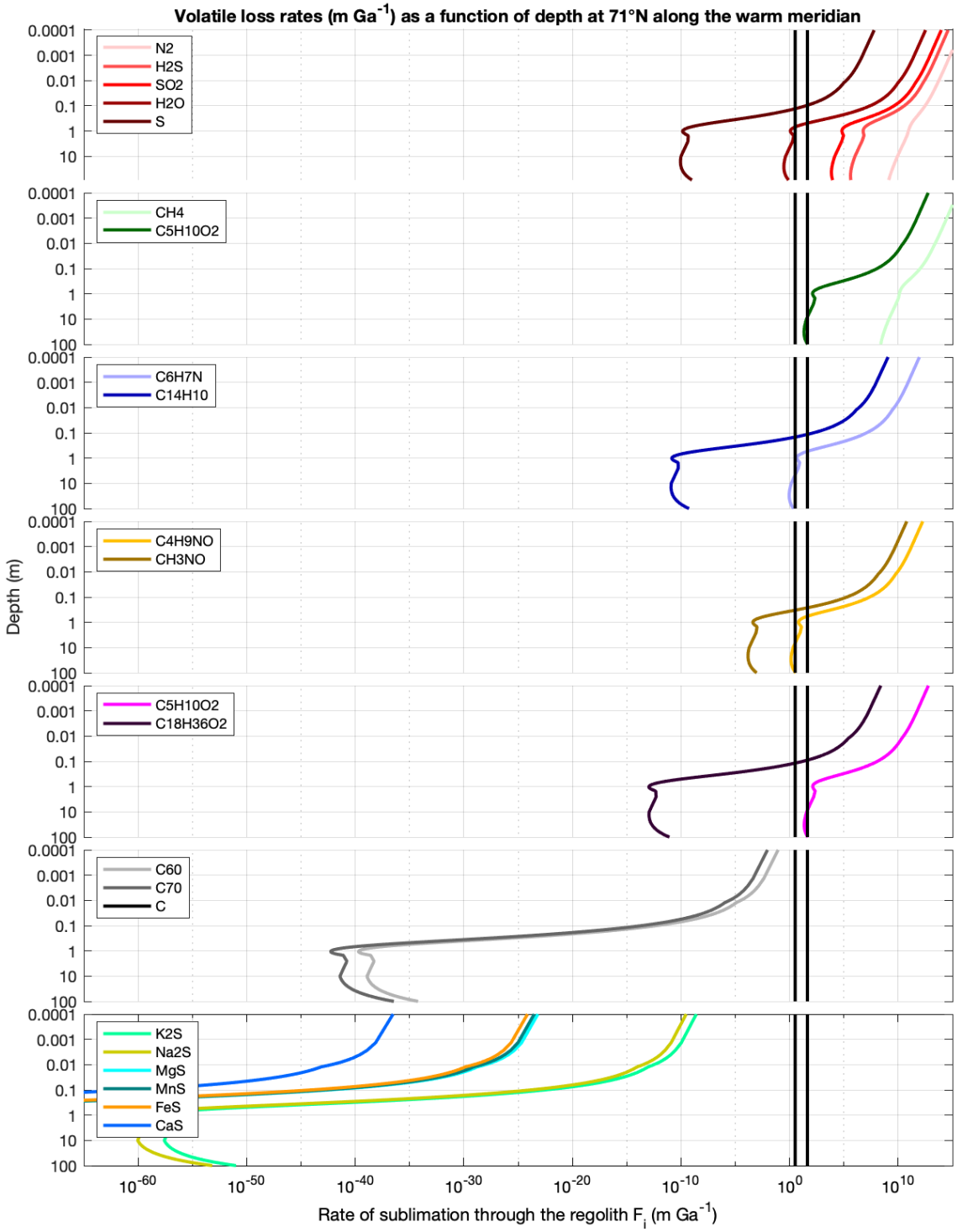
Volatile loss rates (m Ga^{-1}) as a function of depth at 71°N along the warm meridian
Depth (m)
0.0001
0.001
0.01
0.1
1
10
100
N2
H2S
SO2
H2O
S
CH4
C5H10O2
C6H7N
C14H10
C4H9NO
CH3NO
C5H10O2
C18H36O2
C60
C70
C
K2S
Na2S
MgS
MnS
FeS
CaS
10^{-60}
10^{-50}
10^{-40}
10^{-30}
10^{-20}
10^{-10}
10^{0}
10^{10}
Rate of sublimation through the regolith F_i (m Ga^{-1})

effective rate value, which indicates that hollow formation would not be suppressed to less than the minimum effective rate value even under a 100 m-thick regolith lag deposit.

In Figure 1.10, we summarize the volatile phases for which: a) sublimation at the surface is quick enough to account for hollow formation, and b) hollow formation becomes effectively inactive after development of a lag deposit. These are the volatile phases with mass-loss rates that plot to the right of the rightmost vertical black line and to the left of the leftmost vertical black in Figures 1.8 and 1.9. If condition a) is not met, then no hollow forms and, therefore, no lag deposit forms. If condition b) is not met, then hollow depth is not limited by development of a lag deposit and, thus, a lag deposit thickness cannot be calculated. Under the assumption that a single volatile phase is responsible for hollow formation, then the volatile phases that satisfy above conditions a) and b) at both the hot and cold limits could be responsible for hollow formation in a SEALS model framework. The two phases for which conditions a) and b) are met at both the hot and cold limits are S and $C_{18}H_{36}O_2$ (i.e., the two phases in both the right and left panels of Fig. 1.10). If pore-filling volatiles enhance subsurface temperatures in volatile-rich regions (*Section 2.2.2*) then the cold limit of formation would be moved to higher latitudes, perhaps allowing fullerenes to span the full latitudinal range of hollow formation.

Assuming that the depth of a hollow represents the original thickness of the volatile-rich layer minus the thickness of the lag, a percent purity of the original volatile-rich layer can be estimated. For the volatile phases that have a nonzero lag deposit thickness (L), we calculated the percent purity of the original volatile layer as: $\%purity = \frac{d_h}{d_h+L} * 100$ for a hollow of depth d_h (see Table 5 for values of d_h used at each latitude). These values are reported in Figure 1.10. For example, at the hot limit of hollow formation (Fig. 1.10 left panel), S requires a 15 m-thick lag deposit to suppress its sublimation rate to below the limit of effective inactivity, which would be an original S-bearing layer of ~62% purity. At the cold

limit of hollow formation (Fig. 1.10 right panel), S requires a 0.13 m-thick lag deposit to suppress its sublimation rate to below the limit of effective inactivity, which would be an original S-bearing layer of ~99.5% purity.

3.3 Model-Predicted Latitudinal Ranges

In a SEALS hollow formation model, a candidate volatile phase must sublimate quickly enough at the cold limit of hollow formation (see *Section 2.*3 for an explanation of the hot and cold limits of hollow formation) to account for the typical depth of hollows (Table 5); the candidate volatile phase must also be refractory enough at the hot limit of hollow formation that a lag deposit can suppress the loss rate to less than the rate of effective inactivity (minimum effective rate, Table 5). With these two constraints, we derived an expected latitudinal range over which hollows should form for each of the 57 candidate volatile phases in our study. One can think of these latitudinal ranges as representing model-predicted hot and cold limits of hollow formation specific to each volatile phase in our study.

A phase-specific hot limit (low-latitude limit) was calculated as the latitude at which a lag deposit > 100 m-thick would be necessary to suppress the sublimation rate of a phase to less than the rate of effective inactivity (minimum effective rates, Table 5). 100 m was chosen as an extreme upper limit of possible regolith lag deposit thickness. The low latitude limit is represented as the bottom of each colored bar in Figure 1.11. A phase-specific cold limit (high-latitude limit) was calculated as the latitude at which the hollow-formation timescale became longer than a) 300 Myr (top of the colored portion of the bars in Fig. 1.11), and b) 4 Gyr (top of the black portion of the bars in Fig. 1.11). Because both timescales are conservative estimates for the temperature profiles we use (see *Sections 2.2 and 2.3*), our phase-specific high-latitude limits are likely lenient, and the true high-latitude limits may be at lower latitudes.

To summarize our results described above, volatile phases that do not

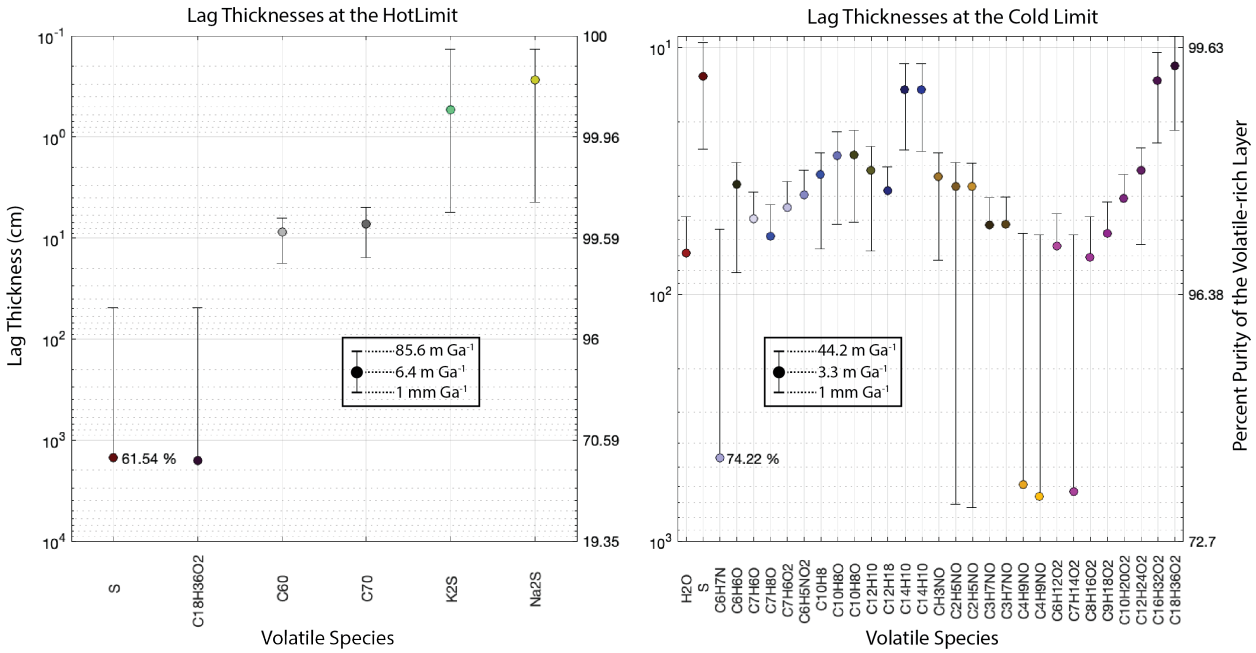

Fig. 1. 10. Lag thickness at which volatile loss rate is equal to specified threshold loss rate values (see legends for values), which correspond to the vertical lines in Figs. 8 and 9. Thicker lag deposits are necessary to suppress volatile loss rates to lower values. Percent purity of the volatile layer for a given lag thickness is plotted on the right axes. Values without lower bars indicate that a lag deposit 100 m-thick is not sufficient to suppress the loss rate to < 1 mm Gyr^{-1}. The two volatiles that are viable at both the hot and cold limits are S and $C_{18}H_{36}O_2$. Volatiles that either do not sublimate fast enough at the surface or cannot be suppressed beneath a volatile lag are not

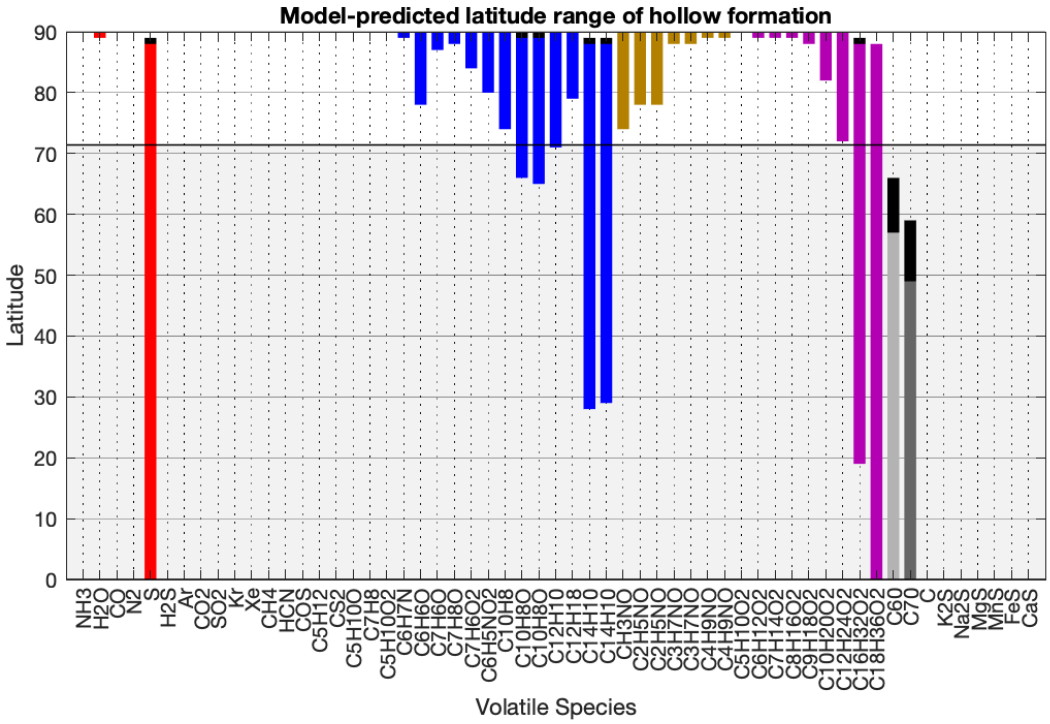

Fig. 1. 11. Model predicted range of latitudes over which each volatile phase is expected to form hollows on horizontal surfaces in a SEALS model framework. The highest model-predicted latitude depends on the timescale used for hollow formation. If the estimate from Blewett et al. (2016) of 300 Myr is used, then the highest latitude predicted for hollow formation is at the top of the solid colored bars. If a conservative estimate of 4 Gyr is used, then the highest latitude predicted for hollow formation is extended as indicated by the black portion of the colored bars. The light gray region between 0°N (hot limit for hollow formation) and 71.4°N (cold limit for hollow formation) indicates the observed limits of hollow formation on a horizontal surface. See *Section*

match the observed limits of hollow formation are considered less likely to be the hollow-forming phase. For the more-volatile classes of compounds (i.e., inorganics, simple organics, aromatic hydrocarbons, linear amides, carboxylic acids), the hot limit imposes a stricter constraint on their viability as hollow-forming phases than the cold limit. This is because, for many volatile phases, even a 100-m thick regolith lag cannot inhibit hollow growth at low- to mid-latitudes and so the constraint imposed by the hot limit is not met. Conversely, for more-refractory phases (i.e., fullerenes, graphite, sulfides), the stricter constraint on their viability as the hollow-forming phase is the cold limit. Given that our calculated phase-specific high-latitude limits are likely lenient (see above), S and $C_{18}H_{36}O_2$ are the two phases that have the best match with the hot and cold limits of hollow formation derived from observation of hollows on the surface. Fullerenes satisfy the hot limit constraint, but do not satisfy the cold limit constraint even if 4 Gyr is the assumed timescale for hollow formation. Even the most volatile sulfides (K_2S and Na_2S) cannot form hollows at 0°N along the warm meridian, and, therefore, do not have a high-latitude limit and do not plot in Figure 1.11.

4. Discussion

Based on our model results, we have narrowed a list of 57 candidate hollow-forming volatile phases down to 3 volatile phases that are viable based on their thermophysical characteristics: S, $C_{18}H_{36}O_2$, and, to a lesser extent, fullerenes. These three volatile phases are the most consistent with the hypothesized behavior of a hollow-forming volatile phase in a SEALS hollow-formation model (as described in our hypothesis in *Section 1.5*). Below we consider broader geological constraints on the viability of these phases as the hollow-forming volatile phase. Specifically, we explore how Stages 1 and 2 of the Blewett et al. (2013) model for hollow formation (see Fig. 1.3) might be accomplished. Elemental sulfur, S, is discussed because it is, perhaps, the best match to the thermophysical properties expected of a hollow-forming volatile

phase as proposed in our hypothesis. We discuss fullerenes because their mid-latitude hollow-formation rate and their expected latitudinal range both agree moderately well with those of observed hollows. We also discuss possible mechanisms for the delivery of fullerenes to and/or the synthesis of fullerenes on the hermean surface in the Pre-Tolstojan Period (~4.6-3.9 Ga, Spudis, 2001; Wagner et al., 2001). Although it is possible that fullerenes may have been generated via space weathering of the hermean graphite crust, we conclude that the volume of fullerenes generated in this way would not have been sufficient to account for hollows. We do not consider $C_{18}H_{36}O_2$ in our discussion because $C_{18}H_{36}O_2$ alone (i.e., without contribution from other comet/asteroid-derived organic compounds) could not have been delivered and sequestered in a large enough volume to be a global hollow-forming layer on Mercury (see Table S1 for reference).

After discussing S and fullerenes, we consider the role sulfides might play in hollow formation. Although sulfides do not exhibit the expected behavior for a hollow-forming volatile in a SEALS model, they have been suggested most frequently in the literature as the species potentially responsible for hollow-formation (Vaughan et al., 2012; Blewett et al., 2013; Helbert et al., 2013; Xiao et al., 2013; Thomas et al., 2014; Thomas et al., 2016; Vilas et al., 2016). Thomas et al. (2014) first suggested that endogenic heat sources may drive volatiles to the surface, contributing to hollow formation. Here, we explore this possibility in detail. Finally, we offer an alternative hollow formation model to SEALS models, wherein thermal decomposition of sulfides in the subsurface via (primarily) impact-related heating drives S-rich fumarolic systems that generate hollows through a diurnal cycle of sublimation and deposition. It should be noted that although fumaroles are commonly associated with water in terrestrial settings, we use this term to mean a vent from which hot gases are emitted.

4.1 Elemental Sulfur

Out of the 57 volatile phases tested in our model, the volatile behavior of S on Mercury is in best agreement with the expected behavior of a hollow-forming phase based on observations of hollows on the surface. If S were the hollow-forming volatile, our model indicates that hollow formation could occur at the observed cold limit at 71°N and potentially as far north as 89°N. Additionally, one would expect a latitudinal dependence on the extent of hollowing, with larger areal extent and deeper hollows closer to the equator, which is consistent with observations (e.g., Fig. 1.2). Hollows generated via sublimation of S are expected to form in a matter of days (~38 days) at the hot pole to ~145 years at 71°N along the warm meridian (measured in Earth days and Earth years, Fig. 1.7). These rates are fast compared to previous rate estimates (Blewett et al., 2016; Blewett et al., 2018), but are in keeping with recent results that suggest hollows could form quickly (Wang et al., 2020b). Additionally, the rate estimates made by Blewett et al. (2016, 2018) are for lateral growth of hollows, whereas our growth estimates are for downward growth. It could be that an initial rapid phase of downward hollow growth occurs, followed by an extended period of lateral hollow growth by scarp retreat (e.g., Blewett et al., 2018).

4.1.1 Possible Formation of a Near-Globally Distributed, Hollow-Sourcing, S-rich Layer within Mercury's Crust

If S were the phase responsible for hollow formation in a SEALS model, then a near-globally distributed S-rich "layer" on the order of 20 to 110 m-thick must exist within the hermean crust, and specifically the LRM. This S-rich layer may have been emplaced during the Pre-Tolstojan and Tolstojan Periods when voluminous secondary crustal production, and associated eruption of volcanic gases, including S and S-bearing phases, covered the primary crust (i.e., what is observed today, presumably, as LRM; Denevi et al., 2009; Denevi et al., 2013b; Marchi et al., 2013; Vander Kaaden and McCubbin, 2015; Klima et al., 2018). Our model results suggest that a hollow-sourcing S-rich layer would need to be

~62% pure at equatorial latitudes and ~99% pure at high latitudes (Fig. 1.10). Sulfur species are a likely product of magmatic activity on Mercury and could have been emplaced through volcanic outgassing and eruptions or magmatic intrusions. Kerber et al. (2009) conservatively estimated the fraction of S in hermean magmas to be 0.05% by weight, and the estimate is much higher, up to 3.68%, for magmas driving pyroclastic deposits. Using 0.05% as an estimate for sulfur in hermean magmas from Kerber et al. (2009) and a lower estimate of 15 km for the thickness of the crust from Sori (2018), a conservative estimate for the volume of sulfur in the hermean crust is 5.6×10^{14} m^3. This volume is equivalent to a ~7.5 m-thick global layer of pure S. If instead we use 3.68% as the estimate for the fraction of S in hermean magmas, then an estimate for the amount of S in the crust of Mercury would correspond to a global layer of pure S ~550 m thick. Thomas et al.'s (2014) nearly global survey of hollows found that hollows cover 5.74×10^{10} m^2 and have an average depth of 47 m. Because hollows have steep sides and flat floors, we can estimate the total volume of hollows, and, therefore, the volume of volatile substance that must have sublimated to generate hollows that are presently observed on the surface, by multiplying hollow area by depth. In this way, we estimate that the total volume of volatiles necessary to be released to form hollows on Mercury is 2.7×10^{12} m^3 (or 1.4×10^{12} m^3 if instead we use 24 m for the average depth of hollows as determined by Blewett et al., 2016; c.f., Wang et al., 2020). These volumes expressed as global layers of pure volatile substance correspond to layers ~1.87 and 3.61 cm thick. Therefore, it seems plausible that enough sulfur was generated via magmatism to account for the volume of material lost to form hollows. A key issue with this estimate for sulfur volume, however, is that most magmatic sulfur will not be in elemental form, but rather in the form H_2S or SO_2 (Kerber et al., 2009). Nevertheless, even if < 1% of magmatic sulfur was deposited as elemental sulfur, it would be sufficient to account for the volume of hollows observed. Below we consider possible scenarios for the emplacement of S in the hermean subsurface as a

global hollow-forming layer through intrusive magmatism or extrusive magmatism and subsequent burial.

The volume of intrusive magmatism is plausibly higher than extrusive magmatism, and intrusive emplacement of S does not require the extra step of burial. While there are no reliable estimates for the ratio of intrusive to extrusive magmatism (I:E) on Mercury (Solomon, 2018), Earth is estimated to have an I:E ~5:1 for oceanic crust (White et al., 2006) and Mars is estimated to have an I:E ~5-12:1 (Greeley and Schneid, 1991; c.f., Black and Manga, 2016). The I:E value for the Moon is thought to be even higher, perhaps 10-30:1 (Kirk and Stevenson, 1989). It may be that the I:E value is smaller for Mercury because of its dense crust (e.g., Sori, 2018), which would increase the buoyancy differences between magmas and the crust enhancing their ability to rise through the crust. On the other hand, Mercury has also experienced global contraction of its crust that would restrict the rise of magmas to the surface (Byrne et al., 2014). If other rocky bodies in the solar system can be used as a guide, then the majority of magma on Mercury may have been emplaced intrusively (i.e., I:E > 1). LRM exposed at the surface appears to have been derived from the lower crust/upper mantle (Murchie et al., 2015). Magmatism at the base of the crust may be a mechanism by which magmatic sulfur species are intruded into the LRM. However, an intrusively emplaced hollow-forming layer of S would require extraction of magmatic sulfur from the melt into relatively pure (~63 – 99% pure) layers of S that could then be exhumed by impacts to form hollows according to Stages 1 and 2 of the hollow-formation model of Blewett et al. (2013) (Fig. 1.3a). Intrusive magmatic sulfur would not likely be emplaced predominantly as S, but rather as sulfides or outgas as H_2S or SO_2.

The sulfur content of extrusive magmatism may be considerably higher than intrusive magma bodies because volatile-bearing magmas would be buoyant and preferentially erupt on the surface. Features that have been interpreted as pyroclastic vents provide evidence that volcanism on Mercury can be volatile-rich and even explosive in the fashion of Hawaiian-type explosive

eruptions (Kerber et al. 2011; Goudge et al., 2014). Goudge et al. (2014) showed that ~78% of Mercury's pyroclastic deposits are Calorian in age or older (i.e., ~3.3 Ga) as determined by the degradation state of the craters hosting such deposits. Sulfur species are likely contributing gases for these eruptions (e.g., Kerber et al., 2009, 2011), and, per Blewett et al. (2013), may have condensed on the surface during nighttime eruptions. The eruption of S-rich volatiles early in Mercury's history and their subsequent rapid sequestration is also consistent with the apparent global volcanic resurfacing of Mercury ~4 Ga (e.g., Marchi et al., 2013).

In light of the voluminous and S-rich volcanism early on Mercury, it is worth considering how this S might concentrate into thick, nearly global layers. It is possible that volcanically erupted/outgassed sulfur species would sublimate on the sunlit side of the planet and undergo deposition on the nightside of the planet (e.g., Sprague et al., 1995) in a diurnal sublimation/deposition cycle that could potentially concentrate volatile phases into thick layers (e.g., Stages 1 and 2 of Fig. 1.3a). Similar high-volume, global, volatile transport by means of sublimation and deposition cycles takes place on other planetary bodies, for example on Mars with the seasonal sublimation/deposition of CO_2 ice (Hess et al., 1979), on Iapetus imparting its global albedo dichotomy (Mendis and Axford, 1974; Spencer and Denk, 2010), on the uranian satellites affecting asymmetrical distributions of H_2O and CO_2 ices (Grundy et al., 2006), as well as on Pluto and Triton perhaps inducing polar wander (Rubincam, 2003; Keane et al., 2016). The distribution of a diurnally induced volatile-rich layer across Mercury would depend on the ancestral spin-orbit resonance state of Mercury. Based on the distribution of large craters on the surface, it has been inferred that the planet was likely in either a 1:1 or 2:1 spin-orbit resonance before being captured into its present 3:2 spin-orbit state, likely at the end of the LHB (Wieczorek et al., 2012; Knibbe and van Westrenen, 2017). If the ancestral spin-orbit resonance of Mercury was synchronous (i.e., 1:1 as suggested by Wieczorek et al., 2012), then one side of the planet would always face the sun and the other hemisphere would be in

perpetual darkness. In this state, a hypothetical hollow-sourcing layer would develop on the dark hemisphere whereas no volatiles would be deposited on the sunlit hemisphere; hollows would be expected to have a strong longitudinal dependence in this case, occurring only on one hemisphere. Conversely, in a 2:1 resonance Mercury would have one solar day per year, and a hypothetical volatile-rich layer would develop globally. If a hollow-forming volatile layer developed in this manner, it would imply that Mercury was not in a synchronous orbit for any significant duration and that a 2:1 resonance more likely dominated throughout the Pre-Tolstojan (Knibbe and van Westrenen, 2017).

Using **Eq. 9** and assuming a 2:1 spin-orbit resonance with Mercury's present-day semimajor axis and orbital eccentricity, and a solar flux of 75% to account for the faint young sun (Newman and Rood, 1977), we estimate that S would sublimate at a rate of 120 m yr^{-1} at 0°E, 0°N (the point where solar noon is at perihelion) and a rate of ~4 m yr^{-1} at 180°E, 0°N (the point where solar noon is at aphelion). These rates constitute an upper estimate for the rate at which S could be sublimated from each hemisphere. For the hemisphere that experiences solar noon at aphelion, it would take ~30 years to sublimate a 110 m-thick layer of sulfur. For the hemisphere that experiences solar noon at perihelion it would only take ~1 year to sublimate a sufficiently thick layer of sulfur. S on the hermean nightside is very stable with a nighttime sublimation rate of only 1 x 10^{-22} m yr^{-1}. Sulfur-bearing gases would have similar differences in stability between the day- and nightsides of the planet. For example, H_2S, which is more volatile than SO_2, sublimates at 2600 km yr^{-1} at 180°E, 0°N, and at a hemispheric nighttime average rate of ~0.2 mm yr^{-1}. The differences in stability between the day- and nightsides could concentrate S and S-bearing gases (and other volcanic gases) on the nightside of the planet as layers of frost. Some portion of the frost layer would sublimate and then migrate from the sunlit hemisphere to the ephemeral cold trap of the dark hemisphere on a diurnal cycle. Loss of more-volatile S-bearing gases to space may contribute to the purification of the volatile layers into mostly elemental S-bearing. The purity of such a volatile layer would

depend on latitude, with more volatile-rich layers deposited at more poleward latitudes. The thicknesses of the frost layers would depend on the eruption rate of volcanic sulfur, which would likely be lower than the daytime sublimation rates, the local topography and temperature of the deposition surfaces, and the probability that a given eruption buries a S-frost layer. To be consistent with the hypothesized hollow-forming volatile layer, S-frost deposits would have to be between ~10 and 110 m thick and ~99% pure at high latitudes (Fig. 1.10). Due to the complexity of this process, it is difficult to say with the simple calculations performed here how likely it is that a hollow-sourcing S layer could have been deposited in this manner in the Pre-Tolstojan to Tolstojan Periods (~4.6 – 3.8 Ga). The dependence of the process on the eruption rate of S could mean that if S-frost layers developed on Mercury, they may have been covered by eruptions before developing into thick layers, and would therefore be thin relative to the expected thickness of the hypothesized hollow-forming layer, and patchy rather than nearly global. This conceptual model for concentration and sequestration of a S-rich volatile layer through global volatile cycling requires detailed modeling of the physical processes involved to better assess its viability.

Assuming that the aforementioned processes successfully concentrated S-rich layers sufficiently thick to account for hollows on the nightside of the planet, these layers would then have to be sequestered by lava flows, as suggested by Blewett et al. (2013). However, burial by lava flows presents another challenge. If S (and sulfur-bearing gases) are vulnerable to volatilization when heated, would lava flows bury the materials or sublimate them? Using terrestrial lava flows over ice as an analog can be illuminating in this regard. Edwards et al. (2012) describe field observations and measurements of the 2010 Fimmvörðuháls lava flows over ice and snow fields. Their observations reveal that, in most cases, ice/snow is not completely, or in many cases even significantly, melted beneath lava flows. The highest rates of melting were ~1 – 4 m day-1 and occurred via heat conduction between the base of fast-moving lava flows in contact with ice. Rates of ~1 – 4 m day-1 are broadly consistent with

rates calculated by Wilson and Head (2007) for subaerial lava flows over ice. The bases of slower moving lava flows observed at Fimmvörðuháls cooled down relatively quickly and did not cause as much melting (only ~cm day-1) as faster moving flows. Ice/snow loss via melting by radiative heating was slow compared to lava-advance rates, and therefore lavas flowed overtop of snow/ice fields rather than melting them as they advanced. In cases where a layer of tephra/breccia covered snow/ice, melting was suppressed. In the case of lava flowing over S-frost layers on Mercury, we might expect even less volatile loss because the latent heat of vaporization for S is 22,120 J mol-1 whereas the latent heat of fusion for water is 334 J mol-1. However, H2S and SO2 are more volatile than water, and may experience more loss. Based on the ability of lava to bury deposits of ice on Earth, it seems plausible that this process could have sequestered S-frost deposits on Mercury if such S-frost deposits existed.

Once buried, it is important to note that the volcanic units must be low porosity/permeability, or in other words, they must form an effective capping unit. Otherwise, the buried volatiles would diffuse through the cover and not remain in the crust as the hypothesized hollow-forming layer. Local instances of venting may occur, perhaps producing rootless cones, and some evidence of pyroclastic vents associated with the LRM have been noted (Kerber et al., 2009; Thomas et al., 2014). Venting could drive off more-volatile S-bearing gases, leaving behind relatively pure S deposits. Other considerations exist for the burial and sequestration of sulfur, such as its stratigraphic position and its stability within the subsurface. Such a layer would likely be stratigraphically above the LRM rather than a constituent of the LRM. Regolith and megaregolith forming processes may also lead to removal and mixing of the layer such that it does not maintain the necessary purity required of the hollow-forming layer.

4.1.2 Excavation of a Hollow-Sourcing, S-Rich Layer, by Impact Processes

Another potential hurdle for hollow formation in a SEALS model framework is the mechanism by which the hypothetical volatile layer is exhumed. Exhumation by the impact cratering process is most often the mechanism proposed because hollows are closely associated with impacts craters. If impacts exhume a S-rich layer, it is not clear whether the S would survive the impact process because temperatures would far exceed its volatilization temperature. It could be that the duration over which the S-rich material is exposed to elevated temperatures is short compared to the volatilization rate at those temperatures, and therefore a majority of the S-rich materials would still be emplaced on the crater floor, walls, and ejecta. But, the modeling necessary to test this hypothesis is outside of the scope of this study. Additionally, the distribution of an impact-exhumed S-rich layer within and surrounding a crater may not be consistent with the distributions of hollows observed within and surrounding craters. Specifically, in complex craters, hollows can occur on the central complexes, floors, walls, and rims of a single crater (e.g., Blewett et al., 2011; Thomas et al., 2014). The materials at each of these locations within and surrounding a crater are excavated from different depths (e.g., Croft, 1980), which is potentially inconsistent with excavation of a single S-rich layer. Lastly, the purity of the layer is unlikely to be maintained during the excavation and emplacement process when mixing with other materials is probable.

4.2 Fullerenes

The model-predicted sublimation rates, hollow-formation timescales, and latitudinal extent of fullerenes match moderately well with the rates, timescales, and latitudinal extent of hollows as observed on the surface. The expected warm-meridian mid-latitude (40°N) sublimation timescales for fullerenes range from 5 to 90 Myr for C_{60} and C_{70}, which are within the estimated (near warm-meridian) mid-latitude timescale of 300 Myr from Blewett et al. (2016). The model-predicted

latitudinal extent of fullerene-generated hollows in the northern hemisphere (0°N to 66°N, Fig. 1.11) is slightly less than the observed extent of hollows in the northern hemisphere (0°N to 71°N, Figs. 1.6, 1.11), but could be extended if heating in the subsurface were enhanced by pore-filling volatiles (*Sections 2.2.2* and *3.2*).

4.2.1 Production of Fullerenes on Mercury

Fullerenes condense spontaneously in carbon vapors, and the C_{60} molecule has exceptional photochemical and thermal stability (Kroto et al., 1985). As such, fullerenes have been hypothesized as ubiquitous in the stellar medium and in chondrites (Krätschmer et al., 1990; Kroto, 1990); although, fullerenes are typically not as abundant as expected, or even present at all, in meteorites (e.g., Kroto, 1992; De Vries et al., 1993; Becker et al., 1994; Heymann et al., 1995; Luann et al., 1999; Pizzarello et al., 2001). Fullerenes are found in several geologic settings on Earth, perhaps most notably in association with the carbonaceous Karelian minerals of Russia, such as shungite (Buseck et al., 1992; Heymann, 1995; Melezhik et al., 2004).

Fullerenes associated with impacts and the interstellar medium are more relevant to Mercury. The C_{60} and C_{70} molecules were found in material related to the Sudbury impact (Becker and Bada, 1994) and in impact-related material from the Cretaceous-Tertiary boundary (Heymann et al., 1994). Fullerenes have been shown to form during impact processes in an experimental setting as well (Radicati Di Brozolo et al., 1994). If fullerenes were ubiquitous in the early solar system (Buseck et al., 1992; Kroto, 1992; De Vries et al., 1993; Heymann et al., 1995), then it is likely they were delivered to Mercury during accretion and through asteroidal and cometary impacts. However, there has been little evidence for fullerenes in lunar rocks and meteorites (Heymann et al., 2003), so an exogeneous source may be unlikely to contribute significantly to a putative fullerene population on Mercury.

Another scenario in which fullerenes could have come to exist on Mercury is via space weathering of a graphite crust. It has been suggested that Mercury accreted from carbon-rich material (e.g., Ebel et al., 2011) and would have formed a graphitic-primary crust through magma ocean processes (Brown and Elkins-Tanton, 2009; Vander Kaaden and McCubbin, 2015). Petrological modeling by Vander Kaaden and McCubbin (2015) predicted that graphite would be stable as a floatation crust. Other workers have shown that carbon (possibly in the form of graphite or nano- to microphase amorphous carbon) could be responsible for spectral darkening of Mercury's surface, and that this carbon could be sourced from a primary graphite crust (Denevi et al., 2009; Riner et al., 2009; Rothery et al., 2010; Riner, 2012; Murchie et al., 2015; Peplowski et al., 2016; Thomas et al., 2016; Trang et al., 2017).

A global, or near global, primary crust of graphite on the surface of Mercury would have been subject to intense space-weathering (e.g., Cintala, 1992; Domingue et al., 2014) until buried by a secondary volcanic crust (e.g., Marchi et al., 2013) and mixed through impact gardening. Trang et al. (2018) reported space-weathering experiments on graphite powders at the University of Hawai'i space-weathering laboratory using a 20 Hz, 1064-nm Nd:YAG pulse laser in which multiple submicroscopic carbon phases and amorphous carbon were produced. However, no explicit mention of the crystalline form of the submicroscopic carbon was made and it is unclear whether fullerenes were produced in this manner. One mechanism for fullerene synthesis in a laboratory setting is through condensation from a carbon vapor generated from a graphite source (e.g., Kroto et al., 1985; Mintmire, 1996; Kozlov et al., 1997). Mercury's graphite crust, combined with its space-weathering environment, may have been a natural laboratory for synthesis of fullerenes on a global scale.

A simple upper estimate of the total volume of fullerenes that could have been produced in the first 200 – 800 Myr of the solar system (when Mercury's graphite crust was likely exposed based on volcanic smooth plains age-estimates, Denevi et al., 2013a; Marchi et al., 2013) can be made using

reasonable values for the vaporization rate due to space-weathering at Mercury and the efficiency with which fullerenes can condense from graphite vapor. Cintala (1992) gives a mean rate for space-weathering-induced vaporization of regolith at Mercury of 1.6×10^{-14} kg m^{-2} s^{-1}. If the total surface area of Mercury is presumed as graphite and 20% of vaporized graphite precipitates to fullerenes (a high end of efficiency for laboratory fullerene synthesis using graphite vaporization, e.g., Mintmire, 1996), then an upper estimate of fullerenes produced over an 800 Myr time span would be 6.01×10^{12} kg. If a constant rate of secondary crustal production covered the graphite primary crust over a 200 Myr time span and a 2% efficiency of fullerene synthesis from carbon vapor is used (Mintmire, 1996), then a lower estimate of 7.51×10^{10} kg of fullerenes would form. Using the density of C_{60} (1650 kg m^{-3}) and the range of masses calculated above, an estimate for the total volume of fullerenes produced on Mercury is ~4.6×10^{7} to 3.6×10^{9} m^3. These volumes are equivalent to a global fullerene layer ~ 0.6 to 48 μm thick. If the above estimates of volumes of fullerenes produced on Mercury encompass the actual upper limit of fullerene volume produced by space-weathering of a hermean graphite crust, then fullerenes would be volumetrically insufficient by themselves to account for the total volume of hermean hollows, equal to ~2.7×10^{12} m^3 (*Section 4.1*).

If fullerenes did form globally on Mercury, they would have been a component of the primary crust in which they formed, which was rapidly buried and later exhumed, perhaps as the LRM observed today (Denevi et al., 2009; Murchie et al., 2015). There would, therefore, be a plausible connection between hypothesized fullerenes and the hollow-sourcing LRM.

If fullerenes are involved in hollow formation, they could be present in the hermean exosphere or within permanently shadowed craters at the poles as possible constituents of dark lag deposits covering ice (e.g., Chabot et al., 2014). Fullerenes exhibit UV/VIS spectral features at 213, 257, and 329 nm (Hare et al., 1991; Ehrenfreund and Foing, 1997), which might be detectable with the Ultraviolet and Visible Spectrometer (UVVS) and Visible and Infrared

Spectrograph (VIRS) instruments, which are part of the Mercury Atmospheric and Surface Composition Spectrometer (MASCS) system onboard the MESSENGER spacecraft (McClintock and Lankton, 2007). However, fullerene absorptions features are too narrow (e.g., Ehrenfreund and Foing, 1997) to be observed in published spectra of hollowed terrain (e.g., Thomas et al., 2016; Trang et al., 2017). Fullerenes also display weak IR spectral features near 7, 8.5, 17 and 19 μm (Krätschmer et al., 1990), which may be detectable with the Mercury Radiometer and Thermal Infrared Spectrometer (MERTIS) on the BepiColombo spacecraft (Hiesinger and Helbert, 2010). Detection of fullerene spectral features in the exosphere and/or in permanently shadowed regions at the poles could be considered indirect evidence that fullerenes play a role in hollow formation.

4.3 Sulfides

Sulfides are present, and relatively abundant on the surface of Mercury (Sprague et al., 1995; Boynton et al., 2007; Denevi et al., 2009; Zolotov et al., 2013; Goudge et al., 2014; Murchie et al., 2015). Sulfides have recently been considered as products of a hermean magma ocean (Parman et al., 2016; Boukaré et al., 2019) and have been considered as candidate hollow-forming materials by several workers (Blewett et al., 2013; Helbert et al., 2013; Thomas et al., 2014; Thomas et al., 2016; Vilas et al., 2016). Sulfides may have formed in relatively pure layers in the upper mantle during the early Mercury magma ocean, or they may have risen to the surface as a sulfide lid (Parman et al., 2016) or sulfide-rich plumes (Boukaré et al., 2019). The thickness of the sulfide lid has an expected lower limit of ~5 km, which would comprise a volume of ~3.7 x 10^{17} m^3. This volume is orders of magnitudes more than necessary to account for the total volume of hollows (*Section 4.1*). There is, therefore, a plausible mechanism to emplace a sufficient volume of sulfide-rich deposits subjacent to, or as a constituent of, the LRM.

The species of sulfides that are suggested to have formed from the Mercury magma ocean are FeS, MnS CaS, MgS, and Na_2S (Vander Kaaden and McCubbin, 2015; Boukaré et al., 2019). However, MnS and FeS are expected in smaller proportions due to the relative scarcity of Fe and Mn on the surface of Mercury, and Na_2S is expected to crystallize out of the magma after CaS and MgS and in smaller proportions (Boukaré et al., 2019). The elements U and Th will likely partition into CaS and MgS, and K will partition into Na_2S (Boukaré et al., 2019). Although pure K_2S is not expected to form, it is useful to consider it as an "extreme endmember" of K substitution into Na_2S.

Our model results suggest that most sulfides are stable on the hermean surface, even at the hot pole, and can persist for billions of years without substantial loss (*Section 3*, Fig. 1.7). For the most volatile sulfide, K_2S, the predicted time necessary to form a typical hollow at the hot pole is ~25 Myr, increasing to ~230 Myr at 40°N, and would form over a time period much longer than the age of Mercury at 71°N. The times necessary to form a typical hollow are similar for Na_2S, taking ~86 Myr at the hot pole, ~887 Myr at 40°N, and orders of magnitude longer than the age of Mercury at 71°N. At the warm pole, the rate of reactive sublimation, even for K_2S, is not fast enough to account for hollow formation. Our results, therefore, show that sulfides cannot be the hollow-forming volatile in a SEALS model framework.

4.3.1 Impact-Induced "Hermeothermal" Systems

If sulfides are responsible for hollows, then solar heating alone is not sufficient to account for hollow formation and additional heat sources are necessary to drive hollowing. In addition to solar heating, some combination of local increases in temperature caused by impact cratering or subsurface magma bodies, lava flows, faulting, or other sources may provide the heat necessary to thermally decompose sulfides. Volatile phases generated through subsurface heating of sulfides could be driven to the surface, forming hollows in the process. Non-crater related hollows are commonly associated with lava flows and

pyroclastic deposits (Xiao et al., 2013; Thomas et al., 2014; Goudge et al., 2014). For example, hollows at higher latitudes (> 50°N) northwest of the Caloris basin are associated with a lava flow front, perhaps indicating a genetic link between the two as suggested by Thomas et al. (2014). Almost all hollowed surface area is associated with impact craters that could provide the heat necessary to decompose sulfides. The local temperature increase in the vicinity of an impact can persist for 10^5 – 10^6 years (e.g., Kring, 2000) depending on the size of the impact and the amount of melt produced. Elevated post-impact temperatures may enable the majority of hollowing to occur within the first several thousands of years after the impact when the local temperature, especially under the central complex and crater floor, is elevated (Kring, 2000; Osinski et al., 2001; Abramov and Kring, 2004).

At present, the only impact for which subsurface temperature has been modeled as a function of time after impact is the Caloris basin-forming impact (e.g., Potter and Head, 2017). Although no models presently exist for the evolution of temperature with time beneath median-sized (~15 km diameter) impacts on Mercury, we can compare to models for the Earth, Moon, and Mars. Abramov et al. (2012) calculated, for oblique impacts, how melt volume scales with impactor size, velocity, and planetary target body (Earth, Moon, and Mars). While they do not include Mercury in their evaluation, it can be inferred that Mercury would experience more melting per impact than any of the three bodies included in their study because: 1) impact velocity strongly controls melt volume production (second only to impactor diameter), and 2) the thermal environment of the target rock significantly affects the total melt volume (Abramov et al., 2012). For both factors Mercury has an environment conducive to the production of melt because impact velocities are high at Mercury due to its proximity to the Sun (Marchi et al., 2005; Domingue et al., 2014) and subsurface temperatures at Mercury are hot relative to the Earth, Moon, and Mars. For impacts on Earth that produce craters with a final diameter of ~12 km, Abramov et al. (2012) predict ~1 km^3 of melt would be produced (their Fig. 1.4). If this volume is considered a

minimum estimate for a similar-sized crater on Mercury, then such an impact would generate > 1 km^3 of melt. Best estimates for melt produced by the Sudbury impact (~180 km diameter), for example, are 8,000 – 10,000 km^3 (Grieve and Cintala, 1992; Wu et al., 1995). A typical melting temperature for basalt can be taken as ~1400 K (Frost and Frost, 2014). Such a volume of melted rock would keep surrounding areas in the subsurface at elevated temperatures for > 10^4 years and drive volatilization from the bottom up (e.g., Rathbun and Squyres, 2002; Abramov and Kring, 2004). Hydrothermal springs around the Sudbury impact, for example, were driven in this manner, and hydrothermal systems on Mars were likely powered by impact heat as well (Rathbun and Squyres, 2002; Schwenzer and Kring, 2009; Ruff et al., 2011).

Similar to hydrothermal systems on Earth and Mars that are driven by impact-generated heat, “hydrothermal-like” systems could be driven by impact-generated heat and melt on Mercury. A more general term for hydrothermal systems that is agnostic to the surface expression of the system and the fluids circulating within them is “geothermal system” or “areothermal system” (for Earth and Mars, respectively). We will call analogous systems on Mercury “hermeothermal systems” to avoid the implication that water is involved in these systems and to avoid invoking particular surface features that are commonly associated with geothermal systems, such as constructional vents, sinter deposits, hot springs, outwash aprons, etc. The fluids in the case of hermeothermal systems would be different from geo- and areothermal fluids because the starting compositions (including presence of water) and oxygen fugacities are significantly different on Mercury (e.g., McCubbin et al., 2017). Sulfides within LRM source material may decompose and deliver S and S-bearing species to the surface. Because of the sulfur-rich composition and gas-dominated rather than liquid-dominated nature of hermeothermal systems, the surface expression would likely be most similar to terrestrial solfataras (e.g., Allard et al., 1991; Caliro et al., 2007), albeit with many differences remaining between them. In the proposed impact-generated hermeothermal systems, sulfur

and sulfur-bearing phases would undergo deposition on the surface in the immediate vicinity of the vent sites, accumulating within the regolith at night, and would sublimate during the day. This diurnal pattern of volatile saturation at night and sublimation during the day at fumarole vent locations combined with the volume lost from thermally decomposing material in the subsurface may drive hollow formation (see *Section 4.4*).

Could sulfides decompose and source sulfur-bearing volatiles (e.g., S, H_2S, SO_2) in an elevated post-impact temperature environment rapidly enough to explain hollow formation? To address this question, we calculated the thermal decomposition rates of sulfides (K_2-, Na_2-, Mg-, and Ca-sulfides) as a function of temperature from 600 to 1500 K at the surface (Fig. 1.12, solid lines) and at 1 km depth (Fig. 1.12, dashed lines). At the surface, even CaS sublimates quickly enough to account for hollow formation at temperatures above ~1100 K. If impact-exhumed LRM is emplaced at high temperatures, the more volatile sulfides (i.e., Na_2S with possible K substitution) will reactively sublimate quickly relative to expected hollow formation rates. Na_2S will sublimate meters per day at temperatures above ~1230 K (Fig. 1.12). If sulfides were heated conductively by a subsurface impact melt body, our model results indicate that K_2S and Na_2S decompose rapidly enough to account for hollow formation at temperatures above ~950 K. MgS and CaS require much longer to decompose when buried, even at basalt melting temperatures. However, our assumption about porosity (i.e., $\phi = 1 - \frac{\overline{\rho}(z)}{G_h \rho_w}$) likely does not hold because fractures may allow volatiles to travel to the surface more easily. In this regard, our calculations are conservative estimates. Nevertheless, Na_2S (with possible K substitution) will more readily decompose directly from the surface after an impact and will more readily deliver sulfur-bearing volatiles to the surface through decomposition in the subsurface than more refractory Mg- and Ca-sulfides.

If sulfides contribute to hollow formation, then it could be a source for exospheric Na, K, and Mg (Potter and Morgan, 1985). The reactive sublimation

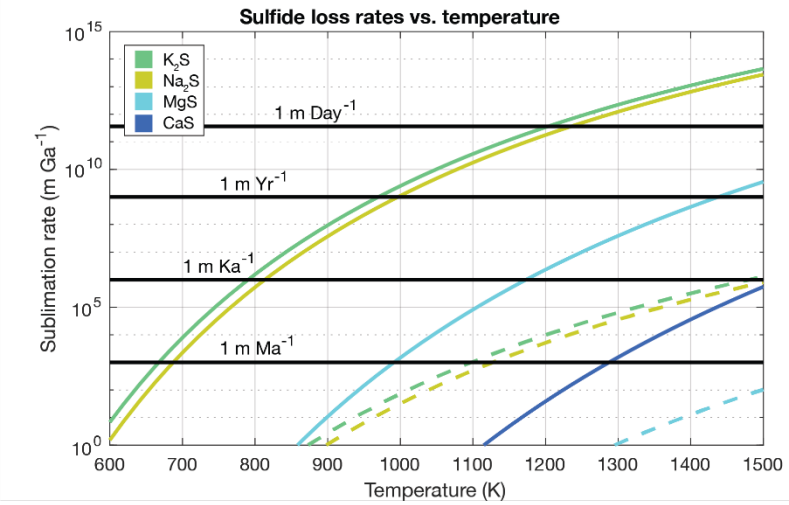

Fig. 1. 12. Sulfide loss rates as a function of temperature between 600 K and 1500 K. Dashed lines are loss rates for sulfides buried at 1 km. At temperatures relevant to a post-impact environment, Na_2S can be thermally decomposed rapidly at the surface, and above the estimated hollow formation rate at temperatures above ~1100 K buried at 1 km. CaS buried at 1 km falls off the plot.

of sulfides within hot LRM on the surface immediately following an impact or thermal decomposition of sulfides within the subsurface and delivery to the surface in a vent system could produce Na, K, and Mg ions that could adsorb to the surface to be launched into the exosphere via solar wind particles, photons, or micrometeorite impacts (Killen et al., 2010; Mangano et al., 2013). Na is lost from the hermean exosphere and some surface mechanism replenishes it (Potter and Morgan, 1985); thermal decomposition of sulfides associated with hollow-formation could be a mechanism for replenishment. S would be produced in this manner as well and should be observable in the hermean exosphere depending on the age of hollows and the expected lifetime of S in the exosphere. A S absorption feature centered at 1813.7 Å would be observable with the ESA BepiColombo PHEBUS UV instrument (see, e.g., Killen et al., 2007).

4.4 A Novel Model for Hollow Formation: Sublimation Cycling Around Fumarole Systems (SCArFS)

Sulfides have been the phase suggested most often in the literature as possibly responsible for hollow formation, but they do not have the appropriate thermophysical characteristics to be responsible for hollow formation in a SEALS model framework in which solar heating is the principal heat source that drives hollow formation. Although the model-predicted latitudinal extent of hollows formed through sublimation of elemental S agrees well with the observed latitudinal extent of hollows, the mechanism by which a global layer of S up to 110 m-thick and 62% to 99% pure could come to exist within Mercury's crust presents several challenges. These challenges include the production of enough volume of S, the concentration of S into thick, nearly pure, layers, the sequestration of those layers through burial by lava flows, and the survival of that layer through the impact exhumation process (*Section 4.1*). While the volatile behaviors of fullerenes match moderately well with those expected from a hollow-forming volatile in a SEALS model, their synthesis on and/or delivery to Mercury

and subsequent sequestration within the crust at high enough volume to be responsible for hollows may be unlikely (*Section 4.2.1*).

Any viable alternative model for hollow formation must account for certain key observables, which include: 1) the close association of hollows with impact craters and the distribution of hollows within and surrounding both simple and complex impact craters, including their occurrence on the steep slopes of central peak structures, crater walls, and the Caloris knobs; 2) the association of hollows with LRM; 3) the possibility for some hollows to form outside the vicinity of impact craters; 4) the trend of decreasing hollow areal extent and depth with increasing latitude; 5) the morphology of hollows (i.e., their flat floors, steep walls, amorphous shape, and depth); 6) the apparent youth of hollows.

Because of the challenges inherent within a SEALS hollow-formation model, we propose an alternative model for hollow formation (Fig. 1.13). Our hollow-formation model involves deposition of S and S-bearing phases, such as chalcogenides[2] and sulfosalts[3], in the vicinity of fumarole vents at night and sublimation during the day in a diurnal cycle. Therefore, we call our model the Sublimation Cycling Around Fumarole Systems model for hollow formation (SCArFS). The SCArFS hollow-formation model is summarized in the following four stages. It should be noted that the events described in Stage 1 would occur throughout the hollow-forming process (i.e., throughout Stages 2 and 3) until the processes that terminate (or slow) hollow formation, described in Stage 4, take place.

---

[2] Chalcogenides are minerals comprised of a chalcogen (group 16 elements, typically excluding oxygen) and an electropositive element, such as the alkali, alkaline earth, or transition metals. Common chalcogenides include pyrite and galena.

[3] Sulfosalts are minerals with the general formula $A_mB_nS_p$, where A is a metal, B is a metalloid, and S is sulfur (or, rarely, a heavier chalcogen).

Stage 1: Embedded heat sources produce volatile phases, such as S, S_2, and H_2S, through thermal decomposition of sulfides within LRM. Sulfur-bearing phases are driven along fractures to the surface in hermean fumarolic systems (Fig. 1.13, Stage 1). Because of the association of hollows with impact craters, we propose that impact melt and related heating are the principal heat sources that would drive thermal decomposition reactions. It is possible that other mechanisms, in addition to thermal decomposition, could liberate S, such as oxidation reactions between sulfides and impact-generated melt (e.g., Weider et al., 2016). It is important to note that other heat sources could drive volatile production in a SCArFS model, including subsurface magma bodies that intrude sulfide-rich LRM (e.g., Xiao et al., 2013; Weider et al., 2016) and heating related to faults (Thomas et al., 2014). Based on the apparent abundance of sulfides within LRM and the higher volatility of Na_2S compared to MgS, CaS, and graphite, our results suggest that the fundamental species involved in Stage 1 of the SCArFS model would be Na_2S (with possible K substitution), but other sulfides are expected to contribute to a lesser degree as well. The volume lost through the destruction of sulfides in the subsurface would, ultimately, be accommodated at the surface as a hollow according to the processes described in Stages 2 and 3.

The thermal decomposition of sulfides would produce gaseous sulfur at the surface immediately following an impact, as well as in the subsurface for longer time periods feeding fumarolic systems. Hot LRM emplaced on the surface as ejecta may produce incipient hollows as sulfides reactively sublimate from the surface.

The immediate products of sulfide decomposition – positively charged metal cations (M^{2+}) and negatively charged sulfur anions (S^{2-}, eq. 10) – would be the intial chemical constituents of the proposed fumarolic systems (Fig. 1.13, Stage 1). Subsequent products would be dependent on available reactants in the subsurface. In the near subsurface, S^{2-} would be susceptible to several reaction pathways. One possibility is that S^{2-} could react with hydrogen in the regolith and

the LRM, implanted via the solar wind, or directly with solar wind hydrogen in the surface and near subsurface (c.f., Blewett et al., 2016 for methane production in a similar reaction) to form H_2S according to the reaction

$$S^{2-}_{(g)} + 2H_{(\text{solar wind})} = H_2S_{(g,s)}$$

H_2S would be stable as a solid phase in the regolith at Mercury nighttime temperatures, which are below the vacuum freezing point of H_2S at ~183 K (Nakayama et al., 1996). Additionally, H_2S could form elemental S if oxidation pathways are availble. One possible oxidation pathway is through UV-stimulated photolysis (Yu et al., 2013; Wang et al., 2020a)

$$H_2S + h\nu \xrightarrow{UV} S^0 + H_2$$

The fumarolic systems proposed herein may be more complex than the simple reactions outlined above, which should be considered as initial hypotheses for the chemical makeup and processes involved in such systems. For example, minerals such as chalcogenides and sulfosalts may be produced if interactions with regolith materials allow. Additionally, it is possible that methane and other C-bearing phases may form by subsurface heating of carbon-bearing material within the LRM (especially if the LRM is H-rich from solar wind saturation, per Blewett et al., 2016; and McCubbin et al., 2017) and contribute to the volatile phases in Stage 1 of the SCArFS hollow-formation model. Future studies should focus on possible reactants and producst within heremothermal systems and the implications for hollow formation.

Stage 2: Volatile phases accumulate within surface materials in the vicinity of fumarole vents at night where S and S-bearing minerals precipitate (Fig. 1.13, Stage 2). The extremely low nighttime temperatures on Mercury would generate a zone of thermal stability for S extending from the surface into the subsurface. This zone can be thought of as analogous to terrestrial permafrost zones(regions in the subsurface where water ice is thermally stable and that can either host water ice or not). The hermean “permafrost zones” we suggest are with

Fig. 1. 13. Sublimation Cycling Around Fumarole Systems (SCArFS) model for hollow formation. Top panel shows a complex crater in the first several thousand years after impact into sulfide-bearing LRM and gives context for Stages 1-4 of the model. *Stage 1:* Heating of LRM produces volatile phases, for instance by thermal decomposition of sulfides. Volatile phases are driven toward the surface along fractures in a fumarole system. The processes of Stage 1 occur throughout hollow formation until hollow formation ceases in Stage 4. To show this, a small panel displaying the processes of Stage 1 is located at the bottom of the Stage 2 and 3 panels beneath a dashed line that indicates a break in space. *Stage 2:* Sulfur and other phases accumulate in the vicinity of fumarole vents on the surface and in near-surface pore spaces at night, becoming structurally integral members of the surface in a “sulfur-rich permafrost” layer. Some amount of gases, especially highly volatile species such as H_2S, would likely continue to vent at night. *Stage 3:* Phases that precipitated on the surface and within the near-surface at night sublimate during the day, widening and deepening hollows. Stages 2 and 3 would repeat on a diurnal cycle. *Stage 4:* Fresh sulfides may precipitate along hollow floors, walls, and rims developing a low porosity capping unit that impedes hollow growth. Hollow formation may also slow when the subsurface heat source cools and thermal decomposition of sulfides terminates. Retention of a S-rich reservoir is anticipated below the influence of diurnal temperature swings and above the influence of subsurface heating.

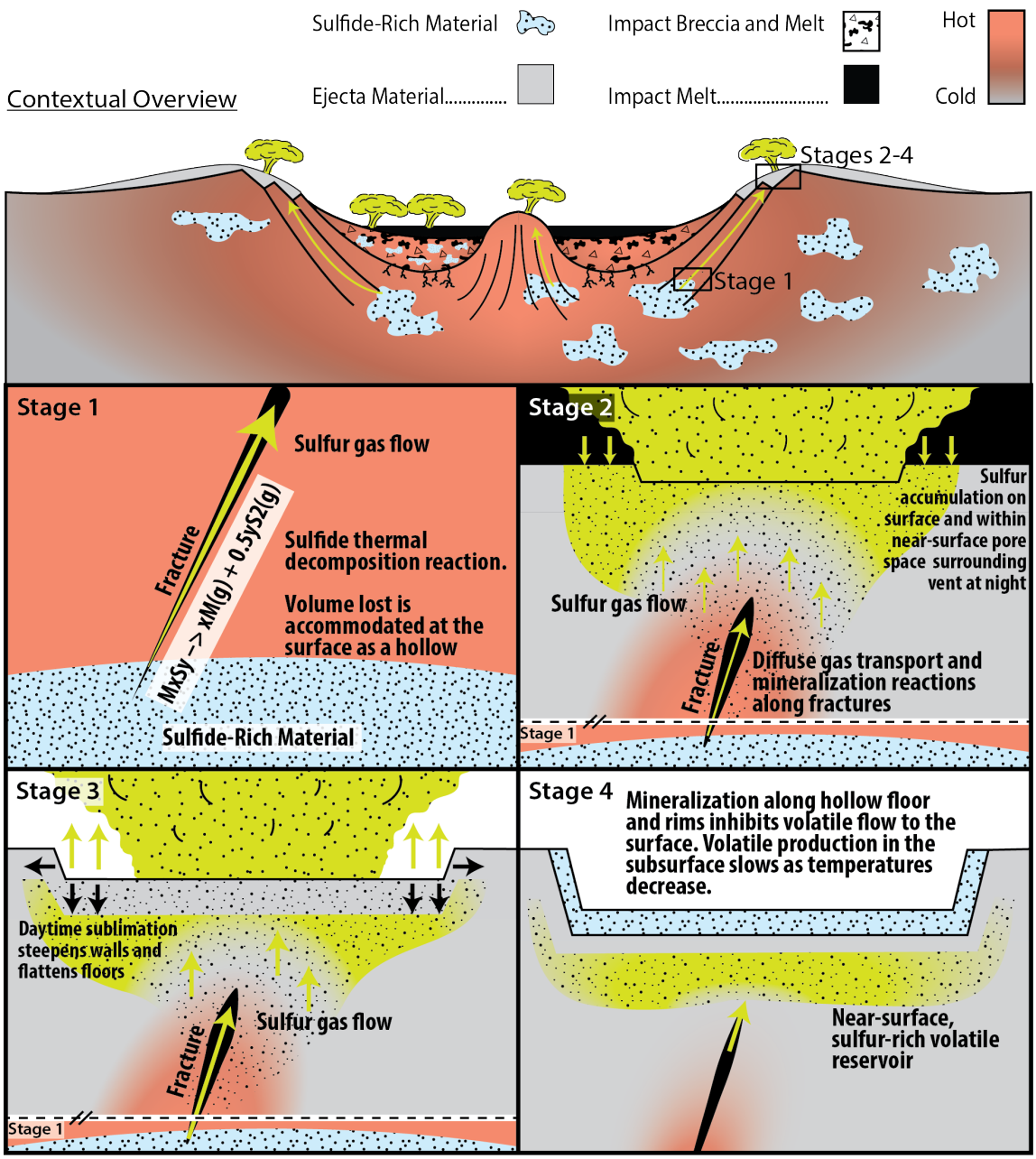
Contextual Overview
Sulfide-Rich Material
Ejecta Material.....
Impact Breccia and Melt
Impact Melt.....
Hot
Cold
Stages 2-4
Stage 1
Stage 1
Sulfur gas flow
Fracture
MxSy –> xM(g) + 0.5yS2(g)
Sulfide thermal decomposition reaction.
Volume lost is accommodated at the surface as a hollow
Sulfide-Rich Material
Stage 2
Sulfur accumulation on surface and within near-surface pore space surrounding vent at night
Sulfur gas flow
Fracture
Diffuse gas transport and mineralization reactions along fractures
Stage 1
Stage 3
Daytime sublimation steepens walls and flattens floors
Sulfur gas flow
Fracture
Stage 1
Stage 4
Mineralization along hollow floor and rims inhibits volatile flow to the surface. Volatile production in the subsurface slows as temperatures decrease.
Near-surface, sulfur-rich volatile reservoir

respect to S, not water, and would be ephemeral on a diurnal cycle. Solid S and S-bearing phases would accumulate on the surface and within near-surface material within the “permafrost zone” at night. The result would be a sulfur-rich surface/near-surface layer containing solid S and, likely, other species.

In the SCArFS model, crystallization of S and other species would have to disrupt the surface layer in order for hollows to form, which could occur by several mechanisms. One such mechanisms would be if the crystalizing phases became structurally integral components of the near-surface layer. This could occur if precipitating volatile species saturate pore spaces and displace other constituents of the near-surface layer. That is, if the total volume of the crystalizing phases is higher than the locally available pore-space volume, then disruption of the pre-existing near-surface layer is expected. Such a process may result in a nightly “inflation” of the surface surrounding a vent as the volume in the area is increased by the crystalizing species.

Some highly volatile phases may continue to vent at night, such as H_2S, but deposition of phases would advance as the night progresses and the surface and near-surface grow colder. Elemental S and S-bearing minerals would preferentially accumulate in the near-surface over other, more-volatile, S-bearing phases (e.g., H_2S, SO_2). A gradient in volatile concentration in the near-surface radiating outward from vent locations might be expected because gas fluxes would be highest near vent sites.

The distribution of fumarole vents, and therefore hollows, would depend on the subsurface distribution of sulfide-rich materials and the connection of those materials to the surface via fracture networks (see e.g., the upper panel contextual overview of Fig. 1.13). Because hollows do not occur everywhere that there are impacts in the LRM, it is likely that the distribution of sulfide-rich material within the LRM is patchy. Sulfide-rich patches may be distributed within the LRM on a scale smaller than the size of a hollow-hosting impact crater (as shown in Fig. 1.13), or on a scale larger than the hollow-hosting crater. If sulfide-rich patches are small relative to the impact, hollows may only be expected in

isolated sections of the crater where fractures intersect a sulfide-rich region. If sulfide-rich areas are large compared to the size of the impact crater, then most fractures might be expected to intersect sulfide-rich material and, therefore, anywhere fracture networks intersect the surface might be expected to host hollows. In either case, in a SCArFS model for hollow formation, hollows are predominantly expected to form where fractures vent gases produced from sulfide decomposition to the surface; for simple craters this corresponds to the rims (French, 1998), and for complex craters this corresponds to central peaks, peak rings, terraced walls and rims (Melosh, 1989; French, 1998). It is possible that sulfide-rich materials could be entrained in the impact melt and breccia lens of a complex crater (Fig. 1.13, contextual overview); in this case, extensive venting, and therefore hollowing, would also be expected on the crater floor, as is observed in, for example, Tyagaraja and Sander craters.

Stage 3: Solar heating drives sublimation weathering during the day that reworks the surface and results in steep walls and flat floors characteristic of hollows (Fig. 1.13, Stage 3). In the SCArFS model, a subsurface heat source drives volatile phases to the surface/near-surface where they accumulate (Stage 2), but solar insolation is the heat source that drives sublimation of the accumulated phases from the surface/near-surface. The nightly process of volatile deposition through upward transport of fumarolic volatiles recharges the “permafrost zone” with new material that sublimates during the day furthering hollow growth in a diurnal cycle. Recharging of the surface is expected while the fumarole system is active, which would depend on the longevity of the heat source. The surface would be reworked by sublimation weathering and other physical and chemical weathering processes. We suggest that processes applicable to thermokarst landscape development (Czudek and Demek, 1970; Kargel, 2013) and in salt weathering (e.g., Melosh, 2011 Ch. 7) may operate in hollow formation. Analogy to permafrost landscapes (molards) has also been drawn to explain the morphology of circum-Calrois knobs on Mercury (Wright et al., 2020), some of which contain hollows. We propose that in the SCArFS

model, solid phase S and S-bearing minerals become structurally integral members of the surface (Stage 2), as is the case with terrestrial ice-rich permafrost, and that removal of these phases results in collapse, flat floors, and steep walls, analogous to *alas* formation in thermokarst landscapes (Czudek and Demek, 1970). In the SCArFS model, broad areas of the surface would synchronously deflate, whereas other models propose a central downward-growing focal point followed by lateral growth (e.g., Blewett et al., 2018). Just how “broad” the area is that deflates would depend on the flux of volatiles at a specific vent location, the architecture of the vent and its subsurface plumbing, and the diffuse nature of volatile phase emplacement.

Because our model results favor elemental S as the hollow-forming phase (*Sections 3* and *4.1*), we suggest that elemental S may have been the predominant phase that precipitated on and within the surface surrounding fumarole vents at night and subsequently sublimated during the day to generate hollows. However, H_2S may be an important phase in these systems as well (*Section 4.4, Stage 1*). The thermal stability of other phases, such as chalcogenides and sulfosalts, should be explored in the future. Where solar insolation is not sufficient to sublimate S (e.g., at high latitudes and in shadowed regions), hollows would not be expected to form because there would be negligible net loss of material from the area. However, S-rich regions on the surface and near-surface would be expected in locations around high-latitude craters where hollows are typically found at lower latitudes. Similarly, S is expected to be relatively stable at depths where the amplitude of surface diurnal temperature swings is sufficiently muted. The depths at which S is relatively stable would vary with both latitude and longitude on Mercury (see Figs. 1.8 – 1.10, *Section 3.2*), but typical depths of a S-rich reservoir would be decimeters near the cold limit of hollow formation to ~15 m near the hot limit of hollow formation (Fig. 1.13 Stages 3 and 4). The expectation of a relatively stable, S-rich volatile reservoir, below the reach of solar heating and above the influence of

subsurface heating, is potentially key to the maintenance of fresh hollow surfaces in the SCArFS model (c.f., *Section 4.4.1*).

Stage 4: Hollow growth ceases (or becomes nearly dormant) when one of three conditions are met: i) the heat source responsible for volatile-phase production from the LRM cools down and, therefore, volatile-phase production stops; ii) the sulfide-rich source is exhausted and no more volatile phases are produced; iii) mineralization along fractures and of the surface creates a capping unit that precludes continued upward transport of volatiles to the surface (Fig. 1.13, Stage 4). The first two conditions involve lowering the volatile production rate to a sufficiently low value that hollow formation can be considered effectively inactive. It could be that above conditions *i* and *ii* are never achieved for some hollows. In such cases, slow and continued hollow growth may be happening today. The third condition requires mineralization of pathways to the surface and of the surface itself with phases that do not sublimate at hermean daytime temperatures (e.g., sulfides). As the pore spaces of hollow floors (and walls) mineralize with refractory phases, rising volatiles would take paths of least resistance to the surface in a process of vent relocation. The vent relocation process could give rise to the irregular shape of hollows because relocation would happen in a quasi-random manner. Clusters of hollows may also form in this way if the vent relocates outside the extent of the original hollow. This process could also lead to hollow clusters aggregating into larger hollows. If the development of a mineralized capping unit inhibits hollow formation, then downward hollow growth would be moderated from the bottom up in a SCArFS model, whereas in a SEALS model hollow growth is terminated from the top down by development of a lag deposit. We suggest that the minerals that act as the “capping” unit may likely be sulfides that (re-)precipitated in the fumarole systems; sulfide precipitation is known to happen in impact-generated geothermal systems (e.g., Grieve, 2005).

Fresh sulfide precipitation along hollow rims and floors may contribute to the relatively bright floors and halos characteristic of some hollows. Recent

spectral analyses of hollows on Mercury and sulfides in the lab indicate that sulfides are present in hollow floors and in their bright halos (Helbert et al., 2013; Thomas et al., 2016; Vilas et al., 2016; Lucchetti et al., 2018; Pajola et al., 2021). MgS has an absorption centered at ~0.62 μm but CaS is spectrally featureless (Helbert et al., 2013). Analyses of Na_2S spectra show that this mineral has a broad absorption similar to that of MgS, but centered at ~0.56 μm (Gradie and Moses, 1984). Although the 0.62-μm absorption of MgS is consistent with some MESSENGER 8-band WAC spectra of the wall and rim hollows of Dominici crater, other spectra display a shorter wavelength absorption feature more consistent with the spectrum of Na_2S (Vilas et al., 2016). Additionally, hollow floors and rims are smooth and/or fine-grained in texture as determined by phase-ratio images (Blewett et al., 2014). It might be expected that fumarole-emplaced minerals would be fine-grained.

In a SCArFS model, it is likely that the majority of hollow formation would occur shortly after the impact ($<10^3 – 10^6$ yrs, depending on how long the subsurface stays hot). However, hollows would appear young through processes that freshen hollow floors and rims over longer timescales, which we describe in further detail in *Section 4.4.1.*

4.4.1 Reasons to Favor a SCArFS Hollow-Formation Model

1) Distribution of hollows in and around impacts. In the SCArFS model, hollows are expected to be predominantly associated with impact craters because they provide the heat and fracture networks necessary to drive hermeothermal systems. The locations of hollows in simple and complex craters agrees well with the expected locations of fumarole vents in both simple and complex craters (see *Section 4.4*, Stage 2). In simple craters, hollows typically are found along crater rims and are found less often on crater floors (Thomas et al., 2014), which would be consistent with where gases are expected to vent at the surface in simple craters (e.g., French, 1998; Oehler and Etiope, 2017). In complex craters, the preference of hollows to form on terraced walls, central

peaks, and central peak rings (Thomas et al., 2014) is consistent with where fractures are expected to vent the subsurface and with where hydrothermal systems have been preserved in terrestrial impact structures (Ames, 1999; Osinski et al., 2001; Osinski et al., 2013). Conversely, in a model for hollow formation where a volatile-rich hollow-forming source material is exhumed by impacts, hollows would be expected anywhere along the impact structure that corresponds to the depth of excavation of the volatile-rich material instead of predominantly along central complexes and terraced walls.

2) Association of hollows with LRM. A SCArFS model does not require a near-globally distributed layer of hollow-forming volatiles, as does the model suggested by Blewett et al. (2013). Instead, hollow-forming volatiles are produced from the sulfide-rich portions of LRM through thermal decomposition or other interactions (e.g., oxidation reactions) with impact melt or magma bodies. We suggest that the production of S (and S-bearing phases) through impact-generated hermeothermal systems is a more direct mechanism for the involvement of S in hollow formation than the concentration and sequestration of near-globally distributed S-rich layers as described in *Section 4.1.1* (see also Blewett et al. 2013, 2016). Our model results indicate that temperatures achieved adjacent to magma bodies or impact generated melt could decompose Na_2S at a rate sufficient to generate hollows, even at a depth of 1 km (Fig. 1.12). MgS and CaS would decompose at lower rates, but could still contribute to hollow formation, especially immediately following an impact when temperatures are highest.

3) Hollows not associated with impacts. There are few examples of hollows separate from an impact heat source. Hollows that do occur apart from impact craters, such as hollows northwest of Caloris basin, are spatially associated with lava flows, pyroclastic vents, red pitted terrain, and/or faults, which implies an association with subsurface heat (Thomas et al., 2014). Fumarole systems could have been stimulated by dikes and sills related to the lava flows, pyroclastic vents, and/or faults, that intruded subsurface sulfide-rich

LRM and generated hollow-forming fumarole systems. Another heat source for the decomposition of sulfides could be radiogenic decay of K, Th, and U, which are expected to strongly partition into sulfides. K is expected to partition into Na_2S and Th and U are expected to partition into MgS and CaS in Mercury's magma ocean (Boukaré et al., 2019). Hollows within small dark patches known as "dark spots" are observed in a variety of terrains and have been suggested to form via high velocity outgassing events (Xiao et al., 2013). Radiogenic self-heating of sulfides and their subsequent decomposition may play a role in small isolated hollows, such as dark-spot hollows.

4) Decreasing area and depth of hollows with increasing latitude. Hollow formation in the SCArFS model requires sublimation from solar heating, otherwise minerals would precipitate on and within the surface, perhaps with some vent formation as is typical in fumarolic systems, but hollows would not form because there would be negligible net loss of material from the system. The dependence of hollow formation on solar heating would impart the observed trend of decreasing depth and areal extent with increasing latitude.

5) Hollow morphology. The steep, rimless walls, flat floors, and amorphous shapes of hollows that are indicative of formation by sublimation (Blewett et al., 2011) are accounted for in a SCArFS hollow-formation model because sublimation is the principal mechanism for forming hollows at the surface (*Section 4.4, Stage 3*). We draw analogy to development of features in thermokarst landscapes, such as alases (Czudek and Demek, 1970). In the SCArFS model, hollows form primarily through downward growth over a broad area. Vent relocation (described above in *Stage 4*) could allow clusters of hollows to form, hollows to widen, and adjacent hollows to merge. Additionally, the likely diffuse nature of volatile emplacement surrounding vents (see *Stage 2* above) could contribute to widening of hollows through slow-acting scarp retreat as volatiles more slowly accumulate further from the vent. Other models for hollow formation suggest that most hollow growth happens laterally through scarp

retreat after an initial downward phase of hollow growth (see, e.g., Blewett et al., 2018).

6) The apparent youth of hollows. In the SCArFS model, the bulk of hollowing is expected to occur shortly after the hollow-hosting impact while the subsurface of the impact site is still hot. Thus, the apparent youth of hollows does not obviously follow within the SCArFS model. We propose two mechanisms, which are natural extensions of processes proposed within the SCArFS model, that could maintain the fresh appearance of hollows. In this way, the lifecycle of hollows in a SCArFS model has two primary phases: 1) a primary phase initiated by introduction of a (typically impact-generated) heat source in which the majority of hollow growth occurs followed by; 2) a maintenance phase of slower hollow growth that is long-lived and possibly currently active.

The first mechanism that could support a long-lived is gradual loss of S from a S-rich, near-surface, reservoir retained beneath hollows (see Fig. 1.13, Stages 3 and 4). A region where S is relatively stable would exist beneath hollows at depths of decimeters to decameters, depending on hollow location (see *Section 4.4, Stage 3)*. The reservoirs would be shallower at colder locations and deeper at warmer locations. Mass loss rates of S from such reservoirs would also depend on hollow location, ranging from 3.3 m Gyr^{-1} from a 13 cm-deep reservoir at the cold limit of hollow formation to 6.4 m Gyr^{-1} from a 15 m-deep reservoir at the hot limit of hollow formation (see Figs. 1.8 – 1.10, *Section 3.2*).

The second mechanism we propose for maintaining the youthful appearance of hollows within the SCArFS model is slow, but continual, hollow growth if conditions *i – iii* of Stage 4 of the SCArFS model are not (completely) achieved. Continued transport of volatiles to the surface throughout the tail-end of impact-induced heating and by the hermeothermal gradient within the megaregolith may be expected. Temperatures within the upper ~1 – 5 km of the hermean crust are influenced by megaregolith properties and have been estimated at ~500 – 720 K (Mohit et al., 2009; Egea-González and Ruiz, 2014). Such temperatures are not sufficient to account for the full depth of hollows in a

SCArFS model but may be sufficient to impart a veneer of youth to hollows. Volatiles produced at depth would have an effective path to the surface provided by the fumarole vent systems, and hollow formation could proceed (per Stages 1 – 3 of the SCArFS model) at a rate on the order of ~1 m Gyr^{-1} (c.f., Fig. 1.12) – so long as the volatile source is not depleted. This second mechanism would also augment the first mechanism through replenishment of the S-rich reservoir beneath hollows.

Any mechanism that maintains a fresh appearance for hollows must compete with mechanisms that degrade hollows, such as space weathering and macro-scale erosional processes. The bright floors and halos of hollows might be expected to diminish over a similar time frame as the bright rays of rayed craters (≤ ~270 Ma, Xiao et al., 2012). If this is the case, then the mechanisms proposed here to maintain a fresh appearance to the surface hollows would act sufficiently quickly (freshening 1 to 6 mm of surface every Myr) to combat surface darkening by space weathering. Erasure of decameter-scale topography is unlikely to occur through surficial space weathering processes, but hollows would be affected by macro-scale erosional processes, such as small impactors that cause "topographic diffusion" (e.g., Fassett and Thomson, 2014). Topographic diffusion is the process of progressive erasure of topography via small impactors (Soderblom, 1970; Hirabayashi et al., 2018). On the Moon, a characteristic erosion rate for features > ~500 m in extent (appropriate for hollows) over the past 3 Ga has been estimated at between 0.2 m Gyr^{-1} (Craddock and Howard, 2000) and 0.4 m Gyr^{-1} (Fassett and Thomson, 2014). Fassett et al. (2017) conservatively estimated that the rate of erosion due to topographic diffusion is a factor of 2 higher on Mercury than on the Moon. Because impact flux scales with distance to the sun (R) as $\frac{1}{R^2}$, the rate of topographic diffusion for Mercury could be as much as 6.7 times that of the Moon's. Therefore, we estimate a characteristic erosion rate for hollows at between 0.4 and 2.68 m Gyr^{-1}. These rate estimates are slower than our estimated freshening rates for hollows, so it is

plausible that hollows could maintain a fresh appearance through geologic time on Mercury via the mechanisms proposed here. It is interesting to note that our upper estimate for erosion by topographic diffusion is not sufficient to completely erase a typical 24 m-deep hollow over a 4 Ga period, even in the absence of mechanisms to refresh hollows. The process of erosion via topographic diffusion is scale-dependent, however, and smaller features are, counterintuitively, expected to experience *lower* rates of erosion via topographic diffusion than larger features (Minton et al., 2019). More rigorous estimates of hollow erosion rates should be made, as well as more detailed modeling of the SCArFS processes to test whether these estimates hold under more detailed scrutiny.

In the SCArFS model, hollow formation could eventually cease if all volatile sources are depleted. Therefore, two endmember classes of hollows are predicted: **1) "degraded" hollows** that no longer have a volatile source, are morphologically and topographically muted, and are dark; and **2) "fresh" hollows** that have a volatile source (either actively sourced from the subsurface or passively sourced from a remnant, near-surface, S-rich reservoir), are morphologically crisp, and are bright. Both classes of hollows would begin their growth directly after introduction of a heat source, typically impact-generated. If this is true, one might expect older craters to have a relatively higher proportion of "degraded" to "fresh" hollows than younger craters because there would have been more time to deplete the volatile source. Thomas et al. (2014) looked at the percentage of crater floor surface area covered by hollows as a function of crater degradation state as a proxy for age (Barnouin et al., 2012). Thomas et al. (2014) found that younger craters have a higher percentage of their floors covered by hollows than do older craters. One interpretation for this trend is that erosional processes mute dormant hollows, obscuring their observation (Thomas et al., 2014). This explanation would be consistent with the SCArFS model in which "degraded" and "fresh" hollows are expected.

7) Some other considerations. The SCArFS model for hollow formation does not require space weathering processes to account for hollow formation.

We do not favor models that require space weathering processes because they act on only the uppermost portion of the surface and downward growth would likely be self-limiting after the buildup of a thin lag deposit. Impact gardening rates are slow (Killen et al., 2007; Domingue et al., 2014; Costello et al., 2019) compared to estimated hollow formation rates (Blewett et al., 2016), and as such, regolith turnover could not replenish volatiles to the surface quickly enough to account for hollow formation. However, the role that space weathering processes may play in the surface appearance of hollows should be explored because space weathering will likely affect the lifetime and spectral properties of sulfides and other materials present on hollow floors and rims (e.g., Domingue et al., 2014). Additionally, Ca, Mg, K, and Na in Mercury's exosphere have a conceivable link to hollows (c.f., Bennett et al., 2016). Reactive sublimation of sulfides at the surface immediately following an impact and/or precipitation of fresh sulfides in fumarolic systems and subsequent space weathering could be replenishing sources for these exospheric species.

Lastly, the SCArFS model can account for hollows in all their settings. Other models for hollow formation can plausibly account for hollows in certain settings, but have difficulty explaining all instances of hollows (see, for example, Section 12.6 of Blewett et al., 2018). We suggest that it is more parsimonious for a single model to explain all instances of hollows rather than adopting several setting-specific explanations for hollow-formation.

4.5 Future Work

In this paper, we showed that elemental S is a viable hollow-forming volatile phase. However, more work is needed to test the hollow-formation model proposed by Blewett et al. (2013) and the SCArFS model proposed here. In the hollow-formation model proposed by Blewett et al. (2013), a near-globally distributed S-rich layer is necessary; whether such a S-rich layer could have been emplaced within the hermean crust is unknown. We discuss a conceptual model for how a hollow-sourcing layer of S-rich material could have been

emplaced in *Section 4.1.1*, but the detailed modeling necessary to test the viability of this conceptual model is outside the scope of this work. If a S-rich hollow-forming layer exists within the hermean crust, then, according to the model of Blewett et al. (2013), hollows across Mercury are formed from material excavated from this layer. Therefore, calculating the depth of excavation associated with hollows both globally across Mercury and locally at individual craters could provide a useful test of the validity of that model. Thomas et al. (2014) presented a preliminary analysis of the depth of excavation of LRM and concluded that LRM is not globally present at a specific depth. However, a detailed study bracketing the range of excavation depths of hollow-sourcing material may prove useful. For example, the presence of a S-rich layer would be supported if hollows could be shown to be sourced from a subsection of the several kilometers-thick LRM.

To test the SCArFS model for hollow formation, more modeling and observational work should be done. We suggest several phases (most importantly, S) that could be present in hermean fumarolic systems (*Sections 4.3.1* and *4.4*), but detailed modeling of the phases that would be produced by heating, melting, and shocking sulfide-rich LRM should be done. The relative volume of volatile phases produced by thermal decomposition of sulfides versus alteration from heating other phases (e.g., C) in LRM is unconstrained. Other mechanisms for producing gases in a hermeothermal system could include degassing of magmas and of impact-melted LRM, as well as oxidation of sulfides. The degree and type of mineralization along fractures and in pore spaces is also unknown. We suggest sulfides may (re-)precipitate from the proposed fumarolic systems, but the mineral species that may form in such systems would be dependent on the fluid composition, the temperatures, and oxygen fugacities involved and may involve other sulfur-bearing species, such as chalcogenides and sulfosalts. The types of minerals deposited would likely evolve over time, as the temperatures surrounding the impact evolve and the fluid composition changes, and with latitude because the solar insolation

differences would drive off different proportions of S and other mineral species. A detailed model of the fluid phases produced and circulated after an impact into sulfide-rich LRM on Mercury (similar to models of impact-generated hydrothermal systems on Earth and Mars, Rathbun and Squyres, 2002; Abramov and Kring, 2004) would be useful in addressing many of these questions.

Statistical analyses of the distribution of hollows within craters would prove useful for distinguishing between expected distributions of hollows in a SEALS model versus a SCArFS model for hollow formation. For example, in a SCArFS model, hollows are expected to be predominantly, but not exclusively, associated with terraced walls and central complexes; whereas in a SEALS model, hollows are expected wherever hollow-sourcing material is exhumed by the impact. Although our preliminary inspection suggests that hollows are predominantly associated with terraced walls and central complexes of complex craters (Fig. 1.A7), this has not been rigorously shown through a statistical analysis.

Detailed observations of hollows are planned with the BepiColombo mission (Rothery et al., 2020). More detailed geomorphological analyses of hollow shapes, depths, and floor structures could be useful in (in)validating the SCArFS model. As part of the Spectrometer and Imagers for Mercury Planetary Orbiter (MPO) BepiColombo Integrated Observatory SYStem (SIMBIO-SYS, Poulet et al., 2015; Cremonese et al., 2020), the BepiColombo mission will image > 20% of the hermean surface with its high-resolution imager (HRIC, Poulet et al., 2015; Cremonese et al., 2020) at a ground sampling distance of 6 m at 480 km altitude (periherm). Targeted images of hollows may reveal that small vents pockmark hollow floors. Constructional vent features may not have formed if most of the phases that were present in the hermeothermal systems (e.g., S) sublimated away. However, some constructional vent features composed, perhaps, of sulfides may be expected. We suggest (in *Section 4.4.1*) that the SCArFS model predicts two endmember classes of hollows: “degraded” and “fresh”. Evidence for “degraded” hollows, while scarce, does exist (Blewett et al., 2018). If the SCArFS model accurately describes hollow formation, then a higher

number of “degraded” hollows likely exist than have presently been observed. Therefore, a prediction from the SCArFS model is that many “degraded” hollows are yet undiscovered on Mercury. More complete high-resolution imaging of Mercury may reveal evidence for “degraded” hollows and allow for classification of hollows into categories of morphological degradation state, similar to that which exists for hermean craters (Barnouin et al., 2012; Kinczyk et al., 2020). Comparison between hollow degradation state and host crater degradation state might help address some of the questions concerning hollow age, timescales over which hollows are active, hollow modification and degradation rates and processes, and the potential for a “lag-time” between impact crater formation and hollow formation (which would be evidence against the SCArFS model). Additionally, the SIMBIO-SYS suite will have a moderate-resolution visible and near-infrared hyperspectral imager (VIHI) with a spectral range of 400 – 2000 nm, and with a spectral resolution of 6.25 nm/pixel. Hyperspectral images of hollow rims and floors could confirm the presence of sulfides within hollows (Helbert et al., 2013; Thomas et al., 2016; Lucchetti et al., 2018; Pajola et al., 2021) and the Mercury Imaging X-Ray Spectrometer (MIXS) will map S abundance across the planet (Bunce et al., 2020). Lastly, if the pore spaces of some sections of hollow floors and rims are mineralized, these units may have a higher thermal inertia than surrounding materials, which could be measured with the MERTIS instrument on BepiColombo (Hiesinger et al., 2020).

4.6 Possible Implications

If hollow formation is linked to hermeothermal systems, then the study of hollows may present a unique opportunity for comparative planetology between geothermal, aerothermal, and hermeothermal systems and their various surface expressions (e.g., hot springs, geysers, mud pots, fumaroles, etc.). On Earth and Mars, erosion and weathering can erase evidence of and preclude observation of deposits and landforms created within geothermal and areothermal systems. Although some processes, such as space weathering and mass wasting, could

erase hollows over time, hollows are likely a more accurate representation of the full and relatively pristine extent of a hermeothermal system than are the surface deposits and landforms left by geothermal and areothermal systems. Therefore, studying hollow morphology, depth, and distribution within and surrounding craters could lead to a fuller understanding of the extent of thermal systems on Earth and Mars where orbit-based evidence of (extinct) thermal systems can be more difficult to detect. Informing the search for extinct thermal systems on Mars is of specific importance because these sites are of astrobiological interest (e.g., Schmidt et al., 2009; Ruff et al., 2011; Squyres et al., 2012; Ruff and Farmer, 2016).

5. Conclusions

We used a thermal model to calculate the loss rate of 57 candidate hollow-forming volatile phases as a function of depth, time, and location on Mercury. We found that only three volatile phases have the appropriate thermophysical characteristics to be plausible hollow-forming volatiles: stearic acid ($C_{18}H_{36}O_2$), fullerenes ($C_{60,70}$), and elemental sulfur (S). Notably, sulfides are shown to be too refractory to be the phase responsible for hollow formation if solar heating drives hollow formation. We summarize our conclusions about the plausibility of $C_{18}H_{36}O_2$, fullerenes, and S as the hollow-forming phase below:

- $C_{18}H_{36}O_2$ is rejected as the volatile phase responsible for hollow formation on the basis that it could not have been delivered to Mercury and sequestered in sufficient volume to account for the observed volume of hollows.
- Fullerenes may have been generated through space weathering of a graphite crust in the Pre-Tolstojan Period, but it is unlikely that a sufficient volume of fullerenes was created in this way to account for hollows (*Section 4.2.1*). If fullerenes were generated on Mercury, it is

possible that they contribute to dark lag deposits in permanently shadowed regions at the poles.

- Elemental S is the most viable candidate for the hollow-forming phase based on its thermophysical characteristics and on the relative abundance of sulfur on Mercury.

If S is the hollow-forming volatile phase, then within the hollow-formation model framework proposed by Blewett et al. (2013) two conditions must be met: 1) a hollow-sourcing layer rich in S must exist within the hermean crust, and 2) this S-rich layer must survive the impact-excavation process and be emplaced on crater central complexes, floors, walls, and rims in a manner consistent with the observed distribution of hollows around impacts. In *Section 4.1.1*, we discuss the possible formation of a near-globally distributed, S-rich, hollow-sourcing layer through a diurnal sublimation/deposition cycle during global volcanic resurfacing of Mercury in the Pre-Tolstojan Period. We suggest that this mechanism cannot be ruled out, but that more detailed modeling is required to assess the viability of this conceptual model (see also *Section 4.5*). In *Section 4.1.2*, we discuss the possibility that a S-rich layer could survive the impact-excavation process and be distributed around hollows in a manner consistent with the observed distribution of hollows around impacts. We suggest that the distributions of hollows observed within and surrounding individual complex craters indicates that, if hollows form from excavated material, this material is likely sourced from a range of depths, which is potentially inconsistent with excavation from a single S-rich layer. However, more work should be done to calculate the depths of excavation for hollow-forming material (*Section 4.5*).

Because of the complications involved with the emplacement and excavation of a S-rich hollow-sourcing layer (*Section 4.1*), we propose an alternative hollow-formation model (*Section 4.4*). We suggest that S may have been produced through the thermal decomposition of sulfide-bearing LRM heated by impact-related, magmatic, or other subsurface heat sources. The

production of sulfur-rich gases would generate fumarolic systems. The S-bearing phases within these fumarole systems would undergo deposition in the vicinity of vents at night, forming patchy sulfur-rich layers, and sublimation during the day to produce hollows in a process analogous to development of thermokarst landscapes (*Sections 4.3.1* and *4.4,* Fig. 1.13). We call our alternative model for hollow formation the Sublimation Cycling Around Fumarole Systems (SCArFS) model. We favor the SCArFS model over SEALS hollow-formation models for reasons delineated in *Section 4.4.1*.

Appendix I

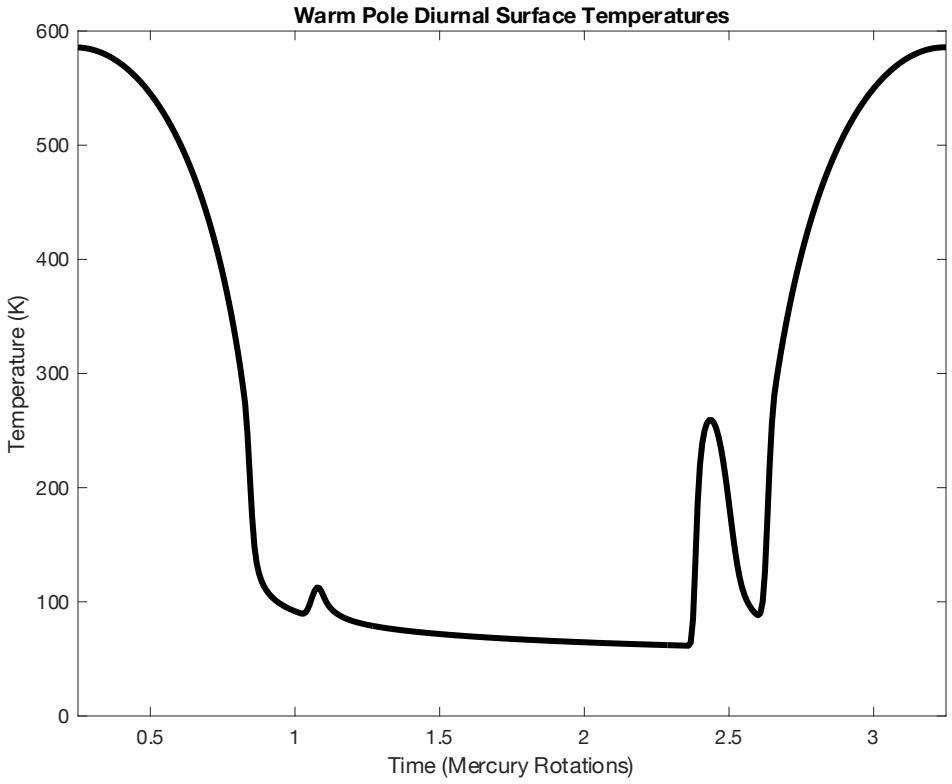

Fig. A1. 1. Diurnal surface temperature at 90°E 0°N. notice the anomalies on the nightside due to Mercury's unique orbital characteristics discussed in Section 1.1.

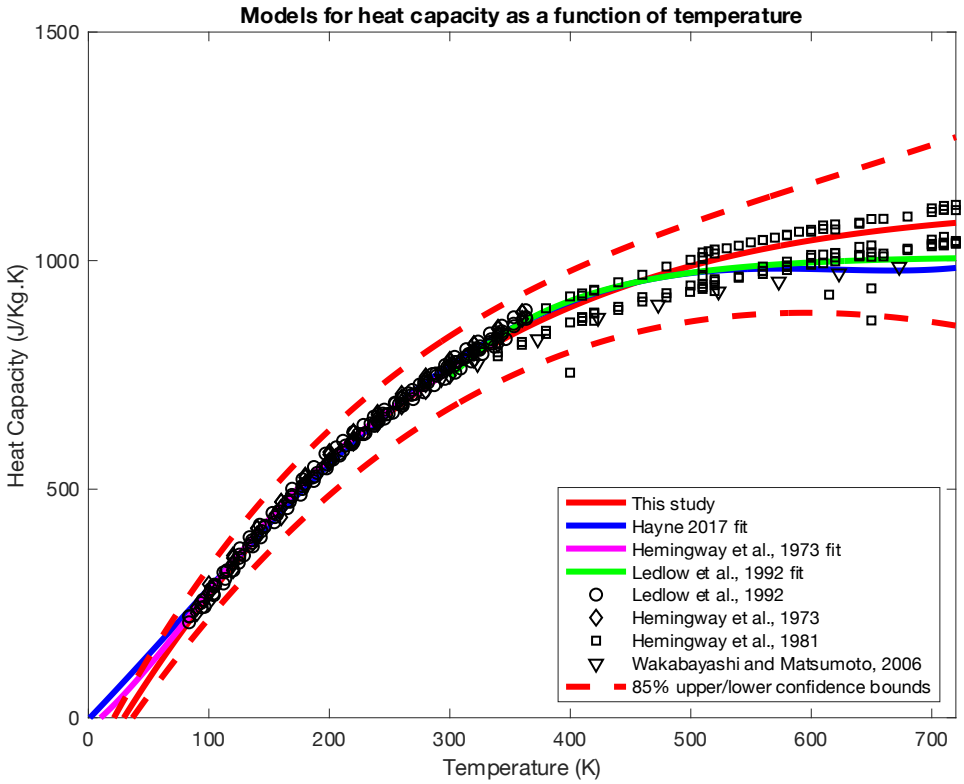

Fig. A1. 2. Polynomial fits to heat capacity data for lunar regolith. Our fit (red) is compared to previous fits.

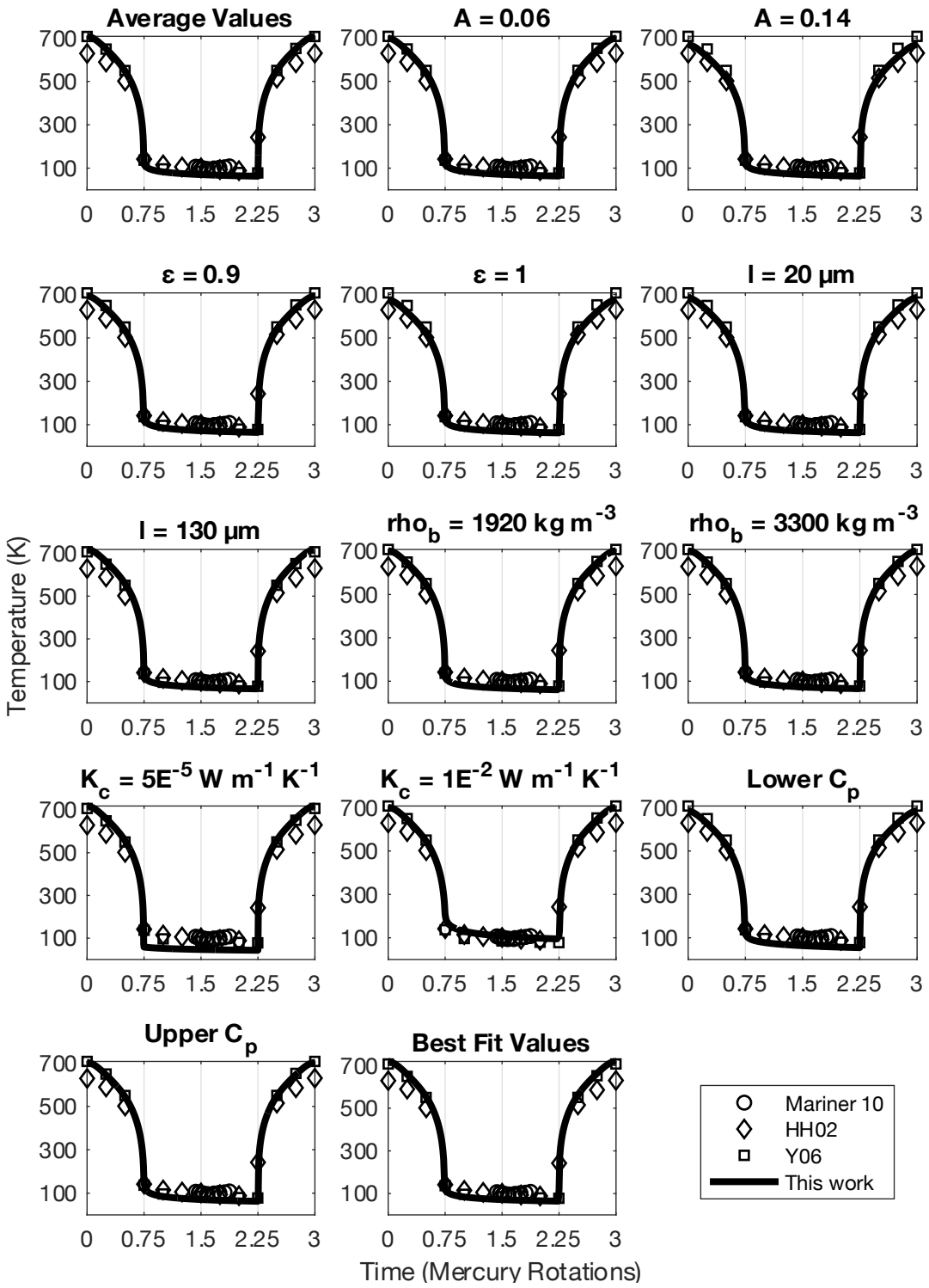

Fig. A1. 3. Surface diurnal temperatures for models run with various parameter configurations. See Table 2 and text for details. Values are compared to Mariner 10 IRR data from Chase et al. (1976), and to model data from Hale and Hapke (2002) (HH02) and Yan et al. (2006) (Y06).

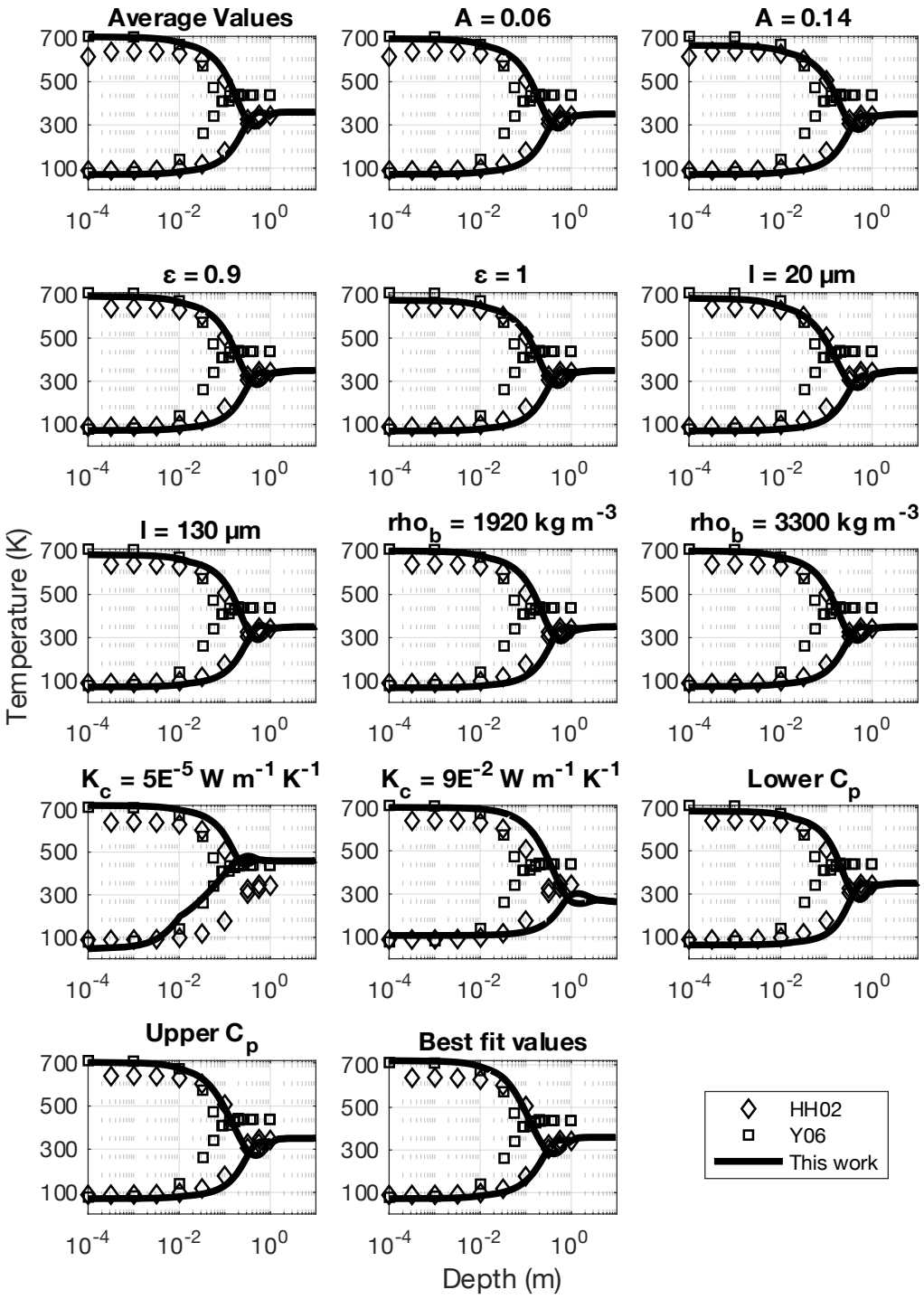

Fig. A1. 4. Noon and pre-dawn temperatures as a function of depth for various parameter configurations (same as those shown in Fig. 1.A3). Values are compared to model runs from Hale and Hapke (2002) (HH02) and Yan et al. (2006) (Y06).

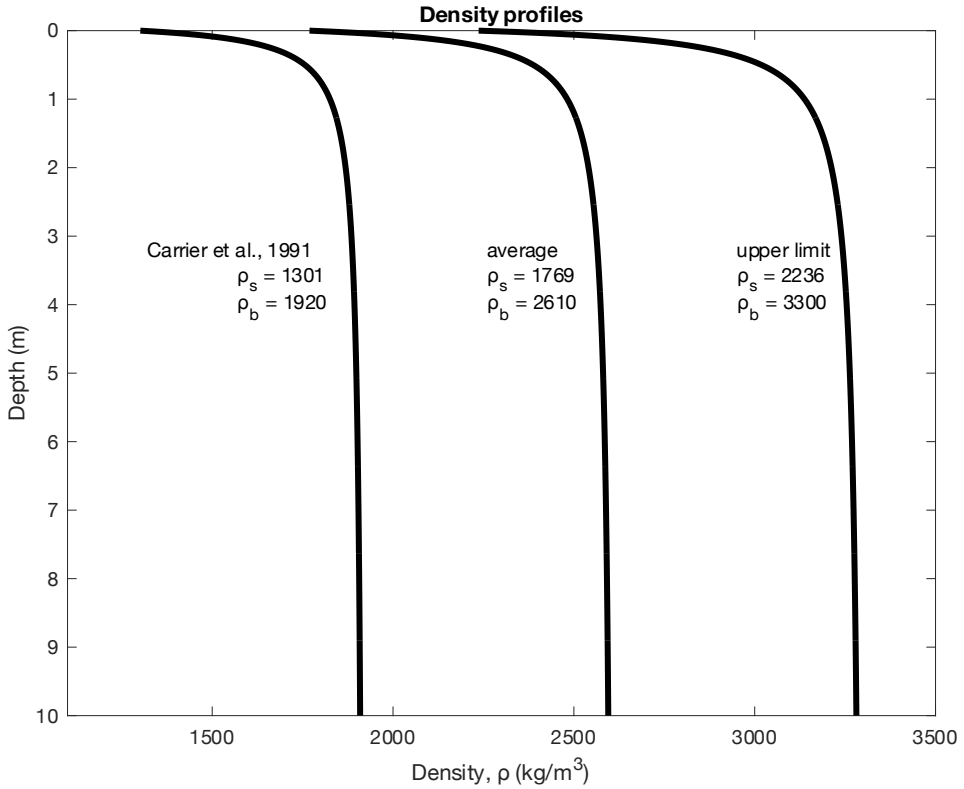

Fig. A1. 5. Upper and lower limit density profiles as a function of depth used in our thermal model.

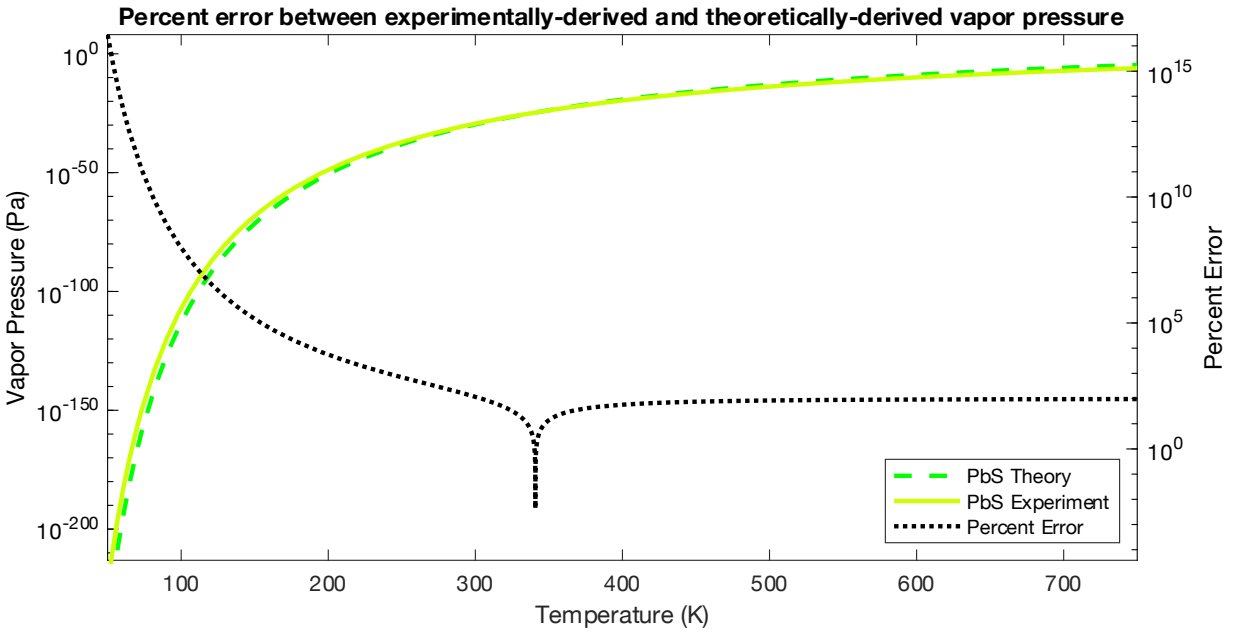

Fig. A1. 6. Percent error between theoretically and experimentally derived vapor pressure curves for PbS. At 340 K the two curves cross and percent error asymptotically approaches zero.

Table A1. 1. Phases likely delivered to or generated on Mercury. a: Botta and Bada (2002), b: Pierazzo and Chyba (1999), c: Kerber et al. (2009).

Meteorites[a]	
Compound Class	**Concentration (ppm)**
Amino acids	17– 60
Aliphatic hydrocarbons	>35
Aromatic hydrocarbons	3319
Fullerenes	>100
Carboxylic acids	>300
Hydroxycarboxylic acids	15
Dicarboxylic and Hydroxydicarboxylic acids	14
Purines and Pyrimidines	1.3
Basic N-heterocycles	7
Amines	8
Amides (linear)	>70
Amides (cyclic)	>2
Alcohols	11
Aldehydes and Ketones	27
Sulphonic acids	68
Phosphonic acids	2
Comets[b]	
Compound	**Concentration (% relative to water)**
H_2O	100
CO	<1– 40
CO2	2–20
H_2CO	<1– 5
CH_3OH	0.9–7
HCOOH	<0.2
CH_4	0.1– 0.5
C_2H_6	0.2–2
$C_{14}H_{10}$	0.15
HCN	0.007– 0.2
CH_3CN	0.01– 0.02
NH_3	0.1–2
H_2CS	<0.1
H_2S	0.1– 1.6
N_2	<1.5
Ar	<17

Table A1. 1 continued

Magma[c]	
Compound	**Concentration (ppm)**
CO	5500
CO_2	8700
H_2O	3600
SO_2	13000
H_2S	500
S	500

Table A1. 2. molecular diameter and mean free path of volatile phases explored in this study. Phases with mean free paths highlighted in red do not meet the assumptions outlined in *Section 2.2.2.*

Class	Molecular form	molecular diameter (m)	mean free path (m)
Inorganics	NH3	2.60E-10	1.15E-06
	H2O	1.62E-10	0.000898
	CO	3.76E-10	1.38E-08
	N2	3.64E-10	1.57E-08
	S	1.80E-10	134
	H2S	3.60E-10	4.45E-07
	Ar	3.40E-10	3.05E-08
	CO2	3.30E-10	6.90E-08
	SO2	3.60E-10	2.39E-06
	Kr	3.60E-10	4.84E-08
	Xe	3.96E-10	1.25E-07
Simple Organics	CH4	3.80E-10	4.80E-08
	HCN	2.19E-10	2.90E-05
	COS	2.76E-10	2.45E-06
	C5H12	6.78E-10	3.39E-06
	CS2	3.30E-10	3.20E-05
	C5H10O	6.78E-10	3.32E-05
	C7H8	5.81E-10	4.96E-05
	C5H10O2	7.92E-10	2.54E-05
Aromatic Hydrocarbons	C6H7N	5.79E-10	0.000338
	C6H6O	5.21E-10	0.00319
	C7H6O	6.02E-10	0.00112
	C7H8O	6.94E-10	0.000348
	C7H6O2	6.02E-10	0.00210
	C6H5NO2	6.03E-10	0.00373
	C10H8	7.10E-10	0.00502
	C10H8O	7.11E-10	0.0524
	C10H8O	7.82E-10	0.0433

Table A1. 2 continued

Class	Molecular form	molecular diameter (m)	mean free path (m)
Aromatic Hydrocarbons	C12H10	9.18E-10	0.0136
	C12H18	6.74E-10	0.00598
	C14H10	9.40E-10	2.33
	C14H10	9.16E-10	2.45
Linear Amides	CH3NO	3.09E-10	0.0285
	C2H5NO	4.20E-10	0.00752
	C2H5NO	4.10E-10	0.00790
	C3H7NO	4.28E-10	0.000913
	C3H7NO	5.22E-10	0.000614
	C4H9NO	5.38E-10	0.000235
	C4H9NO	5.42E-10	0.000231
Carboxylic Acids	C5H10O2	7.87E-10	2.57E-05
	C6H12O2	9.10E-10	5.23E-05
	C7H14O2	1.04E-09	8.43E-05
	C8H16O2	1.16E-09	0.000144
	C9H18O2	1.29E-09	0.000226
	C10H20O2	1.41E-09	0.000363
	C12H24O2	1.66E-09	0.00252
	C16H32O2	2.16E-09	1.41
	C18H36O2	2.41E-09	4.19
Carbon	C60	7.10E-10	4.86E+13
	C70	7.96E-10	6.85E+14
	C	3.00E-07	1.27E+98
Sulfides	K2S	1.73E-09	1380
	Na2S	1.73E-09	6.70E+22
	MgS	8.66E-10	1.32E+40
	MnS	8.66E-10	2.58E+40
	FeS	1.93E-10	4.62E+42
	CaS	2.27E-10	8.07E+57

Table A1. 5. Time in years for each phase to sublimate to the depth of a typical hollow at each latitude (c.f., Table 5).

Compound	0°N	40°N	71°N	
C	8.35211E+47	9.05145E+51	4.14023E+74	Hot Meridian
MgS	2.41196E+16	1.85951E+18	7.30607E+28	
MnS	4.58345E+16	3.58374E+18	1.52394E+29	
FeS	4.20661E+16	3.88499E+18	4.2098E+29	
CaS	3.89343E+24	1.10256E+27	6.46933E+40	
C	1.49897E+60	1.12886E+65	1.84652E+94	Warm Meridian
MgS	1.12862E+22	2.14599E+24	9.65575E+37	
MnS	2.23908E+22	4.33056E+24	2.1578E+38	
FeS	3.41975E+22	8.09019E+24	1.34732E+39	
CaS	9.77554E+31	8.96894E+34	5.01331E+52	

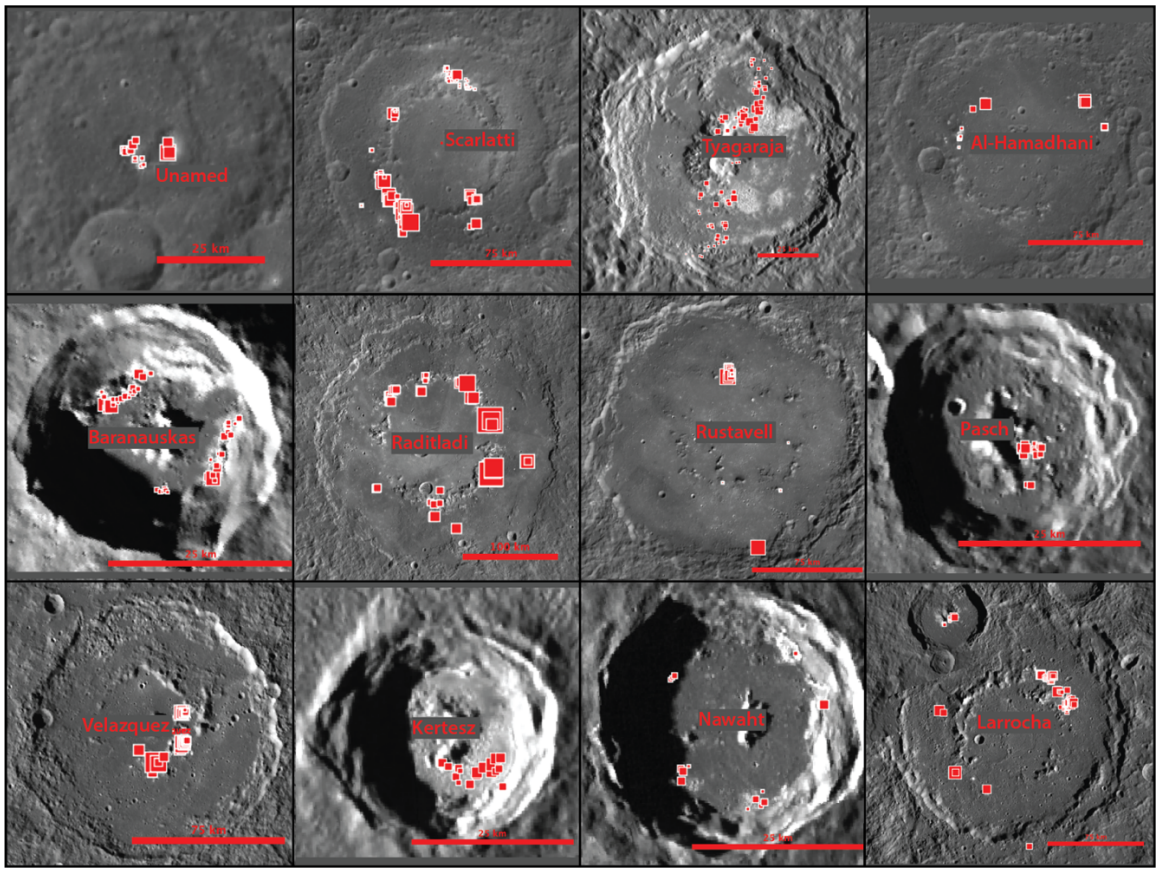

Fig. A1. 7. Collage of representative complex craters that host hollows. The crater name is presented in the center and north is up in all images. Red squares are locations where hollow depths were measured by Blewett et al. (2016). Larger squares represent a deeper value for hollow depth. Note that hollows occur predominantly along central peaks and peak rings and terraced walls. Hollows generally appear to be deeper closer to the central complexes than further from

CHAPTER II
WIDESPREAD ANORTHOSITIC ROCKS IN A PRE-NOACHIAN LAYERED IGNEOUS COMPLEX ON MARS

A version of this chapter has been submitted for publication to the journal *Science* by Michael S. Phillips, Christina E. Viviano, Jeffrey E. Moersch, A. Deanne Rogers, Harry Y. McSween, and Frank P. Seelos.

Phillips, M.S., et al., "Widespread anorthositic rocks in a pre-Noachian layered igneous complex on Mars." *submitted*.

This chapter has been revised to include more details in the methods section and a more general introductory paragraph, as per committee suggestions.

Abstract

Due to its size and observable ancient rock record, Mars is a key planet for understanding primary crust formation on planetary bodies that experience overturn melting, a regime of primary crust formation that Venus and Earth are expected to have undergone as well (Elkins-Tanton, 2012). However, the composition of ancient martian crust is not well-constrained. Recent evidence from orbital detections (Carter and Poulet, 2013; Wray et al., 2013; Eggers et al., 2021), rover observations (Stolper et al., 2013; Sautter et al., 2014; Sautter et al., 2015), and the pre-Noachian martian meteorite NWA 7034 and its pairs (Humayun et al., 2013; Santos et al., 2015) hint at the possibility of evolved compositions in the ancient martian crust and provide some support for the hypothesis of a pervasive, subsurface feldspathic component to the crust based on geodynamic data (Baratoux et al., 2014; Wieczorek et al., 2021). To test this hypothesis, we searched for evolved lithologies using the Compact Reconnaissance Imaging Spectrometer for Mars (CRISM) in crustal blocks uplifted by the Hellas basin-forming impact (Leonard and Tanaka, 2001), which are the most extensive and spatially coherent outcropping of pre-Noachian rock. Here, we present evidence for a pre-Noachian, layered igneous complex >2,000 km in extent in the northern Hellas region that contains feldspathic rocks, which we interpret as anorthositic. The existence of this feldspathic material raises the intriguing possibility that the Hellas-forming impact uplifted a sample of a deep, global, low-density component of the ancient martian crust.

1. Introduction

The formation of the first stable crust (primary crust) on a rocky planetary body depends on the size of the body for several reasons that include the energy associated with accretion, and the relationship between the gravitational acceleration of the body and the buoyancy of solid minerals in a melt (Elkins-Tanton, 2012). Planetary bodies smaller than Mars, such as Mercury and the Moon, are expected to produce primary floatation crusts (e.g., Wood et al., 1970; Vander Kaaden and McCubbin, 2015), but Mars and Earth are large enough that they fall into an “overturn melting” regime of primary crust formation characterized by solidification of a magma ocean into a gravitationally unstable configuration that overturns to produce voluminous depressurization melting and a subsequent primary crust (Elkins-Tanton, 2012). Unlike on Earth, where plate tectonic processes have erased the earliest rocks (>~3.8 Ga) from the geologic record, remnants of martian crust from the pre-Noachian Period (~4.56 to ~4.0 Ga) are exposed at the surface. Therefore, given its intermediate size among terrestrial planets and its observable record of ancient crust, Mars offers a unique opportunity to constrain models of planetary differentiation and primary crust formation.

Though the majority of martian crust formed within the first ~500 Ma post accretion (Phillips et al., 2001; Nimmo and Tanaka, 2005; Morschhauser et al., 2011; Grott et al., 2013), pre-Noachian lithologies remain poorly understood because they are largely buried by younger materials produced over the subsequent ~4-Gyr timespan. By contrast, martian crust younger than ~3.8 Ga (Hesperian) is well-characterized and is dominantly basaltic (McSween et al., 2003). Estimates for early crust composition and volume come from modeling of early mantle thermal and chemical evolution. Such models are constrained primarily by meteorite and remote sensing data for crustal chemistry and geodynamic data for crustal thickness (Righter et al., 1998; Halliday et al., 2001; Elkins-Tanton et al., 2003), which may be misleading because more and better

data are available for younger crustal compositions. In existing models for early Mars crust formation, significant volumes of evolved compositions, such as anorthositic or granitic rocks, while in some cases are permissible, are not favored (Elkins-Tanton et al., 2005). However, recent evidence from an ancient martian meteorite (Humayun et al., 2013), rovers (Stolper et al., 2013; Sautter et al., 2014), and orbital data (Carter and Poulet, 2013; Wray et al., 2013; Eggers et al., 2021) hint at the possibility of a petrologically-evolved component to the Noachian and older crust. Additionally, recent analyses of geodynamic data suggest the presence of an extensive, low-density (e.g., feldspathic) component of the martian crust (Baratoux et al., 2014; Wieczorek et al., 2021). Despite these recent indications for a potentially pervasive feldspathic component to the ancient martian crust, no regional-scale observations of evolved lithologies have been described to date.

We test the hypothesis that an extensive, feldspathic component exists in martian pre-Noachian crust by searching for evolved lithologies in pre-Noachian bedrock uplifted by the Hellas basin-forming impact and exposed within the Noachian hilly (Nh), Noachian massif (Nm), and Noachian crater (Nc) units north of Hellas basin (Fig. 2.1, Appendix II Fig. A2.1; Leonard and Tanaka, 2001) using the Compact Reconnaissance Imaging Spectrometer for Mars (CRISM), a visible to short-wavelength infrared (VSWIR, 0.4 – 4 μm) reflectance spectrometer aboard the Mars Reconnaissance Orbiter (Murchie et al., 2007). The crustal blocks (massifs) were uplifted by post-basin formation extensional processes and are thought to represent deep crust and, perhaps, mantle material (Leonard and Tanaka, 2001; Hamilton and Christensen, 2005). We systematically analyzed and mapped the composition of massifs and uplifted rims of large craters scattered throughout the Nh, Nm, and Nc units, which together represent the most extensive and spatially coherent sampling of pre-Noachian crust on Mars.

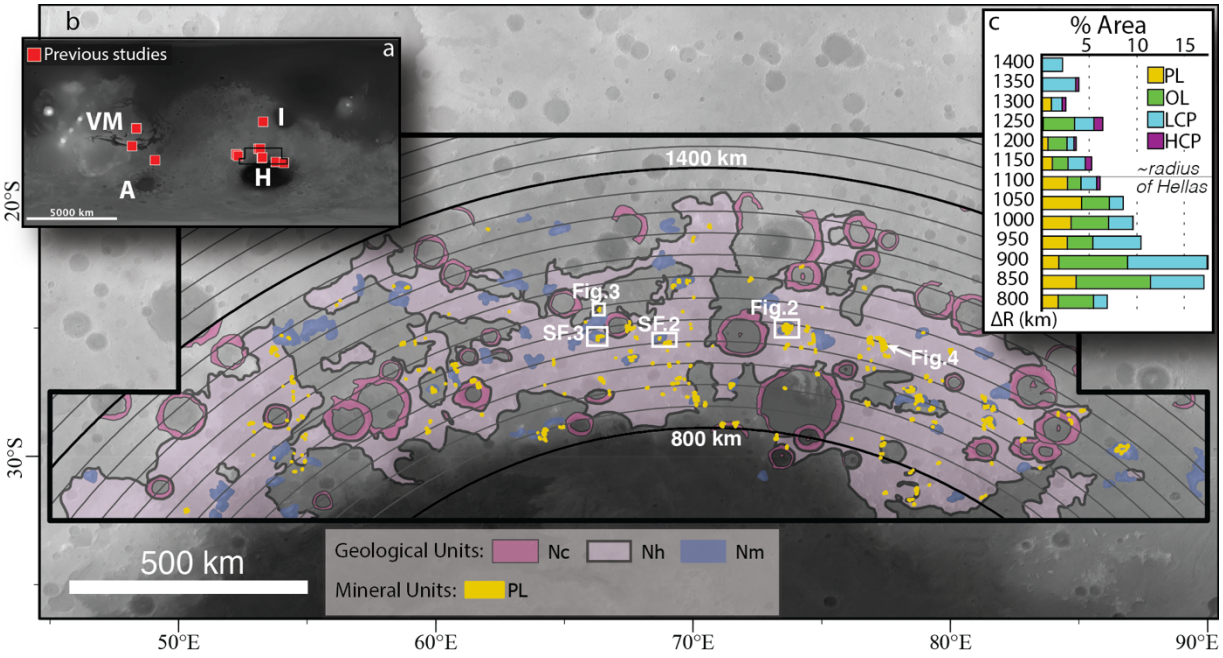

Fig. 2. 1. Map of northern Hellas feldspathic outcrops. a, Context map of Fe-plagioclase-bearing outcrops previously identified on Mars, red squares, see Appendix II Table A2.1 for details. VM = Valles Marineris, A = Argyre, H = Hellas, I = Isidis. **b,** 255 Fe-plagioclase-bearing outcrops mapped in this study in yellow (outlines exaggerated for visibility). Fe-plagioclase-bearing outcrops occur nearly exclusively in Noachian crater (Nc), Noachian hilly (Nh) and Noachian massif (Nm) geological units (Leonard and Tanaka, 2001) displayed overlaid on MOLA/HRSC blended topography. **c,** percent area of primary igneous minerals mapped in this study as a function of distance from the Hellas basin center (ΔR) at 50-km intervals and corrected for the percentage of Nc, Nh, and Nm units in each radial bin. PL = Fe-plagioclase, OL = olivine, LCP = low-Ca pyroxene, HCP = high-Ca pyroxene. Y-axis labels are the maximum radius for each bin and the 800 km bin includes all values < 800km. Note context for Figs. 2.2-2.4 and Appendix II Figs. A2.2-A2.3 (SF.2, 3). See Appendix II Fig. A2.1 for OL, LCP, and HCP mapping.

2. Methods

2.1 Detection of primary minerals with VSWIR reflectance spectra

The CRISM instrument is sensitive to plagioclase with ≥ ~0.05 wt.% ferrous iron (henceforth, “Fe-plagioclase”; Bell and Mao, 1973). The 1.25-μm crystal-field absorption feature of Fe-plagioclase is obfuscated by mafic minerals unless the rock comprises >85 vol% Fe-plagioclase (Carli et al., 2014a; compositions referred to herein as “anorthositic”, with anorthosite being ≥90% plagioclase) or the Fe-plagioclase modal abundance is >50% and its grain size is large compared to the mafic groundmass (such compositions are included in the term “feldspathic”, or rocks with >50% feldspars, Frost and Frost, 2008; Rogers and Nekvasil, 2015). Otherwise, Fe-plagioclase is detectable in the VSWIR if it is mixed with spectrally featureless minerals, such as quartz or other feldspars, as in granitic rocks. The Fe-plagioclase absorption feature can be discerned in reflectance spectra of rock types such as gabbro and norite (Arivazhagan and Anbazhagan, 2011), but the spectra are influenced by the mafic assemblages and display a discernibly broader absorption feature centered closer to 1 μm (Serventi et al., 2013, see also Appendix II Item A). The relatively limited set of circumstances under which Fe-plagioclase is detectable in the VSWIR makes CRISM particularly well-suited for identifying certain feldspathic rocks (see Appendix II Item A for details), including anorthositic and many felsic lithologies.

CRISM mapping data were processed through a custom pipeline (Seelos et al., 2016) that includes photometric and atmospheric corrections (Seelos and Murchie, 2018), and empirical correction for differences between spectra in the cross-track direction known as “spectral smile” (Murchie et al., 2009; Morgan et al., 2011; Seelos et al., 2011; Seelos et al., 2012). The final products of the processing pipeline are 5°x5° mapping tiles with a spatial sampling of 256 pixels per degree. These mapping tiles have improved inter-strip variability in atmospheric residuals compared to previous multispectral map tile products (Seelos et al., 2019).

Spectral parameters were calculated from the multispectral image cubes after the methods of (Viviano-Beck et al., 2014). CRISM spectral parameters were combined into three-band images called browse products. Custom browse product combinations were made for mapping Fe-plagioclase by combining the BD1300, RPEAK1, and LCPINDEX2 spectral parameters (Viviano-Beck et al., 2014) into the R, G, and B channels respectively. BD1300 is sensitive to the 1.25-μm feature of Fe-plagioclase, and RPEAK1, which tracks the wavelength center of peak reflectance between ~0.6 and 1 μm, is useful for distinguishing between plagioclase (high RPEAK1 values) and olivine (low RPEAK1 values). Inserting LCPINDEX2 into the blue channel was useful for aiding in the selection of an appropriate spectrally-neutral denominator spectrum (described below), which must not include a low-Ca pyroxene signature.

This and other CRISM browse product combinations (Viviano-Beck et al., 2014), which included OLINDEX3 and the PFM browse product combination, were imported into ArcGIS Pro for analysis. We used these browse product mosaics to identify areas of interest that plausibly contain Fe-plagioclase, preliminarily distinguish between Fe-plagioclase and olivine, and to identify possible alteration based on visual inspection of the mosaic colors (e.g., yellow is consistent with the presence of Fe-Plagioclase in the BD1300, RPEAK1, LCPINDEX2 composite, Fig. 2.2). A standard deviation stretch, typically of 2 or 3 sigma, was applied to the browse product mosaics for each color band.

To corroborate areas of interest identified within the browse product images, VSWIR spectra were extracted from individual unprojected CRISM mapping strip spectral cubes. Spectral analyses were accomplished using a custom add-on tool for IDL/ENVI and compositions were identified through visual comparison to laboratory and MICA (minerals identified with CRISM analysis, Viviano-Beck et al., 2014) library spectra. Primary igneous minerals were identified based on the presence of broad and diagnostic crystal-field features (Burns, 1993), and secondary alteration minerals were identified based on the presence of narrow hydration and metal-hydroxide bands (Clark and Roush,

1984). Spectra were averaged over areas of interest, typically on the order of 5x5 pixels or larger (Appendix II Table A2.3). Areas of interest were rectangular in unprojected image cubes and thus appear irregularly shaped in the map projected data of Figs. 2.2-2.3 and Appendix II Figs. A2.2-A2.3. Spectra were divided by in-column “denominator spectra”, a common practice for CRISM analysis that reduces column-dependent effects from the CRISM detector and residual atmosphere in the scene. Denominator regions, with the same geometry as the area of interest, were visually selected in IDL/ENVI by interrogating nearby spectra (typically within several to tens of pixels) to locate suitable spectrally neutral regions. Care was taken to avoid pyroxenes, especially low-calcium pyroxene (LCP), in the denominator spectra because the inverse spectrum of pyroxene produces a false 1.25-μm absorption feature in the ratioed spectrum.

In this manner, we extracted CRISM spectra with a diagnostic Fe-plagioclase signature from over 500 areas of interest, resulting in 255 individual Fe-plagioclase outcrops mapped. MSP and HSP scenes from which spectra were extracted for figures in this publication are presented in Appendix II Table A2.2. Once the presence of Fe-plagioclase was confirmed, the locations of the detections were imported into ArcGIS as points used to aid in mapping Fe-plagioclase-bearing outcrops. Mapping was done at a scale of 1:250,000 and interpretations were informed predominantly by the inferred location of Fe-plagioclase from CRISM browse product mapping tiles. Other data products including quantitative thermal inertia (Fergason et al., 2006), high resolution context imagery (Dickson et al., 2018), and geologic maps of the northern Hellas area (Leonard and Tanaka, 2001; Tanaka et al., 2014) were used for later interpretation and analysis.

2.2 Thermal infrared analysis

THEMIS scenes I17073002 and I08749001 were processed after the methods of Bandfield et al. (2004) to atmospherically corrected emissivity multispectral cubes. Emissivity spectra were extracted and averaged, using tools

available in IDL/ENVI, over the same regions of interest from which Fe-plagioclase outcrops were identified in CRISM data. A cubic spline was fit to the emissivity data and minima were calculated over THEMIS bands 3-9 with tools available in MATLAB to find the “cubic spline fit minima” (Ueberhuber, 1997; Rogers and Nekvasil, 2015).

2.1 Visible image analysis

The global CTX map from (Dickson et al., 2018) was imported into ArcGIS for analysis and to facilitate mapping of Fe-plagioclase outcrops. For select locations, HiRISE data were downloaded from hirise.lpl.arizona.edu and imported into ArcGIS to analyze detailed texture, morphology, and character of Fe-plagioclase-bearing outcrops.

3. Results

3.1. VSWIR Detections of Fe-plagioclase

We used CRISM multispectral (MSP, 19 VNIR, 0.4 – 1 μm, channels and 55 SWIR, 1 – 4 μm, channels) and hyperspectral (HSP, 107 VNIR channels and 154 SWIR channels) mapping data that are suited for regional geologic mapping (~180-m ground sampling distance, >85% regional coverage) to identify and map 255 Fe-plagioclase-bearing outcrops in the northern Hellas region (Fig. 2.1). All Fe-plagioclase-bearing outcrops we identified display a diagnostic 1.25-μm absorption feature in their spectra (Figs. 2.2, 2.3), though in some cases spectral features of alteration minerals were identified in the same locations as Fe-plagioclase or nearby (e.g., Appendix II Figs. A2.2, A2.3). Nearly all Fe-plagioclase-bearing outcrops occur within ancient material excavated from depth, either in the rims of large craters or uplifted massifs, within the Nh, Nm, and Nc units of (Fig. 2.1; Leonard and Tanaka, 2001).

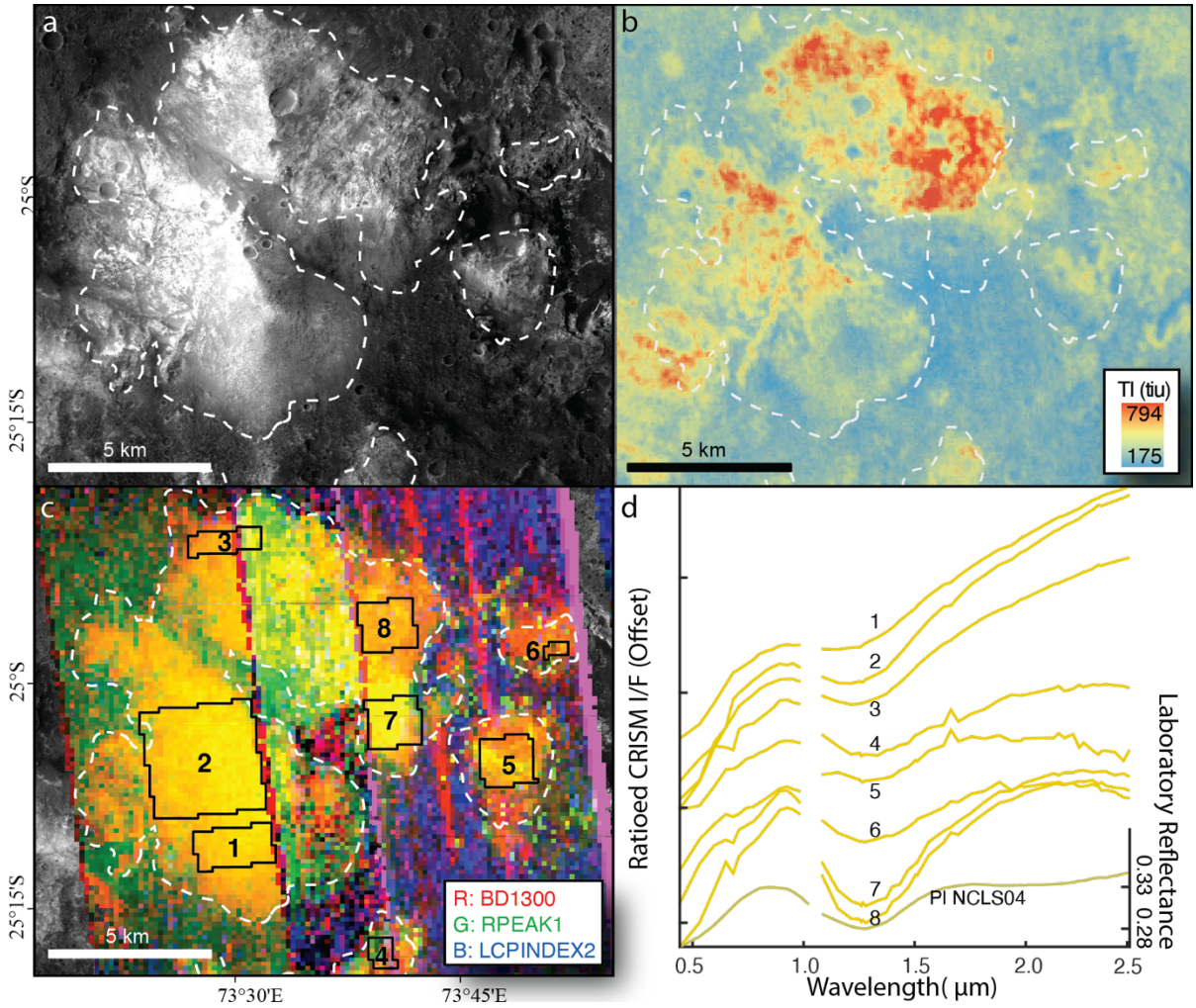

Fig. 2. 2. Fe-plagioclase-bearing massif and associated CRISM spectra. a, Light-toned feldspathic outcrop, outlined in white in panels **a-c,** in a Context Camera mosaic of a Hellas rim massif. **b,** THEMIS thermal inertia (tiu = thermal inertia units) showing relatively high thermal inertia values for the Fe-plagioclase-bearing outcrop. **c,** False-color composite CRISM mosaic with spectral parameters in the RGB channels indicated in the lower right. Yellow tones are consistent with Fe-plagioclase. **d,** CRISM spectra extracted from the 8 regions shown in panel **c** and compared to a laboratory spectrum of plagioclase convolved to CRISM spectral resolution. Ticks are separated by 0.1.

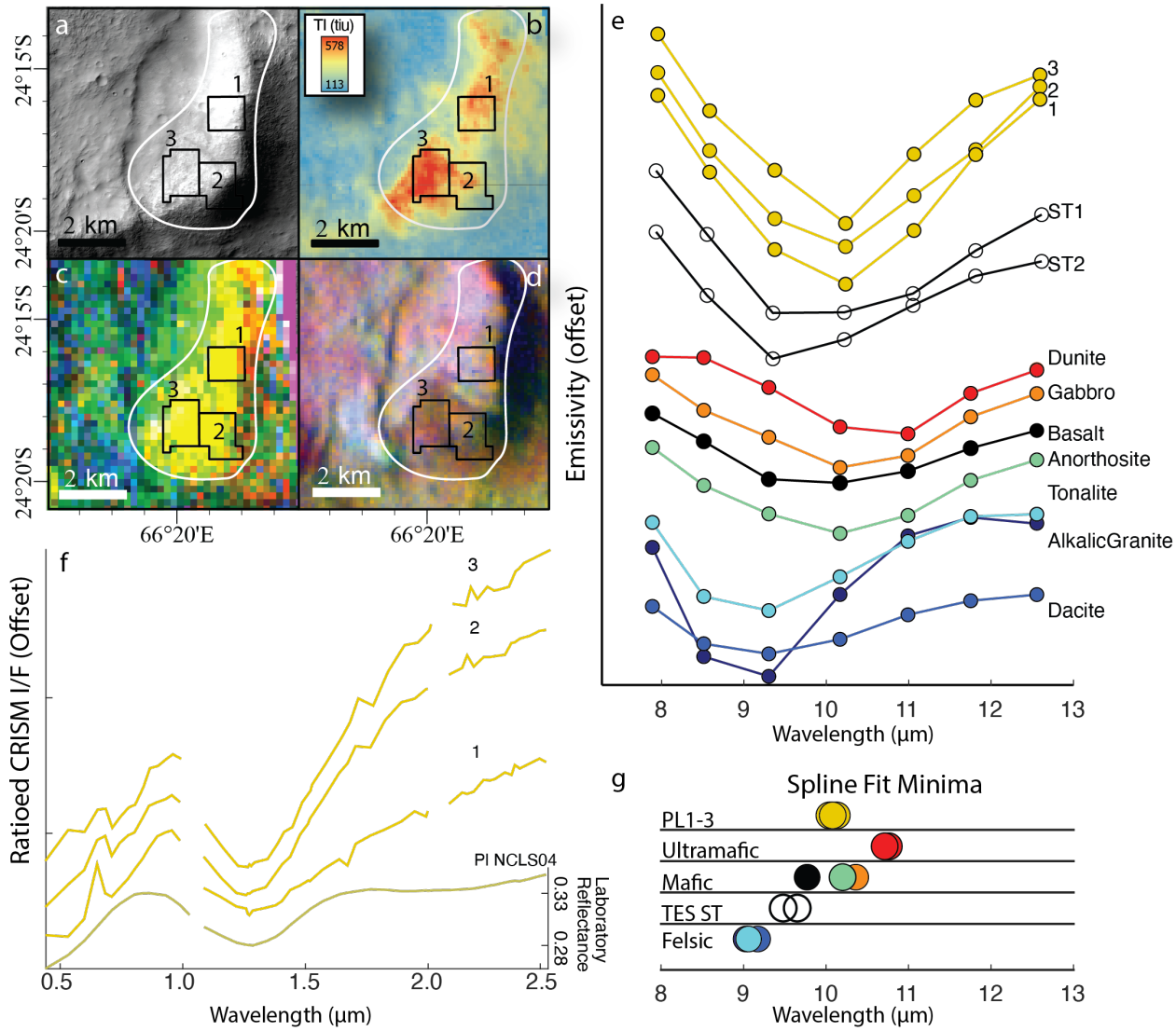

Fig. 2. 3. THEMIS analysis of CRISM-detected feldspathic outcrop. a, CTX mosaic of light-toned feldspathic outcrop in a Hellas-rim massif. **b,** THEMIS thermal inertia (tiu = thermal inertia units) of feldspathic outcrop. **c,** False color composite CRISM mosaic, yellow tones are consistent with Fe-plagioclase. **d,** Decorrelation stretch of THEMIS bands 8, 7, and 5 of THEMIS scene I17073002. In panels **a-d** areas 1-3 indicate locations of extracted CRISM and THEMIS spectra (panels **e** and **f**). **e,** THEMIS spectra compared to TES surface types 1 and 2, martian dust, and lab references[19] convolved to THEMIS band passes. **f,** Ratioed CRISM I/F spectra extracted from areas 1-3 in panels **a-d**. Ticks are separated by 0.1. **g,** cubic spline fit minima of THEMIS spectra, TES surface types, and lab references. Colors match panel **e**. PL1-3 are the SFM of the three Fe-plagioclase areas. SFM standard deviations are contained within the size of the markers.

Fe-plagioclase outcrops span the entire longitudinal extent of the northern Hellas rim (~2200 km) and cluster closer to the basin center with 87% by area of all Fe-plagioclase outcrops located within the 1100-km radius of the Hellas basin (Fig. 2.1). The outcrops are commonly associated with areas of relatively high thermal inertia (Figs. 2.2, 2.3) and appear light-toned and fractured in high resolution visible images (Fig. 2.4). Outcrops with pyroxene- and olivine-dominated CRISM spectral signatures are commonly identified in close proximity to Fe-plagioclase-bearing outcrops (e.g., Appendix II Figs. A2.1-3).

3.2 Thermal infrared analysis

Multispectral thermal infrared spectra from the Thermal Emission Imaging System (THEMIS, Christensen et al., 2004) aboard Mars Odyssey were analyzed (Fig. 2.3 and Appendix II Figs. A2.2, A2.3) to further constrain the composition of several example Fe-plagioclase-bearing outcrops. Silicate minerals produce diagnostic absorption features in the wavelength range to which THEMIS is sensitive (Feely and Christensen, 1999; Christensen et al., 2000). For unaltered silicate rocks, the wavelengths of the emissivity minima are inversely related to the silica content of the rock (Lyon, 1965), such that felsic rocks exhibit emissivity minima at ~9 μm and ultramafic rocks exhibit emissivity minima at ~11 μm (Lyon, 1965; Rogers and Nekvasil, 2015). Anorthositic rocks exhibit minima at ~10.4 μm, close to the minimum expected for mafic compositions such as basalt (Fig. 2.3). Alteration minerals will shift emissivity minima to shorter wavelengths (Bandfield et al., 2004). Therefore, THEMIS emissivity minima are useful for distinguishing felsic from mafic and ultramafic compositions, but THEMIS emissivity minima are, by themselves, insufficient to distinguish anorthositic from basaltic compositions.

We fit a cubic spline to THEMIS multispectral data extracted from high thermal inertia regions that displayed an Fe-plagioclase signature without evidence for alteration and calculated the spline fit minima (SFM, Ueberhuber, 1997) to assess the silica content of the outcrops (Fig. 2.3). These SFM values

are consistent with either basaltic or anorthositic compositions, but not granitic compositions. Additionally, the shapes of THEMIS spectra from Fe-plagioclase outcrops are more consistent with anorthositic spectral shapes than basaltic. Whereas basaltic spectra display a broader “U”-shaped feature, anorthositic spectra exhibit a more peaked “V”-shaped absorption feature (Fig. 2.3).

Outcrops that display low-Ca pyroxene and olivine CRISM spectral signatures in close spatial proximity to Fe-plagioclase outcrops were also analyzed for comparison (Appendix II Figs. A2.2, A2.3). In the absence of alteration, these areas exhibit SFM at longer wavelengths, consistent with ultramafic lithologies such as pyroxenite, harzburgite, dunite, or picrite. THEMIS SFM are at shorter wavelengths in locations where outcrops of Fe-plagioclase and mafic minerals are in close association with alteration minerals, likely due to spectral mixing with the alteration minerals (Appendix II Figs. A2.2, A2.3).

3.3 Morphologic characterization

In addition to data from CRISM and THEMIS, we assessed the character of Fe-plagioclase-bearing outcrops with high-resolution image data from the Context Camera (CTX, Malin et al., 2007) and the High-Resolution Imaging Science Experiment (HiRISE, McEwen et al., 2007). Outcrops with an Fe-plagioclase CRISM signature are light-toned compared to their surroundings and smooth, coherent faces of bare rock are discernable (Fig. 2.4). Fracture and jointing patterns are observed on massifs, commonly at angles of approximately 90° or 60°/120° (Fig. 2.4). Distinct contacts between light-toned and dark-tone materials are common in Noachian massifs that display an Fe-plagioclase signature in CRISM. In HiRISE images, both layered and massive textures are observed, but characteristics indicative of basaltic flows, such as columnar jointing, are not observed.

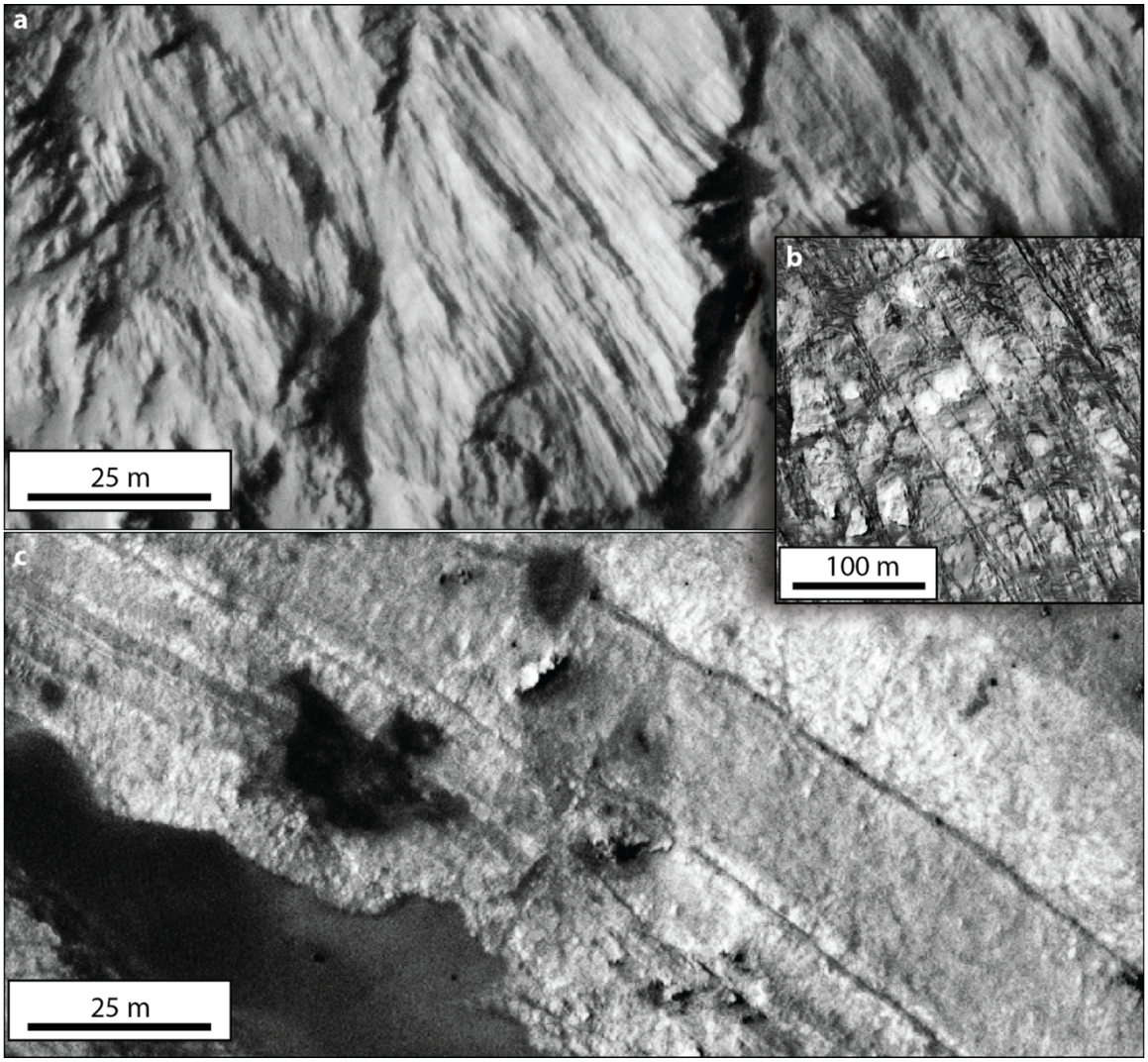

Fig. 2. 4. HiRISE images of CRISM-detected feldspathic outcrops. a, HiRISE image ESP_011683_1540 showing massive texture and light-toned nature of Fe-plagioclase-bearing outcrop on a northern Hellas massif. Location indicated in Fig. 1. **b,** Fe-plagioclase-bearing massif with jointing at ~90° angles (HiRISE scene ESP_037502_1540, location indicated in Appendix II Fig. A2.1). **c,** HiRISE image ESP_011683_1540 showing dark- and light-toned layers in a feldspathic outcrop on a Noachian massif. Location indicated in Fig 2.1.

4. Discussion

4.1 Possible lithology and petrogenesis

Based on the unique 1.25-μm CRISM spectral signatures of Fe-plagioclase, the THEMIS spectral shapes and SFM wavelength locations, and the character of Fe-plagioclase-bearing outcrops in high-resolution images, we conclude that these outcrops are feldspathic and are more likely anorthositic than either felsic or basaltic. The term feldspathic (Frost and Frost, 2008) is conservative because it includes most leucocratic compositions (expect those in which quartz dominates over feldspar), but it excludes most martian basaltic compositions because in those, pyroxenes typically dominate over plagioclase (Papike et al., 2009). We do not favor a felsic (i.e., SiO_2 > 65%) interpretation for the Fe-plagioclase-bearing outcrops because the characteristics of their THEMIS spectra, including the SFM wavelength positions, are not consistent with felsic rocks. We also do not favor basaltic interpretations for Fe-plagioclase-bearing outcrops because the CRISM spectra are more consistent with a composition dominated by plagioclase (>85 vol. %, Serventi et al., 2013) than one with moderate plagioclase abundances (between 50 and 85 vol. %) in a mafic ground mass. It should be noted that “feldspar-phyric basalt” and “porphyritic dolerite”, rocks with megacrystic (>~10 cm) plagioclase grains at modal abundances as high as ~80% (Ashwal, 1993), could plausibly yield the diagnostic 1.25-μm spectral feature diagnostic of Fe-plagioclase (Rogers and Nekvasil, 2015); however, the light-toned appearance and morphologic character of the outcrops in high resolution images are not consistent with basaltic compositions such as these. Remaining feldspathic lithologies consistent with the evidence are anorthositic. Such rocks are light-toned and include leucogabbros, leuconorites, and troctolites with plagioclase modal abundances > 85% and all anorthosites. We prefer an anorthositic interpretation for the Fe-plagioclase-bearing outcrops because these lithologies explain, with the fewest caveats, the pure 1.25-μm CRISM spectral feature, the THEMIS SFM wavelength positions, and the light-toned nature of the outcrops in high-resolution images.

We infer from the widespread longitudinal distribution and similarity between outcrops in spectral and morphologic character across more than 2,000 km in the northern Hellas region, that the 255 anorthositic outcrops represent what was once a laterally-coherent layered igneous complex or many smaller, cogenetic complexes that coalesced over time. Their association with uplifted material in the Nm, Nh, and Nc units suggests the anorthositic outcrops are a window into the deep southern highlands crust and are, perhaps, primary or early secondary crust.

Our detections support inferences made from geodynamic data for a pervasive, subsurface low-density component to the martian crust (Baratoux et al., 2014; Wieczorek et al., 2021), and further suggest that this component may be anorthositic. The sheer extent of the anorthositic exposures implies a massive volume of magma formed the igneous complex. The common association of anorthositic outcrops with pyroxene- and olivine-dominated compositions across a 6-km range of elevation (measured using global High Resolution Stereo Camera and Mars Orbiter Laser Altimeter blended topography, Fergason et al., 2017) and an ~2,200-km lateral extent implies an igneous complex with multiple anorthositic layers interleaved by mafic/ultramafic lithologies. Plausible petrogenetic environments include a lava lake at the surface, a hypabyssal batholith, or several smaller plutons that coalesced into a larger intrusive complex over time.

On the Earth, anorthositic rocks have formed by several mechanisms. Archean (calcic) anorthosites (~2.7-3.7 Ga, $An_{\#} \approx 85\pm5$) appear to have been emplaced in the shallow crust as sills and dikes into gabbroic/basaltic compositions (Ashwal, 1993). Proterozoic (1.1 to 1.6 Ga, $An_{\#} \approx 50\pm10$) “massif-type” anorthosites are the most voluminous of the terrestrial anorthosites and formed locally (1000s of km^2) as plutonic complexes associated with K-rich monzonitic and granitic rocks and, notably, in the absence of mafic/ultramafic rocks (Ashwal, 1993). Anorthosites also form in extensional tectonic settings on Earth through fractional crystallization in layered igneous intrusive complexes

along with pyroxenites, troctolites, and gabbro/norites (Namur et al., 2011) and, at smaller spatial scales, as sills and dikes associated with ocean ridge spreading centers (Ashwal, 1993). Anorthosite layers in layered igneous complexes can reach significant thicknesses. For example, the Mineral Lake intrusion in Wisconsin contains an anorthosite layer over 2 km thick (Ashwal, 1993) and the Stillwater Complex in Wyoming contains “megalayers” of anorthosite several hundreds of meters thick (McCallum, 1980). At even larger scales, anorthosite formed globally on the Moon through either serial magmatism (Longhi, 2003; Borg et al., 2011) or floatation atop a lunar magma ocean (Wood et al., 1970).

The extent and association with mafic/ultramafic lithologies of the northern Hellas anorthositic outcrops are consistent with formation through fractional crystallization processes within an extensive magma body. Additional inferences can be made about the magma from which the plagioclase crystalized based on the presence of ferrous iron in its crystal structure, required to make the mineral detectable with CRISM. Ferrous iron substitution into plagioclase is favored for a magma with low pressure, relatively high silica-content, high FeO/Al_2O_3 ratio, low water-content, low *f*O2, and that cooled relatively rapidly from high temperature (Wenk and Wilde, 1973; Longhi et al., 1976; Smith and Brown, 1988; Lundgaard and Tegner, 2004) (see Appendix II Item B for more details). Such conditions are reasonable to expect for melts produced by decompression melting following cumulate overturn of the early martian mantle (Elkins-Tanton et al., 2005). The combination of the crystal chemistry of the feldspathic outcrops, their extent, spatial association with mafic/ultramafic compositions, and pre-Noachian age is consistent with formation in a fractionally crystalizing magmatic body, such as a lava lake, hypabyssal intrusion, or multiple, cogenetic intrusions.

An anorthositic floatation crust atop a magma ocean, as proposed for the Moon, has been deemed unlikely for Mars based on geochemical models (Elkins-Tanton et al., 2005) and is not supported by the observed stratigraphic layering of feldspathic and mafic/ultramafic lithologies (e.g., Appendix II Fig.

A2.1). We propose that anorthositic compositions formed along with a suite of other lithologies, including orthopyroxenite, harzburgite, and dunite, through extensive fractional crystallization in a single large, or several coalescing, layered igneous complex(es) in the pre-Noachian. A plausible source for the magma is the voluminous melt generated by depressurization following density-driven overturn of the cumulate magma ocean (Elkins-Tanton et al., 2003). Cumulate mantle overturn of the martian magma ocean is predicted to produce two distinct melt chemistries based on the depth from which the melts were derived (Elkins-Tanton et al., 2005). Interestingly, one melt composition is expected to have had an alumina content near zero and would have been incapable of crystalizing plagioclase, whereas the other composition is expected to have been higher in both alumina and silica and could have crystalized Fe-plagioclase (Elkins-Tanton et al., 2005). The lateral distribution on the surface of the two mantle overturn-sourced melts depends on the geometry of the overturn event (Elkins-Tanton et al., 2005). Our work indicates that alumina-rich post-overturn melting rose to form crustal rocks in the northern Hellas region over an area approximately 600 by 2,000 km.

Investigations of other pre-Noachian outcrops exposed in massifs surrounding the Argyre and Isidis impact basins will reveal whether anorthositic compositions in layered igneous complexes are more widespread or whether they are local to the northern Hellas region. Existence of anorthositic outcrops across the southern hemisphere would support the idea that cumulate mantle overturn had a degree-1 geometry (Elkins-Tanton et al., 2005) aligned with the crustal dichotomy and plausibly played a role in the dichotomy formation via hemispherically asymmetric crustal thickening/thinning (Zhong and Zuber, 2001). Conversely, the absence of anorthositic outcrops in pre-Noachian crust at Argyre and Isidis may suggest that the geometry of the martian mantle overturn event was of higher degree (Scheinberg et al., 2014), implying that the leading hypothesis for the formation of the martian crustal dichotomy, a massive north

polar impact (Andrews-Hanna et al., 2008; Marinova et al., 2008), may be the more likely cause.

Because direct sampling of primary crust on Venus and Earth is not possible, the primary crust of Mars may be the best analog we have in the solar system to learn about primary crust formation that results from post-magma ocean overturn melting. Our results indicate that large bodies of magma, produced by depressurization following cumulate mantle overturn, may differentiate at or near the surface and crystallize into primary crust that resembles layered igneous complexes.

Appendix II

Item A: Detecting feldspar in the VSWIR

Although feldspars are typically considered featureless in the VSWIR spectral region, this is not always the case. Feldspars exhibit a crystal field absorption centered around 1.25 μm when minor amounts (> ~0.05 wt%) of Fe^{2+} substitute into the crystal structure (Adams and Filice, 1967; Adams et al., 1973; Adams and Goullaud, 1978). It has been shown by Bell and Mao (1973) that the strength of the 1.25-μm absorption feature of plagioclase is positively correlated with the plagioclase Fe^{2+} content. Because the literature is conflicted concerning to the precise mechanism responsible for Fe^{2+} substitution into plagioclase and the effects of plagioclase $An_{\#}$ (100xCa/[Ca+Na+K]) on the strength of the 1.25-μm absorption feature, further discussion of these topics is warranted.

The ideal formula of plagioclase can be written: MT_4O_8 (Tschermak, 1864). In this formulation, "M" refers to alkali and alkaline-earth metal cations (e.g., Na^+, K^+, Rb^+, Ca^{2+}) with low charges that are situated in relatively large sites in octahedral coordination in the crystal structure. The "T" refers to relatively small tetrahedrally coordinated sites filled by higher-charge cations with smaller ionic radii, typically Al^{3+} and Si^{4+}. The O refers to oxygens bound to the tetrahedrally coordinated cations. It has been suggested that Fe^{2+} may occupy M-sites by substituting for Ca^{2+} (Appleman et al., 1971; Hafner et al., 1971; Hofmeister and Rossman, 1984). However, other studies have shown that ~90% of Fe^{2+} occupies T-sites via the double substitution $Fe^{2+} + Si^{4+} \rightleftarrows 2Al^{3+}$ (Longhi et al., 1976; Adams and Goullaud, 1978; Lundgaard and Tegner, 2004), which forms a solid solution series between $Ca(Fe,Mg)Si_3O_8$ and $CaAl_2Si_2O_8$ (Wenk and Wilde, 1973; Bryan, 1974; Longhi et al., 1976; Sclar and Kastelic, 1979; Smith and Brown, 1988; Dyar et al., 2006). Conversely, Fe^{3+} strictly substitutes for Al^{3+} in T-coordinated sites (Smith and Brown, 1988; Lundgaard and Tegner, 2004). Fe^{2+} in either the M- or T-site will produce the crystal field abortion associated with plagioclase (Burns, 1993), but T-coordinated Fe^{2+} yields an absorption feature 2 orders of magnitude stronger than M-coordinated Fe^{2+} (Hapke, 2012). Because

the two substitution mechanisms for Fe^{2+} into feldspar are Fe^{2+} + Si^{4+} for $2Al^{3+}$ and, more rarely, Fe^{2+} for Ca^{2+}, ferrous iron does not substitute into the crystal structure of alkali feldspars, only plagioclase feldspars (Smith and Brown, 1988). However, a 1.25-μm absorption feature can be observed in alkali feldspars if there are plagioclase impurities contained within the alkali feldspar (Kokaly et al., 2017).

The literature describing the effect of plagioclase $An_{\#}$ on its 1.25-μm absorption feature is conflicted. The number of T-coordinated aluminum sites in plagioclase increases 2-fold from albite ($NaAlSi_3O_8$) to anorthite ($CaAl_2Si_2O_8$). As such, the number of sites available for the double substitution of Fe^{2+} + Si^{4+} ⇄ $2Al^{3+}$ also doubles from albite to anorthite. It might then be expected that the partition coefficient of Fe^{2+} increases with increasing plagioclase $An_{\#}$ and that the strength of the 1.25-μm absorption would also correlate positively with plagioclase $An_{\#}$. However, a positive correlation between plagioclase $An_{\#}$ and Fe^{2+} partition coefficient is not observed (Lundgaard and Tegner, 2004). Instead, the partition coefficient of Fe^{2+} seems to be independent of plagioclase $An_{\#}$ for $An_{\#}$>35 (Lundgaard and Tegner, 2004). Nevertheless, a positive correlation between the $An_{\#}$ of plagioclase and the strength of the 1.25-μm absorption feature has been observed(Adams and Goullaud, 1978; Serventi et al., 2013; Serventi et al., 2015), implying a positive correlation between $An_{\#}$ and Fe^{2+}-content, but these correlations were based on small sample sizes. It is our interpretation that some properties of the magma that correlate positively with $An_{\#}$, such as melt temperature, also correlate positively with the partition coefficient of Fe^{Tot} into plagioclase. Therefore, while higher $An_{\#}$ may commonly be associated with higher plagioclase Fe-content, the relationship is not likely causal. It seems that $An_{\#}$ only correlates with the plagioclase 1.25-μm absorption feature inasmuch as factors of the melt that increase $An_{\#}$ also increase Fe^{2+} partitioning and retention in the plagioclase crystal structure. Because this correlation is unreliable, it is difficult to make an assessment of plagioclase $An_{\#}$ based on its 1.25-μm feature or vice versa.

The amount of Fe^{2+} in plagioclase is not the only factor that controls the observed strength of the 1.25-μm absorption feature. The absorption feature is easily obfuscated if plagioclase is intimately mixed with mafic minerals(Crown and Pieters, 1987; Serventi et al., 2013). If the mafic mineral and plagioclase grain sizes are similar, then plagioclase volumetric abundances >85% are necessary for the 1.25-μm absorption feature to be detectable(Cheek et al., 2013; Serventi et al., 2013; Carli et al., 2014a; Carli et al., 2014b; Serventi et al., 2015). Such high plagioclase abundances are essentially synonymous with an anorthositic lithology (by definition, anorthosite is > 90% plagioclase).

There is some spectral evidence that plagioclase could be detected at lower modal abundances (as low as 50%) if the grain size is large (≥ ~840 μm) compared to an aphanitic pyroxene groundmass(Arivazhagan and Anbazhagan, 2011; Rogers and Nekvasil, 2015). In this case, pyroxene-bearing basalt and andesite with plagioclase phenocrysts could yield a reflectance spectrum that has a 1.25-μm absorption feature due to plagioclase. However, the whole-rock spectrum depends on the mineralogy and relative grain size of the surrounding groundmass and commonly appears as a mixture of mafic minerals and plagioclase, and the plagioclase feature typically appears weak in comparison to the mafic minerals (Arivazhagan and Anbazhagan, 2011; Cheek et al., 2013; Serventi et al., 2013; Carli et al., 2014a; Serventi et al., 2015). Similar spectral mixtures are produced by troctolites, gabbros, and norites (Pieters, 1986; Arivazhagan and Anbazhagan, 2011; Nair and Mathew, 2014).

An Fe-plagioclase spectrum can also be observed in felsic rocks in which minerals other than plagioclase (e.g., quartz, alkali feldspars) are featureless in the VSWIR (Kerr et al., 2011; Metelka et al., 2015). Examples of felsic lithologies include granite and monzonite and their volcanic equivalents, as well as the so-called TTGs – tonalite, trondhjemite, and granodiorite. On Earth, these rock types commonly display spectral absorption features of minerals produced by aqueous alteration of the primary igneous minerals at approximately 1.4 μm, 1.9 μm, and

between 2.2 and 2.4 μm; such spectral features due to aqueous alteration are not necessarily expected for similar rock types on Mars.

Therefore, a wide variety of lithologies can yield a VSWIR spectrum with the 1.25-μm Fe-plagioclase feature, but only anorthositic and felsic lithologies are likely to produce a clear and diagnostic Fe-plagioclase signature, such as those presented in this study.

Item B: Constraints on plagioclase petrogenesis given its detectability in the VSWIR

Because Fe^{2+} is necessary to produce the VSWIR absorption feature in plagioclase and because more Fe^{2+} yields stronger absorptions, here we address the magmatic conditions favorable to Fe^{2+} substitution into plagioclase. It should be noted that the discussion below outlines general trends favorable to Fe^{2+} substitution into plagioclase and that no single condition should be interpreted as necessary.

Several properties of the melt, including the cooling rate, pressure, composition (silica, alumina, ferrous iron, and water contents), and oxygen fugacity (fO_2) effect the partition coefficient of Fe^{2+} into plagioclase (Longhi et al., 1976; Lundgaard and Tegner, 2004). At slower cooling rates plagioclase is able to exclude Fe^{2+} from its crystal structure (Longhi et al., 1976). Slower cooling rates occur in plutonic settings, as opposed to hypabyssal and volcanic settings where melts crystalize more rapidly and the retention of Fe^{2+} in the plagioclase crystal structure is more easily achieved (Longhi et al., 1976). Conversely, a faster cooling rate allows for more impurities to be retained in the crystal structure and is conducive to retaining Fe^{2+} in plagioclase (Wenk and Wilde, 1973; Longhi et al., 1976). A similar effect is observed with pressure; at high pressures, impurities are more easily exsolved from plagioclase than at low pressures, and thus low crystallization pressures are favorable to the retention of Fe^{2+} in plagioclase (Lundgaard and Tegner, 2004).

The activity of Fe^{Tot} in the melt increases with increasing melt polymerization (i.e., with increasing silica content), and the partition coefficient of Fe^{2+} into plagioclase consequently increases with increasing silica content (Lundgaard and Tegner, 2004). Because Fe^{2+} primarily substitutes for Al, a high ratio of Fe^{2+}/Al is also conducive to Fe^{2+} substitution into the plagioclase crystal structure (Wenk and Wilde, 1973; Lundgaard and Tegner, 2004). Increasing the water content of the melt accelerates diffusion of ions between melt and crystals, which has the effect of decreasing the Fe content in plagioclase (Smith and Brown, 1988). Of course, for Fe^{2+} to substitute into the crystal structure of plagioclase, divalent Fe must be present in the melt, which means the fO_2 must be low (Ashwal et al., 1983).

To summarize, a melt optimal for Fe^{2+} substitution into plagioclase would be a high temperature melt that ascends relatively rapidly to a low-pressure environment (hypabyssal or on the surface), with relatively high silica-content, high FeO/Al_2O_3 ratio, low water-content, and low fO_2. These conditions were nearly perfectly met on the Moon during the formation of the ferroan anorthosite crust (FAN), and as such Fe-plagioclase is observed in VSWIR spectra across the lunar highlands (Pieters, 1986).

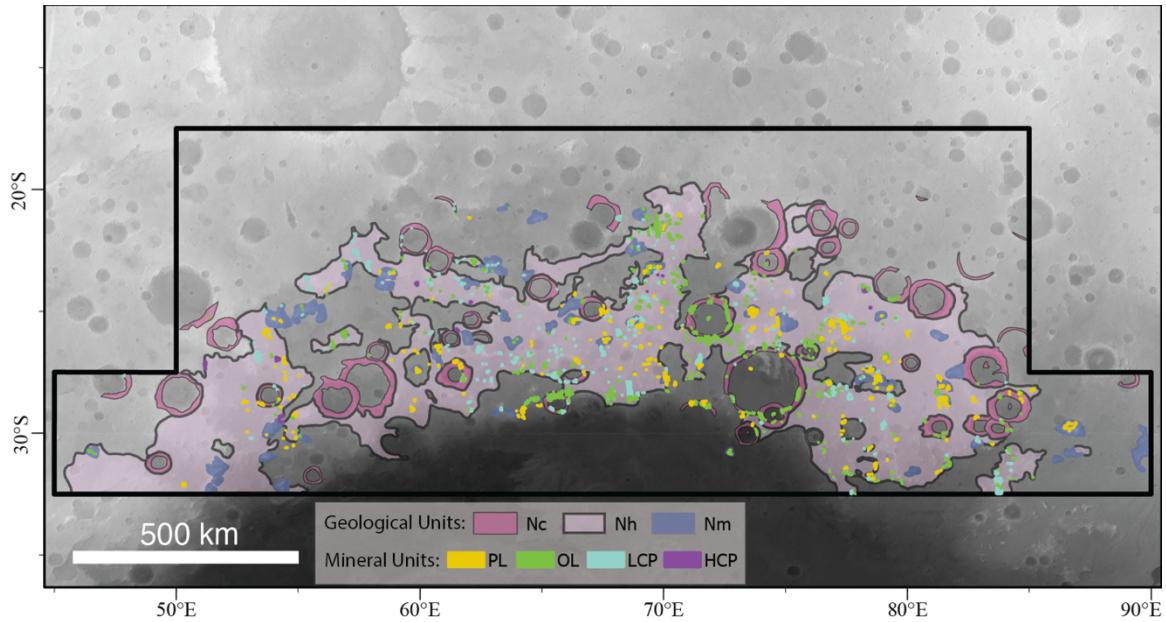

Fig. A2. 1. CRISM-identified outcrops of primary igneous minerals. PL = Fe-plagioclase, OL = olivine, LCP = low-Ca pyroxene, HCP = high-Ca pyroxene; Nc = Noachian crater, Nh = Noachian hilly, and Nm = Noachian massif units (see Leonard and Tanaka (2001) of the main text).

Fig. A2. 2. THEMIS analysis of CRISM-detected feldspathic outcrop and associated low-Ca pyroxene. **a,** CTX mosaic overlaid by THEMIS thermal inertia of feldspathic outcrops (Pl1-3) on a northern Hellas massif and associated with ejecta from an nearby impact, as well as a low-Ca pyroxene (LCP) outcrop and an area containing alteration minerals (Altn). **b,** Decorrelation stretch of THEMIS bands 8, 7, and 5 of THEMIS scene I08749001. **c,** CRISM browse product mapping tile, yellow tones consistent with Fe-plagioclase, blue tones consistent with low-Ca pyroxene. Note the white areas of interest that indicate locations from which CRISM and THEMIS spectra were extracted for panels **d** and **e**. **d,** CRISM spectra over the areas shown in in panels **a-d**. Note the subtle 1.9-μm band present in Pl3 and to a lesser degree in Pl2. Ticks are separated by 0.1. **e,** THEMIS spectra extracted from regions shown in panels **a-d** and compared to TES surface types 1 and 2 and lab references from Rogers and Nekvasil (2015). Note how the character of spectra Pl1-3 change with increasing alteration. **f,** cubic spline fit minima of THEMIS spectra, TES surface types, and lab references. Marker colors correspond to panel **e**. SFM standard deviations are contained within the size of the markers.

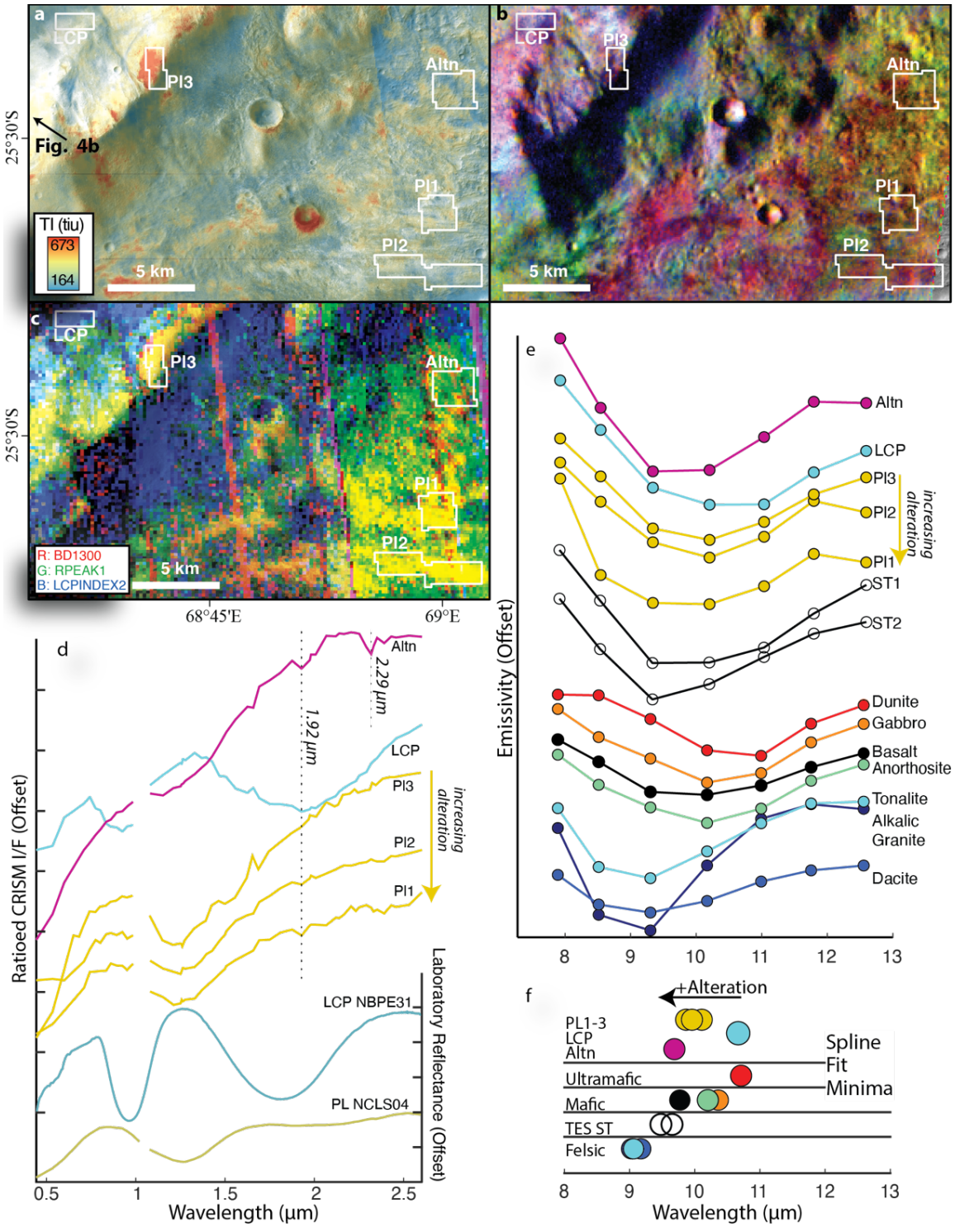
a
LCP
PI3
Altn
PI1
PI2
Fig. 4b
TI (tiu)
673
164
5 km
25°30'S
b
LCP
PI3
Altn
PI1
PI2
5 km
c
LCP
PI3
Altn
PI1
PI2
R: BD1300
G: RPEAK1
B: LCPINDEX2
5 km
25°30'S
68°45'E
69°E
d
Altn
2.29 μm
1.92 μm
LCP
PI3
PI2
PI1
increasing alteration
Ratioed CRISM I/F (Offset)
LCP NBPE31
PL NCLS04
Laboratory Reflectance (Offset)
0.5
1
1.5
2
2.5
Wavelength (μm)
e
Altn
LCP
PI3
PI2
PI1
increasing alteration
ST1
ST2
Dunite
Gabbro
Basalt
Anorthosite
Tonalite
Alkalic
Granite
Dacite
Emissivity (Offset)
8
9
10
11
12
13
f
+Alteration
PL1-3
LCP
Altn
Ultramafic
Mafic
TES ST
Felsic
Spline
Fit
Minima
8
9
10
11
12
13
Wavelength (μm)

Fig. A2. 3. THEMIS analysis of CRISM-detected feldspathic outcrop and associated olivine. **a,** CTX mosaic overlaid by THEMIS thermal inertia of feldspathic (Pl1-2), olivine-bearing (Ol1-4), and alteration mineral-bearing (Altn) outcrops on a northern Hellas massif. The white areas of interest in panels a-d indicate areas from which CRISM and THEMIS spectra were extracted for panels **e-f**. **b,** Decorrelation stretch of THEMIS bands 8, 7, and 5 of THEMIS scene I08749001.**c,** CRISM browse product mapping tile, yellow tones consistent with Fe-plagioclase, red tones consistent with olivine. **d,** CRISM browse product mapping tile, cyan tones consistent with alteration minerals Fe/Mg smectite. **e,** CRISM spectra over the areas shown in in panels **a-d**. Note the subtle 1.9-μm band present in Pl1. Ticks are separated by 0.1. **f,** THEMIS spectra extracted from regions shown in panels **a-d** and compared to TES surface types 1 and 2 and lab references from Roger and Nekvasil (2015). **g,** cubic spline fit minima of THEMIS spectra, TES surface types, and lab references. Marker colors correspond to panel **e**. SFM standard deviations are contained within the size of the markers.

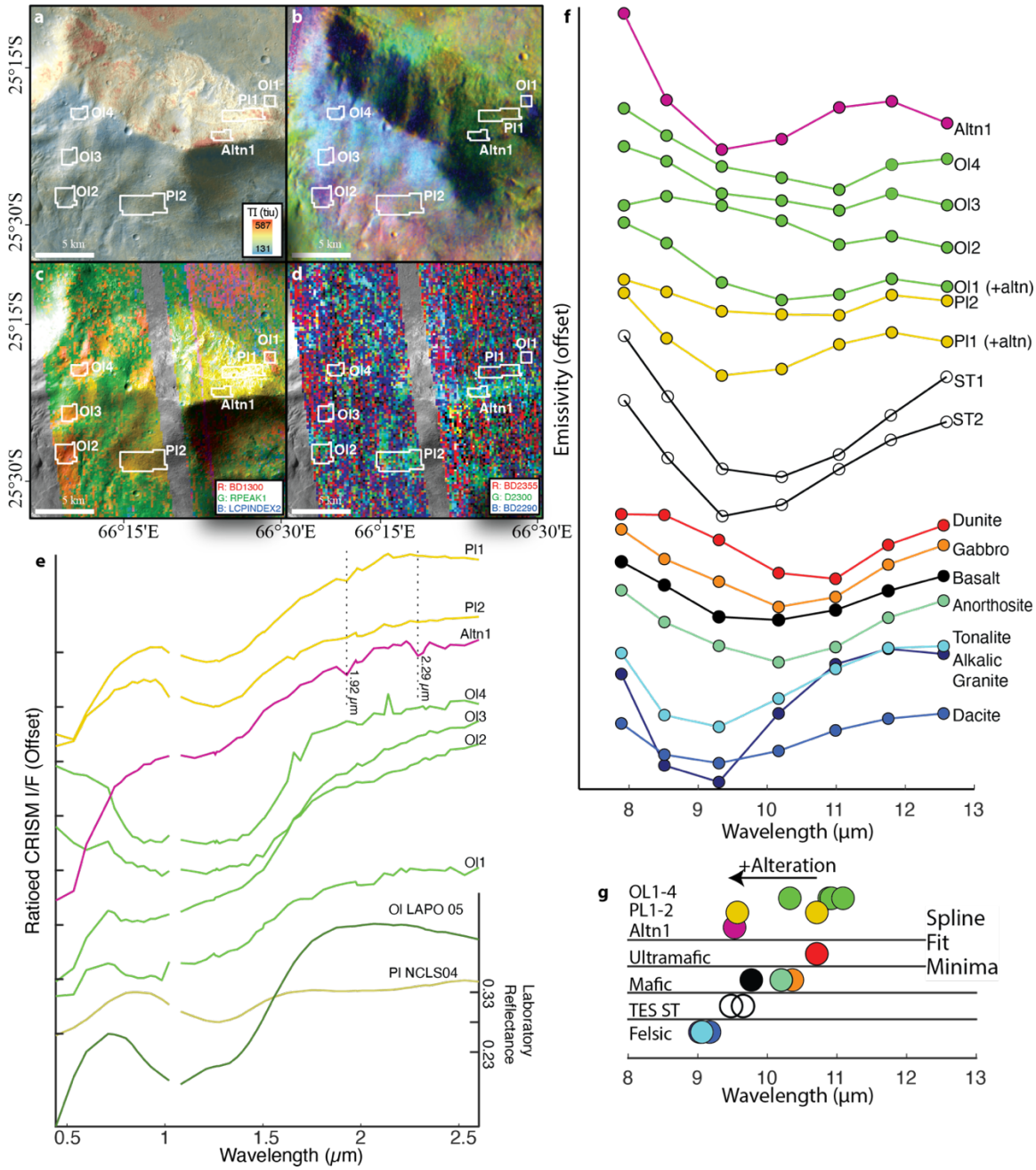
a
b
c
d
e
f
g
Ol1
Pl1
Ol4
Altn1
Ol3
Ol2
Pl2
TI (tiu)
587
131
5 km
25°15'S
25°30'S
66°15'E
66°30'E
R: BD1300
G: RPEAK1
B: LCPINDEX2
R: BD2355
G: D2300
B: BD2290
Emissivity (offset)
Altn1
Ol4
Ol3
Ol2
Ol1 (+altn)
Pl2
Pl1 (+altn)
ST1
ST2
Dunite
Gabbro
Basalt
Anorthosite
Tonalite
Alkalic
Granite
Dacite
8
9
10
11
12
13
Wavelength (µm)
Ratioed CRISM I/F (Offset)
1.92 µm
2.29 µm
Ol LAPO 05
Pl NCLS04
Laboratory Reflectance
0.33
0.23
0.5
1
1.5
2
2.5
Wavelength (µm)
+Alteration
OL1-4
PL1-2
Altn1
Ultramafic
Mafic
TES ST
Felsic
Spline
Fit
Minima

Table A2. 1. CRISM targeted IDs for all previously published detections of Fe-plagioclase on Mars. See Fig. 2.1.

CRISM targeted observations of published feldsaphtic detections		
Region	ID	Lat, Lon
Noachis Terra	FRT00008F08	-21.56 N, 42.10 E
	FRT00009E61	-23.5 N, 44.1 E
Nili Patera	FRT000082EE	8.86 N, 67.28 E
Xanthe Terra	HRL0000927F	2.7 N, 308.3 E
	HRL0000985E	2.81 N, 308.26 E
Valles Marineris	FRT0000B8E2	-14.3 N, 304.4 E
Holden Crater	FRT000064B3	-27.0 N, -34.2E
Tyrrhena Terra	HRL0000B5F9	-16.3N, 63.0E
	FRT0000A26B	-16.5N, 64.7E
	FRT000092B4	-25.3N, 66.2E
	HRS0000C6A0	
	FRT00013005	-24.6N, 66.6E
	FRT00007D60	-28.9N, 79.4E
	FRT00018294	-29.7N, 86.8E

Table A2. 2. CRISM mapping data IDs from which spectra were derived for figures in this publication.

Figure	Area	CRISM ID
2	1–3	MSP0000472E_05
2	4–8	MSP00028F00_01
3	1	MSP0000BCDF_01
3	2	MSP00003E9C_01
3	3	MSP00023629_01
Supp.1	Altn1	MSP000031A6_01
Supp.1	PL1–2	MSP00003874_03
Supp.1	LCP	MSP000150A6_01
Supp.1	Pl3	MSP00028EB5_01
Supp.2	Ol2–4, Pl2	MSP00005B5E_01
Supp.2	Pl1, Altn, Ol1	MSP00003E9C_01

CHAPTER III
ESTABLISHING THRESHOLDS OF IDENTIFICATION FOR PLANETARY FEATURES USING FULLY CONVOLUTIONAL NEURAL NETWORKS: APPLICATION TO HABITATS IN A MARS-ANALOG LANDSCAPE

A version of this chapter will be submitted for publication to the journal *Astrobiology* by Michael S. Phillips, Jeffrey E. Moersch, Nathalie A. Cabrol, Alberto Candela, David Wettergreen, Kimberly Warren-Rhodes, Nancy W. Hinman, and the SETI Institute NAI Team.

Phillips, M.S., et al., “Establishing thresholds of identification for planetary features using deep learning: Application to habitats in a Mars-analog landscape” *submitted*.

This chapter has been revised, according to committee feedback, to include a more general introduction that broadens the relevance of the chapter as well as more detailed results and discussion sections and additional figures in the results to add clarity.

Abstract

The goals of Mars exploration are evolving from describing environments and habitability at global to regional scales to targeting specific locations for biosignature-detection analyses, sample return, and eventual human exploration (Cabrol, 2018; Jakosky et al., 2020). Scientific goals with higher specificity require parallel developments in our ability to confidently identify high-priority, rover-explorable targets from orbit. Here, as part of a larger effort entitled *Changing Planetary Environments and the Fingerprints of Life,* we establish a template for determining the confidence with which planetary features can be identified in images as a function of image spatial resolution. We apply our method to the identification of habitats in the Mars-analog, salt-covered basin, Salar de Pajonales, but the basic principles could be applied to planetary analogs more generally. We found that in images with spatial resolutions comparable to images from the High Resolution Imaging Science Experiment in orbit around Mars, the PolygonRidge habitat class could be identified with 74% to 80% confidence, the Patterned Ground habitat class could be identified with 60% to 65% confidence, and the Dome habitat class could only be identified with 47% to 55% confidence. If PolygonRidge habitats like those at Salar de Pajonales were to be identified on Mars with 85% confidence, our results indicate an imaging system capable of resolving objects on the ground 50 cm or smaller would be necessary. The methodology presented herein provides a template for

establishing thresholds of identification for habitats across Mars-analog environments, which would facilitate in the decision-making process for which habitats should be sought on Mars and the confidence with which they could be identified.

1 Introduction

In this study, we apply fully convolutional neural networks (described in Section 2.1) to the classification of Mars-analog terrain to understand the spatial resolutions necessary to identify high-priority, astrobiology targets. This work is part of a larger effort entitled *Changing Planetary Environments and the Fingerprints of Life*, funded through the NASA Astrobiology Institute (NAI), to understand the types of rocks and outcrops on Mars that are most likely to harbor signs of past or extant life, as well as where and how to search for these rocks (Cabrol, 2018; Warren-Rhodes et al., in review).

In support of this effort, a study was conducted at Salar de Pajonales (SdP), Chile, a Mars-analog, salt-encrusted playa in the Altiplano Puna plateau of South America (Section 2.4). Other manuscripts that have resulted from this effort aim to describe the geology and geomorphology of SdP (Hinman et al., in prep.) and to understand the microbial ecology at SdP (Warren-Rhodes et al., in review) with implications for the search for life on Mars. This work complements that of Hinman et al. (in prep.) and Warren-Rhodes et al. (in review) by linking these primarily ground-based studies to datasets with spatial resolutions attainable through a Mars-helicopter (Farley et al., 2020), and through orbit-based cameras, such as the High-Resolution Imaging Science Experiment (HiRISE, McEwen et al., 2007).

Many types of past martian environments could have hosted life and subsequently preserved its signatures and would be high priority targets for Mars exploration (e.g., Westall et al., 2015; Hays and Beaty, 2017; Onstott et al., 2019; Carrier et al., 2020). We focus on habitats within SdP, an environment that falls under the “subaqueous” category of Hays and Beaty (2017), but the type of study

carried out here could be usefully applied to many terrestrial Mars-analog features and to other planetary analog features as well, habitable or otherwise. Possible applications to features that are not astrobiology targets are many, and include identification of dunes and dune fields, boulders, ridges, chaos terrain, and craters.

1.1 Motivation

This work is motivated, in part, by the evolving Mars exploration objectives that build on the success of NASA's "*follow the water"* Mars exploration strategy (Hubbard et al., 2002). With sample return as an eventual goal, precise targeting of rocks and outcrops that have the highest science value, especially those with the highest probability of containing biosignatures, is a top priority (NRC, 2011; Summons et al., 2011; Hays, 2015; MEPAG, 2018; Jakosky et al., 2020). The increased focus of scientific objectives on locating biosignature-bearing outcrops comes with a need for more precise identification of high-priority, rover-explorable targets from orbit (Hays, 2015; Hays and Beaty, 2017; Cabrol, 2018; MEPAG, 2018; Jakosky et al., 2020 Table VI-1). This process of refining the connection between orbital reconnaissance and rover exploration has been termed "orbit-to-ground science" (e.g., Cabrol et al., 2007; Piatek et al., 2007; Warren-Rhodes et al., 2007).

1.2 Habitability and habitats

The concepts of habitability and habitats and their use in astrobiology have been discussed in detail by many workers (see, e.g., Kasting and Catling, 2003; Gaidos et al., 2005; Nisbet et al., 2007; Lammer et al., 2009; Cockell et al., 2016). Here, we adopt the definition of *habitability* from the NASA Astrobiology Strategy (Hays, 2015, pg. 90) as "the potential for an environment to support life, be it on planet-wide or microscopic scales". As with habitability, many definitions of the term *habitat* exist in the literature (e.g., Whittaker et al., 1973; Block and Brennan, 1993; Hall et al., 1997; Warren-Rhodes et al., 2007; Geert et al., 2013;

Cockell et al., 2016). For our purposes, we adapt the definition from Warren-Rhodes et al. (2007): a (microbial) *habitat* is the physical space within a habitable environment where microbial organisms may reside.

Habitats can be defined across a large range of spatial scales, depending on the application, from planetary to microscopic (e.g., Cockell et al., 2016). Whereas it might be useful in some cases to refer to the entire SdP basin as a habitat, in this work we will only refer to the specific physical features in which microbial organisms may reside as habitats. We describe these features in Section 2.2 (c.f., “macrohabitats” in Warren-Rhodes et al., in review). And by analogy to Mars, while it might be useful in some cases to consider entire regions, basins, or craters as “habitats” (that may have been inhabited or not, Cockell et al., 2012), such a definition does not advance the goal of identifying with orbital data the highest priority rocks or outcrops (i.e., *targets*) to which a rover should be driven for analyses and possible sample collection. Thus, we are concerned with identifying habitats, current or past, in images from orbit at a spatial scale useful for informing landed missions, what we will call the “target-selection scale”.

An aspect of habitats that is important to consider is that they differ in their potential to preserve signs of the organisms that resided within them. Habitats with the potential to preserve evidence of the organisms they housed are referred to as habitats with a “taphonomic window” (e.g., Summons et al., 2011). Such habitats are high priority targets for biosignature-detection missions to Mars (Summons et al., 2011; Hays, 2015).

Other habitats that are interesting from an astrobiological perspective are the so-called, “refugia”, which are the last remaining potential outposts for extant life on Mars (Davila and Schulze-Makuch, 2016; Carrier et al., 2020). Refugia include caves, deep subsurface environments, ices, and salts (Carrier et al., 2020).

Several characteristics make the habitats that we focus on at SdP optimal targets for our study. First, SdP is analogous to evaporite-bearing basins on Mars

(Osterloo et al., 2008; Glotch et al., 2010; Osterloo et al., 2010; Glotch et al., 2016), which are found in Noachian and Hesperian units (Osterloo et al., 2010; Beck et al., 2020) and, based on cross-cutting relationships, some may be even older than the units in which they occur (Osterloo et al., 2010). Evaporite-bearing basins, thus, existed across a timespan when Mars was at its most habitable through its transition into the desert planet it is today (e.g., Cockell, 2014; Ehlmann et al., 2016). Second, the habitats at SdP have a taphonomic window. The salt minerals within salars can isolate and protect organic materials and preserve them exceptionally well (Fish et al., 2002; Fernández-Remolar et al., 2013; Jaakkola et al., 2015). Third, the habitats at SdP are among the refugia class of habitats. Refugia, by definition, have the potential to harbor extant martian organisms (Davila and Schulze-Makuch, 2016; Carrier et al., 2020). If habitats like the ones in SdP were found on Mars, they would be considered high-priority targets as habitats with a long history of sustained habitability both in the past, when Mars experienced periods of persistent liquid water on its surface, and up to the present as refugia. Another appealing quality of refugia is that microbial organisms become spatially confined to them. In salars, including SdP, the refugia habitats enhance water contents through concentration or retention mechanisms (or both) to foster locally habitable microenvironments (Davila et al., 2010; Davila et al., 2015; Warren-Rhodes et al., in review) while the surrounding basin dries out and becomes inhospitable (e.g., Warren-Rhodes et al., 2006; Cockell et al., 2017). This mechanism for the spatial-confinement of life is important because it narrows the search space to specific locations – the refugia – that have the highest probability of containing organisms and their remains (Warren-Rhodes et al., in review). Lastly, habitats like those at SdP are accessible to robotic or human exploration. Unlike caves, deep subsurface, and ices, the other three classes of refugia summarized in Carrier et al. (2020), salt refugia are on the surface of Mars and are readily accessible to explorative missions. The characteristics described above make habitats like those at SdP

ideal targets for the search for life, extinct or extant, if they could be identified on Mars.

1.3 Detecting and identifying

Several standard methods exist for evaluating the spatial resolution of imaging systems (dots per inch, modulation transfer functions, etc.). The spatial resolution of an imaging system can be considered its *detection threshold*; that is, if a system can resolve a feature, it has detected it. This definition of detection is consistent with that of the so-called “Johnson Criteria” (Johnson, 1958), perhaps the most commonly used set of criteria for what constitutes detection, recognition, and identification in (thermal and visible) imaging systems. A common rule of thumb, derivative from the Nyquist Theorem, applicable to most visible imaging systems is that 2 to 3 pixels are necessary to resolve, and therefore detect, a feature in an image. *Identifying* (i.e., assigning as a member of a class) features in an image is not the same as *detecting* features, and it requires higher spatial resolution (Johnson, 1958; Mesnik, 2016). A feature’s *identification threshold* in image spatial resolution will depend on many factors inherent to the feature itself, making a generalizable “rule of thumb” for feature identification, such as exists for feature detection, difficult to establish. Therefore, feature identification thresholds in image spatial resolution are best established on a per feature basis.

1.4 Identifying habitats on Mars

Orbital identification of target-selection-scale habitats like those found in SdP on Mars presents (at least) three challenges with related questions: 1) martian and terrestrial geologic processes differ, so what characteristics must two features in similar environments on Earth and Mars share before we can say they are the same types of features (i.e., belong to the same class)?; 2) chloride-bearing basins on Mars are billions of years old, whereas the habitats in SdP are <10 kyr old, so to what degree have billions of years of modifications confounded

our ability to compare features?; 3) the spatial resolution available from martian orbital assets may be too coarse to identify the habitats in SdP, so are habitats like those at SdP identifiable in currently available orbital images of Mars?

Our goal is to establish a method for addressing this third issue concerning the spatial resolution necessary to identify habitats on Mars that are like those at SdP. Specifically, we aim to determine the spatial resolution necessary to identify habitats like those in SdP on Mars and evaluate whether the resolution of currently available orbital images is sufficient to identify such habitats and with what confidence level it could be done. Because microbial habitats in terrestrial Mars analog environments are often limited in spatial extent (Stan-Lotter et al., 2006; Lynch et al., 2012; Hays et al., 2017), our method for determining thresholds of identification could be usefully applied to habitats in other terrestrial Mars analog environments to further generalize the findings of the present work.

1.5 Organization

The organization of this paper is as follows: in Section 2 we provide a brief background on neural networks, past work with CNNs for planetary geologic remote sensing, and describe our analog field site, Salar de Pajonales, and its relevance to Mars; in Section 3 we describe our data and its collection in the field; in Section 4 we describe our methods; in Section 5 we report our results; lastly, in Section 6 we discuss the implications of this work for the search for evidence of life on Mars, for future instrument design, and for future analog research.

2 Background

In this section, we review recent papers that have explored CNN-based approaches to solving image-classification problems with aerial imagery and in the planetary sciences. We also provide background on the geology of our field site, Salar de Pajonales, with a focus on its suitability as a Mars analog. For a

primer on artificial neural networks and their application to planetary science problems, we refer the reader to Appendix Item A.

2.1 Relevant background on convolutional neural networks

Geologic remote sensing is one of the many domains of research that has benefited from CNNs (Khan et al., 2020, and refs. therein). There are a variety of applications for CNNs in geologic remote sensing, including hyperspectral image classification (Sidike et al., 2018), pan-sharpening (Masi et al., 2016), and super-resolution processing (Dong et al., 2016). In this section we will review studies that have used CNNs for tasks more relevant to this work: semantic segmentation (i.e., pixel-wise classification) of aerial images, impact crater detection in planetary images, and geologic landform detection.

Semantic segmentation of very high-resolution (VHR, GSD < 10 cm) aerial images of urban scenes is a long-standing and still-active area of research (e.g., Rottensteiner et al., 2014). Semantic segmentation of VHR data is different from performing semantic segmentation on lower resolution satellite data (e.g., ASTER, SPOT, etc.) due to the much higher geometric and textural detail (e.g., Maggiori et al., 2017) and (typically) much lower spectral resolution in VHR data compared to satellite data.

Major strides have been made in semantic segmentation of VHR data recently by using CNN-based approaches. Wei et al. (2018) used multiple CNNs to develop a network that can successfully deliver detailed segmentations at vastly different spatial scales. Maggiori et al. (2017) addressed a common issue of imperfect training data by using a two-step approach: first, training on a large, but imperfect dataset, and fine-tuning the network on a smaller but more accurately labeled dataset. A study particularly relevant to the work presented here was conducted by Marmanis et al. (2016). In their study, the authors used a Fully Convolutional Network (FCN, see Appendix Item A, and Shelhamer et al., 2016) to achieve state-of-the art semantic segmentation results on VHR aerial image and DEM data from the International Society for Photogrammetry and

Remote Sensing (ISPRS) semantic labeling benchmark database (Rottensteiner et al., 2012). Features of their approach that are specifically relevant to our work are the incorporation of DEM data in their model and the use of transfer learning (Section 4.3.2). Marmanis et al. (2016) duplicated their network architecture to train on visible data and DEM data in parallel, before concatenating the results of each parallel network in a final series of layers resulting in classification. Additionally, the authors used transfer learning with initial network parameters derived from networks trained on large image databases, such as the ImageNet (Russakovsky et al., 2015), Places (Zhou et al., 2014), and Pascal VOC (Everingham et al., 2010) databases.

A common task in planetary science is the identification and mapping of impact craters. Many attempts have been made for automating this task, but no standard method has been adopted. DeLatte et al. (2019b) review crater counting methods and provide guidance for future crater detection methods using CNN-based approaches. One such method was conducted by Emami et al. (2019). The authors developed a two-stage algorithm for detecting craters on Mars with a supervised classification method as the first stage and a second stage based on CNNs. An approach based completely on CNNs was developed by Wang et al. (2018) for crater identification (i.e., detect a crater and then associate it with a known crater from a reference database). The authors developed an FCN, dubbed CraterIDNet, that can take in an arbitrarily sized input image and deliver detected crater positions, apparent diameters, and identifications (i.e., the name for named craters). Their model was successfully applied to Mars with F1-scores (an evaluation metric, see Section 4.4) consistently over 90%. DeLatte et al. (2019a) developed a crater detection network using a CNN-based U-Net architecture, which is similar to an encoder-decoder network except the encoder and decoder modules are not decoupled (Ronneberger et al., 2015).

While an important task, crater detection is just one type of geologic landform detection for which CNNs can prove useful. Latifovic et al. (2018)

produced maps of geologic terrain over a region of the Northwest Territories in Canada using CNNs. A method employed by Latifovic et al. (2018) that is particularly relevant to this study is the use of a DEM as an input parameter. In total 7 input parameters were used by the authors that consisted of the Landsat-derived components brightness, greenness, and wetness, as well as an 8-m DEM with slope and elevation-variance, and an air photo mosaic. The authors trained their networks *de novo*, without the aid of transfer learning, due to the non-standard input parameters chosen for their study. Their version of the ResNet-34 (He et al., 2015) architecture performed best, mapping distinct terrains in Landsat data with an average accuracy of 76% for locally trained areas. In another relevant study (Palafox et al., 2017), the authors developed a CNN-based model (MarsNet) to detect volcanic rootless cones and transverse aeolian ridges on Mars. MarsNet consists of 5 CNNs and is capable of variable-sized landform detection. Woods et al. (2020) modified an FCN originally designed to hunt for new or anomalous features to segment terrain on Mars in High Resolution Imaging Science Experiment (HiRISE) images (Novelty or Anomaly Hunter – HiRISE – NoAH-H). NoAH-H segments terrain into 14 geologic classes and was tested over the Exo-Mars landing site, Oxia Planum. Woods et al. achieved results (as measured by IoU, see Csurka et al., 2013) generally between 30% and 80% depending on the surface geologic class. The role of DL and CNNs in planetary science is growing, and many tasks for which these approaches would be useful have yet to be explored.

2.2 Geologic Background: Salar de Pajonales as an Analog to Mars

The Atacama Desert and the Altiplano-Puna (hereafter, Altiplano) have long been recognized as terrestrial analogs to martian environments (e.g., McKay et al., 2003; Cabrol et al., 2007; Piatek et al., 2007; Warren-Rhodes et al., 2007; Fairen et al., 2010; Flahaut et al., 2017). The consortium of extreme conditions within the Atacama and Altiplano are severe and sustained dryness (Houston and Hartley, 2003), record-high UV exposure (Cabrol et al., 2014;

Häder and Cabrol, 2020), large amplitude diurnal temperature swings, high rates of evaporation (Houston and Hartley, 2003; Houston, 2006), and high concentrations of salt. Salar de Pajonales (SdP) is situated where the Atacama Desert meets the high-altitude Altiplano (Fig. 3.1a) and the various extreme conditions associated with each culminate in a polyextreme environment. These characteristics, along with an igneous/volcanic geologic context, make salars within the Atacama and Altiplano, and especially those like SdP at the nexus between the two geographic provinces, suitable analogs to martian evaporite-mineral-bearing basins (Flahaut et al., 2017).

SdP is a 97.2 km^2 salt encrusted basin located at 25°08’29”S, 68°46’20”W, 3547 m just west of the active volcanoes Lastarria and Cordon del Azufre of the magmatic arc of the Andes (Fig. 3.1). The surface of SdP is covered, primarily, by halite and contains regions of gypsum and carbonate (Rodríguez-Albornoz, 2018). A minor water source for Altiplano and Atacama basins such as SdP is infrequent precipitation events (Houston and Hartley, 2003), and the major contributer is snowmelt-sourced groundwater from the Andes (Ventra et al., 2013). Magmatic acid emissions contribute HCl and H_2SO_4 to the ground water, which then react with silicates in the subsurface to create brines that are the major source for the anions that form evaporites in basins such as SdP (Pueyo et al., 2001). Our study site lies within a gypsum-dominated area of the salar, designated the “Dome Field” because it contains many domical gypsum structures (tumuli, Warren, 2016, Hinmann et al., in prep).

Chloride deposits on Mars may represent basins similar to SdP in which surface brines evaporated and leave behind a salt-encrusted surface (Glotch et al., 2016). Notably, however, phases such as sulfates and phyllosilicates are absent from martian Chloride basins and halite appears to be the major phase (Glotch et al., 2016; Ye and Glotch, 2019).

Warren-Rhodes et al. (in review) describe the microbial ecology of SdP, and one of their findings is that microbial (chasmo)endolithic communities are not randomly distributed within the site but prefer specific habitats. Two of the

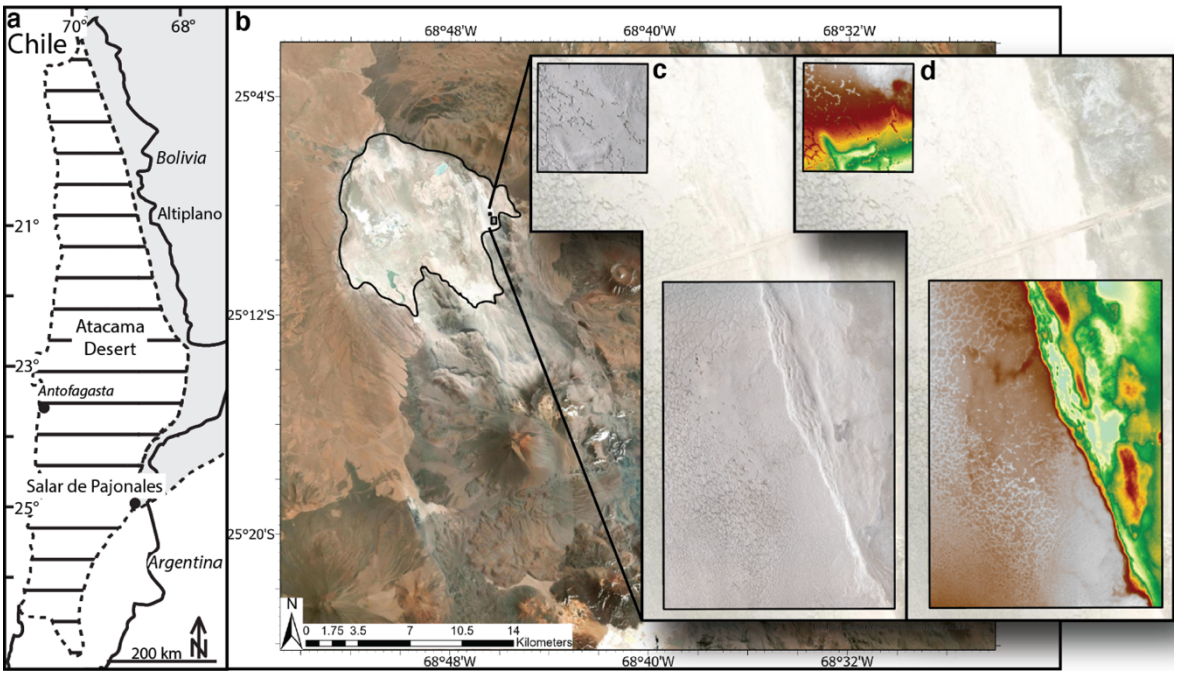

Fig. 3. 1. (**a**) Context map showing location of Salar de Pajonales within Chile. Dashed lines indicate boundaries of the Atacama Desert (horizontal bars) and the Altiplano (solid gray). Solid lines denote country borders. (**b**) Salar de Pajonales basin outlined in black with the locations of the orthophotomosaics (**c**) and DEMs (**d**) processed for this study.

habitats are local topographic highs termed “polygon ridges” and “domes” (Fig. 3.2a, b, e). The other habitat where microbes are found with high probability at SdP is a biological soil crust termed “patterned ground” (Fig. 3.2c, e). The microbial ecology study performed by Warren-Rhodes et al. (in review) to understand which features serve as habitats at SdP was a crucial antecedent step for this study. For more complete descriptions of the geology and surface morphology at SdP see Rodríguez-Albornoz (2018), which describes the geology of the SdP basin, and Hinman et al. (in prep.), which describes the genesis of geomporphologic features – notably domes and ridges – in the field site..

3 Data

The raw data for this study consist of images captured with a small unmanned aerial system (sUAS). The camera onboard the sUAS has a 20-megapixel CMOS sensor with an 8.8 mm, f/2.8 lens, and a mechanical shutter (Table 3.1). Two image-acquisition flight campaigns were undertaken: one on the morning of November 2, 2018 at 9:48AM (Flight 1); and a second on the morning of November 3, 2018 at 9:22AM (Flight 2). See Appendix III for processing reports that include details on both flight campaigns. In Flight 1, 110 images were captured and an ~0.142 km^2 south of the east-west trending road that dissects the salar was used for analysis (Fig. 3.1c, d). In Flight 2, 96 images were captured and an ~0.022 km^2 area north of the east-west trending road that dissects the salar was used for analysis (Fig. 3.1c, d). Image acquisition was automated using a flight mapping software package. Images were captured at intervals sufficient to ensure at least 80% overlap between images in the along-track direction and 70% overlap between images in the cross-track direction. The sUAS was flown at a height of 120 m above the ground in both campaigns, capturing images with a ground sampling distance of approximately 2.6 cm.

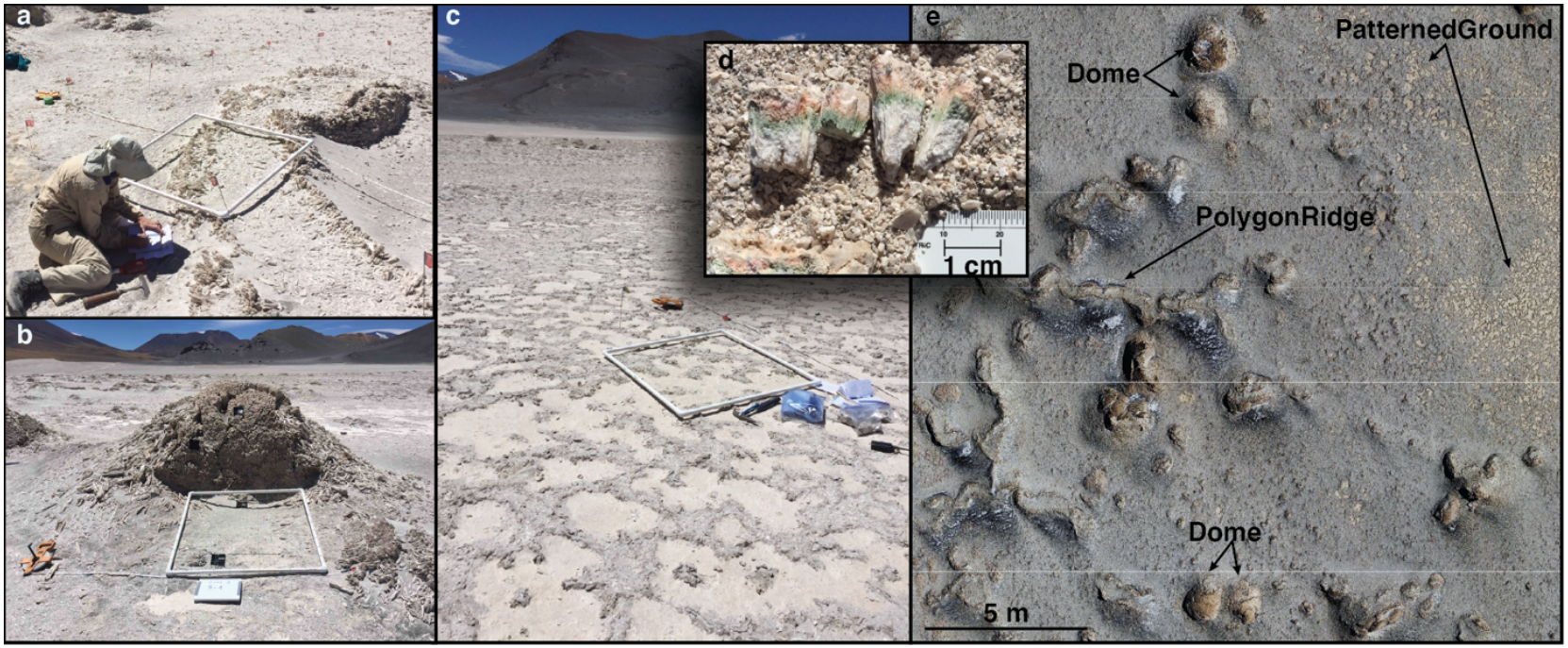

Fig. 3. 2. Ground-based and aerial views of the three microbial habitats at Salar de Pajonales: (**a**) polygon ridge; (**b**) dome; (**c**) patterned ground. For scale, the white quadrat in **a**-**c** is 1 m by 1 m. (**d**) Green and pink pigments associated with the microbial organisms found in these habitats, and (**e**) an aerial view with arrows indicating the habitats.

Table 3. 1. sUAS camera specifications

sUAS (Phantom 4 Pro) Camera Specs		Source
Sensor	20M pixel, CMOS sensor	[1]
Sensor Dimensions (mm)	13.2 x 8.8	[2]
Image Size	5472 x 3648	[1]
Pixel Pitch (μm)	2.41	calculated
Lens	FOV 84°, 8.8mm focal length, f/2.8	[1]
Shutter	mechanical	[1]
MTF10 (green)	0.2815 line pairs/pixel	[3]
Spatial Resolving Power	3.55 pixels	calculated
[1] DJI 2021; [2] dxomark 2021; [3] Cramer et al., 2020		

4 Methods

We trained three types of CNN-based networks using only color (RGB) image data, only digital elevation model (DEM) data, and using both RGB and DEM data (See Section 4.3 for details). By training networks with and without DEM data, we aim to assess the "value-added" by a DEM associated with RGB image data for semantic segmentation. Our approach for evaluating the identifiability of surface features across a range of spatial resolutions is based on convolutional neural networks (CNNs). We chose a CNN-based approach to scene classification instead of a human-based approach to instill objectivity and repeatability in the scene classification task. We trained a new network with the same initial conditions to classify the images at each spatial resolution. A single human analyst with on-the-ground knowledge of the field site would be biased by their knowledge of the field site and by the repetitive nature of the classification task (i.e., identifying features in the same images across many spatial resolutions). While this bias could be eliminated by having different individuals analyze images of the same areas at different resolutions, having many human analysts would introduce uncertainty due to variations in their knowledge of the field site and in their performance classifying the scenes. A CNN-based approach to scene classification, in which the network analyzing images at a given resolution has no information about what the area looks like at other resolutions, assuages these issues.

Before detailing our methods, a clarifying note regarding image spatial resolution is warranted. The measurement we use to relate the spatial resolution of the images in our study is *ground resolved distance (GRD)*: the smallest feature that can be resolved in an image expressed in object-space dimensions, e.g., cm on the ground. The GRD of an image is distinct from the ground sampling distance (GSD) of an image, which is the distance between pixel centers expressed in object-space dimensions. Our approach to evaluating GRD necessary to identify microbial habitats at Salar de Pajonales (summarized in

Fig. 3.3) is as follows: 1) Construct orthophotomosaics and DEMs that span a range of GRDs. 2) Train FCNs (CNN adapted to the semantic segmentation task, see Appendix III Item A) to perform semantic segmentation on the scenes across the range of GRDs with only RGB data, only DEM data, and with RGB+DEM data. 3) Evaluate the performance and assess the output uncertainty of the FCNs to understand identification confidence as a function of GRD and input data type. We provide details for each step below.

4.1 Data preparation

4.1.1 Orthophotomosaic/DEM construction

The sUAS images were used to generate orthophotomosaics with corresponding digital elevation models (DEMs) in a commercial structure from motion (SfM) software package, Pix4dMapper. To generate a point cloud, the SfM software must identify tie points between images. Once a DEM is generated from the point cloud, it is used to create an orthorectified image mosaic (orthophotomosaic). It is important to note that the number and quality of tie points between image pairs is affected by the spatial resolution of the input images. Therefore, we chose to first degrade the resolution of all individual sUAS images and then generate orthophotomosaics and DEMs from the degraded resolution images, rather than create degraded resolution orthophotomosaics and DEMs from the highest resolution products, which would lead to overestimated accuracies of the degraded products. Orthophotomosaics and DEMs were geometrically controlled through the SfM process using manually-selected tie points derived from data available in the Living Atlas of ArcGIS and then georeferenced to our highest resolution orthophotomosaic in ArcGIS.

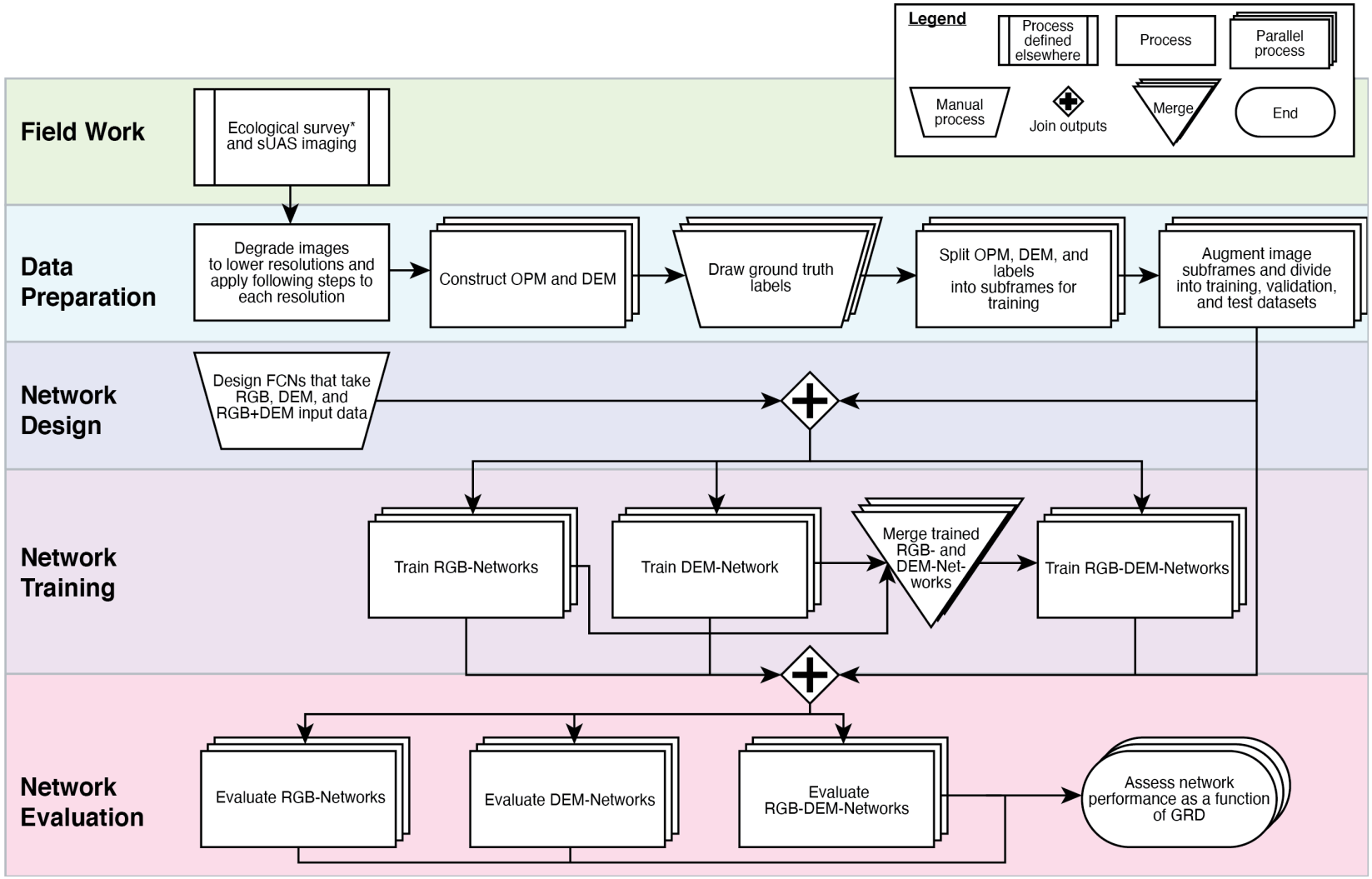

Fig. 3. 3. Flow chart delineating the methodology for this study from collection of images in the field to final assessment of neural network results. OPM = orthophotomosaic. *Ecological survey is described in detail in Warren-Rhodes et al. (in review).

4.1.2 Generation of images spanning a range of ground resolved distances

We generated 8 degraded resolution datasets from the Flight 1 and Flight 2 images for a total of 9 datasets (including the original, full-resolution dataset). We used a standard approach for downsampling the individual sUAS images (e.g., Smith, 1988) by convolving them with a circularly symmetric point spread function (PSF) modeled with a Bessel function of the first kind (J1 Bessel function). Although the PSFs for the individual degraded resolution images that were used as input to the orthophotomosaic and DEM generation process are known, and therefore their GRDs are known, the process of constructing the orthophotomosaics and DEMs induces uncertainties in the GRDs of the final products. Therefore, we empirically assessed the spatial resolution of the output orthophotomosaics following the standard approach of measuring the distance between 10% and 90% response values (Δ10-90 in pixels) of the edge response function (ERF). ERFs were derived from the output orthophotomosaics by finding a sharp edge in the image (e.g., a linear shadow) and extracting a profile across the edge (Fig. 3.4). This value can be related to values measured from a modulation transfer function (MTF) in lines/pixel. We prefer to report spatial resolution values in terms of line pairs/cm rather than lines/pixel; therefore, we report image GRDs by multiplying the Δ10-90 values by two (lines to line pairs) and by the GSD of the images (pixels to cm):

$$\mathrm{GRD} = 2 * \Delta 1090 * \mathrm{GSD}$$

We report these empirically derived GRDs along with other image metrics in Table 3.2.

Another common way to report spatial resolution is in terms of the MTF. A typical number reported for image spatial resolution is the value at which the MTF is reduced to 10% of its maximum contrast (MTF10). We derived MTFs through a Fourier transform of the first derivative of the ERFs and report the MTF10 values for GRD alongside the Δ10-90 values for GRD in Table 3.2.

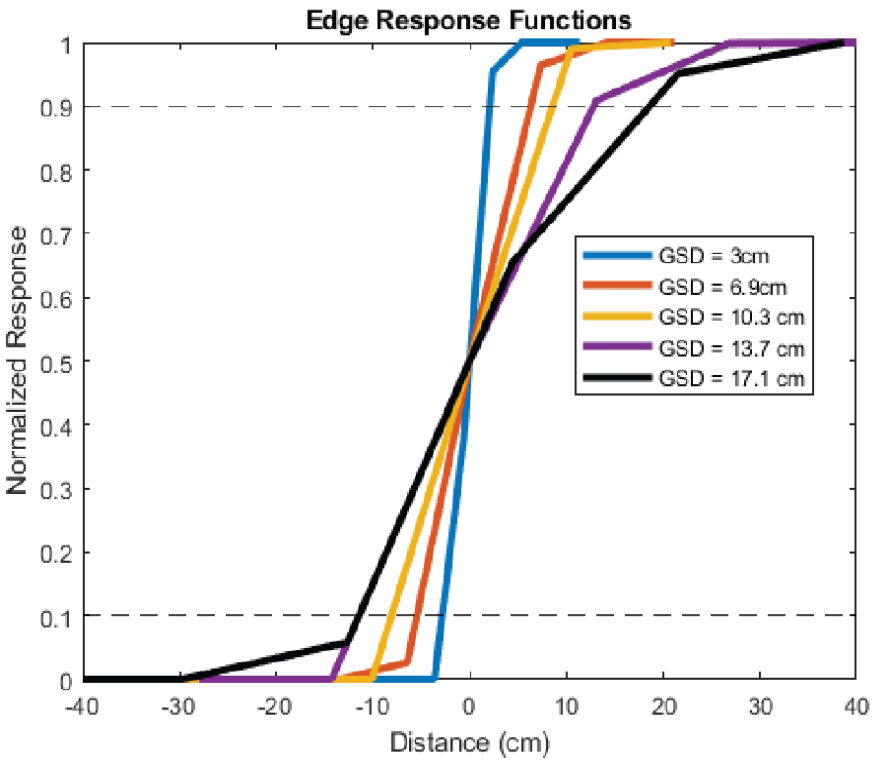

Fig. 3. 4. Example edge response functions derived from orthophotomosaics by measuring a response profile across a sharp edge.

Table 3. 2. Ground sampling distance (GSD), and empirically-determined spatial resolution metrics for the orthophotomosaics generated in this study.

GSD (cm)	Δ10-90 (cm)	GRD (2 x Δ10-90 (cm))	GRD (1/MTF10*)
3.0	4.9	9.8	10.1
6.9	11.8	23.5	22.6
10.3	16.6	33.3	34.5
13.7	24.3	48.5	48.8
17.1	30.0	60.1	59.1
20.5	35.0	70.0	69.7
23.9	40.8	81.7	81.3
27.3	46.7	93.3	92.9
30.8	52.7	105.3	104.9

*MTF10 is the modulation transfer function at 10% contrast.

4.1.3 Ground truth labels

The scenes were classified based on surface texture and morphology into 12 classes (Table 3.3, Fig. 3.5). The classes of particular interest to our study are PolygonRidge, Dome, and PatternedGround because these are the primary microbial habitats at Salar de Pajonales (Warren-Rhodes et al., in review). Ground truth labels (i.e., the standard against which networks will be evaluated) were drawn using the highest resolution orthophotomosaic and DEM in ArcGIS Pro by a remote sensing geologist with on-the-ground field experience at Salar de Pajonales. To mitigate human-induced uncertainty in the quality of the ground truth labels, the labels were only drawn once at the highest resolution and then exported from ArcGIS at the appropriate image dimensions for each dataset. The rasters were aligned on a pixel-by-pixel basis (snapped) to the appropriate orthophotomosaic to ensure the label images overlapped the orthophotomosaics correctly. During training, weights were applied to the classes according to their relative abundance in the training dataset.

4.2 Network design

We chose three network designs for our study (Appendix III Fig. A3.2): an RGB-Network, DEM-Network, and RGB-DEM-Network, which take 3-band RGB image data as input, DEM data as input, and both RGB and DEM data as inputs (delivering a single segmented output image), respectively.

4.2.1 Network inputs

All networks take subframes systematically extracted from the orthophotomosaic and/or DEM products as input. Taking subframes from the orthophotomosaic rather than individual image frames captured by the sUAS is necessary for several reasons:

• the individual sUAS images are often slightly off-nadir, so image frames from the orthophotomosaic are more analogous to orbital-derived images

Table 3. 3. Description of the feature classes defined for this study. Classes that are the primary habitats at SdP are highlighted in green.

	Class	Description
Flat/surface cover	Aeolian Cover	Wind-blown sediment sourced from local gypsum and allochthonous volcanics.
	Mottled Ground	Closely related to Aeolian Cover, but contains many small topographic and textural features, often including eroded remnants of polygon ridges and tumuli.
	Patterned Ground	Centimeter- to decimeter-scale polygons with interiors comprised of the light-toned gypsum that is the salar surface. The exterior rims of patterned ground patches are microbially induced structures known as biological soil crust. Patterned ground often occurs in patches, that, when viewed from above, are themselves patterned in polygon shapes, imparting a sort of fractal nature to their morphology.
	Mud Cracks	Cracks in dried out muddy areas formed by wet/dry cycles.
Positive topographic features	Eroded Ridges and Domes	Large swaths of terrain comprised of the eroded remnants of polygon ridges and domes with minimal (< 10 cm) topographic relief. Individual instances can be similar to uneroded polygon ridges and domes, but the convex-up, arch-shaped tops of the features have been eroded away. With the tops of the features eroded, the hollow interiors, typically infilled with sand, are exposed, which imparts eroded ridges and domes with a trapezoidal cross-sectional shape. Parallel "rails" are commonly indicative of eroded ridges and domes as viewed from above.
	Salt Pan	Hard, flat, salt-pan crust with patches of dark- and light-toned surfaces giving a "splotchy" appearance.
	Drainage-Channel Ridge	Positive topographic features typically on the scale of decameters or larger. Drainage-channel ridges are eroded remnants formed within the eastern drainage channel of SdP.
	Polygon Ridge	Elongate, continuous, positive topographic features that often make up the edges of decameter-scale polygons. Polygon ridges are convex-up, appear as an arch in cross-section, are > ~10cm in relief, and are typically hollow. Tops of ridges can be smooth or "spikey" with several-centimeter-long gypsum blades pointed upward perpendicular to the ridge surface.
	Dome	Domes are circular to sub-circular, domical, positive topographic features with length:width values of ≤ 2:1. Domes are typically isolated from other topographic features, but can be adjacent to polygon ridges and other domes. They appear as an arch in cross-section, are typically > 10 cm in relief, and are hollow. Tops of domes can be smooth or "spikey" with bladed gypsum crystals oriented with their long axes pointed perpendicular to the domical surface creating distinct textures.

Table 3. 3 continued

	Class	Description
Misc.	Objects	Man-made objects and people.
	Border Pixels	Blank pixels that make up the border of the orthophotomosaics and DEMs
	Road	Dirt roads that cross-cut the salar.

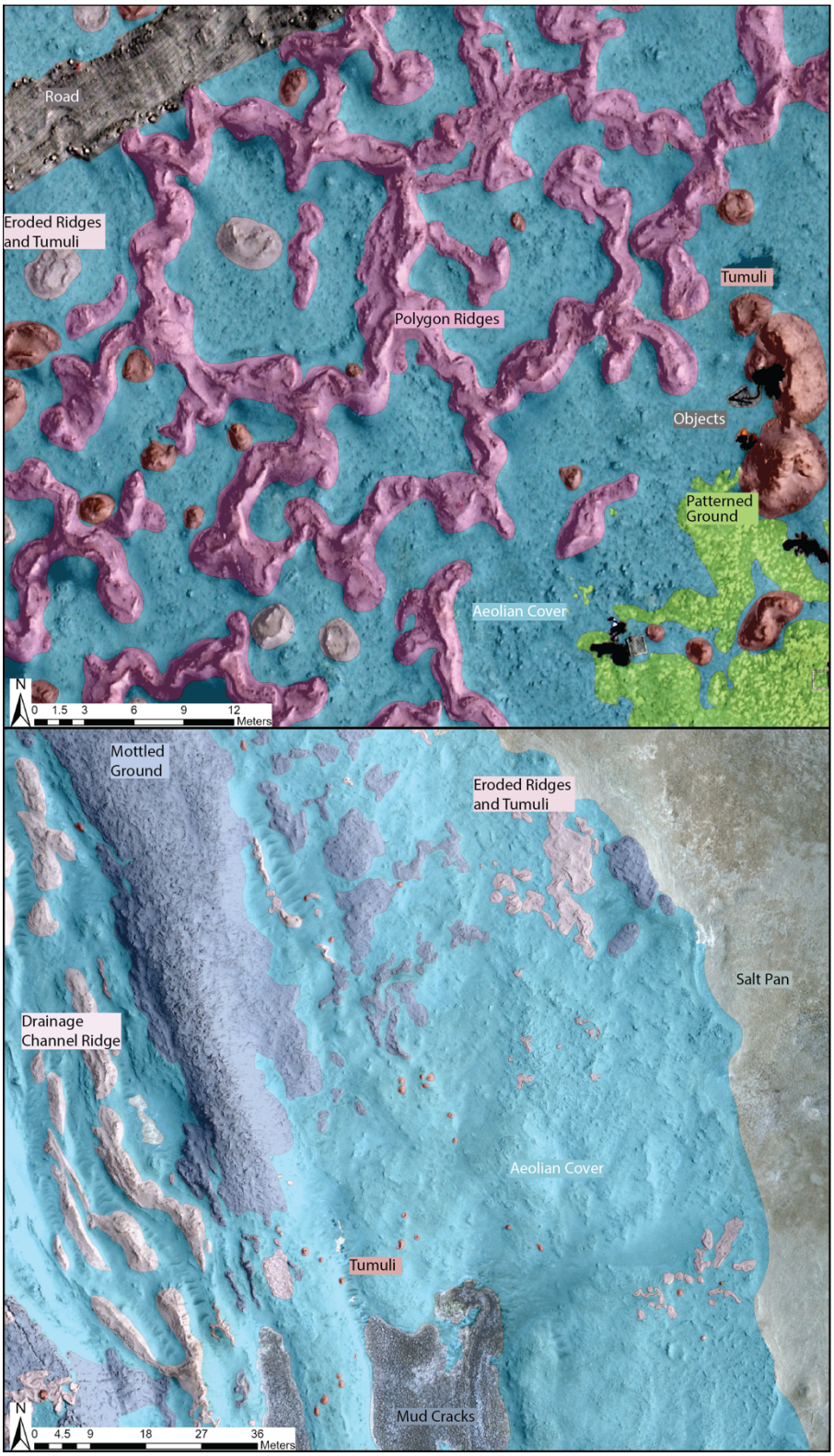

Fig. 3. 5. Feature classes defined for the Salar de Pajonales basin in this study. See Table 3 for class descriptions.

• to minimize the variability in the training setup between networks, we desired to have DEM frames associated with RGB frames to keep the training, validation, and testing datasets constant across network types (RGB, DEM, and RGB-DEM) and across networks trained at each spatial resolution

• for the RGB-DEM networks, it was necessary to have matching RGB and DEM subframes; lastly, the size of the individual sUAS image frames is not ideal for network training.

Because CNNs work by assessing spatial patterns in images, we chose to keep the object-space dimensions (i.e., the spatial extent of the images in meters) of the input subframes constant between the networks trained at different GRDs. We required that the input subframes capture sufficient context so that larger features that we aimed to identify, such as polygon ridges, occupy enough of the scene that their characteristics were recognizable. Two further constraints were that we required input subframe dimensions that were not so large that the high-resolution (small GRD) images were unmanageable to hold in GPU memory during network training and not so small that at large GRDs the input subframes spanned more than a few pixels. Based on the above constraints we arrived at image subframe dimensions approximately 18.5 m by 18.5 m (Table 3.4). The orthophotomosaics were divided accordingly into a total of 708 ~18.5 x 18.5 m subframes with corresponding DEM subframes.

We recognize that different choices could reasonably made for generating network inputs, such as the process for orthophotomosaic and DEM construction described in Section 4.1 or the spatial extent of the subframes. However, irrespective of what choices are made regarding the generation of input images, what matters for feature detection are the final GRD of the images and ensuring the subframes are large enough that the features of interest are recognizable within them.

Table 3. 4. Size of the input images at each ground resolved distance expressed in pixels and meters

GRD (cm)	Image Dimensions (pixels)	Image Dimensions (m)
9.8	625	18.75
23.5	267	18.423
33.3	180	18.54
48.5	134	18.358
60.1	108	18.576
70.0	89	18.334
81.7	76	18.24
93.3	67	18.358
105.3	60	18.54

4.2.2 Network architectures

For the RGB-Network, we used the DeepLabv3+ module (Chen et al., 2015) with the 50-layer deep CNN “Residual Network 50” (ResNet50) pre-trained on over 1 million images (He et al., 2015) from the ImageNet database (Russakovsky et al., 2015) as the network backbone to create an FCN for semantic segmentation. ResNet50 is a well-established CNN ideal for tasks that require recognition of features at multiple scales (e.g., He et al., 2015) and has out-performed other similar networks in satellite image classification tasks (Kadhim and Abed, 2020). Training a version of a network with parameters that were pre-trained on another (typically very large) database to perform a new, yet related, task is known as *transfer learning* (Thrun, 1996). CNNs are very good at transfer learning because the filters learned in the first several layers are typically general enough that they are useful for a wide variety of image classification tasks. Transfer learning has become a common practice when training CNNs to perform a new task because it reliably improves network results and training times (Marmanis et al., 2016; Sherrah, 2016).

For the DEM-Network, we again used DeepLabv3+ with ResNet50 pre-trained on ImageNet as the backbone CNN. Thus, the network architecture for the RBG-Network and DEM-Network are identical; however, we chose different training options for the DEM-Network (see details in *Section 4.2.2*).

The RGB-DEM-Network is simply the RGB-Network and DEM-Network assembled in parallel. We used a technique known as late fusion (Eitel et al., 2015; Guo et al., 2018; Pandeya and Lee, 2021) wherein the two parallel networks are connected by a concatenation layer that feeds into the final sequence of layers that deliver the segmentation result. The RGB-DEM-Network has significantly faster training times than either the RGB- or DEM-Networks because the only network parameters that need further training are those in the final sequence of layers that leads to classification.

An additional modification we made to our networks was to add Bernoulli dropout layers. A Bernoulli dropout layer takes activation values as input and

randomly multiplies each value by either one or zero with some predefined probability (in our case, p = 0.5). Dropout layers are useful for networks trained on datasets that are relatively limited in size because they function as strong network regulators and help avoid over-fitting (e.g., Srivastava et al., 2014). Additionally, when applied at network test time, dropout can be used to quantify network predictive uncertainty by approximating the network Bayesian posterior distribution (Gal and Ghahramani, 2016).

4.3 Network training

For the RGB-Network and DEM-Network we used the adaptive moment estimation (Adam) solver (Kingma and Ba, 2015) with an initial learning rate (see Appendix III Item A) of 0.0001. The learning rate was dropped by a factor of 10 every 10 epochs until the loss rate ceased decreasing, usually > 40 epochs. For training the RGB-Network, we froze the parameters (multiplied the learning rate by zero) in the first convolutional layer block (Appendix III Fig. A3.2) because the established filters in the shallow layers of the network are unlikely to require modification in transfer learning. The last two convolutional layers that feed into the SoftMax classification layer were set to have a learning-rate factor 100 times that the base rate of the network to accelerate learning of these layers.

A potential issue with using transfer learning on the DEM-Networks (which use as their backbone a ResNet50 CNN trained on RGB data) is that DEM data and RGB data have different statistics and may require different convolutional filters even in the shallow layers of the network. To test the efficacy of transfer learning with DEM data, we trained networks both with and without transferred parameters. We found that transfer learning was more effective than randomly initialized parameters. This is possibly because the DEM data, while not the same as RGB data, are still images with edges and texture that can be usefully recognized with the filters developed through training on RGB data. Additionally, to test the sensitivity of the parameters in the shallow network layers to further training, we tested networks where the learning rate factor of the first

convolutional layer block was set to 0, 0.01, 0.1, and 1. We found that setting the learning rate to 0.01 yielded the best results. Therefore, instead of freezing the first convolutional layers, as we did with the RGB-Network, we allowed the network to adjust the filter weights of its shallow layers at a learning rate of 0.01. These hyperparameters for network training are somewhat intuitive, as they allow the established shallow network layer parameters to be modified, but not drastically, tuning the RGB-learned parameters to suit the slightly different needs of the DEM dataset. As with the RGB-Network, we changed the learning-rate factor of the final classification layers to 100.

For training the RGB-DEM-Network, we imported all the parameters learned from training the RGB- and DEM-Networks independently as the network starting condition. The imported parameters were frozen, but the final sequence of layers leading to classification were not frozen. We used the Adam solver with an initial learning rate of 0.01, a learning-rate drop factor of 0.1, and a learning-rate drop period of 5 epochs. Training was carried out until the loss rate flattened, usually between 10 and 20 epochs.

For all networks, input images were normalized prior to training following a standard method of mean subtraction (e.g., He et al., 2015). To increase the volume of our training data and to make the trained networks more generalizable, we performed data augmentation. We augmented our training data through rotations, reflections, and illumination adjustments to achieve an 18-fold increase in data-volume. A 3-fold increase in data was achieved through three 90° rotations of the image frames to 90°, 180°, and 270° from their original orientations. A further 2-fold data-volume increase was achieved through horizontal and vertical reflections of the frames. Lastly, a 3-fold data-volume increase was achieved by adjusting the illumination of the scenes to 0.33 and 0.67 times their original values.

The total dataset (after augmentation) was randomly divided into training (75%), validation (12.5%), and testing (12.5%) datasets. The same random

divisions of data were applied across all GRDs so that the training, validation, and testing datasets for all networks comprised the same images.

4.4 Network evaluation

4.3.1 Performance metrics

To evaluate network performance across GRDs and between classes, we calculated standard evaluation metrics as well as predictive uncertainty for the network outputs (i.e., predictions) and a confidence score (Section 4.3.2). We calculated the following standard metrics on a per class basis to assess the performance of the ResNet50 semantic segmentation network (Table 3.5): 1) Recall; 2) Precision; and 3) Boundary F1 Contour Matching Score (BF-Score). Below is a description of each metric and what it qualitatively captures (for more detail on evaluation metrics see Csurka et al., 2013). For the equations used to calculate each metric see Table 3.5.

Recall is the number of correctly predicted pixels for a given class divided by the total number of pixels in that class as determined by the ground truth labels. Recall penalizes false negative predictions but not false positives. Recall can give a general sense for how well a network performed but can be susceptible to pathologies; for example, if an entire scene were classified as a given class, that class would report a recall of 100%.

Precision is the number of correctly predicted pixels for a particular class divided by the total number of pixels predicted as that class. Precision penalizes false positive predictions but not false negatives. Whereas recall is lenient on liberal predictions, precision can give an unrealistically high score compared to a qualitative assessment of performance when predictions are too conservative. For example, if the network only predicted one pixel for a given class and it was correct, precision would be 100%.

Table 3. 5. Mathematical and qualitative description of network performance metrics used in this study.

Metric	Formulation	Qualitative description
Recall	TP/(TP+FN)	number correct divided by number in class
Precision	TP/(TP+FP)	number correct divided by number of guesses
Boundary F1-Score (BF-Score)	2TP/(2TP+FP+FN)	twice the number of correct guesses divided by the number of guesses plus the number of pixels in the class

It is standard to calculate recall and precision using a threshold value to determine whether predicted and ground truth pixels have a match with each other (e.g., Csurka et al., 2013). This requires a choice in threshold value used to determine whether a classified pixel has a corresponding ground truth boundary label. We chose to calculate threshold values as 10% of a characteristic length scale of the feature being evaluated. For the Dome class, the characteristic length scale was chosen as the average dome diameter (1.61 m), and therefore the threshold value is 16.1 cm. To calculate a characteristic length for the PolygonRidge class, we made 100 measurements of the width across polygon ridge features on a random sample of 33 polygon ridges. These measurements were averaged to arrive at a characteristic length of 2.29 m and a corresponding threshold value of 22.9 cm. Areas of the PatternedGround class are polygonal with length to width ratios typically close to 1, so we calculated a characteristic length for this class as 4*Area/Perimeter (e.g., the diameter of a circle or the length of a side of a square) and found a characteristic length of 1.16 m, and a corresponding threshold value of 11.6 cm.

BF-Score uses both recall and precision in its formulation (Table 5). It captures how well the general shape of the predicted and ground truth classes align. It is useful for capturing a value that is more consistent with the sense one might have from a visual assessment of the predicted and ground truth scenes than either recall or precision.

4.3.2 Uncertainty Quantification and a Confidence Score

While the above-mentioned evaluation metrics can give a good sense for network performance (i.e., proportion of correctly classified pixels), they do not convey either the predictive uncertainty of the network or the confidence a user ought to have in the network outputs. In searching for high-priority targets on Mars, it would be useful to have both a method for quantifying network uncertainty and for evaluating the confidence with which a user should trust the network predictions and associated uncertainties.

The most commonly used methods for characterizing the uncertainty of neural network outputs (Abdar et al., 2020and refs therein) are to use Bayesian neural networks (BNNs, Neal, 1996), approximations of BNNs (e.g., Gal and Ghahramani, 2016) and ensemble learning (e.g., Lakshminarayanan et al., 2017). For networks larger than a few hidden layers, strict calculation of Bayesian uncertainty is intractable. Training ensemble networks is expensive in terms of time and computation power, so we avoided this method in our study because we worked with many large FCNs. Therefore, we approximate a BNN with the Monte Carlo Dropout method (MCDropout, Gal and Ghahramani, 2016) to assess the predictive uncertainty of our networks.

Through the MCDropout method, we approximated the posterior probability distributions of the network predictions for every pixel by generating a Monte Carlo sample (N=100 stochastic forward passes in our case) of network predictions for every test image by keeping dropout layers active at test time (e.g., Gal and Ghahramani, 2015). For our evaluations, we use the input values to the SoftMax classification layer rather than the SoftMax output because distributions of SoftMax input values are approximately normal, which is useful for our uncertainty analysis (e.g., Fig. 3.6). We then calculate the mean and variance of the probability distributions of the SoftMax input values of each class for each pixel. For a given pixel, the class distribution with the highest mean value ($\mathrm{PDF}_{\max}$) is taken as the network prediction. We then solve for the probability (p) with which $\mathrm{PDF}_{\max}$ can be considered a separate distribution from each other predicted PDF by finding the p at which the following function is equal to zero:

$$\mathrm{f(p)} = \mathrm{t_{score}}(\mathrm{PDF_{max}}, \mathrm{PDF_i}) - \mathrm{t_{critical}}(\mathrm{p}, \mathrm{DF})$$

Where $t_{score}(\mathrm{PDF_{max}}, \mathrm{PDF_i})$ is the student's t-score value between $\mathrm{PDF}_{\max}$ and $\mathrm{PDF_i}$, the probability distribution of SoftMax input values for class i. The value $t_{critical}(\mathrm{p}, \mathrm{DF})$ is the critical t-value for a given p and degrees of freedom, $DF = N - 1; N = 100$. The values of p represent the probability that the difference between the expected values of $\mathrm{PDF}_{\max}$ and $\mathrm{PDF_i}$ is unequal to zero. Values of p

calculated in this way can range from 0.5, if two classes have the same means, to (nearly) 1.0 if the difference between the means is large compared to the standard errors of the distributions. A total of eleven probabilities are calculated for each pixel (i.e., the number of classes minus 1), and the minimum probability is converted to a more intuitive "Certainty Score" by applying a linear stretch to arrive at a percentage between 0% and 100%:

$$\text{Certainty Score } \% = (\mathrm{p_{min}} - 0.5) * 200$$

The above formulation gives a certainty value of 0% for a pixel with two (or more) predicted classes that have PDFs with equal expected values, and a certainty value that approaches 100% for pixels where the expected value of the $\mathrm{PDF_{max}}$ class is larger (in a sense directly related to its statistical significance in a Student's T-Test) than the expected value of any other class $\mathrm{PDF_i}$. Examples of the SoftMax input PDFs for all 12 possible classes for a high certainty and a low certainty pixel are shown in Fig. 3.6. These certainty values capture how certain the network is in its prediction for each pixel, but they do not capture how confident a user should be in the network's prediction. That is, the network may have very high certainty about a false prediction, in which case a user ought not have high confidence in the network's predictions.

To represent the degree to which one should trust a network prediction for a given class, i, we formulated a "Confidence Score":

$$\text{Confidence Score}_\mathrm{i} \% = \frac{\mathrm{TP_i} * \mathrm{TC_i} + \mathrm{FP_i} * (100 - \mathrm{FC_i})}{\mathrm{N_i}}$$

Where $\mathrm{TP_i}$ is the number of true positive predictions for class i, $\mathrm{FP_i}$ is the number of false positive predictions for class i, $\mathrm{TC_i}$ is the average network certainty over all $\mathrm{TP_i}$ pixels, $\mathrm{FC_i}$ is the average network certainty over all $\mathrm{FP_i}$ pixels, and $\mathrm{N_i}$ is the total number of pixels predicted as class i. If the network is certain about its false predictions or if it is uncertain about its correct predictions, then the Confidence Score will be low. Conversely, if the network is uncertain about false predictions and certain about its correct predictions, then the Confidence Score will be high.

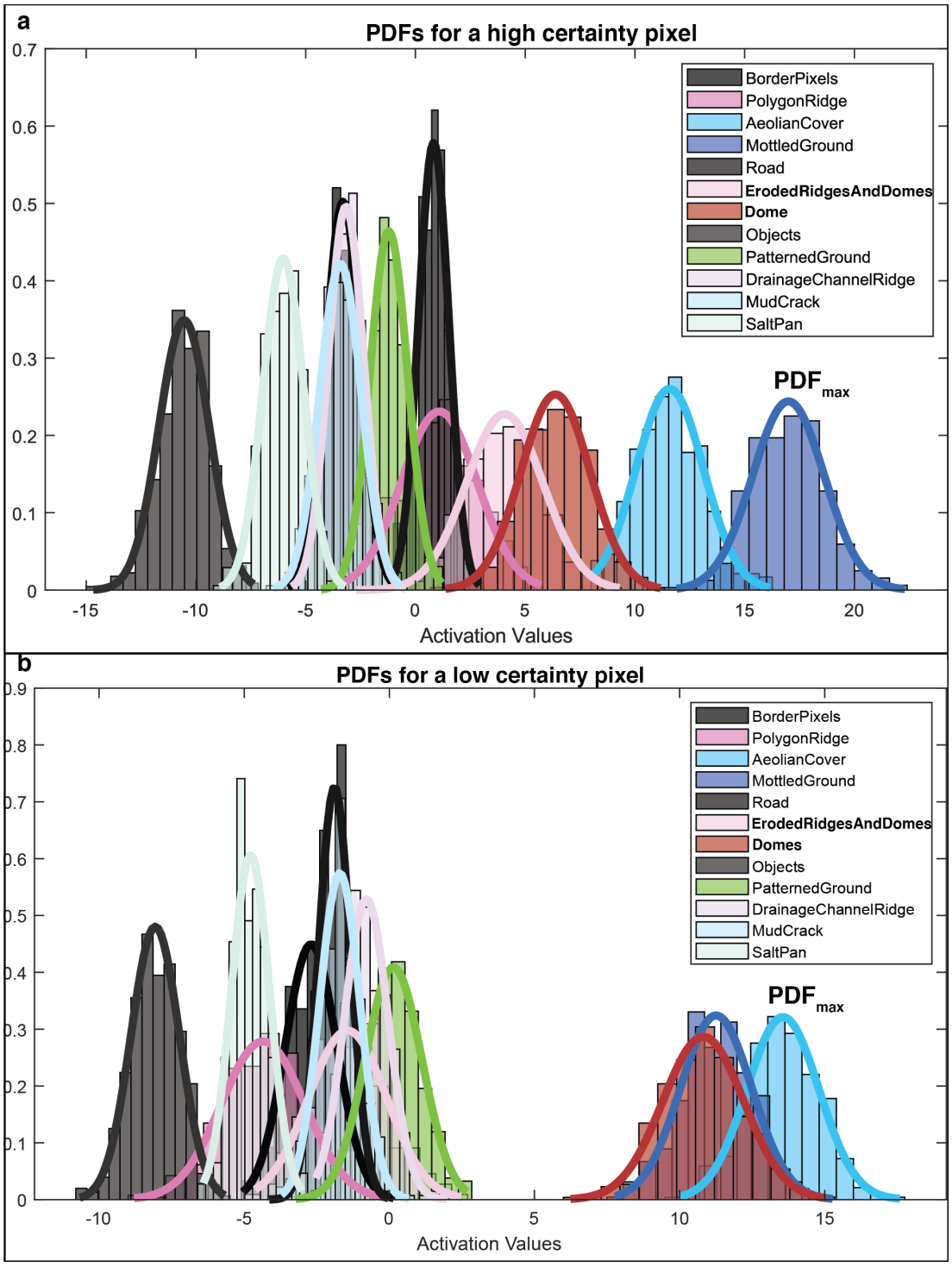

Fig. 3. 6. Probability distributions functions (PDFs) of SoftMax input values of each class for a single pixel. For high certainty pixels (**a**), the expected value of the PDF with the highest mean SoftMax input activation value (PDF_{max}) is much larger than the expected value of any other PDF. For a low certainty pixel (**b**), the expected value of PDF_{max} is not significantly larger than the expected value of other PDFs.

4.3.3 A holistic approach to interpreting network evaluation metrics

Whereas the BF-Score is a measure of how accurately a network segments features, the Confidence Score reports the degree to which a user should trust the network Certainty Scores reported for a given class and enables a more nuanced analysis of network results and feature identification. Confidence Scores can be high even if the boundaries drawn around objects are inaccurate (i.e., BF-Scores are low), and, conversely, Confidence Scores can be low even if BF-Scores are high. If the Confidence Score is high relative to the BF-Score, it means that the Certainty Scores are reporting useful information upon which users should rely; but if the opposite is true, users should be wary of network Certainty Scores because the network is likely overly certain of false predictions.

This distinction between a high BF-Score and a high Confidence Score arises because there are two ways to achieve a high Confidence Score as formulated in this work. The first way is for a network to make accurate predictions with high Certainty Scores associated with those predictions. In this case, the BF-Score and Confidence Score will both be high. The second way is for a network to make mostly (or even entirely) false predictions but to have very low Certainty Scores for those predictions. In this case the BF-Score will be low while the Confidence Score is high. In both scenarios, the Confidence Score correlates with the degree to which a user should trust the Certainty Score a network reports for a given prediction. In practice, this means the Confidence Score, Certainty Score (or other uncertainty quantification measures), and BF-Score (or other accuracy measures) are more useful when interpreted in concert than in isolation.

5 Results

We focus our results on the three classes that serve as microbial habitats at SdP: PolygonRidge, PatternedGround, and Dome. In images with GRDs comparable to HiRISE, the PolygonRidge, PatternedGround, and Dome classes

were identified with Confidence Scores between 74% and 80%, 60% and 65%, and 47% and 55%, respectively (Figs. 3.7-3.15, Tables 3.6-3.11). To identify PolygonRidges with RGB or both RGB and DEM data at a 1-sigma confidence level of 85% would require a GRD < ~50 cm. To identify Domes at approximately the 1-sigma confidence level (84.45%, Table 8) would require RGB and DEM data with a GRD ≤ 9.8 cm. PatternedGround could not be identified at the 1-sigma confidence level at any of the GRDs used in this study.

The RGB-Network (Tables 3.6-3.7 and Figs 3.7-3.9), by all measures, outperformed the DEM-Networks (Tables 3.8-3.9 and Figs 3.8-3.11) and performed similarly to the RGB-DEM-Networks (Tables 3.10-3.11 and Figs 3.12-3.15) at all GRDs. The habitat most confidently identified by any network was the PolygonRidge class with a Confidence Score of 93.81% achieved by the RGB-DEM-Network at a GRD of 9.8 cm. Further details on the results of each network type are reported below. See Appendix III Item C for results on the non-habitat classes in this study.

5.1 RGB-Networks

Across all GRDs explored in this study and by all measures, the RGB-Networks performed better than the DEM-Networks and marginally better than the RGB-DEM-Networks at most GRDs. Examples of RGB-Network predictions and associated Certainty Scores compared to ground truth labels are presented in Figure 3.7. The Precision values, Recall values, BF-Scores, and Confidence Scores for the PolygonRidge, Dome, and PatternedGround classes are presented in Figure 3.8 and associated Table 3.6, and the Certainty Score values are presented in Figure 3.9 and Table 3.7.

The Precision values, Recall values, and BF-Scores for the PolygonRidge class were higher at all GRDs than both the Dome and PatternedGround classes. For all three classes, Precision, Recall, and BF-Score have similar general shapes with increasing GRD. In all cases, there is a GRD over which a sharp decrease in the Precision, Recall, and BF-Score is observed; for the

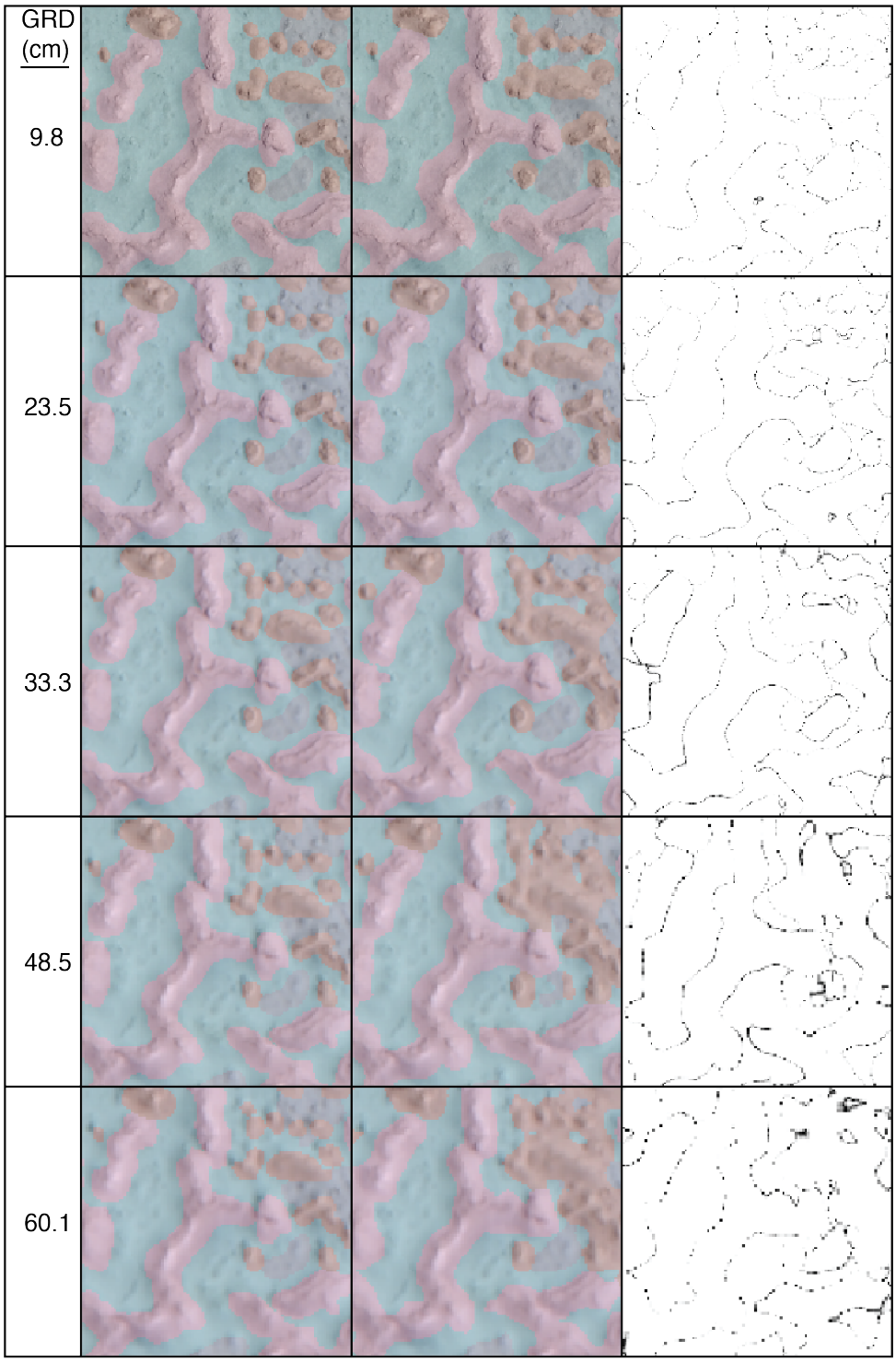

Fig. 3. 7 Examples of RGB-Network predictions (center column) with associated Certainty Scores (right column, black = 0%, white = 100%) and compared to ground truth labels (left column). Pink = PolygonRide, Blue = AeolianCover, Purple = MottledGround, Red = Dome.

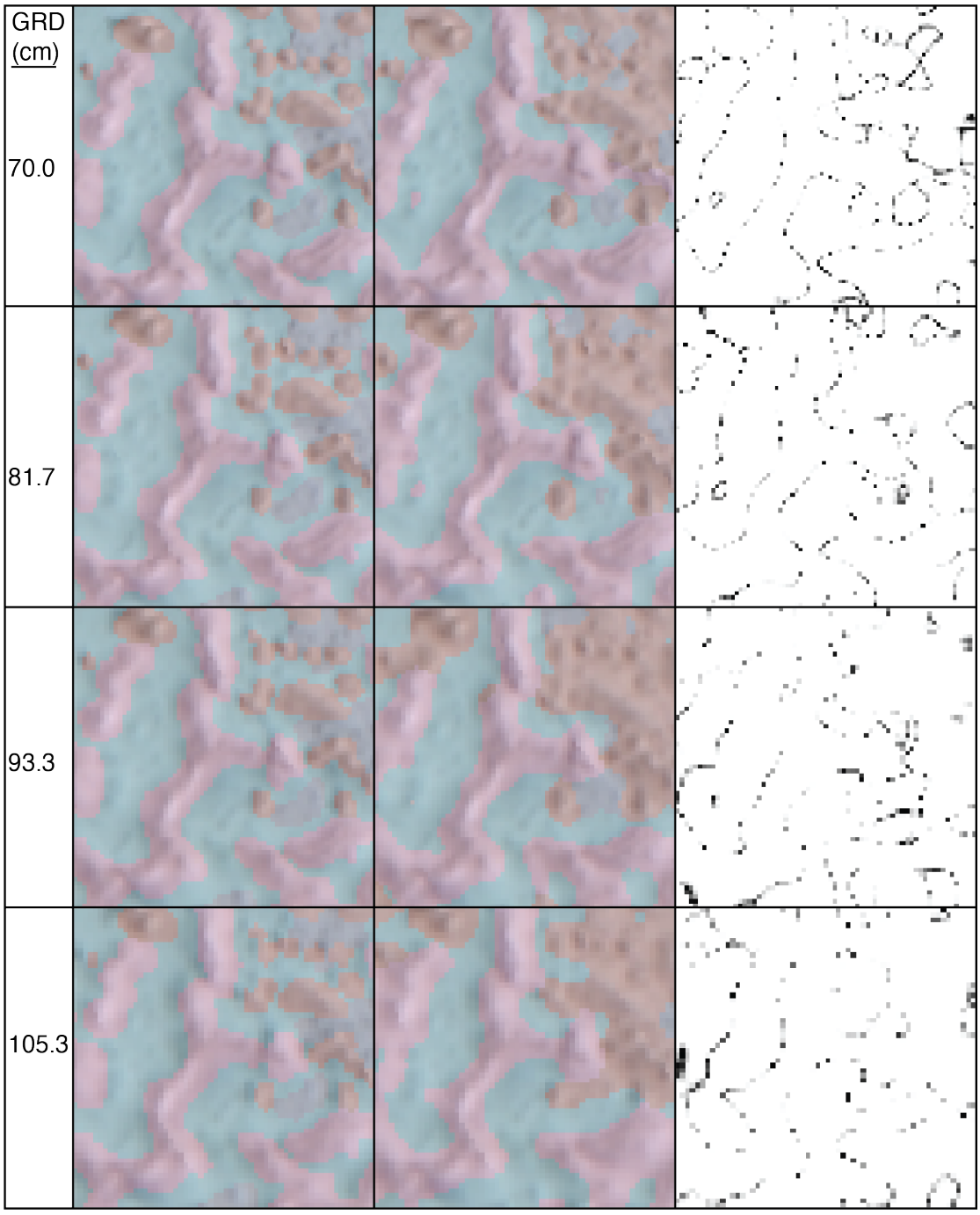

Fig. 3. 7 continued

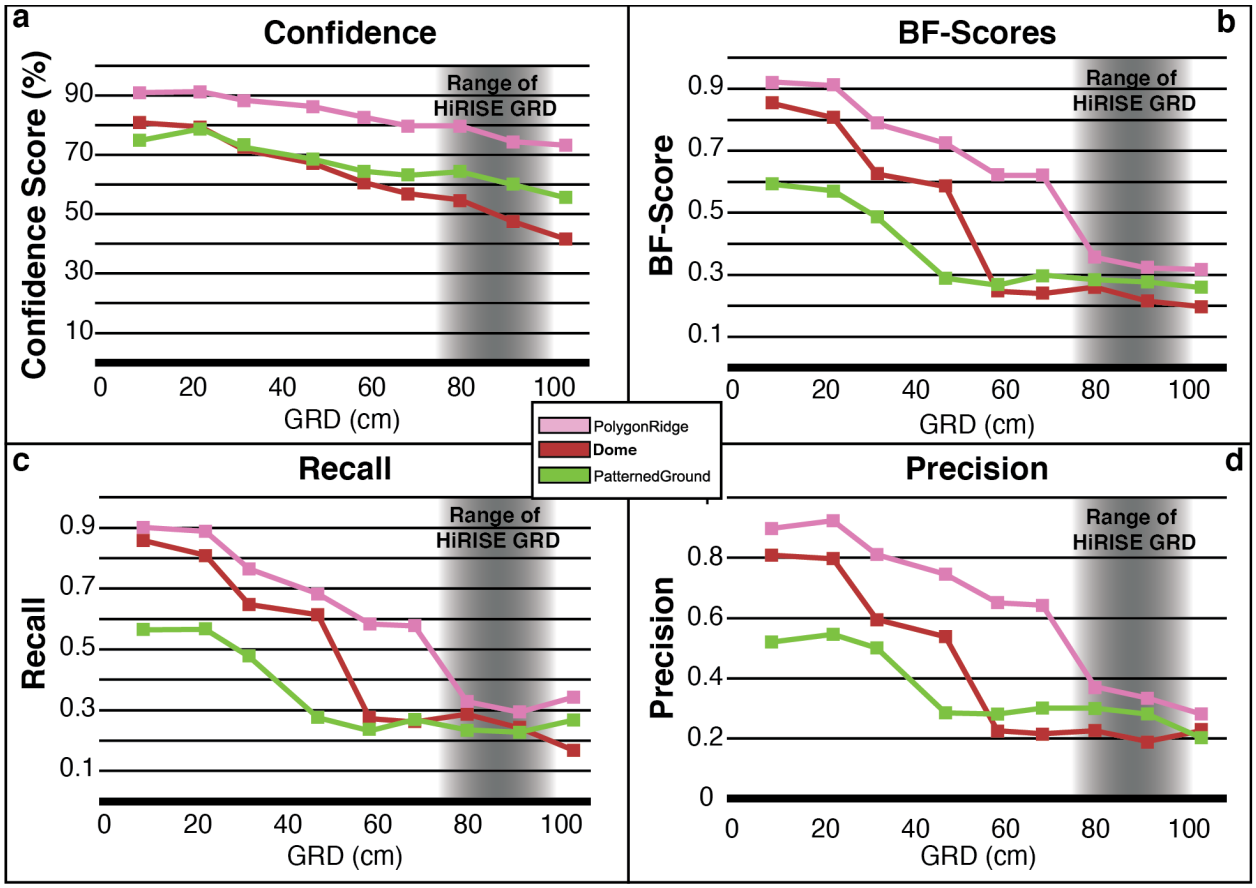

Fig. 3. 8. Performance metrics for RGB-Networks as a function of GRD. (**a**) Confidence Score, (**b**) BF-Score, (**c**) Recall, (**d**) Precision. Range of HiRISE GRDs (75 to 99 cm) is taken as three times typical HiRISE GSDs of 25 to 33 cm.

Table 3. 6. Performance metrics for RGB-Networks

	BF-Score			Recall			Precision		
GRD	Polygon Ridge	Dome	Patterned Ground	Polygon Ridge	Dome	Patterned Ground	Polygon Ridge	Dome	Patterned Ground
9.8	0.922	0.854	0.592	0.902	0.859	0.564	0.898	0.810	0.519
23.5	0.910	0.807	0.571	0.888	0.809	0.567	0.923	0.797	0.546
33.3	0.788	0.626	0.486	0.764	0.648	0.476	0.811	0.595	0.501
48.5	0.725	0.586	0.288	0.683	0.614	0.276	0.745	0.538	0.285
60.1	0.621	0.247	0.266	0.584	0.272	0.232	0.650	0.225	0.281
70.0	0.621	0.239	0.299	0.578	0.260	0.269	0.643	0.216	0.300
81.7	0.356	0.260	0.284	0.329	0.286	0.236	0.371	0.226	0.300
93.3	0.322	0.215	0.276	0.294	0.242	0.227	0.334	0.190	0.281
105.3	0.317	0.197	0.259	0.342	0.167	0.268	0.281	0.225	0.203

Confidence Scores (%)			
GRD	Polygon Ridge	Dome	Patterned Ground
9.8	91.0	80.9	74.9
23.5	91.3	79.4	78.8
33.3	88.3	71.6	72.6
48.5	86.3	67.2	68.5
60.1	82.7	60.7	64.5
70.0	79.8	56.9	63.2
81.7	79.8	54.8	64.3
93.3	74.5	47.6	60.0
105.3	73.3	41.7	55.6

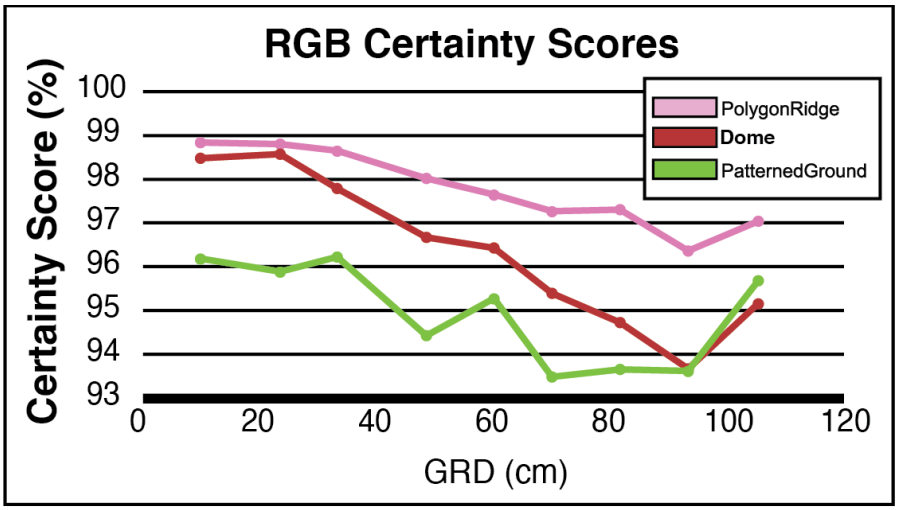

Fig. 3. 9. Certainty Scores for RGB-Network. Note the general decrease in Certainty Score values with increasing GRD.

Table 3. 7. Certainty Scores (%) for RGB-Networks

GRD (cm)	PolygonRidge	Dome	PatternedGround
9.8	98.8	98.5	96.2
23.5	98.8	98.6	95.9
33.3	98.6	97.8	96.2
48.5	98.0	96.7	94.4
60.1	97.6	96.4	95.3
70.0	97.3	95.4	93.5
81.7	97.3	94.7	93.7
93.3	96.4	93.7	93.6
105.3	97.0	95.2	95.7

PolygonRidge class, this drop occurs between GRD = 70.0 cm and GRD = 81.7 cm; for the Dome class the sharp drop occurs between GRD = 48.5 cm and GRD = 60.1 cm; and for the PatternedGround class the drop occurs between GRD = 33.3 cm and GRD = 48.5 cm. After the sharp drop off in Precision, Recall, and BF-Score, these values tend to bottom-out and do not decrease significantly with increasing GRD.

The RGB-Networks identified the PolygonRidge class more confidently than the Dome and PatternedGround classes at all GRDs, with Confidence Scores ranging from ~91% at the smallest GRDs down to ~78% at the largest GRD. At GRDs less than 33.3 cm, the RGB-Networks identified the Dome class with higher confidence than the PatternedGround class, but at GRDs equal to and larger than 33.3 cm, the PatternedGround class was more confidently identified than the Dome class. In other words, the Confidence Scores decrease with increasing GRD more rapidly for the Dome class than for the PatternedGround class. This is different than the pattern observed in the Precision, Recall, and BF-Scores, for which the Dome class outperformed the PatternedGround class from GRD = 9.8 cm to GRD = 60.1 cm.

In general, the Confidence Scores for a given class decrease monotonically with increasing GRD. However, there are exceptions; for example, the Confidence Score for the PatternedGround class increases slightly from GRD = 9.8 cm to GRD = 23.5 cm. It is interesting to note that while the BF-Scores tend to bottom-out for each class above a certain GRD, the Confidence Scores continue to decrease.

The Certainty Scores associated with the RGB-Network predictions are typically high (>99%). The low Certainty Score values are found along the margins between classes. These marginal areas are commonly one to three pixels across, regardless of the GRD of the image. Certainty Scores in the marginal areas are typically <60% and can be as low as 0% (meaning, in some cases, the expected values for two classes were equal).

5.2 DEM-Networks

The network predictions from the DEM-Networks were, by all measures, less reliable than those from the RGB- and RGB-DEM-Networks. The highest DEM-Network BF-Score was 0.471 for the PolygonRidge class at a GRD of 23.5 cm, which is nearly half the highest RGB-Network BF-Score of 0.92 for the PolygonRidge class at a GRD of 9.8 cm. Examples of DEM-Network predictions and associated Certainty Scores compared to ground truth labels are presented in Figure 3.11. The Precision and Recall values, BF-Scores, and Confidence Scores for the PolygonRidge, Dome, and PatternedGround classes are shown in Figure 3.11 and Table 3.8. Certainty Scores are presented in Figure 3.12 and Table 3.9.

As with the RGB-Network, the DEM-Network performed better on the PolygonRidge class than either the PatternedGround or Dome classes as determined by Precision, Recall, BF-Score, and Confidence Score. The Precision values, Recall values, and BF-Scores for the PolygonRidge and Dome classes generally decrease monotonically with increasing GRD. The most prominent exception of this generally monotonic decrease is the interval between GRD = 9.8 cm and GRD = 23.5 cm in the Precision values and BF-Scores. The PatternedGround class does not exhibit a monotonic decrease with increasing GRD in either its BF-Score or Precision values, but the Recall values do generally decrease with increasing GRD.

The DEM-Network most confidently identified the PolygonRidge class at all GRDs. The highest DEM-Network Confidence Score, 64.8%, was for the PolygonRidge class at a GRD of 23.5 cm. This value is 26.5% less than the highest Confidence Score for the RGB-Network. Interestingly, the PatternedGround class, on which the DEM-Network reported lower BF-Score values, has consistently higher Confidence Scores than the Dome class, with exception of the smallest GRD. However, the PatternedGround class Confidence Scores do not exhibit monotonic behavior with increasing GRD, but display an irregular sawtooth pattern with local minima occurring at GRD = 9.8 cm, 33.3 cm,

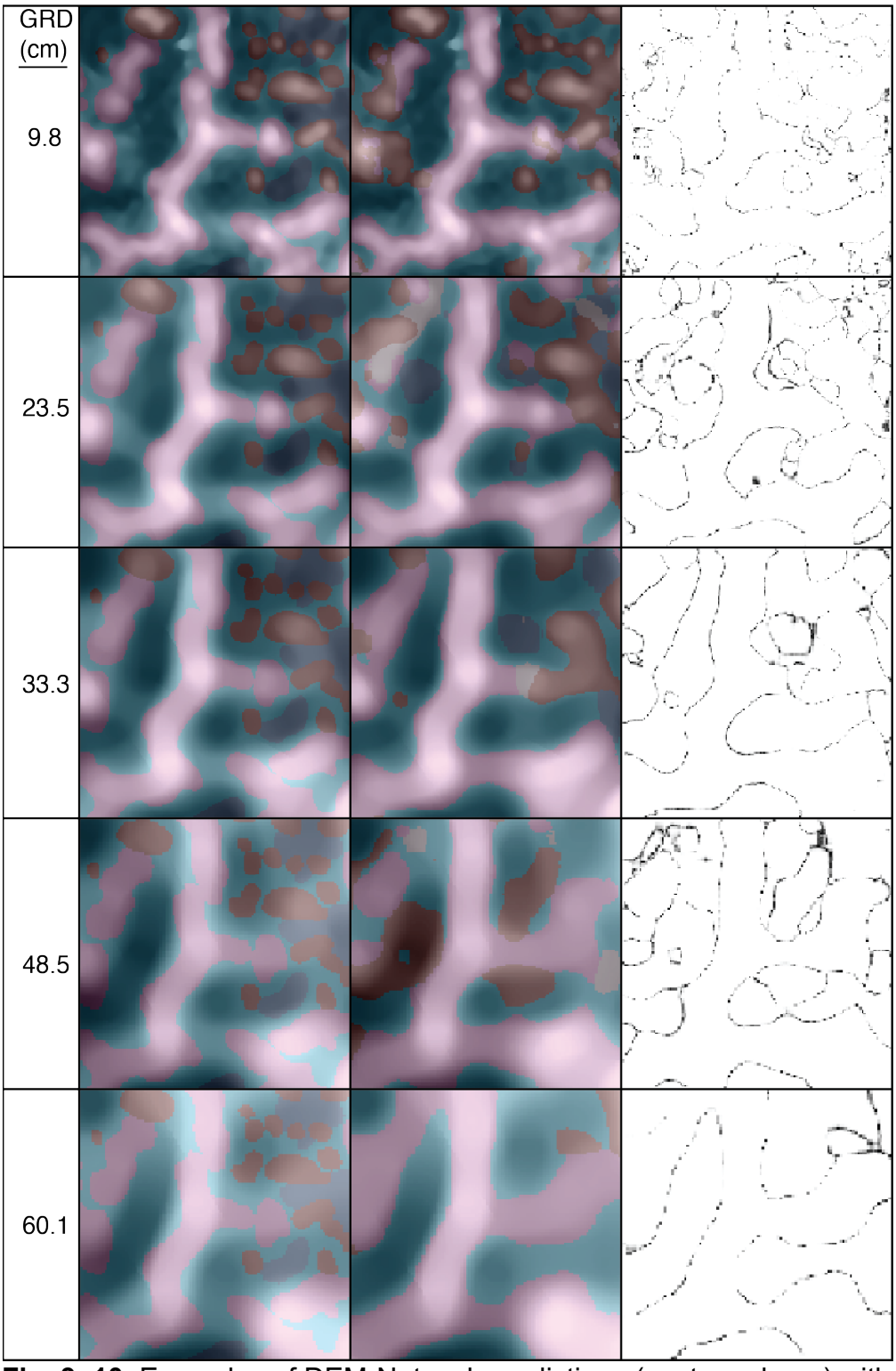

Fig. 3. 10. Examples of DEM-Network predictions (center column) with associated Certainty Scores (right column, black = 0%, white = 100%) and compared to ground truth labels (left column).

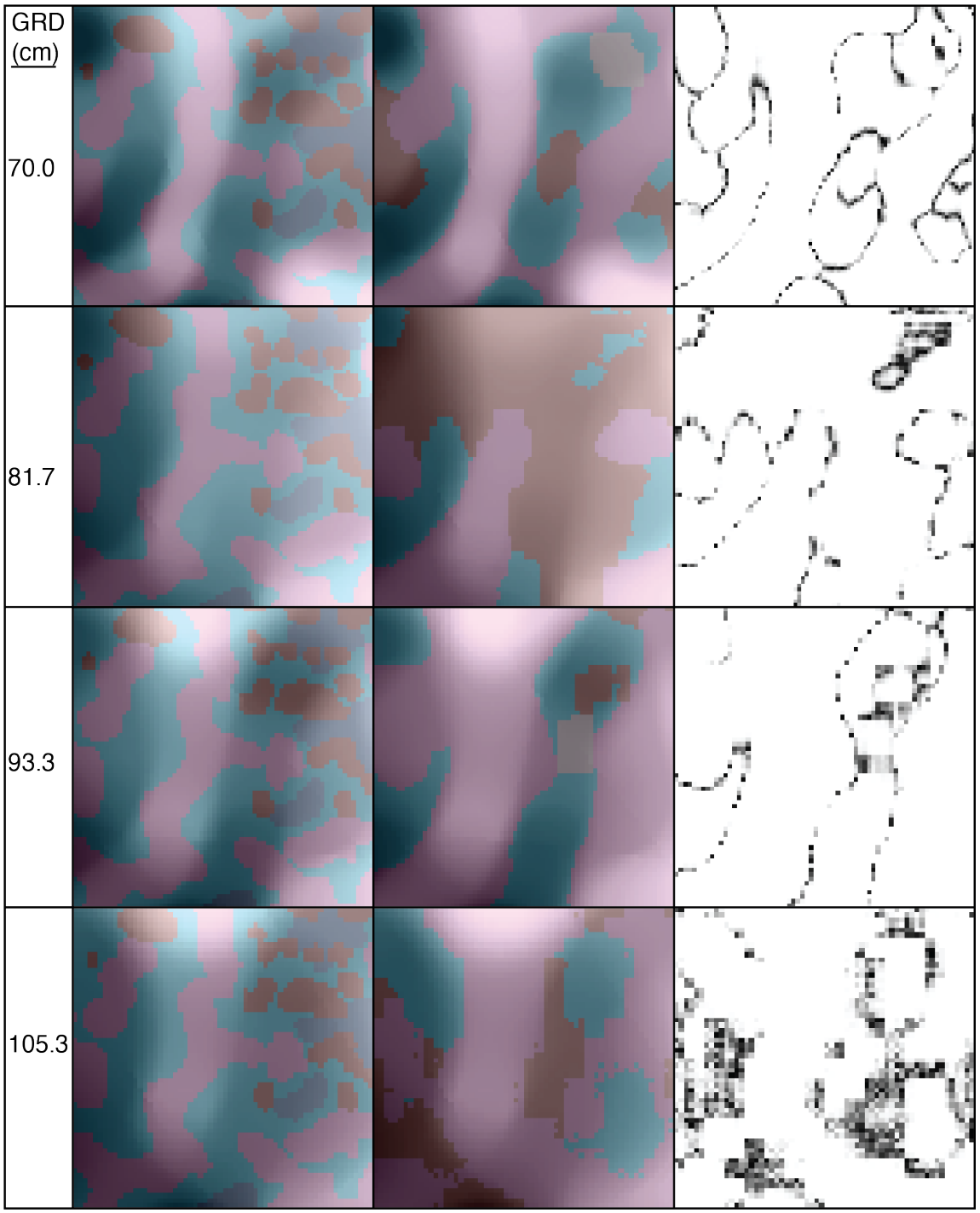

Figure 3.10 continued

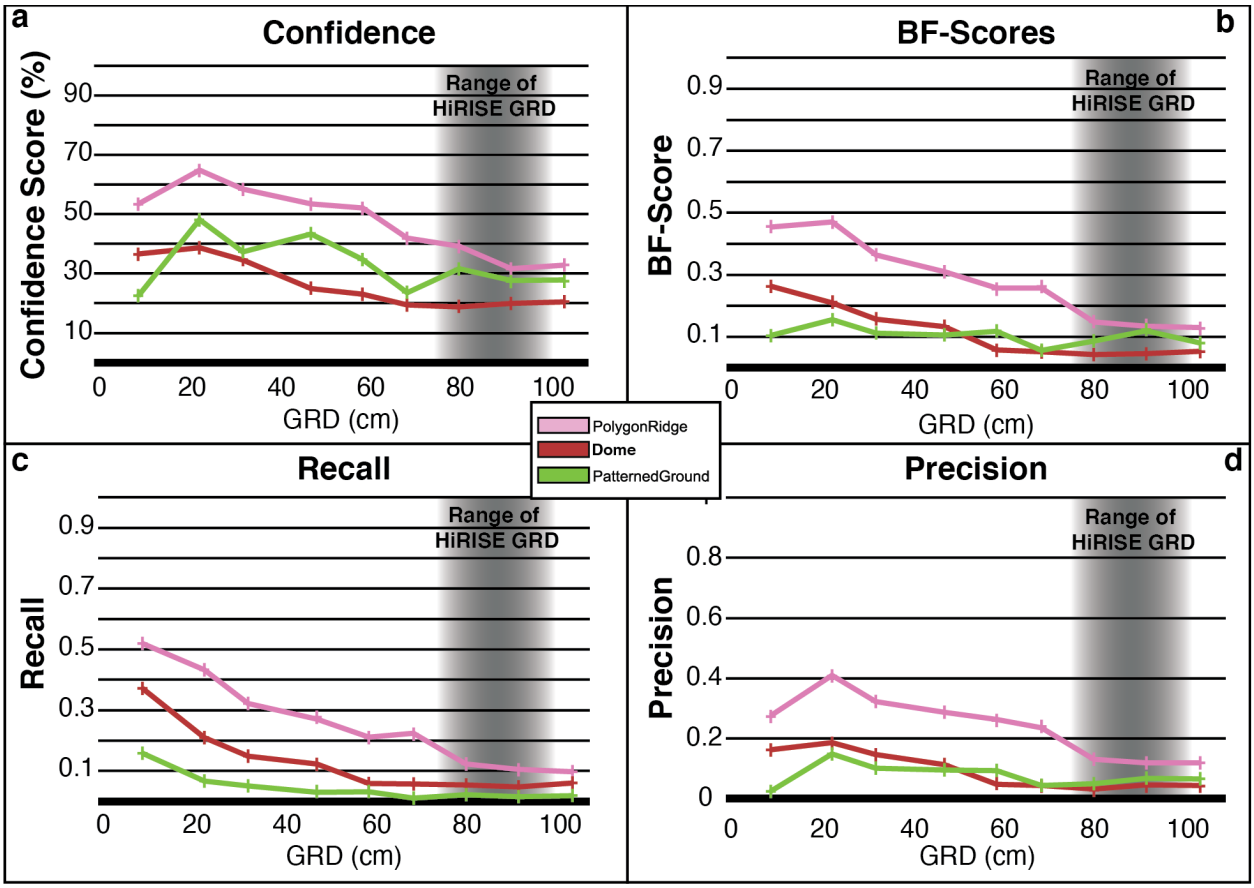

Fig. 3. 11. Performance metrics for DEM-Networks as a function of GRD. (**a**) Confidence Score, (**b**) BF-Score, (**c**) Recall, (**d**) Precision. Range of HiRISE GRDs (75 to 99 cm) is taken as three times typical HiRISE GSDs of 25 to 33 cm.

Table 3. 8. Performance metrics for DEM-Networks

	BF-Score			Recall			Precision		
GRD	Polygon Ridge	Dome	Patterned Ground	Polygon Ridge	Dome	Patterned Ground	Polygon Ridge	Dome	Patterned Ground
9.8	0.454	0.263	0.104	0.519	0.371	0.158	0.275	0.162	0.024
23.5	0.471	0.210	0.156	0.433	0.210	0.067	0.410	0.186	0.148
33.3	0.365	0.156	0.112	0.321	0.149	0.051	0.322	0.146	0.102
48.5	0.310	0.132	0.106	0.271	0.122	0.029	0.287	0.112	0.095
60.1	0.257	0.057	0.118	0.211	0.059	0.032	0.264	0.048	0.093
70.0	0.257	0.052	0.056	0.225	0.058	0.011	0.234	0.044	0.043
81.7	0.147	0.043	0.087	0.122	0.053	0.022	0.132	0.033	0.050
93.3	0.134	0.046	0.120	0.105	0.048	0.015	0.119	0.045	0.068
105.3	0.130	0.053	0.079	0.097	0.060	0.018	0.119	0.044	0.066

Confidence Scores (%)			
GRD	Polygon Ridge	Dome	Patterned Ground
9.8	53.4	36.5	22.5
23.5	64.8	38.6	48.1
33.3	58.5	34.6	37.4
48.5	53.5	25.0	43.4
60.1	52.1	22.9	34.6
70.0	41.9	19.4	23.5
81.7	39.2	18.7	31.6
93.3	31.6	19.9	27.7
105.3	32.9	20.4	27.8

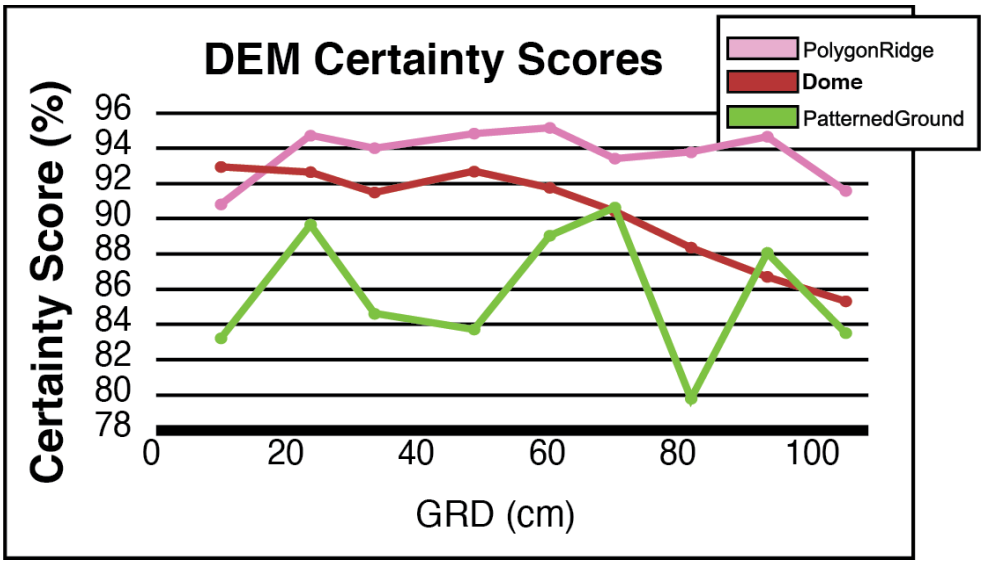

Fig. 3. 12. Certainty Score for DEM-Networks as a function of GRD.

Table 3. 9. Certainty Scores (%) for DEM-Networks

GRD (cm)	PolygonRidge	Dome	PatternedGround
9.8	90.8	92.9	83.2
23.5	94.7	92.6	89.7
33.3	94.0	91.5	84.6
48.5	94.8	92.7	83.7
60.1	95.2	91.8	89.0
70.0	93.4	90.4	90.6
81.7	93.8	88.4	79.8
93.3	94.7	86.7	88.1
105.3	91.6	85.3	83.5

and 70.0 cm. This irregular pattern is likely introduced into the Confidence Scores from the Certainty Scores, which also exhibit an irregular pattern. Consistent with the RGB-Network, the DEM-Network Confidence Scores for the PolygonRidge and Dome classes generally decrease with increasing GRD. The most prominent exception, again, occurs between GRD = 9.8 cm and GRD = 23.5 cm.

The Certainty Scores associated with the DEM-Network results are typically high (>99%) and are lowest along the margins between classes, consistent with the RGB-Network results (Figs. 3.7, 3.10). The marginal areas between classes with low Certainty Scores are typically on the order of one to three pixels across regardless of the GRD of the image and the Certainty Scores observed are commonly <60% and can be as low as 0%.

5.3 RGB-DEM-Networks

The RGB-DEM-Networks outperformed the DEM-Networks by all measures and performed nearly as well as or better than the RGB-Networks at all GRDs. The PolygonRidge class had the highest Precision values, Recall values, BF-Scores, and Confidence Scores of the three habitat classes across all GRDs for the RGB-DEM-Networks. The highest BF-Score achieved by the RGB-DEM-Network was 0.925 for the PoylgonRidge class at a GRD of 9.8 cm. Examples of RGB-DEM-Network predictions and associated Certainty Scores compared to ground truth labels are presented in Figure 3.13. The Precision and Recall values, BF-Scores, and Confidence Scores for the PolygonRidge, Dome, and PatternedGround classes are shown in Figure 3.14 and Table 3.10. Certainty Scores for the RGB-DEM-Networks are presented in Figure 3.15 and Table 3.11.

The overall character of the Precision, Recall, and BF-Score values as a function of GRD produced by the RGB-DEM-Networks are similar to those produced by the RGB-Networks. The general trend is for the Precision values, Recall values, and BF-Scores to decrease with increasing GRD, but sharp drops

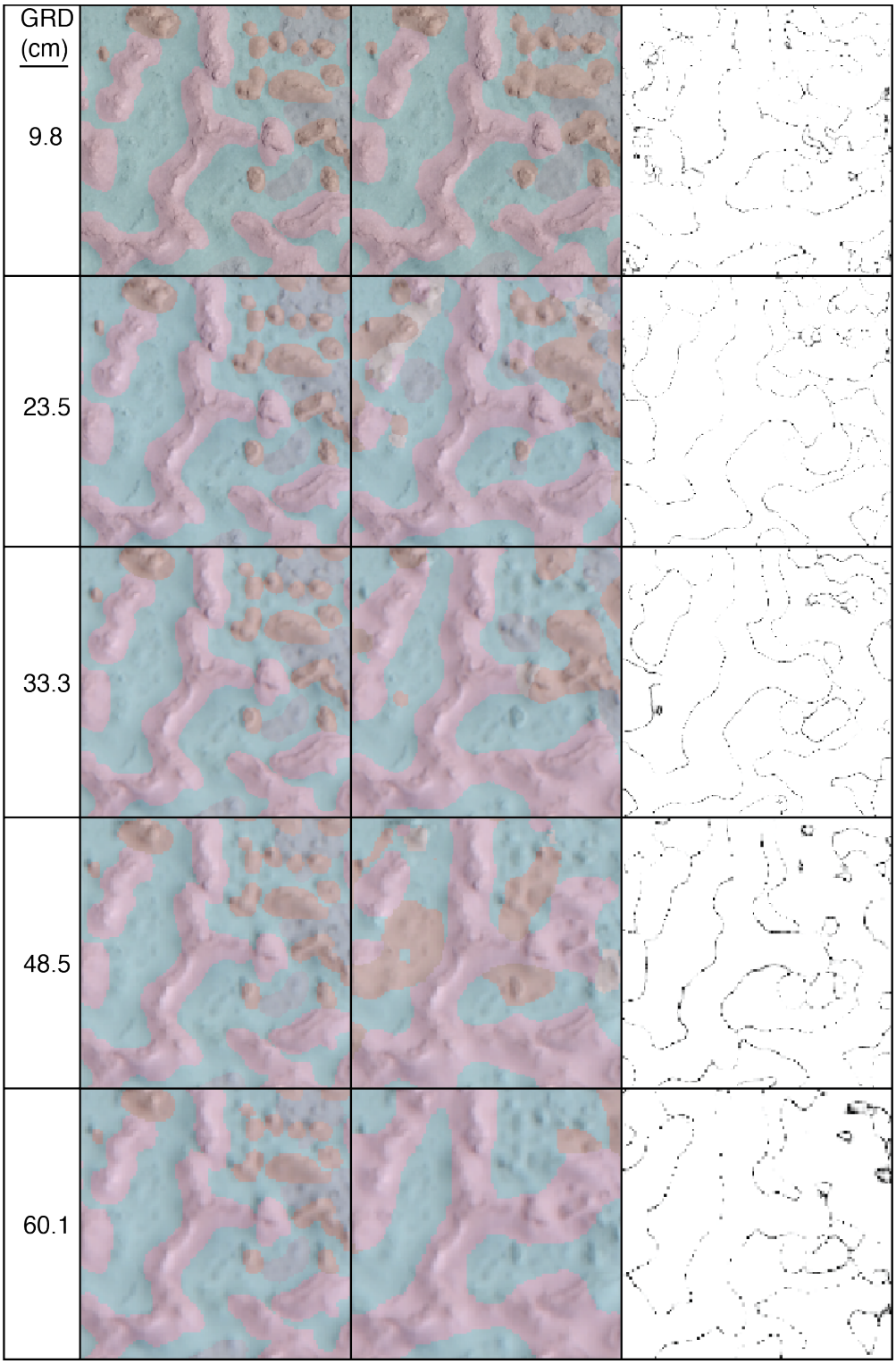

Fig. 3. 13. Examples of DEM-Network predictions (center column) with associated Certainty Scores (right column, black = 0%, white = 100%) and compared to ground truth labels (left column).

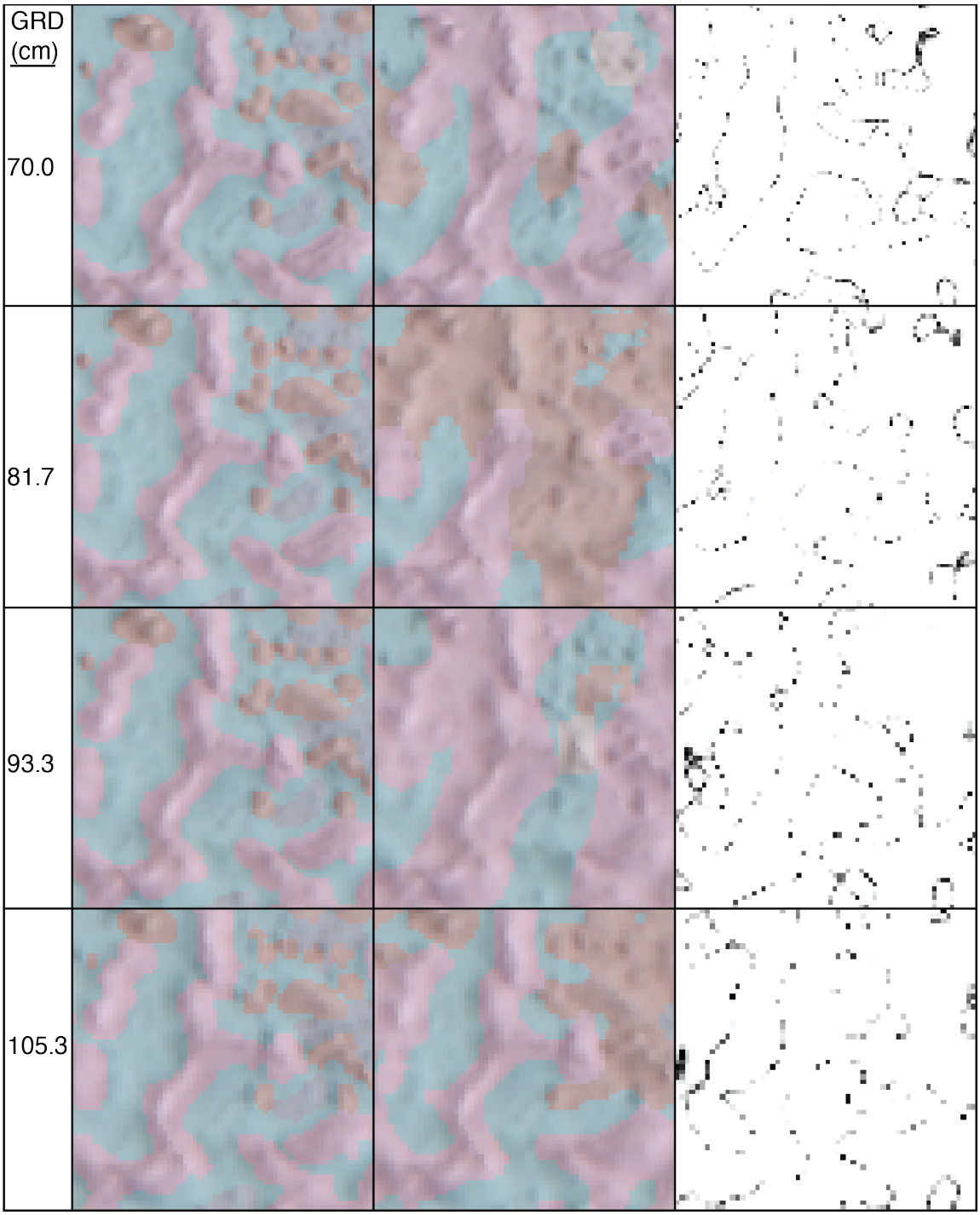

Figure 3. 13 continued

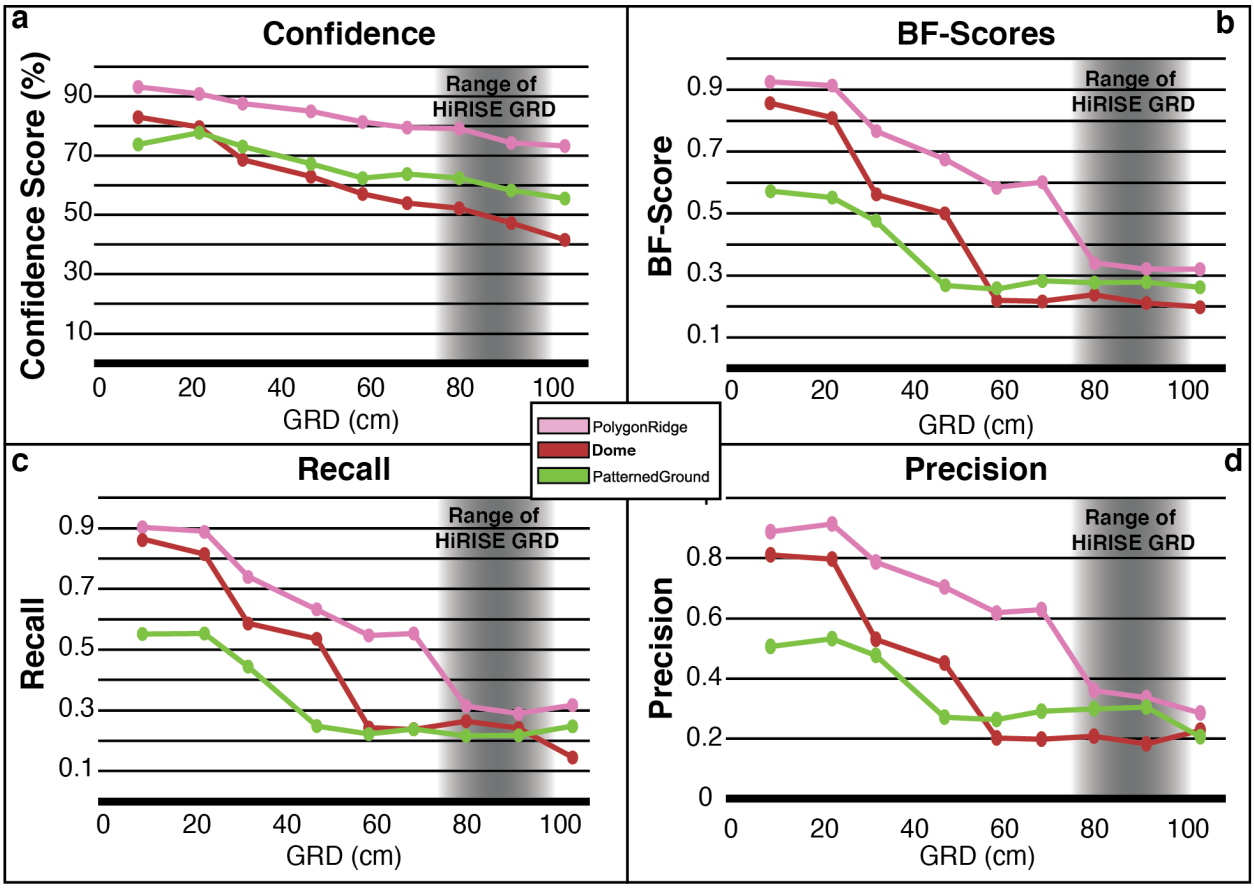

Fig. 3. 14. Performance metrics for RGB-DEM-Networks as a function of GRD. (**a**) Confidence Score, (**b**) BF-Score, (**c**) Recall, (**d**) Precision. Range of HiRISE GRDs (75 to 99 cm) is taken as three times typical HiRISE GSDs of 25 to 33 cm.

Table 3. 10. Performance metrics for RGB-DEM-Networks

	BF-Score			Recall			Precision		
GRD	Polygon Ridge	Dome	Patterned Ground	Polygon Ridge	Dome	Patterned Ground	Polygon Ridge	Dome	Patterned Ground
9.8	0.925	0.857	0.573	0.903	0.864	0.551	0.888	0.811	0.506
23.5	0.913	0.810	0.552	0.889	0.815	0.553	0.913	0.797	0.532
33.3	0.766	0.562	0.475	0.740	0.587	0.444	0.788	0.529	0.477
48.5	0.676	0.500	0.267	0.632	0.535	0.247	0.705	0.451	0.270
60.1	0.585	0.220	0.256	0.546	0.244	0.222	0.618	0.201	0.263
70.0	0.601	0.217	0.282	0.553	0.236	0.238	0.628	0.198	0.291
81.7	0.342	0.238	0.276	0.314	0.263	0.215	0.360	0.207	0.299
93.3	0.321	0.211	0.279	0.290	0.242	0.218	0.336	0.183	0.304
105.3	0.320	0.199	0.262	0.316	0.145	0.248	0.284	0.227	0.205

Confidence Scores (%)			
GRD (cm)	Polygon Ridge	Dome	Patterned Ground
9.8	93.8	84.5	74.6
23.5	90.9	79.7	77.7
33.3	87.5	68.6	73.0
48.5	85.0	63.0	67.2
60.1	81.4	57.1	62.4
70.0	79.5	54.0	63.8
81.7	79.1	52.2	62.5
93.3	74.4	47.3	58.3
105.3	73.3	41.7	55.6

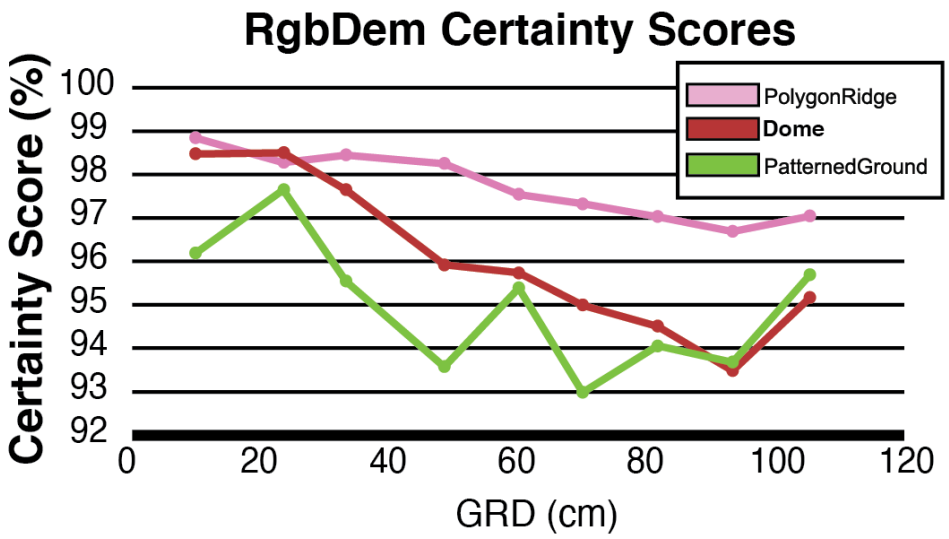

Fig. 3. 15. Certainty Score for RGB-DEM-Networks as a function of GRD.

Table 3. 11. Certainty Scores (%) for RGB-DEM-Networks

GRD (cm)	PolygonRidge	Dome	PatternedGround
9.8	98.8	98.5	96.2
23.5	98.3	98.5	97.7
33.3	98.5	97.7	95.5
48.5	98.3	95.9	93.6
60.1	97.5	95.7	95.4
70.0	97.3	95.0	93.0
81.7	97.0	94.5	94.1
93.3	96.7	93.5	93.7
105.3	97.0	95.2	95.7

in these values occur over a single GRD interval. For the PolygonRidge class this interval is between a GRD of 70.0 cm and 81.7 cm; for the Dome class a sharp drop occurs between GRD = 48.5 cm and GRD = 60.1 cm; and for the PatternedGround class the interval is between a GRD of 33.3 cm and 48.5 cm. The intervals over which a sharp drop in Precision, Recall, and BF-Score occur are consistent across the RGB-, DEM-, and RGB-DEM-Networks. As with both the RGB- and DEM-Networks, the Precision, Recall, and BF-Score values tend to level out with increasing GRD after the sharp drop.

Across all GRDs, the most confidently identified class with the RGB-DEM-Networks was the PolygonRidge class. Confidence Scores range from ~93.8% at the smallest GRDs down to ~73% at the largest GRD. As with the RGB-Network results, at GRDs less than 33.3 cm, the RGB-DEM-Networks identified the Dome class with higher confidence than the PatternedGround class, but at GRDs equal to and larger than 33.3 cm, the PatternedGround class was more confidently identified than the Dome class. This contrasts with the patterns observed in the Precision, Recall, and BF-Scores wherein the Dome class outperformed the PatternedGround class up to a GRD of 60.1 cm.

In general, the Confidence Scores for each class decrease with increasing GRD, however, as with the RGB-Network results, there are exceptions. The Confidence Score for the class PatternedGround increases slightly from GRD = 9.8 cm to GRD = 23.5 cm. The trend observed in the Confidence Scores for all classes is an approximately linear decrease with increasing GRD. It is interesting to note, again, that although the BF-Scores tend to bottom-out at GRDs larger than some value specific to each class, the Confidence Scores, generally continue to decrease. An exception is observed for the PatternedGround class for which the Confidence Scores remain relatively constant between GRD = 48.5 cm and GRD = 70.0 cm.

The Certainty Scores associated with the RGB-DEM-Network predictions are, like the RGB-Network and DEM-Network results, typically high (>99%) even over areas where false predictions were made (Figs. 3.7, 3.10, 3.13). Areas with

low Certainty Score values are along the margins between classes. The marginal areas are commonly one to three pixels across, regardless of the GRD of the image. Certainty Scores in the marginal areas are typically <60% and can be as low as 0%.

6. Discussion

6.1 Interpretation of Confidence Scores

We observed two differences between how the BF-Scores and Confidence Scores trend as a function GRD. First, we found that Confidence Scores remained high relative to BF-Scores as the GRD of the network input images increased. This means that as the accuracies (as measured by the BF-Scores) of the networks drop, the Certainty Scores for each class also drop (Figs. 3.9, 3.12, 3.15), resulting in Confidence Scores that decrease less steeply than BF-Scores with increasing GRD. Second, we did not observe a steep drop in Confidence Scores at the GRDs where the BF-Scores for each class dropped, further indicating that the Certainty Scores drop with the BF-Scores resulting in higher Confidence Scores than BF-Scores.

In this study, low Certainty Scores were predominantly observed at the margins between classes. Therefore, if a network accurately identified the bulk of a feature, but was inaccurate with its boundary, the Confidence Score would remain high relative to the BF-Score. In this way, we consider the Confidence Score a better measure of the identifiability of a feature than accuracy metrics such as the BF-Score.

6.2 General trends in performance metrics and habitat identifiability

The general characteristics of Precision, Recall, and BF-Score values as a function of GRD were relatively consistent between the RGB-, DEM-, and RGB-DEM-Networks (Fig. 3.16). The shapes can be described as having an approximately linear decrease followed by a sharp drop off across a specific GRD interval. We interpret the sharp drops in Precision, Recall, and BF-Score to

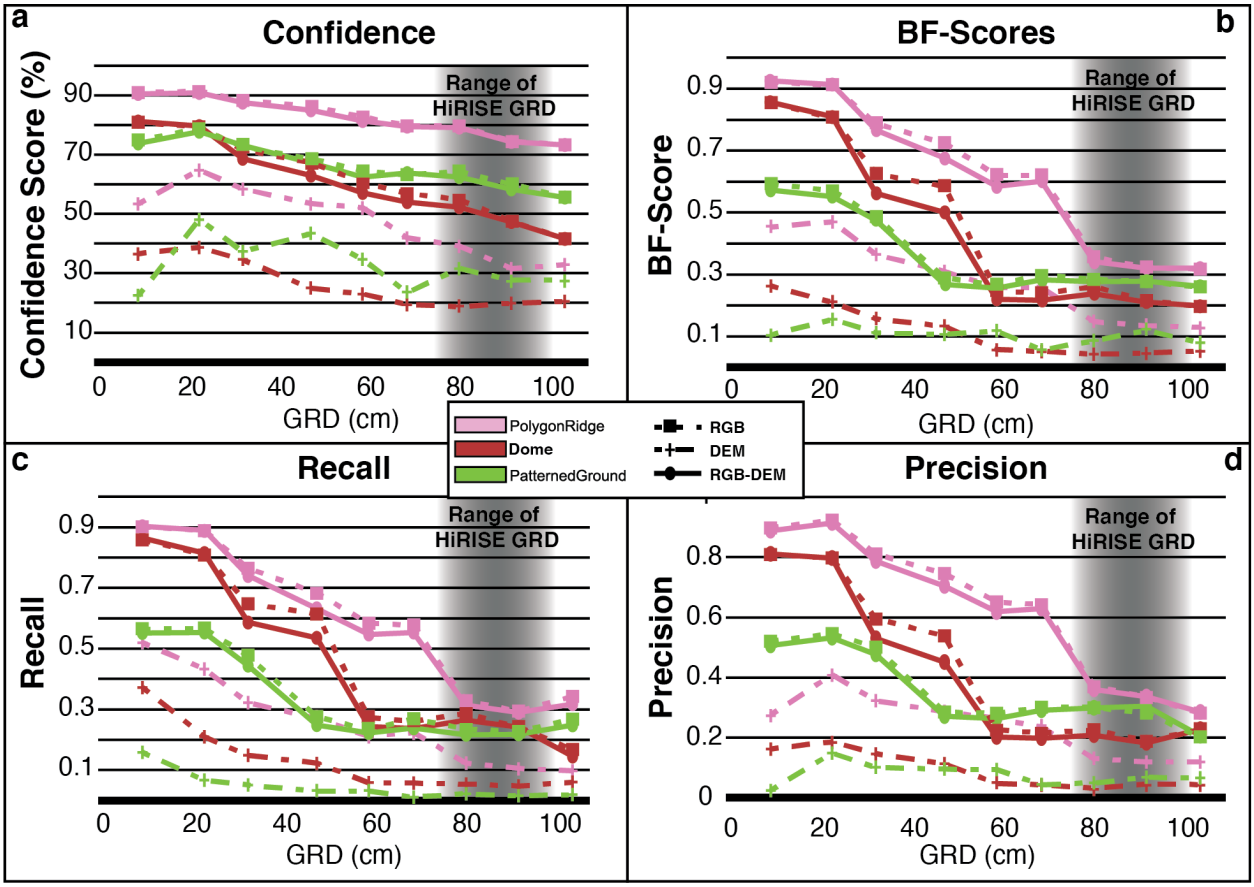

Fig. 3. 16. Comparison of performance metrics for RGB-, DEM-, and RGB-DEM-Networks as a function of GRD. (**a**) Confidence Score, (**b**) BF-Score, (**c**) Recall, (**d**) Precision. Range of HiRISE GRDs (75 to 99 cm) is taken as three times typical HiRISE GSDs of 25 to 33 cm.

indicate that a spatial dimension threshold critical for accurately segmenting (i.e., drawing a boundary around) a feature has been crossed. For the PolygonRidge class, this drop occurs between GRDs 70.0 cm and 81.7 cm, approximately one third the width of a typical PolygonRidge (2.29 m). The networks experience a drop in segmentation performance for the Dome class between GRDs 48.5 cm and 60.1 cm, approximately on third the average Dome diameter (1.61 m). The drop in network performance for the PatternedGround class occurs between GRDs 33.3 cm and 48.5 cm, an interval that is, again, approximately one third the characteristic length scale of the PatternedGround class (1.16 m). The apparent trend is that a sharp drop in the ability to accurately segment a feature occurs at a GRD approximately equal to one third the characteristic length scale of the feature. An analogy can be made to the Nyquist sampling frequency for resolving a feature in an image wherein 2 to 3 pixels are generally required for a feature to be resolved in an image (assuming the quality of the imaging system approaches that of a diffraction limited system).

Our results show a steep increase in the ability to segment a feature will occur when the GRD of the image is one third the length scale of the feature; that is, when the feature is spanned by 9 to 12 pixels. However, to achieve a 1-sigma level of identification confidence (Confidence Score ≥~85%) for the PolygonRidge class, a GRD approximately one fifth its length scale is required, i.e., it must be spanned by 15 to 20 pixels. Conversely, Domes require a GRD ~6% their characteristic length scale (spanned by 50 to 65 pixels) to be identified at the 1-sigma confidence level, and PatternedGround could not be identified at the 1-sigma confidence level at the resolutions studied here.

These results emphasize the complexity and feature-specific nature of establishing identification thresholds in spatial resolution. One contributing factor to the GRD necessary to confidently identify a class may be the presence (or absence) of other classes in the terrain that could be confused with it. For example, the PolygonRidge class could potentially be confused with members of the ErodedRidgesAndDomes class, DrainageChannelRidge class, and large or

elongate members of the Dome class. However, the Dome class could be confused with the many and various small topographic features within the SdP basin that makeup the MottledGround class, and PatternedGround could be confused with other flat surfaces with patterns, such as SaltPan and MudCracks that make up a large majority of terrain. We suggest that the Dome and PatternedGround classes are likely more difficult to distinguish from other features than the PolygonRidge class, so more spatial resolving power is necessary to identify them confidently. Subtleties like these highlight the importance of building Confidence Scores on a feature-by-feature basis and the utility of Confidence Scores for deciding which habitats on Mars have the best chance of being confidently identified.

6.3 A template for building identification confidence curves

The methods by which we derived Confidence Scores for a suite of features provides a template for establishing the identifiability of features as a function of GRD. In our study, the PolygonRidge class was more confidently identified by all networks and across all GRDs than any of the other habitat classes. Confidence Score curves could be used for triaging habitats into a prioritized list of astrobiology targets and for establishing specification requirements for future planetary imaging systems. For example, if the goal were to identify PolygonRidges on Mars with at least 85% confidence, then our results indicate a system capable of capturing images with a GRD of approximately 50 cm or better would be desired. Ideally, such identification confidence curves would exist for many Mars analog environments and the target-selection-scale habitats that could be most confidently identified would be prioritized for exploration and the locations on Mars likely to contain them would be prioritized for targeted high-resolution imaging. This approach would serve to focus Mars exploration from the scale of regional habitability to the target-selection scale – a scale more in line with the evolving goals of the Mars Exploration Program.

This study builds on previous orbit-to-ground science conducted by the Life in the Atacama (LITA) project (e.g., Cabrol et al., 2007). Our investigation represents a first step toward a comparative evaluation of the identifiability of microbial habitats in images taken from overhead across many terrestrial Mars analog environments. Extending this work to establish the most- and least-identifiable habitats within presently-available images of Mars would be useful for triaging habitats into a prioritized list of astrobiology targets and for informing future instrument specification requirements. Other characteristics that would be relevant to such a prioritized list include whether the habitats are refugia (Carrier et al., 2020), the sustainability of their habitability (Ehlmann et al., 2016), whether they have a taphonomic window (Summons et al., 2011), the types of organisms that the habitats harbor (Onstott et al., 2019), and their accessibility to robotic (or human) exploration (Hays, 2015, pg. 109). Additionally, our results are directly applicable to the identification of habitats like those at SdP on Mars if: 1) the same types of features exist on the surface of Mars as they do on Earth, and 2) erosion has not modified their appearance on Mars to the point that they are no longer recognizable.

6.4 DEM data do not enhance semantic segmentation

The performance of the RGB-DEM-Network was, apart from GRD = 9.8, is not significantly better than that of the RGB-Network by itself. Additionally, the DEM-Networks reported BF-Scores and Confidence Scores consistently 2 to 3 times worse than the RGB-Networks. We interpret this to mean that DEM data do not aid in the task of semantic segmentation. Elevation data are desirable for many geomorphological and geological analyses, but semantic segmentation of the features in this study does not appear to be among them. However, under different conditions this may not hold true. For example, if the topography of features were to be more pronounced than this in this study or if the phase angle were less optimal, then DEM data may prove more valuable.

7. Conclusions

In this study we developed one possible method that can serve as a template for determining feature identification confidence as a function of image spatial resolution (ground resolved distance, GRD) using a deep learning-based approach. We applied our method to the identification of microbial habitats in images of the Mars analog environment Salar de Pajonales (SdP). We found that in images with GRDs comparable to those of HiRISE, the PolygonRidge habitat class could be identified with a Confidence Score between 74% and 80%, the Patterned Ground habitat class could be identified with Confidence Scores of 60% to 65%, and the Dome habitat class could only be identified with Confidence Scores between 47% and 55%. The highest Confidence Score achieved in our study was 93.81% (for the PolygonRidge class with the RGB-Network) and the lowest was 22.48% (for the PatternedGround class with the DEM-Network).

We also tested the value a DEM adds to the semantic segmentation task by incorporating DEM data alongside RGB data in a fully convolutional neural network (FCN). We found that adding DEM data does not enhance the FCN performance. We attribute this to the fact that the DEM data confound the signal of the RGB data, which are more reliable for the task of semantic segmentation.

Appendix III

Item A: Primer on Neural Networks

This section is intended to provide a brief background on artificial neural networks (ANNs) to those for whom this topic is unfamiliar. We recognize that ANNs have wide ranging applications but choose to focus this section on the use of ANNs for image classification problems, especially classification of images of planetary surfaces. In this discussion we hope to provide a basis for understanding *convolutional neural networks* (CNNs), which are at the core of the methodology used in this study, and how CNNs can be applied to planetary image classification problems. For a more comprehensive background on deep learning methods, the reader is referred to (Nielsen, 2015; Goodfellow et al., 2018).

Artificial neural networks

An ANN, as the name implies, is a system of interconnected artificial neurons. In our discussion of ANNs, we will refer to artificial neurons simply as "neurons". ANNs take an input and map it to an output, so in this way they can be thought of as elaborate functions that are comprised of increasingly less elaborate sub-functions.

Let us consider an example of a simple kind of ANN called a *multilayer perceptron* (MLP, Rosenblatt, 1962) or *feedforward* network (Fig. A1). Our MLP will take an image of a planetary surface as input and predict a single label for that image as an output. Our MLP consists of four *layers*: an input layer (the image of a planetary surface), two layers of neurons, and an output layer (a predicted label for the image).

Each layer in the network maps multiple inputs to multiple outputs. The layers can be thought of as sub-functions of the network. Between the input layer (often called the visible layer) and output layer are two layers, or 1-dimensional (1D) vectors, of neurons. The layers of neurons between the input and output

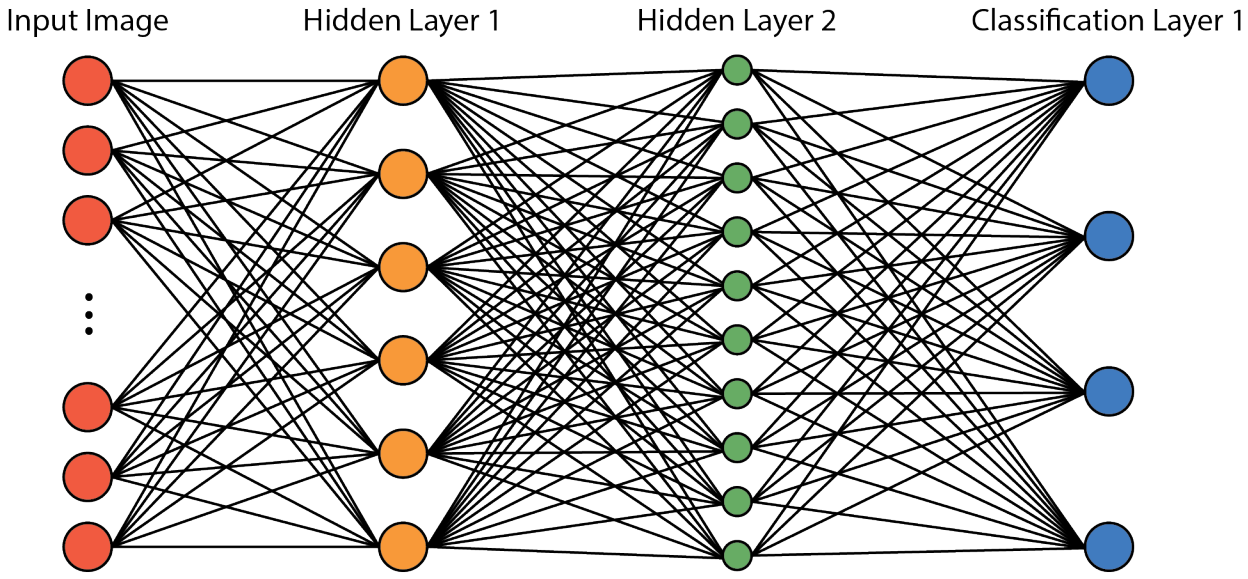

Fig. A3. 1 Multilayer perceptron network with 2 hidden layers. Colored circles represent neurons and black lines represent connections between neurons.

layers are often referred to as the network's *hidden layers* (Goodfellow et al., 2018). Let us assume that our input images are 20 by 20 pixels, our first hidden layer has $n = 6$ neurons, our second hidden layer has $k = 10$ neurons, and our output layer has 4 neurons that correspond to image classification labels. An individual neuron can be thought of as a sub-function to the layer that takes inputs and delivers an output called an *activation*. The neurons in each layer are connected to every neuron in the previous layer such that the activation values of the neurons in layer 1 determine the activation values of each neuron in layer 2.

Networks in which every neuron in one layer is connected to every neuron in the adjacent layers are called *fully connected*, or *dense*. One important characteristic of fully connected layers is that the spatial association of pixels is irrelevant. In image classification, it is easy to see how it could be important to consider the spatial relationship of pixels. We will return to this idea in our discussion of convolutional neural networks.

Each pixel of our input planetary surface image can be thought of as a neuron. It is common practice to normalize the input data, which effectively transforms each pixel to an "activation" value. By thinking of our input image as just another layer of neurons, we can view the whole ANN as a series of cascading patterns. The input image is the first pattern of activated neurons, which determines the pattern neuron activations in the next layer, and so on until a final pattern is created in the output layer corresponding to a label for the scene.

To see how the activation value of a single neuron depends on the activation values of previous neurons, let us consider $a_k^{(2)}$, the activation value of neuron k in the second hidden layer of our MLP:

$$a_k^{(2)} = \sigma(\Sigma_0^n(w_{k,n}a_n^{(1)}) + b_k)$$

The first step in calculating $a_k^{(2)}$ is to multiple the activation value of each neuron in layer 1 by the appropriate weight value, $w_{k,n}$, and then sum the products, $\Sigma_0^n(w_{k,n}a_n^{(1)})$. The weight value, $w_{k,n}$, determines the strength of the connection

between neuron k in layer 2 and neuron n in layer 1 and can be positive or negative (or zero). The weighted sum of activation values is shifted by a bias parameter, b_k. The bias parameter can be thought of as a "threshold" that controls how large or small the $\Sigma_0^n(w_{k,n}a_n^{(1)})$ term must be before it influences the activation value of neuron k in layer 2.

An *activation function*, σ, is applied in an element-wise fashion to the weighted sum and bias values. The activation function is a transformation function that maps activation values that could range from $-\infty$ to ∞ to values that, classically, range from 0 to 1 (Nielsen, 2015). Several activation functions exist, but a common one in modern ANNs is the rectified linear unit (ReLU) function that maps values ≤ 0 to 0 and values > 0 to themselves, i.e., max(0, x) (Ouyang, 2013).

Now that we have explored how a single neuron is connected to all neurons in the layer preceding it, we can consider all neurons in layer 2 and their connections to all neurons in layer 1 with a succinct expression:

$$a^{(2)} = \sigma(W^{(2)}a^{(1)} + b^{(2)})$$

The 1D vector of neuron activation values in layer 2, $a^{(2)}$, is a function of the neuron activation values in layer 1, $a^{(1)}$, multiplied by the matrix of weight values for neurons in layer 2, $W^{(2)}$, and shifted by a 1D vector of biases for the neurons in layer 2, $b^{(2)}$. Each row of the weight matrix, W, corresponds to the weights for a single neuron in layer 2, so that the weight matrix that connects layer 1 to layer 2 is of size n by k (i.e., the number of neurons in layer 1 times the number of neurons in layer 2).

In our example, layer 1 is the first hidden layer of 6 neurons, and layer 2 is our second hidden layer of 10 neurons. So, $W^{(2)}$ contains 60 weight values. Each neuron in layer 2 also has a bias term for a total of $k = 10$ bias terms in $b^{(2)}$. Together, the weights and biases of an ANN are its adjustable *parameters*. The number of adjustable parameters in our simple MLP is $400 \times 6 + 6 \times 10 + 10 \times 4 = 2500$ weights, and $6 + 10 + 4 = 20$ biases for a total of 2520

parameters. It is easy to see how the number of adjustable parameters in increasingly deep networks with larger input image sizes can become quite large.

When a network is said to be *learning* or *training*, this is really the incremental modification of the network parameters to minimize the difference between the actual and the expected output values of the network. The function that quantifies the difference between the actual and expected output values over a single training example is the *loss function*. *Backpropagation* is used to calculate the gradient of the loss function in order to descend the gradient and find a local minimum. The *objective function*, or *cost function*, is comprised of all the loss functions for the whole training data set, for example as a simple sum of loss functions plus a regularization term. Finding a combination of network parameter values that (locally) minimizes the objective function is the goal of network training. A common algorithm used to descend the gradient of the objective function is *stochastic gradient descent*. The *learn rate* of a network is a measure of how quickly the gradient of the objective function is descended during training. One full pass of the training data through the network is called an *epoch*. Typically, dozens to hundreds of epochs are required to arrive at a local minimum of the objective function. To avoid "jumping" out of a stable local minimum point of the objective function, it is common practice to reduce the learn rate by some factor (commonly by 10^{-1}) over a given number of training epochs (typically 10 epochs).

Convolutional neural networks

While feedforward networks, like the one discussed above, can be powerful tools for image classification problems, for planetary science problems the size of these networks is often impractically unwieldy. Enter, *convolutional neural networks* (CNNs).

A CNN is a type of ANN that uses *convolution*[4] instead of simple matrix multiplication in one or more of its layers (LeCun et al., 1989; Goodfellow et al., 2018). Convolution has many advantages over matrix multiplication that include, but are not limited to, sparser connections between network layers, lower memory requirements for the network, and faster network training timeframes (LeCun et al., 2015; Goodfellow et al., 2018).

Many aspects of CNNs were inspired by how the mammalian visual cortex works (Goodfellow et al., 2013; Goodfellow et al., 2018, Ch. 9), and these networks excel at image recognition and classification tasks (Krizhevsky et al., 2017). These qualities of CNNs have made their popularity explode in the past several years (e.g., LeCun et al., 2015) and make them a natural choice for use in planetary image classification problems.

The hidden layers of a CNN are more complex than the hidden layers of simpler networks, such as the MLP described in section 1.2.1. However, a layer in a CNN can still be viewed as a function with inputs, outputs, and trainable parameters. A typical layer in a CNN is comprised of a *convolution stage*, a *detector stage*, and a *pooling stage*. In the convolution stage, many filters (dozens to hundreds) consisting of learnable weight values are passed over the input image. Filters in a convolutional layer can range in size but are typically between 1x1 to 7x7. Filters larger than 1x1 consider the spatial relationship of pixels within their frame, which is an advantage over dense layers. The element-wise multiplication of a filter with its input values is the eponymous convolution operation.

The many filters within a layer are trained, i.e., small modifications are made to the weights, in parallel. The product of a filter convolved with the input

---

[4] It should be noted that convolution as used in the context of CNNs is not precisely the same as the mathematical convolution operation. Specifically, CNNs often employ cross-correlation and call it convolution (Goodfellow et al., 2018).

data is called a *feature map*. With training, the CNN learns weight values for its filters that, when convolved with the input data, produce feature maps that capture some useful quality, or feature, of the input image. In the shallower layers of a network, features that CNNs commonly learn include edges, corners, and lines. Increasingly complex features are extracted in the deeper layers of the network.

In image analysis, capturing edges and textures in images using convolution is common practice. Filters are designed specifically for such purposes. In CNNs, the filters are learnable, so it is not necessary for the architect of the network to hard code feature detectors into the network, and, in fact, networks with supervised filters are outperformed by those with learned filters (LeCun et al., 2015).

After a feature map is produced from the convolution stage, it is passed through an activation function in the detector stage. A common activation function in CNNs is the familiar ReLU function. The purpose of the detector stage is to amplify the features contained within the feature map. One can think of the detector stage as performing a stretch on the feature map to highlight the important parts.

Lastly, the pooling stage extracts a summary statistic from the output of the detection stage. One common example is the *max pooling* operation which extracts the maximum value in a rectangular neighborhood of the input data. The effect is to reduce the size of the output from the detector stage while maintaining the important feature information. In this way, the pooling stage is a data reduction technique that only retains the most important aspects of the feature map. Additionally, the pooling operation imparts *equivariance* to the detection process; that is, it makes the process robust against translation of features in the image (Goodfellow et al., 2018).

Because the input data are gradually downsampled across the CNN, a classic CNN architecture is not built for pixel-wise labeling of an image (semantic segmentation). Deeper layers in a CNN *encode* what is in an image, but the

spatial detail is lost due to combined effects of the convolution operation and the pooling stage of the convolutional layers. Therefore, CNNs are great for telling you *what* is in an image, but not precisely, on a pixel-by-pixel basis *where* in the image it is. Commonly for planetary science image classification problems, knowing exactly where features are and drawing detailed boundaries around those features is desired. Some examples include drawing precise boundaries around impact craters, mapping landforms, drawing boundaries between geomorphologic units, and identifying potential hazards at a landing site.

There are several ways to adapt CNN architectures to the task of semantic segmentation. In *fully convolutional neural networks* (FCN, Shelhamer et al., 2016) and encoder-decoder networks (Badrinarayanan et al., 2017), the full image resolution is recovered by training *deconvolution* layers (the decoder part of encoder-decoder networks). The deconvolution layers upsample data from the previous layer using trainable filters (Shelhamer et al., 2016).

To facilitate the deconvolution results, shallower layers, which retain detailed spatial information, are connected to the deeper upsampling layers that contain rich feature information in a so-called “skip architecture” (Shelhamer et al., 2016). In this way, fine spatial detail from shallower layers of the network can be recovered and used to produce accurate and detailed segmentations at the full resolution of the input image.

A more elaborate approach to semantic segmentation using CNNs was achieved by Chen et al. (2018) with their DeepLabv3+ model. DeepLabv3+ is a framework for modifying an existing CNN architecture for the purpose of semantic segmentation. The DeepLabv3+ model combines convolutions that use Atrous Spatial Pyramid Pooling (ASPP, Chen et al., 2017) with an encoder-decoder architecture to deliver segmentation results with rich contextual information as well as sharp object boundaries (see Chen et al., 2018b, their Fig. 1).

The DeepLabv3+ model builds off previous versions of DeepLab (Chen et al., 2015; Chen et al., 2017; Chen et al., 2018a), specifically using DeepLabv3 as

an encoder module. In this work, we use ResNet50 (He et al., 2016) as the backbone CNN modified to the DeepLabv3+ structure (Chen et al., 2018a) to produce an FCN capable of full resolution semantic segmentation results.

Item B: Neural Network Architecture

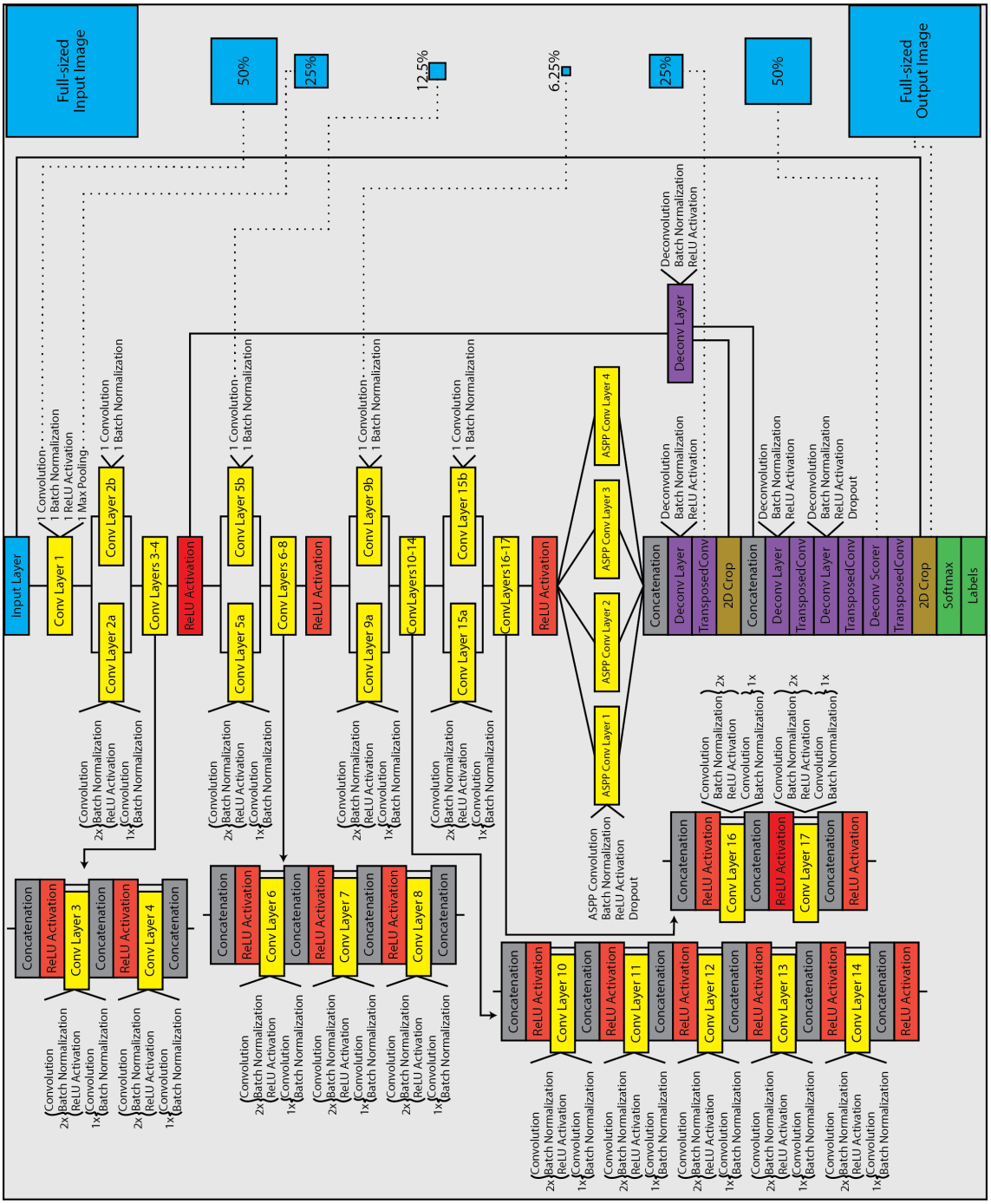

Fig. A3. 2 Network design for RGB- and DEM-Networks used in this study. RGB-DEM-Networks consist of two networks assembled in parallel using the late fusion technique.

Item C: Supplementary Results

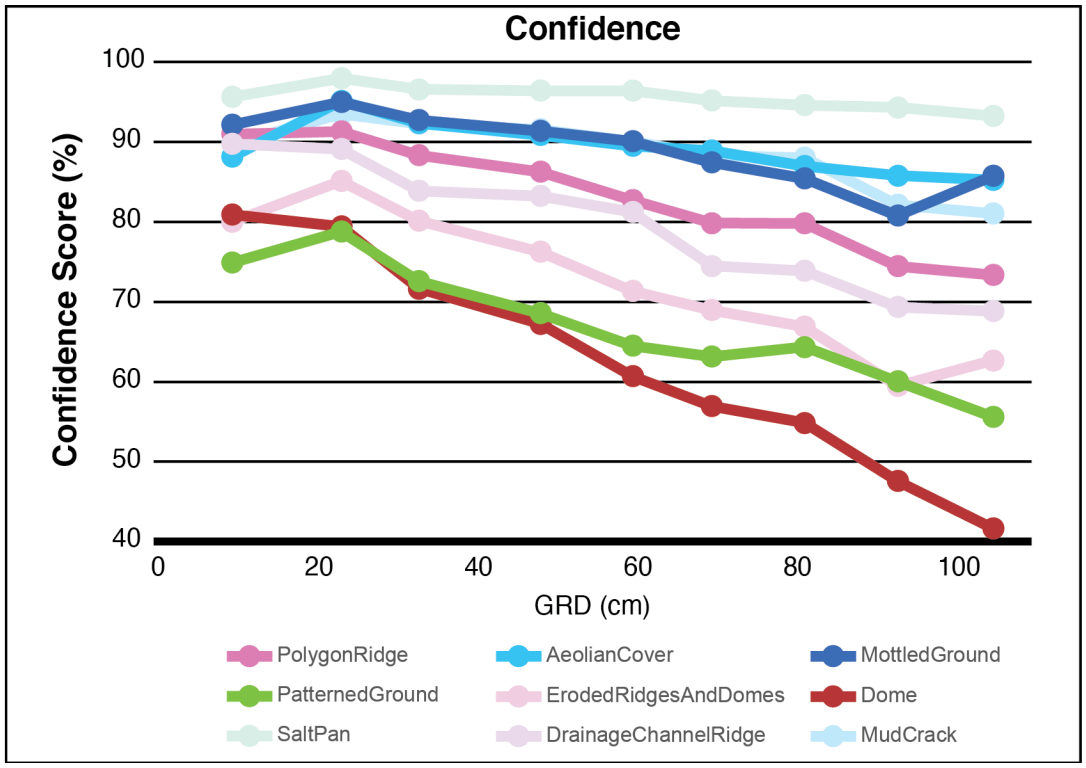

Fig. A3. 3 RGB-Network Confidence Scores as a function of GRD for 9 classes of natural features in this study (excluding Road, BorderPixel, and Object classes because they are not natural features). Note the general trend for all classes is a relatively linear decrease in confidence with increasing GRD. This behavior is distinct from the BF-Score, Recall, and Precision observed for the habitat classes and described in the main text. A plausible cause for the difference in behavior is that as network accuracy decreases, its uncertainty increases. The networks perform better on classes that cover large swaths of terrain, such as the SaltPan, AeolianCover, MottledGround, and MudCrack classes than they do on classes comprised of individual features.

CONCLUSIONS

Mercury: one less enigma?

In this study, thermal and geochemical modeling were used to propose a novel model for the formation of hollows, enigmatic features on the endmember planet Mercury. In this model, hollows were suggested to have formed through diurnally cyclic deposition and sublimation of sulfur-bearing phases brought to the surface in mercurian thermal systems.

In this exploration of Mercury, we suggest that the innermost planet likely hosted sublimation cycling around fumarole systems. A suite of volatile phases that could plausibly have been responsible for hollow formation were eliminated using a geochemical model to calculate sublimation rates, and it was concluded that concluded elemental sulfur (S) is the phase that was most likely responsible for hollow formation. The sulfur and sulfur-bearing phases in these systems may still be trickling out from reservoirs retained meters to tens of meters below the surface today.

A periscope into ancient Mars

In Chapter II of this manuscript, the composition of the ancient crust of Mars in an area north of Hellas basin that contains, perhaps, the most extensive and coherent exposures of pre-Noachian crust on Mars was described. Based on the reflectance spectra that indicate the presence of Fe-plagioclase, the spectral shape and wavelength locations of the cubic spline fit minima of the thermal infrared spectra, and the nature of the Fe-plagioclase-bearing outcrops in high-resolution images, we concluded that the outcrops are rich in feldspar and probably anorthositic

We inferred, from the widespread lateral occurrence and the similarity in composition and character between outcrops across > 2,000 km in the northern Hellas region, that the anorthositic outcrops offer a periscope into an ancient layered igneous complex (or several smaller, cogenetic complexes that merged

over time). This complex likely makes ups a portion of the primary or early secondary martian crust, and more rocks like these may be lurking below the surface more extensively across the planet.

Interestingly, inferences based on geodynamic data have been made for a pervasive, subsurface low-density component to the martian crust (Baratoux et al., 2014; Wieczorek et al., 2021). My results indicate that this component could be anorthositic and provide solid evidence for what the pre-Noachian crust of Mars may have been like. These data can constrain crust-formation models and provide a reference for future studies of similar outcrops on Mars.

A basis for comparing the identifiability of habitats

In this study, I developed a methodological template for establishing feature identification confidence as a function of image spatial resolution based on deep learning. I applied this method to the identification of microbial habitats in images of the Mars analog environment Salar de Pajonales (SdP). The habitat at SdP that is most likely to be confidently identified on Mars (if it exists on Mars as it does on Earth) are meter-scale ridges that makeup the edges of 10s to 100s of meter-scale polygons (PolygonRidges). In images with spatial resolutions similar to those available from cameras in orbit around Mars, the PolygonRidge habitat class could be identified with a confidence of 74% to 80%, whereas other habitats at SdP could only be identified with a confidence between 60% and 65% (PatternedGround) and 48% to 55% (Domes). This study serves as a guide for future studies that could be conducted at many different terrestrial Mars-analog environments so that the relative identifiability of habitats that those environments contain could be compared to each other. The environments that contain rover-explorable habitats with the highest potential to preserve biosignatures could then be targeted for exploration on Mars.

REFERENCES

Abdar, M., Pourpanah, F., Hussain, S., Rezazadegan, D., Liu, L., Ghavamzadeh, M., Fieguth, P., Cao, X., Khosravi, A., Acharya, U., Makarenkov, V. and Nahavandi, S., 2020. A Review of Uncertainty Quantification in Deep Learning: Techniques, Applications and Challenges. ArXiv, abs/2011.06225.

Abramov, O. and Kring, D.A., 2004. Numerical modeling of an impact-induced hydrothermal system at the Sudbury crater. Journal of Geophysical Research: Planets, 109(E10).

Abramov, O., Wong, S.M. and Kring, D.A., 2012. Differential melt scaling for oblique impacts on terrestrial planets. Icarus, 218(2): 906-916.

Adams, J.B. and Filice, A.L., 1967. Spectral reflectance 0.4 to 2.0 microns of silicate rock powders. Journal of Geophysical Research, 72(22).

Adams, J.B., Bell, P.M., Conel, J.E., Mao, H.K., McCord, T.B. and Nash, D.B., 1973. Visible and near-infra-red transmission and reflectance measurements of the Luna 20 soil. Geochimica et Cosmochimica Acta, 37(4): 731-743.

Adams, J.B. and Goullaud, L.H., 1978. Plagioclase feldspars: Visible and near infrared diffuse reflectance spectra as applied to remote sensing. Lunar and Planetary Science Conference(9): 2901-2909.

Allard, P., Maiorani, A., Tedesco, D., Cortecci, G. and Turi, B., 1991. Isotopic study of the origin of sulfur and carbon in Solfatara fumaroles, Campi Flegrei caldera. Journal of Volcanology and Geothermal Research, 48(1): 139-159.

Ames, D., 1999. Geology and regional hydrothermal alteration of the crater-fill, Onaping Formation: Association with zinc lead copper mineralization, Sudbury Structure, Canada. In: D.H. Watkinson and H.L. Gibson (Editors). ProQuest Dissertations Publishing.

Andrews-Hanna, J.C., Zuber, M.T. and Banerdt, W.B., 2008. The Borealis basin and the origin of the martian crustal dichotomy. Nature, 453(7199): 1212.

Appleman, D., Nissen, H.U., Stewart, D., Clark, J., Dowty, E. and Huebner, J., 1971. Studies of lunar plagioclase, tridymite and cristobalite. Proc. Second Lunar Sci. Conf., 2: 117.

Arivazhagan, S. and Anbazhagan, S., 2011. Characterization of reflectance spectra of lunar analog rocks; gabbro and norite. Current Science (Bangalore), 100(5): 761-768.

Ashwal, L., Morrison, D., Phinney, W. and Wood, J., 1983. Origin of Archean anorthosites: Evidence from the Bad Vermilion Lake anorthosite complex, Ontario. Contributions to Mineralogy and Petrology, 82(2): 259-273.

Ashwal, L.D., 1993. Anorthosites. Berlin, Heidelberg : Springer Berlin Heidelberg.

Badrinarayanan, V., Kendall, A. and Cipolla, R., 2017. SegNet: A Deep Convolutional Encoder-Decoder Architecture for Image Segmentation. IEEE transactions on pattern analysis and machine intelligence, 39(12): 2481-2495.

Bandfield, J.L., Rogers, D., Smith, M.D. and Christensen, P.R., 2004. Atmospheric correction and surface spectral unit mapping using Thermal Emission Imaging System data. Journal of Geophysical Research: Planets, 109(E10): n/a-n/a.

Bandfield, J.L., Osterloo, M.M. and Holsclaw, G.M., 2019. Thermophysical properties of Mercury: Revisiting Mariner 10 IRR measurements [2132], Lunar and Planetary Science Conference.

Baratoux, D., Samuel, H., Michaut, C., Toplis, M.J., Monnereau, M., Wieczorek, M., Garcia, R. and Kurita, K., 2014. Petrological constraints on the density of the Martian crust. Journal of Geophysical Research: Planets, 119(7): 1707-1727.

Barnouin, O.S., Zuber, M.T., Smith, D.E., Neumann, G.A., Herrick, R.R., Chappelow, J.E., Murchie, S.L. and Prockter, L.M., 2012. The morphology of craters on Mercury: Results from MESSENGER flybys. Icarus, 219(1): 414-427.

Beck, A.W., Murchie, S.L. and Viviano, C.E., 2020. A search for early- to mid-Noachian chloride-rich deposits on Mars. Icarus (New York, N.Y. 1962), 338: 113552.

Becker, L. and Bada, J.L., 1994. Fullerenes in the 1. 85- billion- year- old Sudbury impact structure. Science, 265(5172).

Becker, L., Bada, J.L., Winans, R.E. and Bunch, T.E., 1994. Fullerenes in Allende meteorite. Nature, 372(6506): 507.

BeipColombo-STR, 2000. BepiColombo System and Technology Study Report, ESA-SCI (2000).

Bell, P.M. and Mao, H.K., 1973. Optical and chemical analysis of iron in Luna 20 plagioclase. Geochimica et Cosmochimica Acta, 37(4): 755-759.

Black, B.A. and Manga, M., 2016. The eruptibility of magmas at Tharsis and Syrtis Major on Mars. Journal of geophysical research. Planets, 121(6): 944-964.

Blewett, D.A., Ernst, C.M., Murchie, S. and Vilas, F., 2018. Mercury's Hollows. In: S.C. Solomon, L.R. Nittler and B.J. Anderson (Editors), Mercury: the view after MESSENGER. Cambridge University Press, Cambridge, pp. 324-345.

Blewett, D.T., Chabot, N.L., Denevi, B.W., Ernst, C.M., Head, J.W., Izenberg, N.R., Murchie, S.L., Solomon, S.C., Nittler, L.R., McCoy, T.J., Xiao, Z.Y., Baker, D.M.H., Fassett, C.I., Braden, S.E., Oberst, J., Scholten, F., Preusker, F. and Hurwitz, D.M., 2011. Hollows on Mercury: MESSENGER Evidence for Geologically Recent Volatile-Related Activity. Science, 333(6051): 1856-1859.

Blewett, D.T., Vaughan, W.M., Xiao, Z., Chabot, N.L., Denevi, B.W., Ernst, C.M., Helbert, J., Amore, M., Maturilli, A., Head, J.W. and Solomon, S.C., 2013. Mercury's hollows: Constraints on formation and composition from analysis of geological setting and spectral reflectance. Journal of Geophysical Research: Planets, 118(5): 1013-1032.

Blewett, D.T., Levy, C.L., Chabot, N.L., Denevi, B.W., Ernst, C.M. and Murchie, S.L., 2014. Phase-ratio images of the surface of Mercury: Evidence for differences in sub-resolution texture. Icarus, 242: 142-148.

Blewett, D.T., Stadermann, A.C., Susorney, H.C., Ernst, C.M., Xiao, Z., Chabot, N.L., Denevi, B.W., Murchie, S.L., McCubbin, F.M., Kinczyk, M.J., Gillis-Davis, J.J. and Solomon, S.C., 2016. Analysis of MESSENGER high-resolution images of Mercury's hollows and implications for hollow formation. Journal of Geophysical Research: Planets, 121(9): 1798-1813.

Block, W.M. and Brennan, L.A., 1993. The Habitat Concept in Ornithology. In: D.M. Power (Editor), Current Ornithology: Volume 11. Springer US, Boston, MA, pp. 35-91.

Borg, L.E., Connelly, J.N., Boyet, M. and Carlson, R.W., 2011. Chronological evidence that the Moon is either young or did not have a global magma ocean. Nature, 477(7362): 70.

Botta, O. and Bada, J., 2002. Extraterrestrial Organic Compounds in Meteorites. An International Review Journal Covering the Entire Field of Geosciences and Related Areas, 23(5): 411-467.

Boukaré, C.E., Parman, S.W., Parmentier, E.M. and Anzures, B.A., 2019. Production and Preservation of Sulfide Layering in Mercury's Mantle. Journal of Geophysical Research: Planets, 121: 18.

Boynton, W., Sprague, A., Solomon, S., Starr, R., Evans, L., Feldman, W., Trombka, J. and Rhodes, E., 2007. MESSENGER and the Chemistry of Mercury’s Surface. Space Sci Rev, 131(1): 85-104.

Brown, S.M. and Elkins-Tanton, L.T., 2009. Compositions of Mercury's earliest crust from magma ocean models. Earth and Planetary Science Letters, 286(3): 446-455.

Bruggeman, D.A.G., 1935. Berechnung verschiedener physikalischer Konstanten von heterogenen Substanzen. I. Dielektrizitätskonstanten und Leitfähigkeiten der Mischkörper aus isotropen Substanzen. Annalen der Physik, 416(7): 636-664.

Bryan, W.B., 1974. Fe-Mg relationships in sector-zoned submarine basalt plagioclase. Earth and Planetary Science Letters, 24(2): 157-165.

Bunce, E.J., Martindale, A., Lindsay, S., Muinonen, K., Rothery, D.A., Pearson, J., McDonnell, I., Thomas, C., Thornhill, J., Tikkanen, T., Feldman, C., Huovelin, J., Korpela, S., Esko, E., Lehtolainen, A., Treis, J., Majewski, P., Hilchenbach, M., Väisänen, T., Luttinen, A., Kohout, T., Penttilä, A., Bridges, J., Joy, K.H., Alcacera-Gil, M.A., Alibert, G., Anand, M., Bannister, N., Barcelo-Garcia, C., Bicknell, C., Blake, O., Bland, P., Butcher, G., Cheney, A., Christensen, U., Crawford, T., Crawford, I.A., Dennerl, K., Dougherty, M., Drumm, P., Fairbend, R., Genzer, M., Grande, M., Hall, G.P., Hodnett, R., Houghton, P., Imber, S., Kallio, E., Lara, M.L., Balado Margeli, A., Mas-Hesse, M.J., Maurice, S., Milan, S., Millington-Hotze, P., Nenonen, S., Nittler, L., Okada, T., Ormö, J., Perez-Mercader, J., Poyner, R., Robert, E., Ross, D., Pajas-Sanz, M., Schyns, E., Seguy, J., Strüder, L.,

Vaudon, N., Viceira-Martín, J., Williams, H., Willingale, D. and Yeoman, T., 2020. The BepiColombo Mercury Imaging X-Ray Spectrometer: Science Goals, Instrument Performance and Operations. Space Science Reviews, 216(8): 126.

Burns, R.G., 1993. Mineralogical Applications of Crystal Field Theory. Cambridge England ; New York, NY, USA : Cambridge University Press, Cambridge [England] ; New York, NY, USA.

Buseck, P.R., Tsipursky, S.J. and Hettich, R., 1992. Fullerenes from the geological environment. Science, 257(5067): 215 - 217.

Byrne, P.K., Klimczak, C., Sengor, A.M.C., Solomon, S.C., Watters, T.R. and Hauck, S.A., II, 2014. Mercury's global contraction much greater than earlier estimates. Nature Geoscience(4): 301-307.

Cabrol, N., 2018. The Coevolution of Life and Environment on Mars: An Ecosystem Perspective on the Robotic Exploration of Biosignatures. Astrobiology, 18(1).

Cabrol, N.A., Wettergreen, D., Warren-Rhodes, K., Grin, E.A., Moersch, J., Diaz, G.C., Cockell, C.S., Coppin, P., Demergasso, C., Dohm, J.M., Ernst, L., Fisher, G., Glasgow, J., Hardgrove, C., Hock, A.N., Jonak, D., Marinangeli, L., Minkley, E., Ori, G.G., Piatek, J., Pudenz, E., Smith, T., Stubbs, K., Thomas, G., Thompson, D., Waggoner, A., Wagner, M., Weinstein, S. and Wyatt, M., 2007. Life in the Atacama: Searching for life with rovers (science overview. Journal of Geophysical Research: Biogeosciences, 112(G4): n/a-n/a.

Cabrol, N.A., Feister, U., Häder, D.-P., Piazena, H., Grin, E.A. and Klein, A., 2014. Record solar UV irradiance in the tropical Andes. Frontiers in Environmental Science, 2(19).

Caliro, S., Chiodini, G., Moretti, R., Avino, R., Granieri, D., Russo, M. and Fiebig, J., 2007. The origin of the fumaroles of La Solfatara (Campi Flegrei, South Italy). Geochimica et Cosmochimica Acta, 71(12): 3040-3055.

Carli, C., Ciarniello, M., Capaccioni, F., Serventi, G. and Sgavetti, M., 2014a. Spectral variability of plagioclase– mafic mixtures (2): Investigation of the optical constant and retrieved mineral abundance dependence on particle size distribution. Icarus, 235: 207-219.

Carli, C., Serventi, G. and Sgavetti, M., 2014b. The Second Conference on the Lunar Highlands Crust and New Directions. VNIR spectral variability of the igneous stratified Stillwater Complex: A tool to map lunar highlands. ammin, 99(10): 1834-1848.

Carrier, B.L., Beaty, D.W., Meyer, M.A., Blank, J.G., Chou, L., DasSarma, S., Des Marais, D.J., Eigenbrode, J.L., Grefenstette, N., Lanza, N.L., Schuerger, A.C., Schwendner, P., Smith, H.D., Stoker, C.R., Tarnas, J.D., Webster, K.D., Bakermans, C., Baxter, B.K., Bell, M.S., Benner, S.A., Bolivar Torres, H.H., Boston, P.J., Bruner, R., Clark, B.C., DasSarma, P., Engelhart, A.E., Gallegos, Z.E., Garvin, Z.K., Gasda, P.J., Green, J.H., Harris, R.L., Hoffman, M.E., Kieft, T., Koeppel, A.H.D., Lee, P.A., Li, X., Lynch, K.L.,

Mackelprang, R., Mahaffy, P.R., Matthies, L.H., Nellessen, M.A., Newsom, H.E., Northup, D.E., O'Connor, B.R.W., Perl, S.M., Quinn, R.C., Rowe, L.A., Sauterey, B., Schneegurt, M.A., Schulze-Makuch, D., Scuderi, L.A., Spilde, M.N., Stamenković, V., Torres Celis, J.A., Viola, D., Wade, B.D., Walker, C.J., Wiens, R.C., Williams, A.J., Williams, J.M. and Xu, J., 2020. Mars Extant Life: What's Next? Conference Report. Astrobiology, 20(6): 785-814.

Carrier, W., 1973. Lunar soil grain size distribution. The moon, 6(3): 250-263.

Carrier, W.D., Olhoeft, G.R. and Mendell, W., 1991. Physical Properties of the Lunar Surface, Lunar sourcebook: a user's guide to the moon.

Carter, J. and Poulet, F., 2013. Ancient plutonic processes on Mars inferred from the detection of possible anorthositic terrains. Nature Geoscience, 6(12): 1008.

Chabot, N.L., Ernst, C.M., Denevi, B.W., Nair, H., Deutsch, A.N., Blewett, D.T., Murchie, S.L., Neumann, G.A., Mazarico, E., Paige, D.A., Harmon, J.K., Head, J.W. and Solomon, S.C., 2014. Images of surface volatiles in Mercury's polar craters acquired by the MESSENGER spacecraft. Geology, 42(12): 1051-1054.

Chase, S.C., Miner, E.D., Morrison, D., Münch, G. and Neugebauer, G., 1976. Mariner 10 infrared radiometer results: Temperatures and thermal properties of the surface of Mercury. Icarus, 28(4): 565-578.

Cheek, L.C., Donaldson Hanna, K.L., Pieters, C.M., Head, J.W. and Whitten, J.L., 2013. The distribution and purity of anorthosite across the Orientale basin: New perspectives from Moon Mineralogy Mapper data. Journal of Geophysical Research: Planets, 118(9): 1805-1820.

Chen, L.-C., Papandreou, G., Kokkinos, I., Murphy, K. and Yuille, A., 2015. Semantic Image Segmentation with Deep Convolutional Nets and Fully Connected CRFs. CoRR, abs/1412.7062.

Chen, L.-C., Papandreou, G., Schroff, F. and Adam, H., 2017. Rethinking Atrous Convolution for Semantic Image Segmentation. ArXiv, abs/1706.05587.

Chen, L.-C., Papandreou, G., Kokkinos, I., Murphy, K. and Yuille, A., 2018a. DeepLab: Semantic Image Segmentation with Deep Convolutional Nets, Atrous Convolution, and Fully Connected CRFs. IEEE Transactions on Pattern Analysis and Machine Intelligence, 40: 834-848.

Chen, L.-C., Zhu, Y., Papandreou, G., Schroff, F. and Adam, H., 2018b. Encoder-Decoder with Atrous Separable Convolution for Semantic Image Segmentation, ECCV.

Christensen, P.R., Bandfield, J.L., Hamilton, V.E., Howard, D.A., Lane, M.D., Piatek, J.L., Ruff, S.W. and Stefanov, W.L., 2000. A thermal emission spectral library of rock-forming minerals. Journal of Geophysical Research, 105(4): 9735-9739.

Christensen, P.R., Jakosky, B.M., Kieffer, H.H., Malin, M.C., McSween, H.Y., Nealson, K., Mehall, G.L., Silverman, S.H., Ferry, S., Caplinger, M. and Ravine, M., 2004. The Thermal Emission Imaging System (THEMIS) for the Mars 2001 Odyssey Mission. Space Science Reviews, 110(1): 85-130.

Cintala, M.J., 1992. Impact-induced thermal effects in the lunar and mercurian regoliths. J. Geophys. Res.-Planets, 97(E12): 947-973.
Clark, P., 2007. Dynamic Planet: Mercury in the Context of Its Environment. Mercury in the Context of Its Environment. Springer New York: New York, NY, New York, NY.
Clark, P.E., 2015. Mercury's Interior, Surface, and Surrounding Environment : Latest Discoveries. New York, NY : Springer New York : Imprint: Springer.
Clark, R.N. and Roush, T.L., 1984. Reflectance spectroscopy: Quantitative analysis techniques for remote sensing applications. Journal of Geophysical Research: Solid Earth, 89(B7): 6329-6340.
Cockell, C.S., Balme, M., Bridges, J.C., Davila, A. and Schwenzer, S.P., 2012. Uninhabited habitats on Mars. Icarus (New York, N.Y. 1962), 217(1): 184-193.
Cockell, C.S., 2014. Trajectories of Martian Habitability. Astrobiology, 14(2): 182-203.
Cockell, C.S., Bush, T., Bryce, C., Direito, S., Fox-Powell, M., Harrison, J.P., Lammer, H., Landenmark, H., Martin-Torres, J., Nicholson, N., Noack, L., O'Malley-James, J., Payler, S.J., Rushby, A., Samuels, T., Schwendner, P., Wadsworth, J. and Zorzano, M.P., 2016. Habitability: A Review. Astrobiology, 16(1): 89-117.
Cockell, C.S., Brown, S., Landenmark, H., Samuels, T., Siddall, R. and Wadsworth, J., 2017. Liquid Water Restricts Habitability in Extreme Deserts. Astrobiology, 17(4): 39-318.
Colombo, G., 1965. Rotational Period of the Planet Mercury. Nature, 208(5010): 575.
Correia, A.C.M. and Laskar, J., 2009. Mercury's capture into the 3/2 spin–orbit resonance including the effect of core–mantle friction. Icarus, 201(1): 1-11.
Correia, A.C.M. and Laskar, J., 2010. Long- term evolution of the spin of Mercury; I, Effect of the obliquity and core-mantle friction. Icarus, 205(2): 338-355.
Costello, E.S., Ghent, R.R. and Lucey, P.G., 2019. Impact Gardening on the Moon and Mercury: The Source, Age, and Depth to Ice at the Poles [1991], 50th Lunar and Planetary Science Conference, Houston, TX.
Craddock, R.A. and Howard, A.D., 2000. Simulated degradation of lunar impact craters and a new method for age dating farside mare deposits. Journal of Geophysical Research: Planets, 105(E8): 20387-20401.
Cramer, M., Zhang, S., Meiβner, H. and Reulke, R., 2020. Quality assessment of high-resolution UAV imagery and products. DGPF.
Crank, J. and Nicolson, P., 1947. A practical method for numerical evaluation of solutions of partial differential equations of the heat- conduction type. Mathematical Proceedings of the Cambridge Philosophical Society, 43(1): 50-67.
Cremonese, G., Capaccioni, F., Capria, M.T., Doressoundiram, A., Palumbo, P., Vincendon, M., Massironi, M., Debei, S., Zusi, M., Altieri, F., Amoroso, M., Aroldi, G., Baroni, M., Barucci, A., Bellucci, G., Benkhoff, J., Besse, S.,

Bettanini, C., Blecka, M., Borrelli, D., Brucato, J.R., Carli, C., Carlier, V., Cerroni, P., Cicchetti, A., Colangeli, L., Dami, M., Da Deppo, V., Della Corte, V., De Sanctis, M.C., Erard, S., Esposito, F., Fantinel, D., Ferranti, L., Ferri, F., Ficai Veltroni, I., Filacchione, G., Flamini, E., Forlani, G., Fornasier, S., Forni, O., Fulchignoni, M., Galluzzi, V., Gwinner, K., Ip, W., Jorda, L., Langevin, Y., Lara, L., Leblanc, F., Leyrat, C., Li, Y., Marchi, S., Marinangeli, L., Marzari, F., Mazzotta Epifani, E., Mendillo, M., Mennella, V., Mugnuolo, R., Muinonen, K., Naletto, G., Noschese, R., Palomba, E., Paolinetti, R., Perna, D., Piccioni, G., Politi, R., Poulet, F., Ragazzoni, R., Re, C., Rossi, M., Rotundi, A., Salemi, G., Sgavetti, M., Simioni, E., Thomas, N., Tommasi, L., Turella, A., Van Hoolst, T., Wilson, L., Zambon, F., Aboudan, A., Barraud, O., Bott, N., Borin, P., Colombatti, G., El Yazidi, M., Ferrari, S., Flahaut, J., Giacomini, L., Guzzetta, L., Lucchetti, A., Martellato, E., Pajola, M., Slemer, A., Tognon, G. and Turrini, D., 2020. SIMBIO-SYS: Scientific Cameras and Spectrometer for the BepiColombo Mission. Space science reviews, 216(5): 75.

Croft, S.K., 1980. Cratering flow fields - Implications for the excavation and transient expansion stages of crater formation, Lunar and Planetary Science Conference, Houston, TX, pp. 2347-2378.

Crown, D.A. and Pieters, C.M., 1987. Spectral properties of plagioclase and pyroxene mixtures and the interpretation of lunar soil spectra. Icarus, 72(3): 492-506.

Csurka, G., Larlus, D. and Perronnin, F., 2013. What is a good evaluation metric? Proceedings of the British Machine Vision Conference: 32.1-32.11.

Cuzzi, J.N., 1974. The nature of the subsurface of Mercury from microwave observations at several wavelengths. The Astrophysical Journal(189): 11.

Czudek, T. and Demek, J., 1970. Thermokarst in Siberia and Its Influence on the Development of Lowland Relief. Quaternary research, 1(1): 103-120.

Davila, A.F., Skidmore, M., Fairen, A.G., Cockell, C. and Schulze-Makuch, D., 2010. New priorities in the robotic exploration of Mars: the case for in Situ search for extant life. Astrobiology, 10(7): 705.

Davila, A.F., Hawes, I., Araya, J.G., Gelsinger, D.R., DiRuggiero, J., Ascaso, C., Osano, A. and Wierzchos, J., 2015. In situ metabolism in halite endolithic microbial communities of the hyperarid Atacama Desert.(Report)(Author abstract). Frontiers in Microbiology, 6.

Davila, A.F. and Schulze-Makuch, D., 2016. The Last Possible Outposts for Life on Mars. Astrobiology, 16(2): 159.

De Vries, M.S., Reihs, K., Wendt, H.R., Golden, W.G., Hunziker, H.E., Fleming, R., Peterson, E. and Chang, S., 1993. A search for C60 in carbonaceous chondrites. Geochimica et cosmochimica acta, 57: 933.

DeLatte, D.M., Crites, S.T., Guttenberg, N., Tasker, E.J. and Yairi, T., 2019a. Segmentation Convolutional Neural Networks for Automatic Crater Detection on Mars. IEEE journal of selected topics in applied earth observations and remote sensing, 12(8): 2944-2957.

DeLatte, D.M., Crites, S.T., Guttenberg, N. and Yairi, T., 2019b. Automated crater detection algorithms from a machine learning perspective in the convolutional neural network era. Advances in space research, 64(8): 1615-1628.

Denevi, B., Chabot, N., Murchie, S., Becker, K., Blewett, D., Domingue, D., Ernst, C., Hash, C., Hawkins, S., Keller, M., Laslo, N., Nair, H., Robinson, M., Seelos, F., Stephens, G., Turner, F. and Solomon, S., 2018. Calibration, Projection, and Final Image Products of MESSENGER's Mercury Dual Imaging System. Space Science Reviews, 214(1): 1-52.

Denevi, B.W., Robinson, M.S., Solomon, S.C., Murchie, S.L., Blewett, D.T., Domingue, D.L., McCoy, T.J., Ernst, C.M., Head, J.W., Watters, T.R. and Chabot, N.L., 2009. The evolution of Mercury's crust: a global perspective from MESSENGER. Science (New York, N.Y.), 324(5927): 613.

Denevi, B.W., Ernst, C.M., Meyer, H.M., Robinson, M.S., Murchie, S.L., Whitten, J.L., Head, J.W., Watters, T.R., Solomon, S.C., Ostrach, L.R., Chapman, C.R., Byrne, P.K., Klimczak, C. and Peplowski, P.N., 2013a. The distribution and origin of smooth plains on Mercury. Journal of Geophysical Research: Planets, 118(5): 891-907.

Denevi, B.W., Ernst, C.M., Meyer, H.M., Robinson, M.S., Murchie, S.L., Whitten, J.L., Head, J.W., Watters, T.R., Solomon, S.C., Ostrach, L.R., Chapman, C.R., Byrne, P.K., Klimczak, C. and Peplowski, P.N., 2013b. The distribution and origin of smooth plains on Mercury. Journal of Geophysical Research-Planets, 118(5): 891-907.

Dickson, J.L., Kerber, L., Fassett, C.I. and Ehlmann, B., 2018. A Global, Blended CTX Mosaic of Mars with Vectorized Seam Mapping: A New Mosaicking Pipeline Using Principles of Non-Destructive Image Editing [#2480]. Lunar and Planetary Science Conference, Houston.

DJI, 2021. https://www.dji.com/phantom-4-pro/info#specs.

Domingue, D.L., Chapman, C.R., Killen, R.M., Zurbuchen, T., Gilbert, J., Sarantos, M., Benna, M., Slavin, J., Schriver, D., Travnicek, P., Orlando, T.M., Sprague, A.L., Blewett, D., Gillis-Davis, J., Feldman, W., Lawrence, D., Ho, G., Ebel, D., Nittler, L., Vilas, F., Pieters, C.M., Solomon, S.C., Johnson, C., Winslow, R.M., Helbert, J., Peplowski, P., Weider, S., Mouawad, N., Izenberg, N. and McClintock, W., 2014. Mercury's Weather- Beaten Surface: Understanding Mercury in the Context of Lunar and Asteroidal Space Weathering Studies, Space Sci. Rev., pp. 121-214.

Dong, C., Loy, C.C., Kaiming, H. and Xiaoou, T., 2016. Image Super-Resolution Using Deep Convolutional Networks. IEEE transactions on pattern analysis and machine intelligence, 38(2): 295-307.

dxomark, 2021. https://www.dxomark.com/Cameras/DJI/Phantom4-Pro---Specifications.

Dyar, M.D., Agresti, D.G., Schaefer, M.W., Grant, C.A. and Sklute, E.C., 2006. Mössbauer Spectroscopy of Earth and Planetary Materials. Annual review of earth and planetary sciences, 34(1): 83-125.

Dzurisin, D., 1977. Mercurian bright patches: Evidence for physio-chemical alteration of surface material? Geophysical Research Letters, 4(10): 3.

Ebel, D.S., Alexander, C.M.O., amp, Amp, Apos and D, 2011. Equilibrium condensation from chondritic porous IDP enriched vapor: Implications for Mercury and enstatite chondrite origins. Planetary and Space Science, 59(15): 1888-1894.

Edwards, B., Magnússon, E., Thordarson, T., Guðmundsson, M.T., Höskuldsson, A., Oddsson, B. and Haklar, J., 2012. Interactions between lava and snow/ice during the 2010 Fimmvörðuháls eruption, south-central Iceland: 2010 FIMMVÖRÐUHÁLS LAVA-SNOW. Journal of Geophysical Research: Solid Earth, 117(B4).

Egea-González, I. and Ruiz, J., 2014. Influence of an insulating megaregolith on heat flow and crustal temperature structure of Mercury. Icarus (New York, N.Y. 1962), 232: 220-225.

Eggers, G.L., Wray, J.J. and Dufek, J., 2021. Compositional Mapping of the Nili Patera Feldspathic Unit: Extent and Implications for Formation. Journal of geophysical research. Planets, 126(2): n/a.

Ehlmann, B.L., Anderson, F.S., Andrews-Hanna, J., Catling, D.C., Christensen, P.R., Cohen, B.A., Dressing, C.D., Edwards, C.S., Elkins-Tanton, L.T., Farley, K.A., Fassett, C.I., Fischer, W.W., Fraeman, A.A., Golombek, M.P., Hamilton, V.E., Hayes, A.G., Herd, C.D.K., Horgan, B., Hu, R., Jakosky, B.M., Johnson, J.R., Kasting, J.F., Kerber, L., Kinch, K.M., Kite, E.S., Knutson, H.A., Lunine, J.I., Mahaffy, P.R., Mangold, N., McCubbin, F.M., Mustard, J.F., Niles, P.B., Quantin-Nataf, C., Rice, M.S., Stack, K.M., Stevenson, D.J., Stewart, S.T., Toplis, M.J., Usui, T., Weiss, B.P., Werner, S.C., Wordsworth, R.D., Wray, J.J., Yingst, R.A., Yung, Y.L. and Zahnle, K.J., 2016. The sustainability of habitability on terrestrial planets: Insights, questions, and needed measurements from Mars for understanding the evolution of Earth- like worlds, pp. 1927-1961.

Ehrenfreund, P. and Foing, B.H., 1997. Fullerenes in space. Advances in Space Research, 19(7): 1033-1042.

Eitel, A., Springenberg, J.T., Spinello, L., Riedmiller, M. and Burgard, W., 2015. Multimodal deep learning for robust RGB-D object recognition. IEEE, pp. 681-687.

Elkins-Tanton, L.T., Hess, P.C. and Parmentier, E.M., 2005. Possible formation of ancient crust on Mars through magma ocean processes. Journal of Geophysical Research: Planets, 110(E12).

Elkins-Tanton, L.T., 2012. Magma Oceans in the Inner Solar System, Annu. Rev. Earth Planet. Sci., pp. 113-139.

Elkins-Tanton, L.T., Parmentier, E.M. and Hess, P.C., 2003. Magma ocean fractional crystallization and cumulate overturn in terrestrial planets: Implications for Mars. Meteoritics & Planetary Science, 38(12): 1753-1771.

Emami, E., Ahmad, T., Bebis, G., Nefian, A. and Fong, T., 2019. Crater Detection Using Unsupervised Algorithms and Convolutional Neural Networks. IEEE transactions on geoscience and remote sensing, 57(8): 5373-5383.

Emery, J.P., Sprague, A.L., Witteborn, F.C., Colwell, J.E., Kozlowski, R.W.H. and Wooden, D.H., 1998. Mercury: Thermal Modeling and Mid-infrared (5–12 μm) Observations. Icarus, 136(1): 104-123.

Ernst, C.M., Denevi, B.W., Barnouin, O.S., Klimczak, C., Chabot, N.L., Head, J.W., Murchie, S.L., Neumann, G.A., Prockter, L.M., Robinson, M.S., Solomon, S.C. and Watters, T.R., 2015. Stratigraphy of the Caloris basin, Mercury: Implications for volcanic history and basin impact melt. Icarus, 250: 413-429.

Everingham, M., Van Gool, L., Williams, C.K.I., Winn, J. and Zisserman, A., 2010. The Pascal Visual Object Classes (VOC) Challenge. International journal of computer vision, 88(2): 303-338.

Fairen, A.G., Davila, A.F., Lim, D., Bramall, N., Bonaccorsi, R., Zavaleta, J., Uceda, E.R., Stoker, C., Wierzchos, J., Dohm, J.M., Amils, R., Andersen, D. and McKay, C.P., 2010. Astrobiology through the ages of Mars: the study of terrestrial analogues to understand the habitability of Mars. Astrobiology, 10(8): 821.

Farley, K.A., Williford, K.H., Stack, K.M., Bhartia, R., Chen, A., de la Torre, M. and Hand, K., 2020. Mars 2020 Mission Overview. Space science reviews, 216(8).

Fassett, C.I. and Thomson, B.J., 2014. Crater degradation on the lunar maria: Topographic diffusion and the rate of erosion on the Moon. Journal of geophysical research. Planets, 119(10): 2255-2271.

Fassett, C.I., Crowley, M.C., Leight, C., Dyar, M.D., Minton, D.A., Hirabayashi, M., Thomson, B.J. and Watters, W.A., 2017. Evidence for rapid topographic evolution and crater degradation on Mercury from simple crater morphometry. Geophysical research letters, 44(11): 5326-5335.

Feely, K. and Christensen, P., 1999. Quantitative compositional analysis using thermal emission spectroscopy: Application to igneous and metamorphic rocks. J. Geophys. Res.-Planets, 104(E10): 24195-24210.

Fergason, R., Hare, T.M. and Laura, J., 2017. HRSC and MOLA Blended Digital Elevation Model at 200m. Astrogeology PDS Annex, U.S. Geological Survey (http://bit.ly/HRSC_MOLA_Blend_v0).

Fergason, R.L., Christensen, P.R. and Kieffer, H.H., 2006. High- resolution thermal inertia derived from the Thermal Emission Imaging System (THEMIS): Thermal model and applications. Journal of Geophysical Research: Planets, 111(E12): n/a-n/a.

Fernández-Remolar, D.C., Chong-Díaz, G., Ruíz-Bermejo, M., Harir, M., Schmitt-Kopplin, P., Tziotis, D., Gómez-Ortíz, D., García-Villadangos, M., Martín-Redondo, M.P., Gómez, F., Rodríguez-Manfredi, J.A., Moreno-Paz, M., De Diego-Castilla, G., Echeverría, A., Urtuvia, V.N., Blanco, Y., Rivas, L., Izawa, M.R.M., Banerjee, N.R., Demergasso, C. and Parro, V., 2013.

Molecular preservation in halite- and perchlorate-rich hypersaline subsurface deposits in the Salar Grande basin (Atacama Desert, Chile): Implications for the search for molecular biomarkers on Mars. Journal of Geophysical Research: Biogeosciences, 118(2): 922-939.

Ferris, J.P., Becker, L., Boering, K.A., Cody, G.D., Ellison, G.B., Hayes, J.M., Johnson, R.E., Klemperer, W., Meech, K.J., Noll, K.S. and Saunders, M., 2007. Exploring organic environments in the solar system: National Research Council Committee on the Assessment of the Nasa Science Mission Directorate Science Plan Task Group on Organic Environments in the Solar System. Washington, D.C. : National Academies Press, Washington, D.C.

Fish, S., A. , Shepherd, T., J. , Mcgenity, T., J. and Grant, W., D. , 2002. Recovery of 16S ribosomal RNA gene fragments from ancient halite. Nature, 417(6887): 432.

Flahaut, J., Martinot, M., Bishop, J.L., Davies, G.R. and Potts, N.J., 2017. Remote sensing and in situ mineralogic survey of the Chilean salars: An analog to Mars evaporate deposits? Icarus, 282: 152-173.

Fountain, J.A. and West, E.A., 1970. Thermal conductivity of particulate basalt as a function of density in simulated lunar and Martian environments. Journal of Geophysical Research, 75(20): 4063-4069.

Fourier, J.B.J., 1822. Théorie Analytique de la Chaleur. In: F. Didot (Editor), Paris.

French, B.M., 1998. Traces of catastrophe: a handbook of shock-metamorphic effects in terrestrial meteorite impact structures, pp. 36-36-5704.

Frost, B.R. and Frost, C.D., 2008. A Geochemical Classification for Feldspathic Igneous Rocks. Journal of Petrology, 49(11): 1955-1969.

Frost, R.B. and Frost, C.D., 2014. Essentials of Igneous and Metamorphic Petrology. Cambridge Univeristy Press.

Gaidos, E., Deschenes, B., Dundon, L., Fagan, K., Menviel-Hessler, L., Moskovitz, N. and Workman, M., 2005. Beyond the Principle of Plentitude: A Review of Terrestrial Planet Habitability. Astrobiology, 5(2): 100-126.

Gal, Y. and Ghahramani, Z., 2015. Bayesian Convolutional Neural Networks with Bernoulli Approximate Variational Inference. ArXiv, abs/1506.02158.

Gal, Y. and Ghahramani, Z., 2016. Dropout as a Bayesian Approximation: Representing Model Uncertainty in Deep Learning. ArXiv, abs/1506.02142.

Geert, A., John, F., Sophie, B. and Jason, M., 2013. Quantifying the effect of habitat availability on species distributions. The Journal of animal ecology, 82(6): 1135-1145.

Glotch, T.D., Bandfield, J.L., Tornabene, L.L., Jensen, H.B. and Seelos, F.P., 2010. Distribution and formation of chlorides and phyllosilicates in Terra Sirenum, Mars. Geophysical research letters, 37(16): n/a.

Glotch, T.D., Bandfield, J.L., Wolff, M.J., Arnold, J.A. and Che, C., 2016. Constraints on the composition and particle size of chloride salt-bearing deposits on Mars. Journal of geophysical research. Planets, 121(3): 454-471.

Goodfellow, I., Bengio, Y. and Courville, A., 2018. Deep learning. The MIT Press.
Goodfellow, I.J., Warde-Farley, D., Mirza, M., Courville, A. and Bengio, Y., 2013. Maxout Networks. In: S. Dasgupta and D. McAllester (Editors), ICML'13, pp. 1319-1327.
Goudge, T.A., Head, J.W., Kerber, L., Blewett, D.T., Denevi, B.W., Domingue, D.L., Gillis-Davis, J.J., Gwinner, K., Helbert, J., Holsclaw, G.M., Izenberg, N.R., Klima, R.L., McClintock, W.E., Murchie, S.L., Neumann, G.A., Smith, D.E., Strom, R.G., Xiao, Z.Y., Zuber, M.T. and Solomon, S.C., 2014. Global inventory and characterization of pyroclastic deposits on Mercury: New insights into pyroclastic activity from MESSENGER orbital data. Journal of Geophysical Research-Planets, 119(3): 635-658.
Gradie, J. and Moses, J., 1984. Spectral Reflectance of Sodium Sulfide: A Colorant on Io?, Lunar and Planetary Science Conference, pp. 2.
Greeley, R. and Schneid, B.D., 1991. Magma generation on Mars: amounts, rates, and comparisons with Earth, moon, and venus. Science (New York, N.Y.), 254(5034): 996.
Grieve, R. and Cintala, M.J., 1992. An Analysis of Differential Impact-melt Crater-Scaling and Implications for the Terrestrial Impact Record. Meteoritics, 27(5): 526-538.
Grieve, R.A.F., 2005. Economic natural resource deposits at terrestrial impact structures. In: I. McDonald, A.J. Boyce, I.B. Butler, R.J. Herrington and D.A. Polya (Editors), Geological Society, London, Special Publications.
Grott, M., Baratoux, D., Hauber, E., Sautter, V., Mustard, J., Gasnault, O., Ruff, S.W., Karato, S.I., Debaille, V., Knapmeyer, M., Sohl, F., Van Hoolst, T., Breuer, D., Morschhauser, A. and Toplis, M.J., 2013. Long-Term Evolution of the Martian Crust-Mantle System. Space Science Reviews, 174(1-4): 49-111.
Grundy, W., Young, L., Spencer, J., Johnson, R., Young, E. and Buie, M., 2006. Distributions of H2O and CO2 ices on Ariel, Umbriel, Titania, and Oberon from IRTF/SpeX observations. Icarus (New York, N.Y. 1962), 184(2): 543-555.
Guo, Z., Li, X., Huang, H., Guo, N. and Li, Q., 2018. Medical image segmentation based on multi-modal convolutional neural network: Study on image fusion schemes. 2018 IEEE 15th International Symposium on Biomedical Imaging (ISBI 2018): 903-907.
Häder, D.P. and Cabrol, N.A., 2020. Monitoring of Solar Irradiance in the High Andes. Photochemistry and photobiology, 96(5): 1133-1139.
Hafner, S.S., Virgo, D. and Warburton, D., 1971. Oxidation state of iron in plagioclase from lunar basalts. Earth and Planetary Science Letters, 12(2): 159-166.
Hale, A.S. and Hapke, B., 2002. A Time-Dependent Model of Radiative and Conductive Thermal Energy Transport in Planetary Regoliths with Applications to the Moon and Mercury. Icarus, 156(2): 318-334.

Hall, L., S. , Krausman, P., R. and Morrison, M., L. , 1997. The Habitat Concept and a Plea for Standard Terminology. Wildlife Society bulletin, 25(1): 173-182.
Halliday, A.N., Wänke, H., Birck, J.L. and Clayton, R.N., 2001. The Accretion, Composition and Early Differentiation of Mars. Space Science Reviews, 96(1): 197-230.
Hamilton, V.E. and Christensen, P.R., 2005. Evidence for extensive, olivine-rich bedrock on Mars. Geology, 33(6): 433-436.
Hapke, B., 2012. Theory of Reflectance and Emittance Spectroscopy. Cambridge : Cambridge University Press.
Hare, J.P., Kroto, H.W. and Taylor, R., 1991. Preparation and UV / visible spectra of fullerenes C 60 and C 70. Chemical Physics Letters, 177(4): 394-398.
Hauck, S.A., Dombard, A.J., Phillips, R.J. and Solomon, S.C., 2004. Internal and tectonic evolution of Mercury. Earth and Planetary Science Letters, 222(3): 713-728.
Hawkins, S.E., Boldt, J.D., Darlington, E.H., Espiritu, R., Gold, R.E., Gotwols, B., Grey, M.P., Hash, C.D., Hayes, J.R., Jaskulek, S.E., Kardian, C.J., Keller, M.R., Malaret, E.R., Murchie, S.L., Murphy, P.K., Peacock, K., Prockter, L.M., Reiter, R.A., Robinson, M.S., Schaefer, E.D., Shelton, R.G., Sterner, R.E., Taylor, H.W., Watters, T.R. and Williams, B.D., 2007. The Mercury Dual Imaging System on the MESSENGER Spacecraft. Space science reviews, 131(1-4): 247-338.
Hayne, P.O., Bandfield, J.L., Siegler, M.A., Vasavada, A.R., Ghent, R.R., Williams, J.P., Greenhagen, B.T., Aharonson, O., Elder, C.M., Lucey, P.G. and Paige, D.A., 2017. Global Regolith Thermophysical Properties of the Moon From the Diviner Lunar Radiometer Experiment. Journal of Geophysical Research: Planets, 122(12): 2371-2400.
Hays, L. (Editor), 2015. NASA Astrobiology Strategy.
Hays, L. and Beaty, D., 2017. Conference Report: Biosignature Preservation and Detection in Mars Analog Environments, pp. 1.
Hays, L.E., Graham, H.V., Des Marais, D.J., Hausrath, E.M., Horgan, B., McCollom, T.M., Parenteau, M.N., Potter-McIntyre, S.L., Williams, A.J. and Lynch, K.L., 2017. Biosignature Preservation and Detection in Mars Analog Environments. Astrobiology, 17(4): 363-400.
He, K., Xiangyu, Z., Shaoqing, R. and Jian, S., 2015. Delving Deep into Rectifiers: Surpassing Human-Level Performance on ImageNet Classification. IEEE, pp. 1026-1034.
He, K., Xiangyu, Z., Shaoqing, R. and Jian, S., 2016. Deep Residual Learning for Image Recognition. IEEE, pp. 770-778.
Head, J.W., Murchie, S.L., Prockter, L.M., Solomon, S.C., Strom, R.G., Chapman, C.R., Watters, T.R., Blewett, D.T., Gillis-Davis, J.J., Fassett, C.I., Dickson, J.L., Hurwitz, D.M. and Ostrach, L.R., 2009. Evidence for intrusive activity on Mercury from the first MESSENGER flyby. Earth and Planetary Science Letters, 285(3-4): 251-262.

Heiken, G., Vaniman, D.T. and French, B.M., 1991. The Lunar sourcebook: a user's guide to the moon. Cambridge University Press, New York, NY.

Helbert, J., Maturilli, A. and Amore, M., 2013. Visible and near-infrared reflectance spectra of thermally processed synthetic sulfides as a potential analog for the hollow forming materials on Mercury. Earth and Planetary Science Letters, 369 370: 233.

Hemingway, B.S., Robie, R.A. and Wilson, W.H., 1973. Specific heats of lunar soils, basalts, and breccias from the Apollo 14, 15, and 16 landing sites between 90 and 350 K Lunar and Planetary Science Conference, pp. 2481 - 2487.

Hemingway, B.S., Krupka, K.M. and Robie, R.A., 1981. Heat capacities of the alkali feldspars between 350 and 1000 K from diffential scanning calorimtry, the thermodynamic functions of the alkali feldspars from 298.15 to 1400 K, and the reaction quartz + jadeite = analbite. American Mineralogist, 66: 14.

Hess, S., Henry, R. and Tillman, J., 1979. The seasonal variation of atmospheric pressure on Mars as affected by the south polar cap. Journal of Geophysical Research: Solid Earth, 84(B6): 2923-2927.

Heymann, D., Chibante, L.P.F., Brooks, R.R., Wolbach, W.S. and Smalley, R.E., 1994. Fullerenes in the Cretaceous-Tertiary boundary layer. Science, 265(5172): 645 - 647.

Heymann, D., 1995. Search for ancient fullerenes in anthraxolite, shungite, and thucolite, pp. 237-239.

Heymann, D., Chibante, L.P.F. and Smalley, R.E., 1995. Determination of C 60 and C 70 fullerenes in geologic materials by high-performance liquid chromatography. Journal of Chromatography A, 689(1): 157-163.

Heymann, D., Jenneskens, L.W., Jehlička, J., Koper, C. and Vlietstra, E., 2003. Terrestrial and Extraterrestrial Fullerenes. Fullerenes, Nanotubes and Carbon Nanostructures, 11(4): 333-370.

Hiesinger, H. and Helbert, J., 2010. The Mercury Radiometer and Thermal Infrared Spectrometer (MERTIS) for the BepiColombo mission. Planetary and Space Science, 58(1-2): 144-165.

Hiesinger, H., Helbert, J., Alemanno, G., Bauch, K.E., D'Amore, M., Maturilli, A., Morlok, A., Reitze, M.P., Stangarone, C., Stojic, A.N., Varatharajan, I. and Weber, I., 2020. Studying the Composition and Mineralogy of the Hermean Surface with the Mercury Radiometer and Thermal Infrared Spectrometer (MERTIS) for the BepiColombo Mission: An Update. Space science reviews, 216(6).

Hirabayashi, M., Fassett, C.I., Minton, D.A., Collins, G.C., Davison, T.M. and Ermakov, A.I., 2018. Topographic Diffusion as a Cause of Variations in Crater Density on Ceres., Lunar and Planetary Science Conference., Houston, TX.

Hofmeister, A. and Rossman, G., 1984. Determination of Fe 3+ and Fe 2+ concentrations in feldspar by optical absorption and EPR spectroscopy. Physics and Chemistry of Minerals, 11(5): 213-224.

Houston, J. and Hartley, A.J., 2003. The central Andean west-slope rainshadow and its potential contribution to the origin of hyper-aridity in the Atacama Desert. International Journal of Climatology, 23(12): 1453-1464.
Houston, J., 2006. Evaporation in the Atacama Desert: An empirical study of spatio-temporal variations and their causes. Journal of Hydrology, 330(3): 402-412.
Hubbard, G.S., Naderi, F.M. and Garvin, J.B., 2002. Following the water, the new program for Mars exploration. Acta astronautica, 51(1): 337-350.
Humayun, M., Nemchin, A., Zanda, B., Hewins, R.H., Grange, M., Kennedy, A., Lorand, J.P., Göpel, C., Fieni, C., Pont, S. and Deldicque, D., 2013. Origin and age of the earliest Martian crust from meteorite NWA 7533. Nature, 503(7477): 513.
Jaakkola, S.T., Ravantti, J.J., Oksanen, H.M. and Bamford, D.H., 2015. Buried Alive: Microbes from Ancient Halite. Trends in microbiology (Regular ed.), 24(2): 148-160.
Jakosky, B.M., Zurek, R.W., Byrne, S., Calvin, W., Curry, S., Ehlmann, B., Eigenbrode, J., Hoehler, T.M., Horgan, B., Hubbard, S., McCollom, T.M., Mustard, J., Putzig, N., Rucker, M., Wolff, M. and Wordsworth, R.D., 2020. Mars, the Nearest Habitable World - A Comprehensive Program for Future Mars Exploration.
Johnson, J., 1958. Analysis of image forming systems, Image Intensifier Symposium. Warfare Electrical Engineering Department, U.S. Army Research and Development Laboratories, Ft. Belvoir, Va.
Kadhim, M.A. and Abed, M.H., 2020. Convolutional Neural Network for Satellite Image Classification. In: M. Huk, M. Maleszka and E. Szczerbicki (Editors), Intelligent Information and Database Systems: Recent Developments. Studies in Computational Intelligence, ACIIDS.
Kargel, J.S., 2013. Mercury's Hollows: Chalcogenide Pyro-Thermokarst Analog of Thermokarst on Earth Mars and Titan [2840], Lunar and Planetary Science Conference. LPI, Houston, TX.
Kasting, J.F. and Catling, D., 2003. Evolution of a Habitable Planet. Annual review of astronomy and astrophysics, 41(1): 429-463.
Keane, J.T., Matsuyama, I., Kamata, S. and Steckloff, J.K., 2016. Reorientation and faulting of Pluto due to volatile loading within Sputnik Planitia. Nature (London), 540(7631): 90-93.
Kerber, L., Head, J.W., Solomon, S.C., Murchie, S.L., Blewett, D.T. and Wilson, L., 2009. Explosive volcanic eruptions on Mercury: Eruption conditions, magma volatile content, and implications for interior volatile abundances. Earth and Planetary Science Letters, 285(3): 263-271.
Kerber, L., Head, J.W., Blewett, D.T., Solomon, S.C., Wilson, L., Murchie, S.L., Robinson, M.S., Denevi, B.W. and Domingue, D.L., 2011. The global distribution of pyroclastic deposits on Mercury: The view from MESSENGER flybys 1-3. Planetary and Space Science, 59(15): 1895-1909.

Kerr, A., Rafuse, H., Sparkes, G., Hinchey, J. and Sandeman, H., 2011. Visble/Infrared spectroscopy (VIRS) as a research tool in economic geology: background and pilot studies from Newfoundland and Labrador. Geological Survey Report, 11(1): 145-166.

Khan, A., Sohail, A., Zahoora, U. and Qureshi, A.S., 2020. A survey of the recent architectures of deep convolutional neural networks. The Artificial intelligence review, 53(8): 5455.

Killen, R., Cremonese, G., Lammer, H., Orsini, S., Potter, A., Sprague, A., Wurz, P., Khodachenko, M., Lichtenegger, H., Milillo, A. and Mura, A., 2007. Processes that Promote and Deplete the Exosphere of Mercury. Space Science Reviews, 132(2-4): 433-509.

Killen, R.M., Potter, A.E., Vervack, R.J., Bradley, E.T., McClintock, W.E., Anderson, C.M. and Burger, M.H., 2010. Observations of metallic species in Mercury's exosphere. Icarus, 209(1): 75-87.

Kinczyk, M.J., Prockter, L.M., Byrne, P.K., Susorney, H.C.M. and Chapman, C.R., 2020. A morphological evaluation of crater degradation on Mercury: Revisiting crater classification with MESSENGER data. Icarus (New York, N.Y. 1962), 341: 113637.

Kingma, D.P. and Ba, J., 2015. Adam: A Method for Stochastic Optimization. CoRR, abs/1412.6980.

Kirk, R.L. and Stevenson, D.J., 1989. The competition between thermal contraction and differentiation in the stress history of the Moon. Journal of Geophysical Research, 94(B9): 12133.

Klima, R.L., Denevi, B.W., Ernst, C.M., Murchie, S.L. and Peplowski, P.N., 2018. Global Distribution and Spectral Properties of Low-Reflectance Material on Mercury. Geophysical Research Letters, 45(7): 2945-2953.

Knibbe, J.S. and van Westrenen, W., 2017. On Mercury's past rotation, in light of its large craters. Icarus, 281: 1-18.

Kokaly, R.F., Clark, R.N., Swayze, G.A., Livo, K.E., Hoefen, T.M., Pearson, N.C., Wise, R.A., Benzel, W.M., Lowers, H.A., Driscoll, R.L. and Klein, A.J., 2017. USGS Spectral Library Version 7. 1035, Reston, VA.

Kozlov, B.N., Kirillov, S.N. and Marnyrin, B.A., 1997. Formation of fullerenes in laser ablation of graphite in a vacuum. Proc. SPIE, 3093(NLMI 9): 233.

Krätschmer, W., Lowell, D.L., Fostiropoulos, K. and Donald, R.H., 1990. Solid C60: a new form of carbon. Nature, 347(6291): 354.

Kring, D.A., 2000. Impact events and their effect on the origin, evolution, and distribution of life. GSA Today, 10(8): 1-7.

Krizhevsky, A., Sutskever, I. and Hinton, G., 2017. ImageNet classification with deep convolutional neural networks. Communications of the ACM, 60(6): 84-90.

Kroto, H., 1992. C60 : the celestial sphere which fell to earth. Nanotechnology, 3(3): 111-112.

Kroto, H.W., Heath, J.R., O'Brien, S.C., Curl, R.F. and Smalley, R.E., 1985. C60: Buckminsterfullerene. Nature(318): 162-163.

Kroto, H.W., 1990. Fullerene cage clusters. The key to the structure of solid carbon. Journal of the Chemical Society, Faraday Transactions, 86(13): 2465-2468.
Lakshminarayanan, B., Pritzel, A. and Blundell, C., 2017. Simple and Scalable Predictive Uncertainty Estimation using Deep Ensembles, NIPS.
Lammer, H., Bredehöft, J.H., Coustenis, A., Khodachenko, M.L., Kaltenegger, L., Grasset, O., Prieur, D., Raulin, F., Ehrenfreund, P., Yamauchi, M., Wahlund, J.E., Grießmeier, J.M., Stangl, G., Cockell, C.S., Kulikov, Y.N., Grenfell, J.L. and Rauer, H., 2009. What makes a planet habitable? The Astronomy and astrophysics review, 17(2): 181-249.
Latifovic, R., Pouliot, D. and Campbell, J., 2018. Assessment of Convolution Neural Networks for Surficial Geology Mapping in the South Rae Geological Region, Northwest Territories, Canada. Remote Sensing, 10(307).
Leckey, J.H. and Nulf, L.E., 1994. Thermal decomposition of mercuric sulfide, Oak Ridge Y-12 Plant.
LeCun, Y., Boser, B., Denker, J.S., Henderson, D., Howard, R.E., Hubbard, W. and Jackel, L.D., 1989. Backpropagation Applied to Handwritten Zip Code Recognition. Neural Computation, 1(4): 541-551.
LeCun, Y., Bengio, Y. and Hinton, G., 2015. Deep learning. Nature, 521(7553): 436-444.
Ledlow, M.J., Burns, J.O., Gisler, G.R., Zhao, J.H., Zeilik, M. and Baker, D.N., 1992. Subsurface emissions from mercury: VLA radio observations at 2 and 6 centimeters. Astrophysical Journal, 384(2): 640-655.
Leonard, G.J. and Tanaka, K.L., 2001. Geologic map of the Hellas Region of Mars. In: G. Survey and A. United States. National Aeronautics and Space (Editors), Hellas Region of Mars. Reston, VA : The Survey ; Denver, CO : For sale by USGS Information Services, Reston, VA : Denver, CO.
Lodders, K. and Fegley, B., 1998. The planetary scientist's companion. New York : Oxford University Press, New York.
Longhi, J., Walker, D. and Hays, J.F., 1976. Fe and Mg in plagioclase, Lunar and Planetary Science Conference. Pergamon Press, Houston, TX, pp. 1281-1300.
Longhi, J., 2003. A new view of lunar ferroan anorthosites: Postmagma ocean petrogenesis. Journal of Geophysical Research: Planets, 108(E8): n/a-n/a.
Luann, B., Theodore, E.B. and Louis, J.A., 1999. Higher fullerenes in the Allende meteorite. Nature, 400(6741): 227.
Lucchetti, A., Pajola, M., Galluzzi, V., Giacomini, L., Carli, C., Cremonese, G., Marzo, G.A., Ferrari, S., Massironi, M. and Palumbo, P., 2018. Mercury Hollows as Remnants of Original Bedrock Materials and Devolatilization Processes: A Spectral Clustering and Geomorphological Analysis. Journal of geophysical research. Planets, 123(9): 2365-2379.
Lundgaard, K. and Tegner, C., 2004. Partitioning of ferric and ferrous iron between plagioclase and silicate melt. Contributions to Mineralogy and Petrology, 147(4): 470-483.

Lynch, R.C., King, A.J., Farías, M.E., Sowell, P., Vitry, C. and Schmidt, S.K., 2012. The potential for microbial life in the highest-elevation (6000 m.a.s.l.) mineral soils of the Atacama region. Journal of Geophysical Research: Biogeosciences, 117(G2).

Lyon, R.J.P., 1965. Analysis of rocks by spectral infrared emission (8 to 25 microns). Economic Geology, 60(4): 715-736.

Maggiori, E., Tarabalka, Y., Charpiat, G. and Alliez, P., 2017. Convolutional Neural Networks for Large-Scale Remote-Sensing Image Classification. IEEE transactions on geoscience and remote sensing, 55(2): 645-657.

Malin, M.C., Caplinger, M.A. and Davis, S.D., 2001. Observational evidence for an active surface reservoir of solid carbon dioxide on Mars. Science (New York, N.Y.), 294(5549): 2146.

Malin, M.C., Bell, J.F., Cantor, B.A., Caplinger, M.A., Calvin, W.M., Clancy, R.T., Edgett, K.S., Edwards, L., Haberle, R.M., James, P.B., Lee, S.W., Ravine, M.A., Thomas, P.C. and Wolff, M.J., 2007. Context Camera Investigation on board the Mars Reconnaissance Orbiter. Journal of Geophysical Research: Planets, 112(E5): n/a-n/a.

Mangano, V., Massetti, S., Milillo, A., Mura, A., Orsini, S. and Leblanc, F., 2013. Dynamical evolution of sodium anisotropies in the exosphere of Mercury. Planetary and Space Science, 82-83(C): 1-10.

Marchi, S., Morbidelli, A. and Cremonese, G., 2005. Flux of meteoroid impacts on Mercury. Astronomy & Astrophysics, 431: 1123-1127.

Marchi, S., Chapman, C.R., Fassett, C.I., Head, J.W., Bottke, W.F. and Strom, R.G., 2013. Global resurfacing of Mercury 4.0–4.1 billion years ago by heavy bombardment and volcanism. Nature, 499(7456): 59.

Marinova, M., M. , Aharonson, O. and Asphaug, E., 2008. Mega-impact formation of the Mars hemispheric dichotomy. Nature, 453(7199): 1216.

Marmanis, D., Wegner, J.D., Galliani, S., Schindler, K., Datcu, M. and Stilla, U., 2016. SEMANTIC SEGMENTATION OF AERIAL IMAGES WITH AN ENSEMBLE OF CNNS. ISPRS annals of the photogrammetry, remote sensing and spatial information sciences, III-3: 473-480.

Masi, G., Cozzolino, D., Verdoliva, L. and Scarpa, G., 2016. Pansharpening by Convolutional Neural Networks. Remote sensing (Basel, Switzerland), 8(7): 594.

McCallum, I.S., 1980. The Stillwater Complex: A review of the geology. University of Washingotn, Seattle.

McClintock, W.E. and Lankton, M.R., 2007. The Mercury Atmospheric and Surface Composition Spectrometer for the MESSENGER Mission. Space science reviews, 131(1): 481-521.

McCubbin, F.M., Vander Kaaden, K.E., Peplowski, P.N., Bell, A.S., Nittler, L.R., Boyce, J.W., Evans, L.G., Keller, L.P., Elardo, S.M. and McCoy, T.J., 2017. A Low O/Si Ratio on the Surface of Mercury: Evidence for Silicon Smelting? Journal of Geophysical Research: Planets, 122(10): 2053-2076.

McEwen, A.S., Eliason, E.M., Bergstrom, J.W., Bridges, N.T., Hansen, C.J., Delamere, W.A., Grant, J.A., Gulick, V.C., Herkenhoff, K.E., Keszthelyi, L., Kirk, R.L., Mellon, M.T., Squyres, S.W., Thomas, N. and Weitz, C.M., 2007. Mars Reconnaissance Orbiter's High Resolution Imaging Science Experiment (HiRISE. Journal of Geophysical Research: Planets, 112(E5): n/a-n/a.

McKay, C.P., Friedmann, E.I., Gómez-Silva, B., Cáceres-Villanueva, L., Andersen, D.T. and Landheim, R., 2003. Temperature and moisture conditions for life in the extreme arid region of the Atacama desert: four years of observations including the El Niño of 1997-1998. Astrobiology, 3(2): 393.

McSween, H.Y., Grove, T.L. and Wyatt, M.B., 2003. Constraints on the composition and petrogenesis of the Martian crust. Journal of Geophysical Research: Planets, 108(E12): n/a-n/a.

Melezhik, V.A., Filippov, M.M. and Romashkin, A.E., 2004. A giant Palaeoproterozoic deposit of shungite in NW Russia: genesis and practical applications. Ore Geology Reviews, 24(1): 135-154.

Melosh, H.J., 1989. Impact cratering : a geologic process. New York : Oxford University Press ; Oxford : Clarendon Press, New York : Oxford.

Melosh, H.J., 2011. Planetary Surface Processes. Cambridge, UK ; New York : Cambridge University Press.

Mendis, D.A. and Axford, W.I., 1974. Satellites and Magnetospheres of the Outer Planets. Annual review of earth and planetary sciences, 2(1): 419-474.

MEPAG, 2018. Mars Scientific Goals, Objectives, Investigations, and Priorities: 2018. D. Banfield, ed., 81 p. white paper posted October, 2018 by the Mars Exploration Program Analysis Group (MEPAG) at https://mepag.jpl.nasa.gov/reports.cfm.

Mesnik, B., 2016. Detection, Recognition, and Identification - Thermal vs. Optical IP Camera. Kintronics IP Security Solutions, https://kintronics.com/detection-recognition-and-identification-using-thermal-imaging-vs-optical-ip-camera/.

Metelka, V., Baratoux, L., Jessell, M.W. and Naba, S., 2015. Visible and infrared properties of unaltered to weathered rocks from Precambrian granite-greenstone terrains of the West African Craton. Journal of African Earth Sciences, 112: 570-585.

Mintmire, J.W., 1996. Fullerene formation and annealing. Science, 272(5258): 45.

Minton, D.A., Fassett, C.I., Hirabayashi, M., Howl, B.A. and Richardson, J.E., 2019. The equilibrium size-frequency distribution of small craters reveals the effects of distal ejecta on lunar landscape morphology. Icarus (New York, N.Y. 1962), 326: 63-87.

Mitchell, D.L. and de Pater, I., 1994. Microwave Imaging of Mercury's Thermal Emission at Wavelengths from 0.3 to 20.5 cm. Icarus, 110(1): 2-32.

Mohit, P.S., Johnson, C.L., Barnouin-Jha, O., Zuber, M.T. and Solomon, S.C., 2009. Shallow basins on Mercury: Evidence of relaxation? Earth and planetary science letters, 285(3): 355-363.

Moore, J.M., Mellon, M.T. and Zent, A.P., 1996. Mass Wasting and Ground Collapse in Terrains of Volatile-Rich Deposits as a Solar System-Wide Geological Process: The Pre-Galileo View. Icarus, 122(1): 63-78.

Morgan, F., F., M.J., Wiseman, S.M., Seelos, F.P., Murchie, S.L., C., M.P. and Team, a.t.C., 2011. Improved algorithm for CRISM volcano scan atmospheric correction. Lunar and Planetary Science Conference, 42: #2453.

Morrison, D., 1970. Thermophysics of the planet Mercury. Space Sci Rev, 11(2): 271-307.

Morschhauser, A., Grott, M. and Breuer, D., 2011. Crustal recycling, mantle dehydration, and the thermal evolution of Mars. Icarus, 212(2): 541-558.

Murchie, S., Arvidson, R., Bedini, P., Beisser, K., Bibring, J.P., Bishop, J., Boldt, J., Cavender, P., Choo, T., Clancy, R.T., Darlington, E.H., Des Marais, D., Espiritu, R., Fort, D., Green, R., Guinness, E., Hayes, J., Hash, C., Heffernan, K., Hemmler, J., Heyler, G., Humm, D., Hutcheson, J., Izenberg, N., Lee, R., Lees, J., Lohr, D., Malaret, E., Martin, T., McGovern, J.A., McGuire, P., Morris, R., Mustard, J., Pelkey, S., Rhodes, E., Robinson, M., Roush, T., Schaefer, E., Seagrave, G., Seelos, F., Silverglate, P., Slavney, S., Smith, M., Shyong, W.J., Strohbehn, K., Taylor, H., Thompson, P., Tossman, B., Wirzburger, M. and Wolff, M., 2007. Compact Reconnaissance Imaging Spectrometer for Mars (CRISM) on Mars Reconnaissance Orbiter (MRO). Journal of Geophysical Research: Planets, 112(E5): n/a-n/a.

Murchie, S.L., Seelos, F.P., Hash, C.D., Humm, D.C., Malaret, E., McGovern, J.A., Choo, T.H., Seelos, K.D., Buczkowski, D.L., Morgan, M.F., Barnouin-Jha, O.S., Nair, H., Taylor, H.W., Patterson, G.W., Harvel, C.A., Mustard, J.F., Arvidson, R.E., McGuire, P., Smith, M.D., Wolff, M.J., Titus, T.N., Bibring, J.P. and Poulet, F., 2009. Compact Reconnaissance Imaging Spectrometer for Mars investigation and data set from the Mars Reconnaissance Orbiter's primary science phase. Journal of Geophysical Research-Planets, 114.

Murchie, S.L., Klima, R.L., Denevi, B.W., Ernst, C.M., Keller, M.R., Domingue, D.L., Blewett, D.T., Chabot, N.L., Hash, C.D., Malaret, E., Izenberg, N.R., Vilas, F., Nittler, L.R., Gillis-Davis, J.J., Head, J.W. and Solomon, S.C., 2015. Orbital multispectral mapping of Mercury with the MESSENGER Mercury Dual Imaging System: Evidence for the origins of plains units and low-reflectance material. Icarus, 254: 287-305.

Nair, A.M. and Mathew, G., 2014. Effect of bulk chemistry in the spectral variability of igneous rocks in VIS-NIR region: Implications to remote compositional mapping. International Journal of Applied Earth Observations and Geoinformation, 30: 227-237.

Nakayama, H., Yamaguchi, H., Sasaki, S. and Shimizu, H., 1996. Pressure-temperature phase diagram of molecular crystal H2S by Raman spectroscopy. Physica. B, Condensed matter, 219-220: 523-525.

Namur, O., Charlier, B., Pirard, C., Hermann, J., Liegeois, J.-P. and Auwera, J.V., 2011. Anorthosite formation by plagioclase flotation in ferrobasalt and implications for the lunar crust.(Report). Geochimica et Cosmochimica Acta, 75(17): 4998.

Neal, R.M., 1996. Bayesian Learning for Neural Networks. Lecture Notes in Statistics, 118. Springer New York, New York, NY.

Newman, M.J. and Rood, R.T., 1977. Implications of Solar Evolution for the Earth's Early Atmosphere. Science (New York, N.Y.), 198(4321): 1035.

Nielsen, M.A., 2015. Neural Networks and Deep Learning. Determination Press.

Nimmo, F. and Tanaka, K., 2005. Early crustal evolution of Mars. Annual Review of Earth and Planetary Science, 33: 133-161.

Nisbet, E., Zahnle, K., Gerasimov, M.V., Helbert, J., Jaumann, R., Hofmann, B.A., Benzerara, K. and Westall, F., 2007. Creating Habitable Zones, at all Scales, from Planets to Mud Micro-Habitats, on Earth and on Mars. Space science reviews, 129(1): 79-121.

Nittler, L.R., Starr, R.D., Weider, S.Z., McCoy, T.J., Boynton, W.V., Ebel, D.S., Ernst, C.M., Evans, L.G., Goldsten, J.O., Hamara, D.K., Lawrence, D.J., McNutt, R.L., Schlemm, C.E., Solomon, S.C. and Sprague, A.L., 2011. The major-element composition of Mercury’s surface from MESSENGER X-ray spectrometry. Science (New York, N.Y.), 333(6051): 1847.

NRC, 2011. Vision and voyages for planetary science in the decade 2013-2022. In: S. National Research Council . Committee on the Planetary Science Decadal, B. National Research Council . Space Studies and S. National Research Council . Division on Engineering and Physical (Editors), Washington, D.C.

Oehler, D.Z. and Etiope, G., 2017. Methane Seepage on Mars: Where to Look and Why. Astrobiology, 17(12): 1233.

Onstott, T.C., Ehlmann, B.L., Sapers, H., Coleman, M., Ivarsson, M., Marlow, J.J., Neubeck, A. and Niles, P., 2019. Paleo-Rock-Hosted Life on Earth and the Search on Mars: A Review and Strategy for Exploration. Astrobiology, 19(10): 123-1262.

Osinski, G.R., Spray, J.G. and Lee, P., 2001. Impact-induced hydrothermal activity within the Haughton impact structure, arctic Canada: Generation of a transient, warm, wet oasis. Meteoritics & Planetary Science, 36(5): 731-745.

Osinski, G.R., Tornabene, L.L., Banerjee, N.R., Cockell, C.S., Flemming, R., Izawa, M.R.M., McCutcheon, J., Parnell, J., Preston, L.J., Pickersgill, A.E., Pontefract, A., Sapers, H.M. and Southam, G., 2013. Impact-generated hydrothermal systems on Earth and Mars. Icarus, 224(2): 347-363.

Osterloo, M.M., Hamilton, V.E., Bandfield, J.L., Glotch, T.D., Baldridge, A.M., Christensen, P.R., Tornabene, L.L. and Anderson, F.S., 2008. Chloride-bearing materials in the southern highlands of Mars. Science (New York, N.Y.), 319(5870): 1651.

Osterloo, M.M., Anderson, F.S., Hamilton, V.E. and Hynek, B.M., 2010. Geologic context of proposed chloride-bearing materials on Mars. Journal of Geophysical Research: Planets, 115(E10): n/a-n/a.

Paige, D.A., Siegler, M.A., Harmon, J.K., Neumann, G.A., Mazarico, E.M., Smith, D.E., Zuber, M.T., Harju, E., Delitsky, M.L. and Solomon, S.C., 2013. Thermal stability of volatiles in the north polar region of Mercury. Science (New York, N.Y.), 339(6117): 300.

Pajola, M., Lucchetti, A., Semenzato, A., Poggiali, G., Munaretto, G., Galluzzi, V., Marzo, G.A., Cremonese, G., Brucato, J.R., Palumbo, P. and Massironi, M., 2021. Lermontov crater on Mercury: Geology, morphology and spectral properties of the coexisting hollows and pyroclastic deposits. Planetary and Space Science, 195: 105136.

Palafox, L.F., Hamilton, C.W., Scheidt, S.P. and Alvarez, A.M., 2017. Automated detection of geological landforms on Mars using Convolutional Neural Networks. Computers & geosciences, 101: 48-56.

Pandeya, Y.R. and Lee, J., 2021. Deep learning-based late fusion of multimodal information for emotion classification of music video. Multimedia Tools and Applications, 80(2): 2887-2905.

Papike, J.J., Karner, J.M., Shearer, C.K. and Burger, P.V., 2009. Silicate mineralogy of martian meteorites. Geochimica et cosmochimica acta, 73(24): 7443-7485.

Parman, S.W., Parmentier, E.M. and Wang, S., 2016. Crystallization of Mercury's Sulfur-Rich Magma Ocean [2990], Lunar and Planetary Science Conference.

Peplowski, P.N., Lawrence, D.J., Evans, L.G., Klima, R.L., Blewett, D.T., Goldsten, J.O., Murchie, S.L., Mccoy, T.J., Nittler, L.R., Solomon, S.C., Starr, R.D. and Weider, S.Z., 2015. Constraints on the abundance of carbon in near-surface materials on Mercury: Results from the MESSENGER Gamma-Ray Spectrometer. Planetary and Space Science, 108: 98-107.

Peplowski, P.N., Klima, R.L., Lawrence, D.J., Ernst, C.M., Denevi, B.W., Frank, E.A., Goldsten, J.O., Murchie, S.L., Nittler, L.R. and Solomon, S.C., 2016. Remote sensing evidence for an ancient carbon- bearing crust on Mercury. Nature Geoscience, 9: 273-278.

Pettengill, G.H. and Dyce, R.B., 1965. A Radar Determination of the Rotation of the Planet Mercury. Nature, 206(4990): 1240.

Phillips, M.S., Emery, J.P. and Moersch, J.E., 2016. Hollows on Mercury: No geographic trends in reflectance [2178], Lunar and Planetary Science Conference.

Phillips, R.J., Zuber, M.T., Solomon, S.C., Golombek, M.P., Jakosky, B.M., Banerdt, W.B., Smith, D.E., Williams, R.M.E., Hynek, B.M., Aharonson, O. and Hauck, S.A., II, 2001. Ancient geodynamics and global-scale hydrology on Mars. Science, 291(5513): 2587-2591.

Piatek, J.L., Hardgrove, C., Moersch, J.E., Drake, D.M., Wyatt, M.B., Rampey, M., Carlisle, O., Warren-Rhodes, K., Dohm, J.M., Hock, A.N., Cabrol, N.A.,

Wettergreen, D.S., Grin, E.A., Diaz, G.C., Coppin, P., Weinstein, S., Cockell, C.S., Marinangeli, L., Ori, G.G., Smith, T., Jonak, D., Wagner, M., Stubbs, K., Thomas, G., Pudenz, E. and Glasgow, J., 2007. Surface and subsurface composition of the Life in the Atacama field sites from rover data and orbital image analysis. Journal of Geophysical Research-Biogeosciences, 112(G4).

Pierazzo, E. and Chyba, C.F., 1999. Amino acid survival in large cometary impacts. Meteoritics & Planetary Science, 34(6): 909-918.

Pieters, C.M., 1986. Composition of the lunar highland crust from near-infrared spectroscopy. Reviews of geophysics (1985), 24(3): 557-578.

Pizzarello, S., Huang, Y., Becker, L., Poreda, R.J., Nieman, R.A., Cooper, G. and Williams, M., 2001. The Organic Content of the Tagish Lake Meteorite. Science, 293(5538): 2236-2239.

Pollard, W.G. and Present, R.D., 1948. On gaseous self-diffusion in long capillary tubes. Physical Review, 73(7): 762-774.

Potter, A. and Morgan, T., 1985. Discovery of Sodium in the Atmosphere of Mercury. Science, 229(4714): 651-653.

Potter, R.W.K. and Head, J.W., 2017. Basin formation on Mercury: Caloris and the origin of its low-reflectance material. Earth and Planetary Science Letters, 474(C): 427-435.

Poulet, F., Rodriguez-Ferreira, J., Arondel, A., Dassas, K., Eng, P., Lami, P., Langevin, Y., Longval, Y., Pradel, P. and Dami, M., 2015. The pre-flight calibration setup of the instrument SIMBIO-SYS onboard the mission BepiColombo. Planetary and Space Science, 117: 82-95.

Pueyo, J.J., Chong, G. and Jensen, A., 2001. Neogene evaporites in desert volcanic environments: Atacama Desert, northern Chile. Sedimentology, 48(6): 1411-1431.

Radicati Di Brozolo, F., Bunch, T.E., Fleming, R.H. and Macklin, J., 1994. Fullerenes in an impact crater on the LDEF spacecraft. Nature(369): 37 - 40.

Rankin, D.W.H., 2009. CRC handbook of chemistry and physics, 89th edition, edited by David R. Lide. Taylor & Francis Group, pp. 223-224.

Rathbun, J.A. and Squyres, S.W., 2002. Hydrothermal Systems Associated with Martian Impact Craters. Icarus, 157(2): 362-372.

Reiss, P.M., 2019. In-situ Thermal Extraction of Volatiles from Lunar Regolith, Technical University of Munich, Munich.

Righter, K., Hervig, R. and Kring, D., 1998. Accretion and core formation on Mars: molybdenum contents of melt inclusion glasses in three SNC meteorites. Geochimica et Cosmochimica Acta, 62(12): 2167-2177.

Riner, M.A., Lucey, P.G., Desch, S.J. and McCubbin, F.M., 2009. Nature of opaque components on Mercury: Insights into a Mercurian magma ocean. Geophysical Research Letters, 36.

Riner, M.A., 2012. Spectral effects of space weathering on Mercury: The role of composition and environment. Geophysical research letters, 39(12).

Rivera-Valentin, E.G. and Barr, A.C., 2014. Impact-induced compositional variations on Mercury. Earth and Planetary Science Letters, 391(C): 234-242.

Robinson, M.S., Murchie, S.L., Blewett, D.T., Domingue, D.L., Hawkins, S.E., Head, J.W., Holsclaw, G.M., McClintock, W.E., McCoy, T.J., McNutt, R.L., Prockter, L.M., Solomon, S.C. and Watters, T.R., 2008. Reflectance and color variations on Mercury: Regolith processes and compositional heterogeneity. Science, 321(5885): 66-69.

Rodríguez-Albornoz, C., 2018. Geology and controls on microbiota of the Salar de Pajonales (7.209.000 - 7.226.500 N. - 510.000 – 530.000 E), Universidad Católica del Norte Antofagasta, Antofagasta, Northern Chile.

Rogers, A.D. and Nekvasil, H., 2015. Feldspathic rocks on Mars: Compositional constraints from infrared spectroscopy and possible formation mechanisms. Geophysical Research Letters, 42(8): 2619-2626.

Ronneberger, O., Fischer, P. and Brox, T., 2015. U-Net: Convolutional Networks for Biomedical Image Segmentation. Lecture Notes in Computer Science. Springer International Publishing, Cham, pp. 234-241.

Rosenblatt, F., 1962. Principles of neurodynamics; perceptrons and the theory of brain mechanisms. Spartan Books, Washington.

Rothery, D., Marinangeli, L., Anand, M., Carpenter, J., Christensend, U., Crawford, I.A., De Sanctis, M.C., Epifani, E.M., Erard, S., Frigeri, A., Fraser, G., Hauber, E., Helbert, J., Hiesinger, H., Joy, K.H., Langevin, Y., Massironi, M., Milillo, A., Mitrofanov, I., Muinonen, K., Naranen, J., Pauselli, C., Potts, P., Warell, J. and Wurz, P., 2010. Mercury's surface and composition to be studied by BepiColombo. Planetary and Space Science, 58(1-2): 21-39.

Rothery, D.A., 2015. Planet Mercury : From Pale Pink Dot to Dynamic World. Cham : Springer International Publishing : Imprint: Springer.

Rothery, D.A., Massironi, M., Alemanno, G., Barraud, O., Besse, S., Bott, N., Brunetto, R., Bunce, E., Byrne, P., Capaccioni, F., Capria, M.T., Carli, C., Charlier, B., Cornet, T., Cremonese, G., D'Amore, M., De Sanctis, M.C., Doressoundiram, A., Ferranti, L., Filacchione, G., Galluzzi, V., Giacomini, L., Grande, M., Guzzetta, L.G., Helbert, J., Heyner, D., Hiesinger, H., Hussmann, H., Hyodo, R., Kohout, T., Kozyrev, A., Litvak, M., Lucchetti, A., Malakhov, A., Malliband, C., Mancinelli, P., Martikainen, J., Martindale, A., Maturilli, A., Milillo, A., Mitrofanov, I., Mokrousov, M., Morlok, A., Muinonen, K., Namur, O., Owens, A., Nittler, L.R., Oliveira, J.S., Palumbo, P., Pajola, M., Pegg, D.L., Penttilä, A., Politi, R., Quarati, F., Re, C., Sanin, A., Schulz, R., Stangarone, C., Stojic, A., Tretiyakov, V., Väisänen, T., Varatharajan, I., Weber, I., Wright, J., Wurz, P. and Zambon, F., 2020. Rationale for BepiColombo Studies of Mercury's Surface and Composition. Space science reviews, 216(4).

Rottensteiner, F., Sohn, G., Jung, J., Gerke, M., Baillard, C., Benitez, S. and Breitkopf, U., 2012. THE ISPRS BENCHMARK ON URBAN OBJECT CLASSIFICATION AND 3D BUILDING RECONSTRUCTION. ISPRS

annals of the photogrammetry, remote sensing and spatial information sciences, I-3: 293-298.
Rottensteiner, F., Sohn, G., Gerke, M. and Wegner, J.D., 2014. Theme section "Urban object detection and 3D building reconstruction". ISPRS Journal of Photogrammetry and Remote Sensing, 93: 143-144.
Rubincam, D.P., 2003. Polar wander on Triton and Pluto due to volatile migration. Icarus, 163(2): 469-478.
Ruff, S.W., Farmer, J.D., Calvin, W.M., Herkenhoff, K.E., Johnson, J.R., Morris, R.V., Rice, M.S., Arvidson, R.E., Bell, J.F., Christensen, P.R. and Squyres, S.W., 2011. Characteristics, distribution, origin, and significance of opaline silica observed by the Spirit rover in Gusev crater, Mars. Journal of Geophysical Research: Planets, 116(E7).
Ruff, S.W. and Farmer, J.D., 2016. Silica deposits on Mars with features resembling hot spring biosignatures at El Tatio in Chile. Nature communications, 7: 13554.
Rumble, J.R. (Editor), 2018. CRC handbook of chemistry and physics. Chemical Rubber Company handbook of chemistry and physics. Cleveland, Ohio, CRC Press., Cleveland, Ohio.
Russakovsky, O., Deng, J., Su, H., Krause, J., Satheesh, S., Ma, S., Huang, Z., Karpathy, A., Khosla, A., Bernstein, M., Berg, A.C. and Fei-Fei, L., 2015. ImageNet Large Scale Visual Recognition Challenge. International journal of computer vision, 115(3): 211-252.
Salvail, J.R. and Fanale, F.P., 1994. Near-Surface Ice on Mercury and the Moon: A Topographic Thermal Model. Icarus, 111(2): 441-455.
Santos, A.R., Agee, C.B., McCubbin, F.M., Shearer, C.K., Burger, P.V., Tartèse, R. and Anand, M., 2015. Petrology of igneous clasts in Northwest Africa 7034: Implications for the petrologic diversity of the martian crust. Geochimica et Cosmochimica Acta, 157: 56-85.
Sautter, V., Fabre, C., Forni, O., Toplis, M.J., Cousin, A., Ollila, A.M., Meslin, P.Y., Maurice, S., Wiens, R.C., Baratoux, D., Mangold, N., Le Mouélic, S., Gasnault, O., Berger, G., Lasue, J., Anderson, R.A., Lewin, E., Schmidt, M., Dyar, D., Ehlmann, B.L., Bridges, J., Clark, B. and Pinet, P., 2014. Igneous mineralogy at Bradbury Rise: The first ChemCam campaign at Gale crater. Journal of Geophysical Research: Planets, 119(1): 30-46.
Sautter, V., Toplis, M.J., Wiens, R.C., Cousin, A., Fabre, C., Gasnault, O., Maurice, S., Forni, O., Lasue, J., Ollila, A., Bridges, J.C., Mangold, N., Le Mouelic, S., Fisk, M., Meslin, P.Y., Beck, P., Pinet, P., Le Deit, L., Rapin, W., Stolper, E.M., Newsom, H., Dyar, D., Vaniman, D., Clegg, S. and Wray, J.J., 2015. In situ evidence for continental crust on early Mars. Nature Geoscience(8): 605-609.
Scheinberg, A., Elkins-Tanton, L.T. and Zhong, S.J., 2014. Timescale and morphology of Martian mantle overturn immediately following magma ocean solidification. Journal of Geophysical Research: Planets, 119(3): 454-467.

Schmidt, M.E., Farrand, W.H., Johnson, J.R., Schroder, C., Hurowitz, J.A., McCoy, T.J., Ruff, S.W., Arvidson, R.E., Marais, D.J.D., Lewis, K.W., Ming, D.W., Squyres, S.W. and de Souza, P.A., 2009. Spectral, mineralogical, and geochemical variations across Home Plate, Gusev Crater, Mars indicate high and low temperature alteration. Earth and Planetary Science Letters, 281(3-4): 258-266.

Schreiner, S.S., Dominguez, J.A., Sibille, L. and Hoffman, J.A., 2016. Thermophysical property models for lunar regolith.(Report). Advances in Space Research, 57(5): 1209.

Schubert, G., Ross, M.N., Stevenson, D.J. and Spohn, T., 1988. Mercury's thermal history and the generation of its magnetic field. In: F. Vilas, C.R. Chapman and M.S. Matthews (Editors), Mercury. University of Arizona Press, Tucson, pp. 429-460.

Schwenzer, S.P. and Kring, D.A., 2009. Impact-generated hydrothermal systems capable of forming phyllosilicates on Noachian Mars. Geology (Boulder), 37(12): 1091-1094.

Sclar, C.B. and Kastelic, R.L., 1979. Iron in Anorthite: an Experimental Study, pp. 1087.

Seelos, F.P., S. L. Murchie, D. C. Humm, O. S. Barnouin, M. F. Morgan, H. W. Taylor, C. Hash and Team, a.t.C., 2011. CRISM data processing and analysis products update—Calibration, correction, and visualization. Lunar and Planetary Science Conference, 42: #1438.

Seelos, F.P., M. F. Morgan, H. W. Taylor, S. L. Murchie, D. C. Humm, K. D. Seelos, O. S. Barnouin, C. E. Viviano and Team, a.t.C., 2012. CRISM Map Projected Targeted Reduced Data Records (MTRDRs)—High level analysis and visualization data products. Planetary Data: A Workshop for Users and Software Developers.

Seelos, F.P., Viviano-Beck, C.E., Morgan, M.F., Romeo, G., Aiello, J.J. and Murchie, S.L., 2016. CRISM Hyperspectral Targeted Observation PDS Product Sets — TERs and MTRDRs. Lunar and Planetary Science Conference: 1783.

Seelos, F.P. and Murchie, S.L., 2018. CRISM Mapping Data Empirical Radiometric Reconciliation for the Next-Generation Mars Global Multispectral Map. Lunar and Planetary Science Conference: 2325.

Seelos, F.P., Cartwright, S.F.A., Romeo, G. and Murchie, S.L., 2019. CRISM Next Generation Mars Global Multispectral Map - Hydrated Mineralogy Spectral Parameter Mapping, pp. 2635.

Serventi, G., Carli, C., Sgavetti, M., Ciarniello, M., Capaccioni, F. and Pedrazzi, G., 2013. Spectral variability of plagioclase–mafic mixtures (1): Effects of chemistry and modal abundance in reflectance spectra of rocks and mineral mixtures. Icarus, 226(1): 282-298.

Serventi, G., Carli, C. and Sgavetti, M., 2015. Spectral variability of plagioclase-mafic mixtures (3): Quantitative analysis applying the MGM algorithm. Icarus, 254: 34.

Shelhamer, E., Long, J. and Darrell, T., 2016. Fully Convolutional Networks for Semantic Segmentation. arXiv:1605.06211.
Sherrah, J., 2016. Fully Convolutional Networks for Dense Semantic Labelling of High-Resolution Aerial Imagery. ArXiv, abs/1606.02585.
Sidike, P., Asari, V.K. and Sagan, V., 2018. Progressively Expanded Neural Network (PEN Net) for hyperspectral image classification: A new neural network paradigm for remote sensing image analysis. ISPRS journal of photogrammetry and remote sensing, 146: 161-181.
Smith, J.V. and Brown, W.L., 1988. Chemical Properties, Feldspar Minerals: Volume 1 Crystal Structures, Physical, Chemical, and Microtextural Properties. Springer Berlin Heidelberg, Berlin, Heidelberg, pp. 298-390.
Smith, S., W., 1988. Digital Signal Processing.
Soderblom, L.A., 1970. A model for small-impact erosion applied to the lunar surface. Journal of Geophysical Research, 75(14): 2655-2661.
Solomon, S.C., McNutt, R.L., Gold, R.E. and Domingue, D.L., 2007. MESSENGER Mission Overview. Space science reviews, 131(1-4): 3-39.
Solomon, S.C., 2018. Mercury : the view after Messenger. View after Messenger.
Sori, M.M., 2018. A thin, dense crust for Mercury. Earth and Planetary Science Letters, 489: 92-99.
Soter, S. and Ulrichs, J., 1967. Rotation and Heating of the Planet Mercury. Nature, 214(5095): 1315.
Spencer, J.R. and Denk, T., 2010. Formation of Iapetus' extreme albedo dichotomy by exogenically triggered thermal ice migration. Science (American Association for the Advancement of Science), 327(5964): 432-435.
Sprague, A.L., Hunten, D.M. and Lodders, K., 1995. Sulfur at Mercury, elemental at the poles and sulfides in the Regolith. Icarus, 118(1): 211.
Spudis, P.D., 2001. The Geological History of Mercury. In: M. Robinson (Editor), Workshop on Mercury: Space Environment, Surface, and Interior., The Field Museum, Chicago, IL.
Squyres, S.W., Arvidson, R.E., Bell, J.F., Calef, F., Clark, B.C., Cohen, B.A., Crumpler, L.A., de Souza, P.A., Farrand, W.H., Gellert, R., Grant, J., Herkenhoff, K.E., Hurowitz, J.A., Johnson, J.R., Jolliff, B.L., Knoll, A.H., Li, R., McLennan, S.M., Ming, D.W., Mittlefehldt, D.W., Parker, T.J., Paulsen, G., Rice, M.S., Ruff, S.W., Schroder, C., Yen, A.S. and Zacny, K., 2012. Ancient Impact and Aqueous Processes at Endeavour Crater, Mars. Science, 336(6081): 570-576.
Srivastava, N., Hinton, G., Krizhevsky, A., Sutskever, I. and Salakhutdinov, R., 2014. Dropout: a simple way to prevent neural networks from overfitting. J. Mach. Learn. Res., 15(1): 1929–1958.
Stan-Lotter, H., S. Leuko, A. Legat and Fendrihan, S., 2006. The assessment of the viability of halophilic microorganisms in natural communities. Elsevier, Methods in Microbiology: Extremophiles: 15.

Stolper, E.M., Baker, M.B., Newcombe, M.E., Schmidt, M.E., Treiman, A.H., Cousin, A., Dyar, M.D., Fisk, M.R., Gellert, R., King, P.L., Leshin, L., Maurice, S., McLennan, S.M., Minitti, M.E., Perrett, G., Rowland, S., Sautter, V. and Wiens, R.C., 2013. The petrochemistry of Jake_M: a martian mugearite. Science (American Association for the Advancement of Science), 341(6153): 1239463-1239463.

Summons, R.E., Amend, J.P., Bish, D., Buick, R., Cody, G.D., Des Marais, D.J., Dromart, G., Eigenbrode, J.L., Knoll, A.H. and Sumner, D.Y., 2011. Preservation of Martian organic and environmental records: final report of the Mars biosignature working group.(News & Views: Report). Astrobiology, 11(2): 157.

Tanaka, K.L., Robbins, S.J., Fortezzo, C.M., Skinner, J.A. and Hare, T.M., 2014. The digital global geologic map of Mars: Chronostratigraphic ages, topographic and crater morphologic characteristics, and updated resurfacing history, pp. 11.

Thomas, R.J., Rothery, D.A., Conway, S.J. and Anand, M., 2014. Hollows on Mercury: Materials and mechanisms involved in their formation. Icarus, 229: 221-235.

Thomas, R.J., Hynek, B.M., Rothery, D.A. and Conway, S.J., 2016. Mercury's low-reflectance material: Constraints from hollows. Icarus, 277: 455-465.

Thrun, S., 1996. Explanation-Based Neural Network Learning: A Lifelong Learning Approach. Kluwer Academic Publishers, Boston, MA.

Tjaden, B., Cooper, S.J., Brett, D.J., Kramer, D. and Shearing, P.R., 2016. On the origin and application of the Bruggeman correlation for analysing transport phenomena in electrochemical systems. Current Opinion in Chemical Engineering, 12(C): 44-51.

Trang, D., Lucey, P.G. and Izenberg, N.R., 2017. Radiative transfer modeling of MESSENGER VIRS spectra: Detection and mapping of submicroscopic iron and carbon. Icarus, 293: 206-217.

Trang, D., Gasda, P.J., Corley, L.M., Gillis-Davis, J.J. and Lucey, P.G., 2018. Space Weathering of Graphite: Application to Mercury, Lunar and Planetary Science Conference.

Tschermak, G., 1864. Die Feldspatgruppe.

Ueberhuber, C.W., 1997. Numerical Computation 1: Methods, Software, and Analysis. Springer Berlin / Heidelberg, Berlin, Heidelberg.

Ulrichs, J. and Campbell, M.J., 1969. Radiative heat transfer in the lunar and mercurian surfaces. Icarus, 11(2): 180-188.

Vander Kaaden, K.E. and McCubbin, F.M., 2015. Exotic crust formation on Mercury: Consequences of a shallow, FeO- poor mantle. Journal of Geophysical Research: Planets, 120(2): 195-209.

Vasavada, A.R., Paige, D.A. and Wood, S.E., 1999. Near-Surface Temperatures on Mercury and the Moon and the Stability of Polar Ice Deposits. Icarus, 141(2): 179-193.

Vaughan, W.M., Helbert, J., Blewett, D.T., Head, J.W., Murchie, S., Gwinner, K., McCoy, T.J. and Solomon, S.C., 2012. Hollow-forming layers in impact craters on Mercury: Massive sulfide or chloride deposits formed by impact melt differentiation? Lunar and Planetary Science Conference, 43.

Ventra, D., Diaz, G.C. and boer, P.l., 2013. Colluvial sedimentation in a hyperarid setting (Atacama Desert, northern Chile): Geomorphic controls and stratigraphic facies variability. Sedimentology, 60(5): 1257.

Vilas, F., Domingue, D.L., Helbert, J., D'Amore, M., Maturilli, A., Klima, R.L., Stockstill-Cahill, K.R., Murchie, S.L., Izenberg, N.R., Blewett, D.T., Vaughan, W.M. and Head, J.W., 2016. Mineralogical indicators of Mercury's hollows composition in MESSENGER color observations. Geophysical Research Letters, 43(4): 1450-1456.

Viviano-Beck, C.E., Seelos, F.P., Murchie, S.L., Kahn, E.G., Seelos, K.D., Taylor, H.W., Taylor, K., Ehlmann, B.L., Wisemann, S.M., Mustard, J.F. and Morgan, M.F., 2014. Revised CRISM spectral parameters and summary products based on the currently detected mineral diversity on Mars. Journal of Geophysical Research: Planets, 119(6): 1403-1431.

Wagner, R.J., Wolf, U., Ivanov, B.A. and Neukum, G., 2001. Application of an Updated Impact Cratering Chronology Model to Mercury's Time-Stratigraphic System. In: M. Robinson (Editor), Workshop on Mercury: Space Environment, Surface, and Interior., The Field Museum, Chicago, IL.

Wakabayashi, S. and Matsumoto, K., 2006. Development of slope mobility testbed using simulated lunar soil. JAXA research and development memorandum.

Wang, H., Jiang, J. and Zhang, G., 2018. CraterIDNet: An End-to-End Fully Convolutional Neural Network for Crater Detection and Identification in Remotely Sensed Planetary Images. Remote sensing (Basel, Switzerland), 10(7): 1067.

Wang, Y., Liu, Y. and Wang, Y., 2020a. Oxidation absorption of hydrogen sulfide from gas stream using vacuum ultraviolet/H2O2/urea wet scrubbing system. Process safety and environmental protection, 140: 348-355.

Wang, Y., Xiao, Z., Chang, Y. and Cui, J., 2020b. Lost Volatiles During the Formation of Hollows on Mercury. Journal of geophysical research. Planets, 125(9): n/a.

Warren, J.K., 2016. Evaporites: A Geological Compendium. Springer International Publishing AG, Cham.

Warren-Rhodes, K., Rhodes, K., Pointing, S., Ewing, S., Lacap, D., Gómez-Silva, B., Amundson, R., Friedmann, E. and McKay, C., 2006. Hypolithic Cyanobacteria, Dry Limit of Photosynthesis, and Microbial Ecology in the Hyperarid Atacama Desert. Microbial Ecology, 52(3): 389-398.

Warren-Rhodes, K., Weinstein, S., Dohm, J., Piatek, J., Minkley, E., Hock, A., Cockell, C., Pane, D., Ernst, L.A., Fisher, G., Emani, S., Waggoner, A.S., Cabrol, N.A., Wettergreen, D.S., Apostolopoulos, D., Coppin, P., Grin, E., Diaz, C., Moersch, J., Oril, G.G., Smith, T., Stubbs, K., Thomas, G., Wagner, M. and Wyatt, M., 2007. Searching for microbial life remotely:

Satellite-to-rover habitat mapping in the Atacama Desert, Chile. Journal of Geophysical Research: Biogeosciences, 112(G4): G04S05-n/a.
Warren-Rhodes, K., Cabrol, N., Phillips, M., Tebes, C., Hinman, N.W., Rhodes, K., Ayma, D., Bishop, J., Boyle, L., Chong-díaz, G., Demergasso, C., Hofmann, M., Hutchinson, N., Javiera, C., Moersch, J., Mondro, C., Noffke, N., Parro, V., Rodriguéz, C., Sabron, P., Sarazzain, P., Wettergreen, D., Zacny, K. and Team, S.I.N., in review. Decoding Microbial Spatial Patterns as a Blueprint for Biosignature Detection on Mars and Beyond.
Watson, K., Murray, B.C. and Brown, H., 1961. The behavior of volatiles on the lunar surface. Journal of Geophysical Research, 66(9): 3033-3045.
Watson, K., 1964. The thermal conductivity measurements of selected silicate powders in vacuum from 150 to 350 K, California Institute of Technology.
Wei, H., Feng, R., Wang, L. and Gao, L., 2018. Adaptive Spatial-Scale-Aware Deep Convolutional Neural Network for High-Resolution Remote Sensing Imagery Scene Classification, IGARSS 2018 - 2018 IEEE International Geoscience and Remote Sensing Symposium, pp. 4736-4739.
Weider, S., Nittler, L., Starr, R.D., Boynton, W., Evans, L., Goldsten, J., McCoy, T., McNutt, R., Schlemm, C.E., Solomon, S.C. and Sprague, A.L., 2011. MAJOR-ELEMENT ABUNDANCES OF SURFACE MATERIALS ON MERCURY: FIRST RESULTS FROM THE MESSENGER X-RAY SPECTROMETER. Meteorit. Planet. Sci., 46: A248-A248.
Weider, S.Z., Nittler, L.R., Starr, R.D., McCoy, T.J., Stockstill-Cahill, K.R., Byrne, P.K., Denevi, B.W., Head, J.W. and Solomon, S.C., 2012. Chemical heterogeneity on Mercury's surface revealed by the MESSENGER X-Ray Spectrometer. Journal of Geophysical Research: Planets, 117(E12).
Weider, S.Z., Nittler, L.R., Starr, R.D., Crapster-Pregont, E.J., Peplowski, P.N., Denevi, B.W., Head, J.W., Byrne, P.K., Hauck, S.A., Ebel, D.S. and Solomon, S.C., 2015. Evidence for geochemical terranes on Mercury: Global mapping of major elements with MESSENGER's X-Ray Spectrometer. Earth and Planetary Science Letters, 416: 109-120.
Weider, S.Z., Nittler, L.R., Murchie, S.L., Peplowski, P.N., McCoy, T.J., Kerber, L., Klimczak, C., Ernst, C.M., Goudge, T.A., Starr, R.D., Izenberg, N.R., Klima, R.L. and Solomon, S.C., 2016. Evidence from MESSENGER for sulfur- and carbon-driven explosive volcanism on Mercury. Geophysical Research Letters, 43(8): 3653-3661.
Wenk, H. and Wilde, W., 1973. Chemical anomalies of lunar plagioclase, described by substitution vectors and their relation to optical and structural properties. Contributions to Mineralogy and Petrology, 41(2): 89-104.
Westall, F., Foucher, F., Bost, N., Bertrand, M., Loizeau, D., Vago, J.L., Kminek, G., Gaboyer, F., Campbell, K.A., Bréhéret, J.-G., Gautret, P. and Cockell, C.S., 2015. Biosignatures on Mars: What, Where, and How? Implications for the Search for Martian Life. Astrobiology, 15(11): 998-1029.
Whipple, F.L., 1950. A comet model. I. The acceleration of Comet Encke. The Astrophysical Journal, 111: 375.

White, S.M., Crisp, J.A. and Spera, F.J., 2006. Long-term volumetric eruption rates and magma budgets. Geochemistry, Geophysics, Geosystems, 7(3): <xocs:firstpage xmlns:xocs=""/>.

Whittaker, R.H., Levin, S.A. and Root, R.B., 1973. Niche, Habitat, and Ecotope. The American naturalist, 107(955): 321-338.

Wieczorek, M., Knapmeyer-Endrun, B., Panning, M., Plesa, A.C., McLennan, S., Nimmo, F., Gyalay, S., Michaut, C., Broquet, A., Samuel, H., Rivoldini, A., Smrekar, S.E. and Banerdt, W.B., 2021. Global Character of the Martian Crust Revealed by InSight Seismic Data, Lunar and Planetary Science Conference. LPI, Virtual.

Wieczorek, M.A., Correia, A., Le Feuvre, M., Laskar, J. and Rambaux, N., 2012. Mercury's spin-orbit resonance explained by initial retrograde and subsequent synchronous rotation. Nat. Geosci., 5(1): 18-21.

Wilson, L. and Head, J.W., 2007. Heat transfer in volcano–ice interactions on Earth. Annals of Glaciology, 45: 83-86.

Wood, J.A., Dickey, J.S., Jr., , Marvin, U.B. and Powell, B.N., 1970. Lunar anorthosites and a geophysical model of the moon. Proceedings of the Apollo 11 Lunar Science Conference, 1(Mineraolgy and Petrology): 965.

Woods, M., Karachalios, S., Petrocelli, D., Barrett, A., Balme, M. and Joudrier, L., 2020. NOAH-H: Automatic Classification of HIRISE Images Using Deep Learning Applied to EXOMARS Landing Site Selection Support and Future Mars Rover Operations [#5080], i-SAIRAS2020, Virtual Conference.

Wray, J.J., Hansen, S.T., Dufek, J., Swayze, G.A., Murchie, S.L., Seelos, F.P., Skok, J.R., Irwin, R.P. and Ghiorso, M.S., 2013. Prolonged magmatic activity on Mars inferred from the detection of felsic rocks. Nature Geoscience, 6(12): 1013-1017.

Wright, J., Conway, S.J., Morino, C., Rothery, D.A., Balme, M.R. and Fassett, C.I., 2020. Modification of Caloris ejecta blocks by long-lived mass-wasting: A volatile-driven process? Earth and planetary science letters, 549: 116519.

Wu, J., Milkereit, B. and Boerner, D., 1995. Seismic Imaging of the Enigimatic Sudbury Structure. Journal Of Geophysical Research-Solid Earth, 100(B3): 4117-4130.

Xiao, Z.Y., Strom, R.G., Blewett, D.T., Chapman, C.R., Denevi, B.W., Head, J.W., Fassett, C.I., Braden, S.E., Gwinner, K., Solomon, S.C., Murchie, S., Watters, T.R. and Banks, M.E., 2012. The Youngest Geologic Terrains on Mercury, Lunar and Planetary Science Conference.

Xiao, Z.Y., Strom, R.G., Blewett, D.T., Byrne, P.K., Solomon, S.C., Murchie, S.L., Sprague, A.L., Domingue, D.L. and Helbert, J., 2013. Dark spots on Mercury: A distinctive low-reflectance material and its relation to hollows. Journal of Geophysical Research-Planets, 118(9): 1752-1765.

Yan, N., Chassefiere, E., Leblanc, F. and Sarkissian, A., 2006. Thermal model of Mercury's surface and subsurface; impact of subsurface physical heterogeneities on the surface temperature. In: R. Grard (Editor). Oxford-New York, International: Elsevier, Oxford-New York, pp. 583-588.

Yaws, C.L., 2014. Thermophysical properties of chemicals and hydrocarbons.
Ye, C. and Glotch, T.D., 2019. Spectral Properties of Chloride Salt-Bearing Assemblages: Implications for Detection Limits of Minor Phases in Chloride-Bearing Deposits on Mars. Journal of geophysical research. Planets, 124(2): 209-222.
Yu, Y., Zhang, T., Zheng, L. and Yu, J., 2013. Photocatalytic degradation of hydrogen sulfide using TiO2 film under microwave electrodeless discharge lamp irradiation. Chemical engineering journal (Lausanne, Switzerland : 1996), 225: 9-15.
Zhang, J.A. and Paige, D.A., 2009. Cold-trapped organic compounds at the poles of the Moon and Mercury: Implications for origins. Geophysical Research Letters, 36(L16203).
Zhong, S. and Zuber, M.T., 2001. Degree-1 mantle convection and the crustal dichotomy on Mars. Earth and Planetary Science Letters, 189(1): 75-84.
Zhou, B., Lapedriza, A., Xiao, J., Torralba, A. and Oliva, A., 2014. Learning deep features for scene recognition using places database, Proceedings of the 27th International Conference on Neural Information Processing Systems - Volume 1. MIT Press, Montreal, Canada, pp. 487–495.
Zolotov, M.Y., Sprague, A.L., Hauck, S.A., Nittler, L.R., Solomon, S.C. and Weider, S.Z., 2013. The redox state, FeO content, and origin of sulfur-rich magmas on Mercury. Journal of Geophysical Research: Planets, 118(1): 138-146.

VITA

Michael S. Phillips was born in Harrison, OH on September 16, 1991, to Jack and Christina Phillips. Upon graduating High School, he received a full tuition scholarship to attend Marietta College in Marietta, OH. He earned his Bachelor of Science degree from Marietta College in 2014, majoring in Geology, minoring in Mathematics, earning *magna cum laude* honors, and membership in the Phi Beta Kappa honor society as well as the Kappa Mu Epsilon Mathematics honor society. After a brief (and boring) foray in the insurance industry, he spent a year in West Virginia working as a substitute K-12 teacher and with Young Life Ministry. He then commenced his graduate studies in the Fall of 2015 at The University of Tennessee, Knoxville. While at UTK, Michael earned the Chancellor's Fellowship, the Dawn and Lawrence Taylor Doctoral Research Fellowship, a NASA Mars Data Analysis Program grant, and the award for Professional Promise presented by the Department of Earth and Planetary Sciences Faculty. Michael will continue his research career at the Johns Hopkins University Applied Physics Laboratory as a postdoctoral researcher.